ATCHAFALAYA BAR CHANNEL NUMERICAL HYDRODYNAMIC AND FLUID / SETTLED MUD MODELING

Allen M. Teeter and Billy H. Johnson
Computational Hydraulics and Transport LLC
PO Box 569
Edwards, Ms 39066

September 2005

Prepared for: U.S. Army Corps of Engineers, New Orleans District

US Army Corps of Engineers ®

New Orleans District

CONTENTS

EXECUTIVE SUMMARY

A numerical model study was performed as part of a feasibility study of Lower Atchafalaya River channel deepening. Since the existing channel is difficult to maintain, a limited study of structural alternatives that might alleviate shoaling was also performed. The 20-ft-deep by 400-ft-wide bar channel extends some 18 miles offshore of Atchafalaya Bay to provide assess to the Gulf of Mexico. The channel was cut through shallow water and is not confined by jetties. Fine-grained sediment shoals form quickly with controlling depths of 13-14 ft at shoal peaks typically located near the extent of salinity intrusion, which for normal conditions is offshore, and where depths outside the channel are only about 10 ft.

Because of funding limitations, annual maintenance dredging of the bar channel has been limited to about 10 Mcyd even though project depths are not always maintained. Various operational measures have been tried by the U.S. Army Corps of Engineers, yet project depths have not been maintained for more than a couple of months each year. The mass of sediment dredged annually, though large, represents only about 5 percent of the estimated annual sediment outflow from the bay. Wind-wave resuspended bed sediment contributes most to suspended sediment in the area surrounding the channel and currents regularly cross the channel, flowing mainly to the west. The source and transport mode of shoal material can still be debated but likely involve intermittent suspended transport of river-derived sediments in a wide area offshore of the bay as well as in the channel.

The three-dimensional, curvilinear, hydrostatic hydrodynamics model CH3DZ was modified to include single-grain, cohesive sediment suspended transport and bed transport of fluid mud on a slope. Fluid mud and settled-bed sedimentation processes were included. A model mesh extending 60 miles long-shore and about 40 miles cross-shore was developed. The model has about 3,000 surface and 20,000 total cells with a maximum of 25 layers. Each layer is 2 ft thick except for the top layer where the thickness varies with the tide. Year-long simulations were performed for the period of 2001-2002 when extensive field data were collected.

After the model was validated to field data, the existing channel (24-ft-deep with over-depth and advanced maintenance allowances) was deepened to 30 and 38 feet total-depth and lengthened by 8.7 and 14.3 miles to reach appropriate water depths for testing in the model. Both existing and +50-yr future conditions were modeled, though shoaling results were not significantly different. Final shoal volume, a measure of the maintenance volume presently dredged annually, increased by 115 and 170 percent for 30- and 38-ft-deep channels. Increases for hypothetical two-dredging cycles per year maintenance were 108 and 156 percent. The average shoaling rate, related to how

quickly the shoal forms and how long project conditions persist after dredging, increased by 101 and 137 percent relative to the existing 24 ft channel.

Structural plans involving 13 alternative jetties, artificial reefs (similar to long lateral dikes), and combinations thereof were tested, some with 24- and some with 38-ft-deep channels. Equal-length, continuous jetty pairs of 14.2- to 22.5-mile length reduced final shoal volume by 30 to 62 percent relative to base conditions. Jetty pairs reduced shoal volumes by maintaining channel flows and thus increasing current speeds, blocking lateral flows across the channel, and reducing channel salinities. Shoals were displaced to mainly seaward of the jettied channels. Plan tests indicated that there is probably an optimum amount of flow to contain in a jettied channel. Too much flow increased shoal volume seaward of jettied channel. A plan with a single jetty on the up-drift (east) side of the channel was found to be about as effective as an equal-length jetty pair. The single jetty had an opposite effect on channel salinities. A 10.7-mile-long artificial reef extending across the bar channel at its inshore end reduced final shoal volume by 24 percent and average shoaling rate by 47 percent relative to base conditions. Reefs were intended to divert bay outflow, along with riverine sediments, from the vicinity of the bar channel.

As an add-on to the original work, three value-engineering plans including (a) flanking sediment traps, (b) channel cross-cuts as a destratification measure, and (c) a sloped channel reach with a sump were tested in the model. The latter came closest to meeting design objectives that were to allow newly-deposited fluid mud to slide on the slope into the sump before they gained hydraulic shear strength. While the sloped-channel sump was kept clear by dredging, project depths over 15,000 ft of the plan reach were maintained and another 5,000 ft reach had reduced shoal heights.

LIST OF TABLES

LIST OF FIGURES

PREFACE

The U.S. Army Corps of Engineers District, New Orleans, funded this modeling study of the Lower Atchafalaya River (LAR) Bar Channel under contract DACW-29-02-C-0072. The study was part of a feasibility study for channel deepening and was conducted between 2003 and 2005. The points of contact in the District were Ms. Nancy Powell, Chief Hydrology Section, and Mr. Dave Beck.

Dr. Nan D. Walker of Louisiana State University's Coastal Studies Institute provided information from the BAYWATCH monitoring system and her cooperation in assembling these data is acknowledged.

Drs. Billy H. Johnson and Allen M. Teeter of Computational Hydraulics and Transport LLC (CHT) located in Edwards, Mississippi, conducted the study and prepared the report. This report should be cited as:

Teeter, A. M. and Johnson, B. H. (2005). "Atchafalaya Bar Channel Numerical Hydrodynamic and Fluid / Settled Mud Modeling," Computational Hydraulics and Transport LLC, Edwards, Mississippi.

ATCHAFALAYA BAR CHANNEL NUMERICAL HYDRODYNAMIC AND FLUID / SETTLED MUD MODELING

PART I: INTRODUCTION

Background

The U.S. Army Engineer District, New Orleans, of the Mississippi Valley Division (MVN) is conducting a feasibility study for the deepening of the Lower Atchafalaya River (LAR) Bar Channel along with the navigation channels of the Atchafalaya River and the Chene, Boeuf, and Black Bayous originally authorized by Congress in 1911 and re-authorized at its present dimensions in 1968. The work discussed in this report only addresses the deepening of the LAR Bar Channel. This portion of the navigation project between channel station 475+00 and 1396+00 ft is the straight, 20-ft-deep by 400-ft-wide channel that extends 17.4 mi from the vicinity of Eugene Island (South Louisiana state plane 3,265,128 ft East and 316,885 ft North) out into the Gulf of Mexico to the present –24 ft MLG (Mean Low Gulf) contour (Figure 1). The basic shoaling problem in the bar channel is the formation of what is commonly called fluid mud, which is comprised of high concentrations (e.g. 5-300 g/l) of fine-grained sediments. As fluid mud develops, and concentrations increase to above 60-180 g/l, mud layers are formed that can no longer move as density currents.

The purpose of this study was to test shoaling response to channel depth and certain structural measures in a physics-based numerical model to help identify best approaches for project channel development.

This report is composed of Parts. Before presenting model results, several topics such as site conditions, fluid mud processes, data needs and sources, and modeling strategy are discussed. Site conditions, basic characteristics of fluid mud, and the particular processes in operation in the LAR Bar and Atchafalaya Bay system that result in the formation of bar-channel fluid mud are discussed in Part II. Data sources are

presented in Part III. The LAR Bar Channel model is described in Part IV and hydrodynamic model validation is presented in Part V. Sediment model validation, and results from production, sensitivity, and structural alternative runs are presented in Part VI. Numerical model sensitivity tests were performed as part of this study to shed light on sediment sources, as well as to test model sensitivity.

Additional details of the general approach are present in the next section. The modeling strategy, additional model developments required, the physical area represented, the approach for model validation, boundary conditions required, and scenarios to be simulated with the validated model are all discussed in this Part. Theoretical details of the numerical model are contained in Appendices A and B.

As an add-on to the original scope of work, three additional plans were tested in the model. These plans came from a November-2003 value-engineering workshop conducted by MVN to identify possible solutions to the LAR Bar Channel maintenance problems (GVI, 2003). Those test plans were not part of the feasibility study and required modification to the numerical grid. Model test descriptions and results are presented in Appendix C.

Modeling Approach

For the feasibility study, it is necessary to develop annual maintenance requirements for the bar channel both for existing and future conditions. To aid in the development of these requirements, the MVN requested that Computational Hydraulics and Transport LLC (CHT) develop a three-dimensional (3D) numerical hydrodynamic and sediment transport model of the LAR bar and bay system. The need for three-dimensional modeling is indicated by the occurrence of appreciable salinity and density stratification in the LAR Bar Channel. The basic computer code selected, upon which the final model is based, is called CH3DZ (Curvilinear Hydrodynamics in 3 Dimensions – Z Plane). With the addition of the fluid and settled mud computations embedded within CH3DZ, the resulting model is referred to as CH3DZ-FM. Computations are performed for the three components of the flow velocity, the two-dimensional water surface field, and the 3D salinity and suspended sediment fields, along with computations for the sediment bed.

As discussed in detail later, many different types of time and spatially varying data are required to conduct a large 3D numerical modeling study. The U.S. Army Engineer Research and Development Center (ERDC) collected data in and near the bar channel (Teeter et al. 2003). These data provided insight into the formation and transport of fluid mud in the channel, and were used in the validation of the 3D numerical model. In addition, data from the Louisiana State University (LSU) monitoring programs, along with data collected by the USGS and the MVN, were identified for use in the 3D model study. Available data and their sources are discussed in Part III.

The validated model was then used to address the impact on the formation of fluid mud due to channel deepening, future anticipated changes in bay bathymetry, and structural alternatives such as the construction of jetties and reefs. Each of these

scenarios was a one-year simulation. In addition, many sensitivity-type runs were made to assess the impact of varying the freshwater inflow and the sediment concentrations attached to it, varying the wind field, varying the sediment concentration on the open ocean boundary, varying the bed structure, and extending the numerical grid farther into the Gulf.

Model Developments

As previously noted, the particular hydrodynamic model that was selected for coupling with fluid / settled mud computations is called CH3DZ (Johnson, et al 1991, 1993). The Z-plane version of CH3D allows for an accurate computation of long-term stratification of salinity in a deep channel with shallow areas adjacent to the channel with modest grid resolution. CH3DZ has been applied in numerous studies to assess the impact of channel deepening, construction of dredged material disposal islands, etc on circulation and salinity in large water bodies. Examples are Upper Chesapeake Bay, Chesapeake and Delaware Canal, Delaware Estuary / River, and the San Juan Estuary (Kim and Johnson, 1998; Johnson, et al 1999; and Bunch, et al 2000). Theoretical details concerning CH3DZ are given in Appendix A.

A major effort in the early phase of the study was to develop the capability to model the transport of fine-grained sediments and the formation of a fluid mud layer capable of moving over non-moving mud layers in the LAR Bar Channel. As noted in Part II, fluid mud layers in the bar channel are generally about 2 m thick, with only the upper 0.5 m or less capable of moving as a fluid mud density current. Concentrations of the fine-grained sediment are generally around 150 to 350 g/l over the lower 1.5 m and 50 to 150 g/l in the moving fluid mud layer. These capabilities were accomplished by developing within CH3DZ a sediment transport / diffusion subroutine with settling / entrainment terms and a sediment bed module. As previously noted, the resulting model is called CH3DZ-FM. The theory behind the development of the fluid mud / settled mud module embedded in CH3DZ and fully coupled with the hydrodynamic computations is presented in Appendix B.

Since the density current is driven by the horizontal pressure gradient, it is a function of the combined influence of suspended sediment and salinity on the density of the water. Therefore, the equation of state for the water density was modified to reflect the contribution of suspended sediment to the water density.

Bottom sediments are susceptible to erosion and re-suspension into the water column, as well as, deposition to the bed. Erosion primarily results from wind driven waves. An algorithm based on an analytical approach was developed in CH3DZ-FM that utilizes specified winds to generate the contribution of wind-generated waves to the bottom shear stress.

As the computations proceed over a time frame of a year, dredging of the channel takes place. Developments in CH3DZ-FM allow the model user to prescribe dredging

locations and volumes. As channel bottom material is dredged and/or deposition takes place, the number of vertical layers representing the water depth changes with time.

Validation Approach

Model validation to field data involves showing how well the model reproduces water surface elevations, water velocity, salinity, suspended sediment concentrations, and the formation and transport of the channel fluid mud. Hydrodynamic model validation is performed first, since the sediment model is sensitive to hydrodynamic conditions. Validation concerning the formation and movement of fluid mud is demonstrated by showing how well the numerical model reproduces observed suspended sediment and shoal volumes. During the validation and production simulations, pre-programmed maintenance dredging is imposed along the channel. How well these dredging volumes can be imposed on the simulations depends on how well the model reproduces the formation and transport of fluid mud in the channel. In other words, if the dredging records indicate that X-volume of material was dredged in a particular location at a particular time, but the model does not show enough shoaling, the volume discrepancy is tabulated in model results. Vertical profiles of suspended sediment were compared at locations where field measurements were made. Vertical profiles in the fluid mud bed likewise allow comparison to field data. In addition, snapshots of the computed bar channel bottom profile are output and compared with observed channel profiles. Many one-year simulations were required to validate the model.

The period of record selected for model validation is important. Interior data must be available for comparison with model calculations along with boundary data to drive the model computations. Locations of ERDC data stations are shown in Figure 2. Interior data on water surface elevations, currents, and salinity were available from early 2001 through 2002 from the LSU BAYWATCH stations (Figure 1). Both these and the ERDC data were extremely useful for model validation. Another important consideration is whether the validation period contains many of the typical processes that impact the hydrodynamics of the water body, e.g., a range of freshwater inflows, fronts passing through that result in water surface setups and set-downs, etc. Since the period of September 2001 to August 2002 contains extensive interior data, appears to be representative of a typical year as far as the movement of fronts through the area, and contains a range of freshwater inflows, this period was selected for the model validation simulation.

Production Scenarios

After demonstrating that the numerical model accurately reproduces water surface elevations, water currents, salinity, suspended sediment concentrations, and the formation of fluid mud shoal in the navigation channel, the validated model was applied to determine the impact on salinity intrusion and dredging requirements in the channels of three different channel deepening plans, a future anticipated change in bay bathymetry, and structural alternatives such as jetties and reefs. The validated model was applied for each plan condition over the same simulation period as used for model validation, i.e.,

September 2001 to August 2002. However, to provide insight on the formation of fluid mud due to the freshwater inflow and the sediment attached to the inflow, ocean sediment boundary conditions, and wind fields, sensitivity runs were made with those boundary conditions varied.

PART II: CONDITIONS AFFECTING SHOAL FORMATION

Basin Inputs

The LAR Bar Channel is at the seaward end of the Atchafalaya River that receives from the Mississippi and Red Rivers 30 percent of their 31°-North-latitude combined flow. This inflow carries with it about 94 million tons per year of sediment into the top of the Atchafalaya River Basin. Some of this sediment load deposits in the basin or in the two deltas that have formed in the Atchafalaya Bay. The Atchafalaya Bay is a shallow bay complex with an average depth of about 5 ft, and is being filled by seaward-growing river deltas at the mouths of the LAR and Wax Lake Outlet. The Atchafalaya Bay area is shown in Figure 1.

Sediment delivered to the bay was reported to be 88 million tons per year by Huh et al. (1996). The Atchafalaya Bay traps an estimated 25 percent of the total sediment input (Thomas et al. 1988). About 76 percent of silts and 95 percent of clays were found to escape the bay. Accordingly, roughly 18 million dry-tons per year silts and 27 million dry-tons per year clays reach Eugene Island, the upstream end of the LAR Bar Channel. The average measured suspended loads (1979 to 1999) for LAR and Wax Lake Outlet is 82.2 million dry-tons per year (USACE 2002). Channel maintenance dredging amounts to roughly 3 million dry-tons of sediment per year (assuming average dredging and 400 dry-kg/m^3 solids content for dredged material).

The Atchafalaya Bay system is the site of a former active Mississippi River delta that was abandoned some 6,000 years ago. Processes of erosion and subsidence have formed open-water and lowland areas that can be seen today in the configuration of the bay system. Coastal Louisiana has been built by alternating Mississippi River deltas over geologic time. Presently, appreciable land area along this coastal region is being lost through erosion and subsidence (Letter 1982). As the result of active sedimentation processes, the coastal waters that flow past the LAR Bar Channel carry above-average concentrations of fine-grained sediments.

Coastal Conditions

The total area of the Atchafalaya, Cote Blanche, and Vermilion Bays is about 700 mi^2. Separating the Atchafalaya Bay from the coastal ocean is a remnant barrier called Point Au Fer Shell Reef. Previously, the reef had extensive subaerial areas. However, by the 1980s the subaerial extent of the reef was much reduced and depths were greater than was the case in the 1960s (Letter 1982).

The coastal area surrounding the LAR Bar Channel has depths ranging from 5 to 20 ft as seen in Figure 2. Salinities are unusually fresh for a coastal area due to the large

freshwater outflow from the Atchafalaya River and Bay. Depending on set-downs and setups in the water surface, surface salinities at mean discharge range from less than 0.5 to 5 ppt at the upstream end of the channel. The LAR Bar Channel is vertically stratified with respect to salinity. Salinities average about 6 ppt in Vermilion Bay (Donnell et al. 1991).

Tides are diurnal with a mean range of 1.9 ft at Eugene Island. DiMarco and Reid (1998) found diurnal and semi-diurnal tidal current components to be higher near the Atchafalaya Bay than elsewhere along the Texas-Louisiana continental shelf (5 and 6 cm/sec, respectively) and account for over 40 percent of the total current variance. The coastal drift is normally to the west at 5-10 cm/sec but can reverse direction for short periods of time during winter frontal passages. Adams, Wells, and Coleman (1982) made measurements of near-bottom currents directly seaward of the bar channel in 30-ft water depth. For the 4.5 months of observation, net flow was to the west (< 5 cm/sec) but was punctuated with short but intense flows to the east associated with winter storms. Fluid mud accretes along the eastern Chanier Plain coast down-drift (west) of the Atchafalaya Bay complex (Huh et al. 2001).

Current measurements made in 2002 adjacent to the channel (Teeter et al. 2003) indicated currents predominantly to the west crossing the channel (68 percent of all occurrences), typically at 30 cm/sec and with maximums of 60 to 80 cm/sec. Net flows were to the west, typically 10 cm/sec. Coastal flows sweep east to west across the upper channel water column while currents near the channel bottom are primarily upstream as the result of density and mixing effects associated with river flow into coastal waters (gravitational circulation).

Frontal passages are frequent, occurring 30-40 times per year (Huh et al. 2001), and associated wind and atmospheric pressure fluctuations cause appreciable setups and set-downs in water levels. Walker and Hammack (2000) reported average water level changes for the ten largest 1995-1996 front-forced events in Atchafalaya Bay were 0.7-1.0 m. The results of these water level changes were large NW-SE exchanges of water between the Atchafalaya Bay system and the coastal ocean. Wind events also are responsible for greatest resuspension and suspended sediment concentrations (Walker and Hammack 2000).

Channel-bottom sediments in the LAR Bar Channel are fine mud. Sediment grain size information from a 1996 MVN pre-dredging sampling (16 channel samples) indicated average 16, 50, and 84 percentile size values of 1, 7, and 51 μm, respectively (Teeter et al. 2003). There were trends in grain-size statistics along the channel. The sorting statistic had the most significant seaward-decreasing trend (p-value < 0.01). There was a joint seaward trend for the channel sediments to be finer, better sorting (smaller sorting), and more skewed toward the fine end of the distribution (p-value < 0.05). This trend could reflect deposition occurring down the channel north-to-south.

Surficial bed sediments on an 8- by 8-nautical-mile grid surrounding the LAR Bar Channel had mean grain sizes ranging from 7 to 41 μm (Teeter et al. 2003). Sediment

was significantly coarser (mean size 16 versus 12 μm) and more graded (sorting 4.1 versus 3.8) to the east of the channel. Trends in the grain size statistics indicated sediment transport to the west. Moisture content and organic content (loss on ignition) averaged 115 percent and 5.8 percent.

General Fluid Mud Characteristics

Fluid mud refers to a concentrated suspension of fine-grained, cohesive sediment. Several properties distinguish fluid mud from other natural suspensions: (a) fluid muds are slow to settle; (b) fluid muds have flow properties very different from water; and (c) fluid muds form sharp interfaces with overlying suspensions. As a result of these properties, fluid muds can concentrate in certain locations and cause maintenance problems in coastal navigation channels. Examples of U.S. harbor channels where fluid mud has occurred include Savannah, Charleston, Mayport, Calcasieu, Sabine, Mobile, Gulfport, and San Francisco Bay (USACE 1991; Alexander et al. 1997). The only U.S. open-coastal area where fluid muds deposit is along the eastern Chanier Plain, Louisiana. Fluid mud, associated with large river and sediment inflows, also occurs along the coasts of Korea, China, India, the North Sea, and Brazil (for example, see Vinzon and Paiva 2002). Fluid mud can also occur in localized areas near fine-grained, dredged material disposal operations (Teeter 2000).

Cohesion between fine-grained sediment particles, especially clays, has a great influence on fluid mud formation and characteristics. Cohesion results when fine clay-mineral and organic particles collide and form aggregates. Electrical and London-van der Waals forces, Brownian motion, fluid shear, and differential particle settling are some of the factors which cause particles to aggregate. Electrostatic layers surround clay particles and aggregates, resulting in effective solids volume much greater than the space actually occupied, cushion inter-particle collisions, and restrict water movement. The more aggregate bonds formed per unit volume the more cohesive the sediment becomes.

Therefore, sediment volume concentration, clay type, particle-size distribution and shape influence cohesion. Ionic concentration or salinity, and other water chemistry conditions, are also important. When particles come into sufficiently close contact, they can form tight, primary bonds, which are not easily broken by shear. Clays are platy particles, and bonds can be edge-to-face, edge-to-edge, or face-to-face. Particles can aggregate at greater inter-particle distances, but the resulting bonds are much weaker and easily broken. Organic filaments add to most natural mud structures. Natural muds are composed of sediments arranged in a number of aggregate orientations and a corresponding range of bond strengths (USACE 1991).

Fluid mud exhibit hindered settling. Fine-grained suspensions have concentration-dependent settling rates, which increase up to a suspension concentration of roughly 1 g/l. Fluid muds, having concentrations of roughly 5 to 300 g/l, are in the concentration range where settling rate decreases with increasing concentration (USACE 1991). Floc and particle interactions cause this hindered settling behavior. Settling rates decrease by orders of magnitude over the fluid-mud concentration range. The result is

that a layer of fluid mud, once formed, will persist for some time before densifying. Physical disturbances such as wave motions and simple shearing or deposition disrupt the formation of water vents and further slows settling and consolidation (Teeter 2002).

Fluid mud exhibits density, viscous, elastic, and psuedo-plastic properties (resulting from cohesion) very different from water (Teeter 1992, 2000, and 2002). These properties can isolate and/or distinguish a fluid mud layer from overlying flow and bed layers. Fluid mud layers can resist turbulent impingement and mixing with an overlying suspension. A fluid mud layer can also move as the result of gravity, bed slope, or shear stress on its upper layer. For example, fluid mud layers have been observed to move with strong tidal flows in channels (Vinzon and Paiva 2002), away and down-slope from pipeline discharges (Teeter 2000), and near vessels underway in channels (Alexander et al. 1997).

Fluid mud forms sharp interfaces with overlying water columns and between fluid mud layers of varying fine-grained sediment concentrations. These properties have made depth determination problematic in fluid mud channels. Acoustic sounding instruments detect the reflections, which occur at sharp density steps or gradients in the medium. Conventional acoustic sounding devices operating at 200 kHz normally detect the fluid mud interface even though the lower-layer density may be quite low (10's g/l). Lower-frequency sounding devices often detect two or more depths associated with density steps, while lead-line soundings may measure a different depth level in the same channel (Alexander et al. 1997).

Fluid Mud Occurrence in the LAR Bar Channel

The Atchafalaya bar channel is a site where large quantities of fine-sediment, freshwater, and seawater converge to form fluid mud. Low-velocity and stratified flow conditions trap fluid mud near the channel bottom (Teeter et al. 2003). The surrounding water is shallow, suggesting that frequent dredging will be required (USACE 1991), and large shoal volumes occur. About 9 to 11 million cubic yards (Mcyd) are dredged from the LAR Bar Channel annually. Recent bathymetric surveys and sampling indicate that dredging has had limited success cleaning out the channel. The sources of channel-shoal sediments are not certain but probably associated with lateral currents across the channel. A discussion of sediment sources is presented in a later subsection.

Flocculated suspended material, formed in the channel by river-ocean mixing or moving laterally into the channel, tends to become trapped in the channel prism by a combination of settling, stratification-reduced turbulent mixing, and upstream near-bottom currents (Teeter et al. 2003). The profile of the LAR Bar Channel shoal has a peak or hump at about Channel Station 800+00 near ERDC stations C and D (Figure 1). Shoaling is rapid and steady state so final shoal volumes are developed only 60 days or so after dredging.

Recent fluid mud profiles performed by ERDC (Teeter et al. 2003) indicate that sharp vertical concentration gradients occur over the top 0.5 m of the shoal. Fluid-mud

concentrations near the shoal surface are 10 to 100 g/l and increase quickly with depth to 250 to 350 g/l. Considering the previous discussion, it is appropriate to separate fluid mud into two zones. The surface zone is most likely mobile while the deeper zone is static and will be referred to as the fluid mud bed.

Modes of Fluid Mud Transport

Under most flat-bottom conditions, fine-grained cohesive sediments are transported solely in suspension. Because maximum floc settling velocities are only 1-2 mm/sec, vertical cohesive sediment concentration profiles are more uniform, and material does not move in contact with the bed, as compared to the case of coarse-grained sediment transport. Another transport mode that might occur under low bed slope is fluid mud streaming. This can occur as a fluid mud layer, liquefied by vertical wave stresses and lacking hydraulic strength, is moved along the bed in the direction of residual wave motion (Sakakiyama and Bijker 1989). Where tidal energy is low and where most incident wave energy is dissipated by viscous losses within the fluid mud layer, wave-mean mass transport under non-breaking waves (fluid mud streaming) can be important transport mode (Mehta and Kirby 2001). Fluid mud layers are able to appreciably attenuate and transform surface waves into lower-frequency asymmetric quasi-solitary surface fluctuations.

Fluid mud streaming probably occurs along the Chanier Plain of southwest Louisiana where mud liquefaction and wave attenuation have been observed, the shoreline is prograding, and migrating mud banks are known to deposit mud layers on land (Wells 1983; Kemp 1986). The outflow plume of the Atchafalaya Bay, typically 30-40 km wide, eventually concentrates into a shore-attached mud stream with westward transport. The cross-shore extent of fluid mud is compressed as it migrates westward beginning off the Freshwater Bayou area (see Figure 1). Solitary waves have been observed here along with pronounced wave attenuation (Huh et al. 2001). The fluid mud transport is mainly cross-shore with only a small long-shore component. While Huh et al. (2001) did not use the term “fluid mud streaming,” the onshore wave transport of the mud they described appears to be the same as that described by Sakakiyama and Bijker (1989).

Several ERDC field observations suggest that fluid mud streaming is not operating near the LAR Bar Channel. Bed densities in the area adjacent to the channel, with average surface densities of about 1,400 kg/m^3 (range of about 1,300 to 1,680 kg/m^3, n=64), are higher than in areas where liquefaction of bed sediments has been observed. Reported representative measured bed densities include 1,080 kg/m^3 for Tampa Bay, below about 1,200 kg/m^3 for the density stratified Lake Okeechobee bed (Li and Mehta 2001), and less than 1,200 kg/m^3 for the Surinam coast of northeast South America (Wells and Coleman 1981). It is difficult to reconcile grain-size distributions from the area surrounding the channel to those of the channel shoal if direct mass transport of bed sediments were taking place into the channel shoal. Grain-size distributions of channel shoal sediment are finer and better-sorted than those of the nearby area indicating sediment reworking and grain-size segregation. Inspection of wave spectra from the area

adjacent to the bar channel suggests that high-frequency damping does not occur. Wave spectra exhibit normal spectral slopes and shapes. When bimodal wave spectra occurred, the higher frequency did not appear to be damped rather the low frequency was accentuated.

It would require a sophisticated field measurement program to establish with absolute certainty whether fluid mud streaming into the LAR Bar Channel occurs. Transport in suspension would seem to be sufficient to explain channel shoaling. For example, Walker and Hammack (2000) estimated that an average winter storm resuspends and transports about 450,000 dry-tons of sediment from the bay onto the inner shelf in suspension. TSM levels are very high for an open-coast area. For the purposes of this study, fluid mud stream will be considered a minor transport mode compared to transport in suspension.

Sediment Sources

Identification of sediment sources can be important to managing sedimentation problems. Local coastal bed erosion, more general coastal erosion, and river inputs are three possible sources of sediment to the bar channel shoal. A new bathymetric survey of the bar-channel area by NOAA began in 2005 - at the end of this study. Preliminary survey results became available during the preparation of this report and indicate that depths both east and west of the channel have decreased by as much as 3 ft over the last 70 yr, despite a general rise in apparent sea level. This would seem to eliminate local bed erosion as the ultimate source of the shoal material since it means that this area is experiencing appreciable long-term net deposition or aggradation. The shape of this aggradation suggests that the sediment source is the bay outflow. Multi-spectral satellite and high-altitude aerial images have indicated that the Atchafalaya Bay plume extends 30- to 40-km-wide over this area and often past the 33-ft depth-contour. Frequent wind events, especially winter storms, greatly increase plume area and TSM levels in the vicinity of the bar channel (Huh et al. 1996; Walker and Hammack 2000; Huh et al. 2001). Maximum cross-shore plume extents of 75 km and long-shore plume extents of 180 km east and west of the bay have been noted. Walker and Hammack (2000) estimated that 75 to 80 percent of the satellite-observed turbidity was from resuspension of inner shelf bed sediments. This suggests that sediment initially delivered by the bay outflow is being reworked, and intermittently transported cross-shore and long-shore down-drift.

Appreciable erosion has been reported along much of the Louisiana coastline for decades as the result of subsidence, sea level rise, and degradation of wetlands. Louisiana coastal wetlands, on the order of square miles per year, have been replaced by open water area. Water depths have generally increased in areas where this has occurred. Conversely, as the LAR and Wax Lake Outlet flows and sediment loads have increased since the 1940s to the current levels described in an earlier subsection, wide spread deposition on bay bottom, appreciable loss of bay volume, and formation of subaerial delta land have occurred relatively near to the bar channel.

The ERDC study observed shoal development that suggested lateral sediment sources rather than down-channel sources, and shoal volume fluctuated in time depending on storms rather than river inflow. For example, shoal volume suddenly changed from 4.4 Mcyd on 24 March 2003 to 6.6 Mcyd on 14 April 2003 during below normal river inflow. Also, correlations between salinity and total suspended material (TSM) sampled along the flanks of the channel near the shoal and winds and river inflow (*Qr*) indicated that TSM levels were not the result of direct transport down the channel. While there were statistically significant trends with lower salinities and higher TSM associated with higher *Qr*, correlation coefficients R^2 were only 0.074 and 0.049, respectively. Correlation between salinity and TSM was also very low ($R^2 = 0.020$). Statistical distributions of salinity were normal (gaussian) while TSM data were log-normally distributed, indicating different physical process operating on these conditions. In the case of TSM, that process was probably wind and wind-wave resuspension. TSM values were better correlated to wind speed than to *Qr* (and the distribution of wind-speed squared was about log-normal).

The ultimate source of the shoal sediment is probably the river inflow, based on its magnitude, proximity to the bar channel, and apparent affect on local deposition in the area surrounding the channel. Evidence from the ERDC study suggests that the sediment is not transported directly down the channel but rather is mainly transported indirectly from the river intermittently through the bay and over a wide area affected by bay outflow plume and then eventually along paths that cross the channel. This view is supported by remote-sensed images showing widespread resuspension of sediments a wide area surrounding the channel during wind events. Only a small fraction of the river flow is carried in the channel (the ERDC study estimated that the tidal-averaged or net flow through 3000-ft transects including the channel was only about 2 percent of the river inflow). The causal factor for intermittent transport is the erosive forces generated sporadically by winds and waves. During more quiescent time, sediments can deposit and TSM values around the bar channel become much lower than in the river. Much sediment reworking in the area adjacent to the bar channel is evident in the ERDC grain size distributions, which have greater mean sizes and sorting than the channel shoal sediments.

PART III: DATA SOURCES

Many data are required to conduct a 3D numerical modeling study. Data must be available to construct the basic numerical representation of the physical system, as well as, to construct boundary conditions that drive the computations. In addition, for the numerical model to be a viable tool for addressing engineering problems, it must be validated to field data collected in the interior of the modeled domain. The different types of data required and sources for those data for this study are briefly discussed below. A more detailed discussion of exactly how the data were used in the modeling study is given in Part V.

Several field data collection efforts were conducted during the model simulation period. LSU operated the Atchafalaya-Vermillion Bay Physical Measurements Program (BAYWATCH) funded primarily by MVN. Dr. Nan Walker, LSU, was the principal investigator. Data were collected offshore by the LSU Wave–Current Information System for Coastal Louisiana (WAVCIS, see Figure 3) that was funded by a consortium of state and federal agencies. However, the WAVCIS data were not available for the study

During the period of January 2002 to February 2003, ERDC conducted a field data collection program in and near the LAR Bar Channel for MVN. Long-term data were collected at instrument platforms installed in pairs located 1500 ft east and west of the channel. Six stations were established by driving piles at locations east and west of the channel in the area covering the channel length where the thickest shoal typically develops. Automatic water samplers, two current meters, and tide and wave gages were deployed at these six locations over six week periods. The locations of all data stations relative to the numerical grid to be discussed later are shown in Figure 4, with the ERDC stations labeled as A, B, C, D, E, and F.

During instrument service trips, acoustic current profile (ADCP) transect lines, salinity and temperature profiles, mud samples, and suspended sediment samples were collected by boat between pairs of fixed platforms. Three transect lines were established between instrument piles along the channel. Bed material samples were also collected over a grid surrounding the LAR Bar Channel.

Geometry / Bathymetry

Model bathymetry is based on the bathymetry (Figure 5) from the ERDC two-dimensional (2D) Atchafalaya Bay model (Letter and Powell, in preparation). Shoreline geometry definition came from electronic NOAA charts of the area. The ERDC Atchafalaya Bay model is based on the most recent bathymetry available. However, some of that information is based on survey information as old as 1935. Some spot measurements of depth were made near data collection stations during the ERDC study.

The MVN regularly surveys the bar channel, and some survey lines extend to cover areas adjacent to the channel. The NOAA survey begun in 2005 was not available.

Upland Discharges and Sediment Loads

Daily water discharges from the Lower Atchafalaya River at Morgan City, LA; Wax Lake Outlet at Calumet, La; and the Vermillion River at Perry, LA are required as boundary input data and were available from the USGS.

Daily fine-grain sediment loads (expressed as suspended sediment concentrations) are required during the model simulations at the same locations indicated for water discharge. These daily data were developed using appropriate discharge-sediment rating curves.

Wind, Wave, Water Level, and Currents

Wind speed/direction, water levels, and salinity within the model domain are required. Some of these data primarily came from the LSU Atchafalaya-Vermillion Bay Physical Measurements Program (BAYWATCH). Data were requested from the LSU Wave–Current Information System for Coastal Louisiana (WAVCIS), but were never provided. The locations of the various data stations in these two programs were previously presented in Figures 1 and 3.

Wind information collected during the ERDC field study near the study area was compared to winds that came from the BAYWATCH Cypremort Point station (BW-01). The ERDC winds were first adjusted from the 3 m measurement height to 10 m by the usual 1/7th power law. The result of this adjustment was that $U_{10m} = 1.19\ U_{3m}$. Regression fits were made with and without intercepts using various regression methods. Regression models without intercepts better estimated the variance of the ERDC observations. A factor of 1.97 times the Cypremort Point wind speed was found to best estimate the ERDC wind speeds for 687 observations (multiple-$R^2 = 0.83$). Based on this result, a revised wind field was applied to the sediment model.

Salinity and Suspended Sediments

ERDC collected long-term data at instrument platforms. Automatic water samplers and salinity and temperature profiles, and suspended sediment samples were collected by boat between pairs of fixed platforms. About 850 water samples were collected automatically at 6 am and 6 pm by the samplers from the platforms. Water samples at surface, mid-depth, and near-bottom depths were collected at channel centerline locations between instrument piles. A conductivity-salinity-temperature-depth probe was used to make vertical profiles at selected locations.

Some additional insights on suspended sediment concentrations in the area were obtained from Teeter and Pankow (1989), Walker and Hammack (2000), Van Heerden and Kemp (2000), and Letter and Powell (in preparation).

Bed Material and Fluid Mud Characteristics

ERDC collected bed material samples outside the channel along depth contours and lines parallel to the channel, using a small box corer. The samples were analyzed for moisture and organic content, and grain-size distribution. ERDC also collected fluid mud samples with a special sampler that collects four discrete samples over a 4-ft vertical distance in the shoal and then analyzed for density structure and grain size. Additional information on the density structure of the shoal became available in mid-2004 as the result of new survey capabilities being developed by MVN.

Addition bed-material information and sediment characteristics such as settling rates and hindered- or zone-settling rates were presented by Teeter and Pankow (1989) for the Atchafalaya Bay.

PART IV: THE LAR BAR CHANNEL NUMERICAL MODEL

Numerical Grid

The first step in any numerical modeling study is the generation of a suitable grid that captures the geometry and bathymetry of the modeled system. Depending on the length of the simulation period, there are often trade offs with regard to grid resolution and computing efficiency. The Gulf of Mexico portion of the numerical grid extends from just west of Southwest Pass to slightly east of Four League Bay (see Figure 1). Vermilion Bay, West Cote Blanche Bay, East Cote Blanche Bay, Atchafalaya Bay, and Four League Bay are all contained within the grid. In addition, Wax Lake Outlet and the Atchafalaya River up to near Morgan City, LA (see Figure 1) are represented in the numerical grid. The horizontal resolution of the grid varies in different portions of the system, with the total number of active horizontal cells being 3008. The numerical grid consists of vertical layers that are 2.0 ft thick, except for the top layer whose thickness varies with the movement of the water surface. The navigation channel and deeper areas contain several vertical layers, however, much of the grid covering the shallow bays are only 1-3 layers deep. The complete computational grid contains 20,189 active computational cells. With a computational time step of 45 seconds, a one-year simulation of CH3DZ-FM requires three days of computing time on a Personal Computer operating at a speed of 2 GHz.

Adequate bathymetry data exist to assign water depths on the numerical grid. As discussed in Part III, existing bay bathymetry data were obtained from the recent 2D delta growth modeling conducted by Letter and Powell (in preparation). The National Ocean Survey of NOAA has recently packaged complete survey data sets into the GEODAS system to make more detailed survey information available to the public than is published on nautical charts. Depths from GEODAS, the numerical grid, and repeated ERDC observations for the three ERDC stations to the west of the channel were compared. The ERDC observations were repeated over various tidal conditions that made possible a reasonable estimate of the depth relative to mean tide level MTL. Table 1 compares results along with the 95 percent confidence interval (CI) for the ERDC mean depths. Results show good comparison between the GEODAS and grid depths, but the field observations appear to be appreciable shallower at station A, even though local apparent sea level rise should be adding to the depths with time. This would seem to cast some doubt on the quality or consistency of the bathymetry information available

The existing bathymetry data are sufficient for the current study, where the major focus is on the bar navigation channel. However, during the actual design of structural alternatives, new bathymetry data near the location of the structures will be needed. The planform numerical boundary-fitted grid of the system and its associated bathymetry is illustrated in Figure 6. As discussed in Appendix A, computations are made on the transformed plane shown in Figure 7.

Boundary Forcings

In addition to interior data being required for model validation, as discussed in Part III and Appendix A, CH3DZ-FM requires various types of time-varying boundary conditions over the simulation period. In the application of a three-dimensional hydrodynamic / sediment transport model the following boundary conditions must be prescribed:

- Time-varying water surface elevations on the ocean boundary at each computational cell on the ocean boundary
- Time-varying salinity and suspended sediment concentrations (and temperature if modeled) at each computational cell along the ocean boundary and also in each vertical layer on the ocean boundary
- Time-varying and spatially varying-winds over the computational grid
- If temperature is modeled, time-varying meteorological data are required to compute equilibrium temperatures and surface heat exchange coefficients. Temperature was not modeled in this study.
- At flow boundaries, e.g., the Atchafalaya River, the connection with the Intracoastal Waterway into West Cote Blanche Bay, the Vermilion River, and the Wax Lake outflow channel, the time-varying discharge must be specified. In addition, the salinity, and suspended sediment concentration of the flow must be specified.
- At the sea bottom, sediment characteristics must be prescribed.

The locations of boundary input data are shown in Figure 8.

Specifying the proper water surface elevations on the open ocean portion of the grid is important. The net coastal drift is toward the west , and it is important to capture this circulation pattern. After much experimentation, the following approach was taken in this study. First the global ADCIRC model (Westerink et al 1992) was run with actual wind fields specified over the model grid shown in Figure 9. Computed water surface elevations from ADCIRC were saved at the locations of the four corners of the CH3DZ-FM grid (see Figure 8). However, from an inspection of recorded water surface elevations inside the bay it was obvious that the ADCIRC results did not reproduce the observed sub-tidal setups and set-downs well. Therefore, it was decided to filter the recorded data to yield a sub-tidal component and to then add this component to an ADCIRC run that only gave the tidal constituents, i.e. the wind was shut off on the ADCIRC grid. Figures 10 to 13 show the tidal constituent record at the four corners, whereas Figure 14 shows the subtidal component from the record at the BAYWATCH 03 station. Water surface elevations at intermediate points between the corners are computed internally through interpolation.

Salinity data specified on the open ocean boundary are related to freshwater inflow into the system, i.e., the flow at Simmesport, LA. An algorithm was developed using information provided by the MVN. The respective values provided for the salinity at the four corners for different freshwater inflows are shown in Table 2. As with the

water surface elevations, interpolation is employed to specify values of salinity on grid cells between the corners of the grid.

Suspended sediment concentrations were taken to be Gulf background levels with a wind-dependent component added to account for storm effects. Background levels were assumed to be 8 mg/l at the offshore boundary and 27 mg/l along the coastline. The wind speed (less 2 m/sec) times 15 was added to the specified concentration at the offshore boundary, while the wind speed (less 2 m/sec) times 30 was added to the specified suspended sediment concentration along the coastline. Teeter and Pankow (1989) present some suspended sediment concentration measurements from the offshore area of the numerical grid. Letter and Powell (in preparation) present a compilation of 1-km resolution satellite images of the area.

Discharge data during the simulation period at the upstream boundary of the Atchafalaya River, the Wax Lake Outlet, and the connection into the West Cote Blanche Bay (The Jaws) are all based on data from the USGS gage at Simmesport, LA. The Simmesport discharge was divided among these three inflow points based upon data provided by the MVN. Table 3 shows the distribution specified. Discharge data from the Vermilion River was determined from the USGS gage located at Perry, LA. Plots of the freshwater inflows at these locations are shown in Figures 15 and 16. The salinity attached to each discharge is assumed to be zero.

The concentrations of fine-grained sediments attached to these inflows were determined from a sediment-concentration rating curve at Morgan City and Calumet stations. Suspended sediment in the inflows at LAR and Wax Lake were specified as four times the local inflows taken to the 0.35 power. The suspended sediment concentrations at these points ranged from roughly 175 to 290 mg/l over the year of simulation, depending on inflow. The other three inflow points in Table 3 were specified to have constant 140 mg/l. With these inflows and suspended sediment specifications, the total sediment input for the one-year simulations was 55 million dry-tons. LAR and Wax Lake totals were 29.3 and 24.4 million dry-tons of sediment for the year.

Some of the ERDC and LSU BAYWATCH data stations collected wind data. Data from The BAYWATCH Cypremort Point station (BW-01) were most continuous in time and thus were selected to be used uniformly over the entire grid. The east / west and north / south components of the wind are shown in Figures 17 and 18, respectively.

Initial Conditions

Initial conditions for the water surface elevation and the velocity fields were set by assuming values of zero. Initial conditions for the salinity field were obtained by constructing a field from observed data at the beginning of the simulation period, i.e. 1 September 2001.

To initiate the computations, sediment characteristics must be specified over the bottom of the modeled area, including the navigation channel. A universal bed layer

profile was specified as described in the subsection that follows, but truncated from the bottom up to present bed-surface concentrations variously over the grid. Initial bed surface concentrations by areas were determined by sensitivity testing. For example, the high-velocity areas of Southwest Pass, LAR, and Wax Lake Outlet were specified with high initial bed surface concentrations so that massive erosion would not occur. Eventually, the sediment model was operated for many years with bed changes saved and used to bring the bed strength to approximate local hydrodynamic stress conditions. Details are described in Part VI.

Sediment Characteristics

Sediment parameters were specified uniformly for the entire grid. Conditions such as salinity and salinity stratification, current and wind-wave shear stress, residual circulations and tidal fluctuations operate on the suspended and bed sediments to make characteristics such as settling velocity and erodibility non-uniform over the model domain.

Model settling velocity constant and enhanced ranges were specified to have concentration limits of 60 and 960 mg/l (C_{ll} and C_{ul}; see Appendix B for definitions of parameters). The maximum and minimum *Ws* were 0.8 and 0.05 mm/sec (*a1* and $a1\ (C_{ll} / C_{ul})^n$). The exponent applied in the enhanced range was 1.0 (*n*). With these parameter values, settling rates are similar to those found by Teeter and Pankow (1989). The salinity at which *Ws* decreased to half its fully-flocculated oceanic value was 0.54 ppt (*c1* = 0.03 and *c2* = 0.6).

Consolidation test data from Teeter and Pankow (1989) were used to fit alternate empirical hindered settling *Wh* curves of the R-Z type (as described in Appendix B)

$$Wh = Wh_o (1 - b1\ Cs)^{b2} \quad , \quad Cs < 1/b1$$

where *Cs* is the solids content of the material and I-K type

$$\mathrm{Wh} = z' (1 - b1\ Cs)^3 / (b1\ Cs) \quad , \quad Cs < 1/b1$$

(Islam and Karamisheva 1998) where *b1* is the inverse of the final settled concentration, and *b2*, Wh_o, and *z'* are empirical parameters.

Test sediments were from a fine channel deposit from the station F described by Teeter and Pankow (1989). The sediment had a median grain diameter D50 of 2.2 μm, 5 percent greater than 74 μm, and 25 percent greater than 16 μm. The Cation Exchange Capacity of the sediment was 22 to 36 meq/100g (moderate). The parameter *b1* was estimated from field sediment density profiles to be the inverse of 725 kg/m^3.

Sediment experiments with 40- to 159-kg/m^3 initial concentration were first used to fit the hindered settling equations. Results are presented in Figure 19. The LAR bed layer model was then used to simulate two 144-kg/m^3-initial concentration experiments

of 100- and 30.5-cm initial heights. The same bed structure and model parameters were used for both model tests. Since the LAR bed model did not have a layer with a top concentration of 144 kg/m^3, numerical tests had about 33 percent of sediment in layer 2 (109 kg/m^3) and the remaining 67 percent in layer 3 (159 kg/m^3). Results are presented in Figure 20 and demonstrate that the bed-layer model is capable of reproducing experimental data reasonably well.

The I-K expression had no clear advantage so the R-Z expression was used in the model. Though laboratory data are available with which to estimate hindered settling, considerable uncertainty exits in describing the field process. Hindered settling depends on the formation of mm-scale vents in the fluid mud which allow the escape of pore water from the material as it settles. Drastic decreases in settling have been observed to occur as the result of agitation of the material or appreciable settling fluxes. In the case of the LAR Bar Channel, fluid mud agitation could come from surface waves, currents, internal waves, vessel passage, or fluid mud underflows.

The hindered settling reference was set at 0.015 mm/sec (Wh_o), the exponent at 10.0 (*b2*), and the fully settled *Cs* at 800 kg/m^3 (1 / *b1*) after some trial and error testing and comparison to field fluid mud density profiles.

Fluid mud yield stress parameters were set at *TUY1* = 16,320 Pa (at a volume concentration of 1.0) and *TUY2* = 3.3 as found for an estuarine fluid mud in Texas (Teeter et al. 2002). Numerous sensitivity tests were performed comparing model suspended sediment concentration to observed field values while adjusting erosion parameters within observed ranges. Settled-bed erosion threshold parameters were finally set at *d1* = 1.8E-7 and *d2* = 2.5. The excess shear stress exponent was set at *m1* = 1.5. Erosion rate parameters were set at *s1* = 9.5 and *s2* = 0.35. Depositional threshold τ_{cd} was set at 0.017 Pa. The fluid mud entrainment regime limit was set at 150 kg/m^3. Seven layers were specified in the bed layer model. The concentration *Cs* and fully-settled thickness *Hso* characteristics of those layers and corresponding erosion thresholds τ_{ce}, erosion rate parameters *M*, yield stress τ_y, and hindered settling *Wh* are presented in Table 4.

PART V: HYDRODYNAMICS VALIDATION

As previously noted, field data were available from the ERDC study and the LSU BAYWATCH Program for the period of 1 September 2001 to 31 August 2002. Again, the locations of the data stations are shown in Figures 1 and 4. Validation of the hydrodynamics consisted of illustrating that the model responds properly to basic processes, e.g. setups and set-downs in the boundary water surface elevation and changes in freshwater inflow, along with direct comparisons of the computed water surface, velocity, and salinity fields with observed data from the two sources noted above.

Basic Processes

Figure 21 is a plot of the computed salinity at mid-depth in the channel at the ERDC-EF transect with the total freshwater inflow superimposed. Note that inflow values have been divided by 15 so that inflow plots on the same scale as the salinity. It can clearly be seen that the salinity responds well to the freshwater inflow. For the first 2000 hours of the simulation the inflow is relatively low, i.e. around 100,000 cfs, and the salinity is relatively high. However, as the inflow increases to a maximum of about 450,000 cfs, the salinity at this location is basically driven to zero.

Figure 22 shows the same plot of salinity at the ERDC-EF transect with the subtidal component of the boundary water surface elevation divided by 2 superimposed. In order to more clearly show the dependence of the salinity on subtidal fluctuations, the timeframe of hours 5,500 to 7,500 has been plotted. It can clearly be seen that the computed salinity is greatly dependent on the subtidal component of the water surface elevation. As the water surface experiences a set-down due to winds over the Gulf resulting from weather fronts, the salinity decreases dramatically, whereas, when setups occur, dramatic increases in salinity are seen. These are proper responses to basic processes that are seen in the field data presented later.

Water Surface Elevations

Water surface elevation data for portions of the simulation year, i.e. 1 September 2001 – 31 August 2002 were available at the BAYWATCH stations. Figures 23 to 26 show comparisons of the computed and observed values at BW-01, BW-03, and BW-04. Again, the locations of these stations are shown on Figure 1. Generally the computed elevations agree fairly well with the observed data. However, with so much of the water surface records being composed of a strong subtidal component (see Figure 14) and with the uncertainty associated with the ocean boundary condition on water surface elevations, the comparisons aren't as good as would be desired if the computations were being used to predict real time water surface elevations.

Figure 25 shows a plot of the comparison of water surface elevations at BW-03 from hour 5,500 to hour 7,500. Recall that the data at BW-03 were used to generate the subtidal component shown in Figure 14 that was used to construct the ocean boundary

condition. The susperposition of the tidal record on the subtidal record can clearly be seen.

Velocities

Observed velocity data were available at both the BAYWATCH and ERDC stations shown in Figures 1 and 4. All of the velocity comparisons have been broken into comparisons of the east / west and north / south components. Figures 27 and 28 show the two velocity components at BW-01. The observed maximum values are slightly higher than the computed ones. Taking an average over the period in which observed data were available yields an observed residual current with E/W and N/S components of 0.25 and 2.33 cm/sec, respectively. The computed values are -0.53 and 1.47 cm/sec. Thus it can be seen that the residual current at BW-01 is relatively low.

Figures 29 and 30 show similar plots at BW-03. Here it can be seen that the range is about the same for the observed and computed velocity components. However, the N/S observed residual is 2.95 cm/sec (directed into the bay), whereas the computed residual is -6.75 cm/sec (directed out of the bay). It is believed the current meter at BW-03 had an offset error since there is no known study indicating that the residual current in Southwest Pass is directed into the bay.

The E/W and N/S components of the velocity at BW-04 are presented in Figures 31 and 32. It can be seen that the maximum magnitude of the computed N/S component is larger than the observed while that of the observed is larger for the E/W component. However, the computed and observed residual current at BW-04 agrees quite well. The observed N/S residual component is -0.70 cm/sec, with the computed being 0.62 cm/sec. The observed E/W component is -6.80 cm/sec with the computed being -6.79 cm/sec. Thus, both the observed data and the model indicate there is a strong residual current directed toward the west at station BW-04.

Figures 33 to 36 show velocity comparisons between the model and the ERDC data at the A and E stations. Very little velocity data were collected at the other stations during the simulation period. It can be seen that when the current is directed toward the east the comparisons are better than when the flow is toward the west. However, both the observed and computed residual E/W components are directed toward the west. For example at Station A, the observed value is -13.95 cm/sec, whereas the computed value is -9.86 cm/sec. Studies have concluded that the residual flow in Atchafalaya Bay and the adjacent Gulf is directed to the west with a magnitude around 10 cm/sec (see Part II). This is likely a result of the fact that the longterm direction of the E/W component of the wind is to the west. In addition, the outflow from the Mississippi River is directed toward the west due to the Coriolis force and may also be a factor.

Figure 37 is an interesting plot of the mid-depth velocity in the navigation channel at the end of the delta. From an inspection of Figure 15 of the freshwater flow from the Atchafalaya River, it can be seen that during the high flow events the model computes velocities near 300 cm/sec. In fact the average over the entire year-long simulation is 121

cm/sec. Thus, in the restricted channel at this location the bottom shear stress is quite high, resulting in a large impact on sediment transport.

Although the computed and observed velocities are significantly different at times during the simulation period, there are times when they agree very well. Obviously, much of the velocity record is a function of the setups and set-downs in the ocean water surface elevation boundary condition. Again, there is some uncertainty in the specification of that boundary condition. However, the basic behavior of the flow field in the bay and the adjacent Gulf is computed properly, i.e. with a net westward drift as reported in the literature.

Salinity

Salinity data were available for portions of the simulation period at the BAYWATCH and ERDC stations. As previously discussed, the basic processes that primarily determine the transport and resulting distribution of salinity in the bay such as freshwater inflow and episodic events resulting from the passage of weather fronts are modeled well. However, the uncertainty in the ocean water surface elevation boundary condition should again be remembered when inspecting the comparisons of observed and computed salinity that are presented.

Figure 38 shows plots of observed salinity at the BW-01, BW-03, and BW-04 stations. An interesting observation is that at times the salinity at stations BW-01 and BW-04 exceeds the salinity near the entrance to Southwest Pass (BW-03). One's normal intuition would to be to guess that the salinity at BW-03 would always be higher than the salinity at BW-01 and BW-04 since these stations are much closer to the freshwater inflow sources. However, an inspection of Figure 39 showing the computed salinity at those stations reveals the same result. It appears that during episodic events that force high salinity ocean water to the west the salinity at stations BW-01 and BW-04 can indeed be higher than at the entrance to Southwest Pass.

Figures 40 and 41 show comparisons of observed and computed near-surface salinities at BW-01 and BW-04. Saline water only exists at those stations for basically the first 2,500 hours of the simulation. At BW-04, the comparison is quite good and reflects the dependence of the salinity on both the freshwater inflow and the subtidal component of the water surface elevation. The observed mean salinity and computed mean agree extremely well with the observed value being 1.52 ppt and the computed value being 1.56 ppt. The comparison at BW-01 isn't as good. For example the impact of the large episodic event that occurred around hour 1,000 shows up in the computation of a salinity in excess of 15 ppt while the observed data do not reflect the event. Unless the meter wasn't functioning properly, the reason is unknown. The mean observed salinity at BW-01 is 4.05 ppt with the computed mean being 1.76 ppt. It does appear reasonable for the mean salinity at BW-01 to be higher than at BW-04 since this station is farther from the sources of freshwater input. The RMS error at BW-01 and BW-04 is almost the same, with values of 2.30 ppt and 2.27 ppt, respectively.

Figures 42 to 46 show comparisons of observed and computed mid-depth salinity at several of the ERDC stations. The major conclusion to be drawn from these plots once again is that the model computes the proper response of the salinity to freshwater inflow and episodic events in the water surface. It can be seen that rapid changes occur in the salinity over relatively short periods of time at all stations. The impact of freshwater inflows obviously is greater at stations E and F (Figures 45 and 46) since they are closer to the mouth of the Atchafalaya River.

With most of the bay being extremely shallow, the salinity is relatively well mixed over most of the bay. However, in the deeper navigation channel stratification can exist. It is important to demonstrate that the numerical hydrodynamic model computes stratification in the bar channel similar to that observed. Figures 47 and 48 show plots of near surface and near-bottom computed salinities along with a few observed values from the ERDC dataset at the AB and CD transects. Similar levels of stratification are seen in both the computed and observed salinities. This serves to demonstrate that vertical turbulence is computed properly in the deeper navigation channel.

Extended Grid Test

During one of the internal technical reviews, the question was asked as to whether the numerical grid should be extended farther into the Gulf. To answer this question, the grid shown in Figure 49 was created. All of the bathymetry on the original grid was the same on that part of the extended grid. Comparisons of the velocity components at the ERDC-E station computed on the original grid with those computed on the extended grid are presented in Figures 50 and 51. It can be seen that there is very little difference between the two computations. Similar results were obtained at other locations. With the velocities virtually identical, it can be assumed that transport on both grids is virtually the same. Therefore, it was decided that the original grid was adequate for the purpose of the study.

PART VI: SEDIMENT MODEL SIMULATIONS

The sediment model validation was performed separately and after the hydrodynamic model adjustment and validation, even though the two models are fully coupled, since the sediment model is sensitive to hydrodynamic conditions. As described earlier, CH3DZ was modified to include single-grain, cohesive sediment suspended transport and bed transport of fluid mud on a slope. Both settled mud and fluid mud processes are included in the model and applied depending on the local surface concentration or density. Depending on the sediment surface density, cohesive sediment transport is treated either as settled mud (particle erosion and floc deposition) or as fluid mud (fluid entrainment and settling). A layered bed structure simulates the formation of a surface layer through hindered-settling consolidation of freshly deposited material and tracks the descent of an erosive surface into the bed, if necessary. Wind wave resuspension is an important process to suspended sediment, and wind is used in both the hydrodynamic and sediment transport sub-models. A model module computes down slope gravity forces and density-dependent yield stress through the fluid mud layer and moves material accordingly. Details of the sediment model formulation are presented in Appendix B and the sediment parameters used were described in Part IV.

The sediment model was tested repeatedly during the adjustment phase, as described in Part IV. The objectives of the adjustment were to match suspended sediment and shoaling conditions in the model to observed values. Since the actual dredging and disposal operation and initial shoal conditions were not matched in the model, the shoal volume objective was to match typical pre-dredge survey volumes at the end of the model year, rather than the actual time-history observed during 2001-2002. Also, since the model wind data were from a site roughly forty miles removed from the study area, the overall suspended sediment statistics are a better gauge of model performance than the time-series comparison. Winds are critical to resuspension and suspended sediment concentrations. Over distances of this magnitude, winds can be expected to be quite different at any given point in time, while overall wind-field statistics are expected to be more similar.

Sediment Model Validation

The model was adjusted and validated using the base 24-ft-channel production run. The existing geometry and boundary conditions compiled for the period of 1 September 2001 to 1 September 2002 were used in the validation. The channel was initialized to -24 ft elevation. A 90-day dredging period between days 120 and 210 was specified during which 100 kcyd per day were removed from the channel.

The model suspended sediment and salinity results were compared to ERDC data collected at stations alongside the channel. The ERDC and channel stations are shown in Figure 2. The ERDC data were compared to model results in two ways. A point-by-point comparison to the ERDC suspended material data collected at 6 am and 6 pm daily was made. This comparison is presented in Table 5. Note that there were no data

available for ERDC Station D. All ERDC data were also compared to all model data in Table 6. Much of the ERDC data was collected after the model simulation period. The phasing of winds is critical to total suspended material (TSM) levels. The winds used in the model are from the Cypremort Point site far removed from the study area and therefore the wind phasing used in the model is questionable. The assumption is that the statistical distribution of the winds imposed in the model is similar to those experienced in the study area. Therefore, assuming sufficient ERDC samples were collected to represent variations in the wind field, comparing entire data sets is a valid comparison.

A comparison of the statistical distributions on the point-by-point suspended sediment data collected by ERDC during the simulation period is shown in Figure 52. A comparison of time-series plots of point-by-point data is shown in Figure 53.

The ERDC study also collected snapshot profiles of suspended sediment and salinity along the channel centerline between the monitoring station pairs. Six such channel profiles were collected during the simulation period. Those data and results from the model along the channel are presented in Figures 54 to 59. When viewing these results it should be remembered that the model reproduces the proper behavior of salinity fluctuations (Figures 42 to 46). However, due to uncertainties in the open ocean water surface matching computed salinities with observed values on an hourly basis is difficult.

The shoal volume was also compared to field observations. After dredging and well before the end of the simulation year the model displayed a quasi-steady shoal volume of 7.02 Mcyd to -24 ft. The ERDC study estimated the shoal volume (to -24 ft) at between 8.2 and 9.2 Mcyd. A plot showing the longitudinal distribution of the channel shoal in the model for select times during and after dredging is presented in Figure 60. The model shoal distribution is similar to those observed in the field where the peak shoal height occurs about channel station 750+00 ft to 850+00 and overall shoal extends from about 550+00 to 1330+00 ft.

Production Runs

Production runs were performed for 24, 30 and 38 ft channel depth (project depth plus over depth and advanced maintenance) and for existing and future conditions (six runs total). All runs started with empty, flat channels and included dredging periods. Since the simulations started with empty channels, the dredging periods were scheduled for the middle of the year to allow shoals to form both before and after dredging. The middle of the year corresponds to high wind conditions and high river inflows. Therefore, shoaling rates during dredging periods were very high.

Dredging schedules were assumed for production and sensitivity runs. Dredging in the runs began at day 120 or starting in January. Dredging lasted 90, 105, or 114 days respectively depending on channel depth. Dredging in the model consisted of instantaneously shoal volume reductions of 100, 100, or 120 kcyd (depending on channel depth) once per day. If a run had insufficient shoal volume at any particular time and

place to accommodate scheduled dredging, a volume error was recorded. Otherwise, the planned dredging volume was removed from shoal material greater than 109 kg/m^3.

The future condition (+50 yr or 2052) was created following the MVN/ERDC Atchafalaya Reevaluation Study. The subaerial area within the Atchafalaya Bay was increased from 11.1 to 65.1 sq mi. These areas generally follow estimated and predicted values found in the MVN/ERDC study. Some minor bay-bottom deepening was also incorporated into the future condition. Bay-portions of existing and future grids are compared in Figure 61. The same total inflow was used for the future as in the existing condition. However, the LAR and Wax Lake Outlet (WLO) flow splits were altered for the future condition. The flow at Morgan City (MC) will be 54.5 percent of the total inflow, resulting in the Calumet flow being 45.5 percent of the total. The MC and Calumet flows were distributed to the model boundary as in the existing condition and described in Table 3. Thus, LAR will be 87.3 percent of MC and WLO will be 100 percent of Calumet. As in the existing condition, the Jaws will receive the Charenton River inflow plus 5.8 percent of the MC. West Vermilion Bay will receive 2.9 percent of MC inflow. The Vermilion River will receive the existing Vermilion River inflow. The sediment concentration in the LAR and WLO inflows will be four times the local inflows taken to the 0.35 power as in the existing condition. The inflow sediment concentration in the Western bays will be 140 mg/l. Total sediment supply to the bay is therefore unchanged and about 55 million dry-tons.

Production run results are presented in Table 7. Presented there are median suspended sediment results for the ERDC stations, median channel station (CS) at points just above the channel bottom, and a median TSM stratification parameter $\Delta TSM / \overline{TSM}$ calculated as the bottom to top difference in TSM divided by the depth-mean TSM. Also presented in this table, and tables to follow, is a variability parameter similar to a geometric standard deviation (std). This parameter was calculated by dividing the difference between the 84th and 16th percentile values by the median value of the time series. For example, a table entry of "100 (1)" would indicate that the 16th percentile value of the time-series was about 50 and the 84th percentile value was about 150.

Time-series plots of shoal volume are shown in Figures 62 and 63 for existing and future conditions. Salinity results from the production runs are presented in Tables 8 and 9. These results are from the same locations as the TSM results, and the standard deviation (std) and stratification parameter were calculated using the same procedure as for TSM except that the stratification parameter was not normalized. Thus, the salinity stratification parameter ΔS represents the surface to bottom difference in salinity. Under conditions of near-zero median salinities, the standard deviation is not always meaningful. For standard deviations greater than 100 the notation (*) was used in the tables.

Channel profiles of TSM and salinity are presented for 24- and 38-ft-deep channel at hour 2,000 (Figures 64 and 65), hour 4,000 (Figures 66 and 67), hour 6,000 (Figures 68 and 69), and hour 8,000 (Figures 70 and 71) for existing conditions. Increases in suspended sediment and salinity values and stratifications resulting from increased

channel depth are displayed in these figures. Shoal profiles at select times for the six production runs are presented in Figures 72 to 77.

Sensitivity Runs

Sensitivity tests on various parameters were performed using 24 and 38 ft channels and existing or future conditions. Two variations of each parameter were made (four runs for each parameter). The production runs were used as the Base runs. The difference between existing and future conditions was much smaller than differences in shoaling caused by channel depth changes. Wind sequencing, wind-wave shear stress, river sediment load, freshwater inflow, ocean TSM boundary condition, and bed initialization sensitivity tests were performed.

Wind and wave conditions were altered by splitting the year-long wind record in two parts and splicing then back together to make the wind conditions begin in March and end in February during the model run. This changed the seasonality of wind conditions and had the effect of starting the dredging period in July instead of January with respect to the winds (but not freshwater inflow). This test was labeled Season. Another test split the wind record into 54 parts each 6.67 days long. The pieces were then randomly reassembled which should have the effect of erasing wind seasonality. This test was labeled Uniform. Results for existing conditions are presented in Table 10. Figures 78 and 79 present plots of shoal volume time histories for 24 and 38 ft channels.

River inflow *Qr* was increased (1.5 times the base) and decreased (0.5 times the base) to test model sensitivity to total freshwater and sediment inflows. Total sediment inputs for the year were thus 82.5 and 27.5 million dry-tons. Inflow sediment concentration was specified using the same relationship as in the production runs. Results for suspended sediment and shoaling are presented in Table 11. Shoal volume time histories are shown in Figures 80 and 81. Sensitivity tests also varied freshwater inflow *Qf* independent of the sediment inflow. The sediment inflow was held the same as in the base run while *Qf* was increased (1.5 times the base) and decreased (0.5 times the base). Results are presented in Table 12. Shoal volume time histories are shown in Figures 82 and 83 for 24 and 38 ft channels. Future conditions were used for these sensitivity tests. The effects of *Qr* and *Qf* tests on salinity conditions are presented in Table 13.

The ocean boundary suspended sediment conditions are specified on inflowing conditions and rather uncertain. Not much suspended sediment data exist at the model boundary. Sensitivity tests both increased the suspended sediment (2 times the base) and decreased the suspended sediment (0.5 times the base). Results for existing conditions are presented in Table 14. Shoal volume time histories are shown in Figures 84 and 85 for 24 and 38 ft channels.

Wind-wave shear stress τ was increased (1.25 times the base) and decreased (0.75 times the base). Results for existing conditions are presented in Table 15. Shoal volume time histories are shown in Figures 86 and 87 for 24 and 38 ft channels.

Model sensitivity tests of bed-sediment source were performed. Results for future conditions are presented in Table 16. Runs used previous simulation results to initialize bed structures - equivalent to running the model as long as three years with repeating annual boundary conditions. Base runs were first used to initialize a pair of runs (labeled I in Table 16). Results of those runs were then used to re-initialized beds in another pair of runs (labeled II in Table 16). Shoal volume time histories are shown in Figures 88 and 89 for 24 and 38 ft channels.

Sensitivity of model results to changes in the fluid mud flow module was tested sequentially by (a) increasing the vertical resolution to 1.6 mm ("Improved COBDFLW" in the table), (b) increasing (doubling) fluid mud layer thickness, (c) decreasing surface density (in layer 0), and (d) changing (increasing and decreasing) fluid mud layer thickness. Results are presented in Table 17. A new base run was produced using a combination of changes in Table 17 and with the sediment yield stress parameter *TAY1* at the validation run value of 16,320 Pa. The *TAY1* value was then increased (to 24,480 Pa) and decreased (to 8,120 Pa). Model sensitivity to the salinity factor controlling settling rate *Ws* was tested. The *Ws* reduction factor was decreasing by 50 percent. Sensitivity to the hindered settling reference value Wh_o was tested by reducing it by 50 percent. Results of these tests are presented in Table 18.

Model sensitivity to the path of the deepened channel was tested. A deepened channel might have to be curved to avoid offshore structures and/or pipelines. Also, the shortest distance to deep water is slightly to the south. The model mesh was modified to curve the seaward end of the 38-ft-deep channel to the south. The curved channel model grid is shown in Figure 90. The deepened channel simulation was repeated with the curved grid to test the sensitivity of model results to such a change. Results are shown in Table 19 and indicate a very small change in model results.

Sensitivity runs gave some indications as to the sediment source to the channel shoal. Wind seasonality sensitivity tests indicated that when high winds correlate to high river discharge (the base condition), TSM levels at the ERDC stations were generally higher as sediment was frequently stirred and not allowed to deposit long-term (except in the channel). River discharge affected channel TSM levels as well as the TSM at the ERDC stations, but to a lesser extent than the corresponding input variation. The implication is that a much greater magnitude of bed sediment is available to intermittent resuspension by wind events than is delivered annually by the river input. Freshwater inflow sensitivity runs (with constant sediment input) indicated that discharge is involved in delivering sediment to the ERDC TSM stations. The wind shear stress sensitivity results were similar to wind seasonality and river discharge results with respect to the importance of out-of-channel TSM on channel shoaling. Ocean boundary sensitivity runs indicated that the major sediment source is not at the model boundary. Bed initialization tests indicated the source of sediment is not the pre-existing (old) bed. With the bed structure imposed in the model and the same forcings by wind-waves and currents, the erosion would have decreased with time if the source were the old bed. Instead, TSM and channel shoaling actually increased slightly during the first repeated year and then

decreased on the second repeated year – apparently seeking steady-state values in equilibrium with the bed and the river input of sediment. Apparently, the bed reservoir of river-input sediments is quite large compared to the annual river input. Together, sensitivity runs indicate that the ultimate source of the sediment is the river but most material arrives at the channel shoal along pathways other than the channel itself, similar to indications from field information described in Part II..

Structural Alternatives Tests

Two structural alternatives were tested in the next modeling phase using existing conditions with 24 and 38 ft-deep channels. The structural alternatives tested in the model included channel-side jetties and long-shore artificial reefs and combinations thereof. All structures were full depth, subaerial, and non-submerging. Jetties are commonly used coastal structures that can reduce channel shoaling. The rationale for jetties was that they would confine channel flow and prevent lateral flow of water and sediment into or out of the channel. Reef structures are similar to lateral or contraction dikes but in this case much longer. The rationale for the reefs was that they might deflect freshwater outflow from the bay to the west, 75 to 80 percent of which is moving seaward outside the navigation channel at Eugene Island. In this way, less sediment-laden water would cross the channel. A reef in combination with prevailing coastal flows might move the freshwater and sediment source away from the area of the channel. With these principles in mind, a number of structural alternative plans were developed to test the effects of structure scale on performance, e.g. jetty length on shoal reduction.

The structural alternative test plans are described as:

Jetty1. Two 96,650-ft-long solid jetties were installed into the existing model condition with a 38-ft-deep channel between channel stations 496+00 and 1462+50 ft. The spacing between the jetties was 800 ft to allow for the channel width, and channel and jetty side slopes. The out-of-channel depth at the offshore end of the jetties was about 24 ft MLG. See Figure 91.

Jetty2. Two 118,900-ft-long solid jetties were installed into the existing model condition with a 38-ft-deep channel between channel stations 496+00 and 1685+00 ft. The spacing between the jetties was 800 ft to allow for the channel width, and channel and jetty side slopes. The out-of-channel depth at the offshore end of the jetties was about 26 ft MLG. See Figure 92.

Jetty3. Two 75,000-ft-long solid jetties were installed into the existing model condition with a 38-ft-deep channel between channel stations 496+00 and 1246+00 ft. The spacing between the jetties was 800 ft to allow for the channel width, and channel and jetty side slopes. The out-of-channel depth at the offshore end of the jetties was about 18 ft MLG. See Figure 93.

Jetty4. A single 75,000-ft-long solid jetty on the east side of the channel was installed into the existing model condition with a 38-ft-deep channel between channel stations

496+00 and 1246+00 ft. *Jetty4* is similar to *Jetty3* except that only a single jetty on the east side of the channel was installed. The out-of-channel depth at the offshore end of the jetties was about 18 ft MLG. See Figure 94.

RJ5. A reef-jetty combination consisting of a short jetty system identical to *Jetty3* and a reef on both sides of the channel extending a total of about 44,460 ft from the western tip of Point Au Fer Island was installed in the existing model condition with a 38-ft-deep channel. The reef crossed the area of the channel at about channel station 616+00 ft and mainly followed along the 10- to 12-ft depth contour. See Figure 95.

RJ6. A reef-jetty combination consisting of a short jetty system similar to *Jetty3* with a connected reef on the east side of the channel extending a total of about 22,900 ft to the western tip of Point Au Fer Island was installed in the existing model condition with a 38-ft-deep channel. The reef connected to the jetty system at about channel station 604+00 ft at an out-of-channel depth of about 10 ft. A 2,350-ft gap between 616+00 and 640+00 ft was installed in the west jetty. See Figure 96.

RJ7. A reef-jetty combination identical to *RJ6* with the addition of two offshore islands was installed into the existing model condition with 38-ft-deep channel. One island was connected to the east jetty and was about 19,100-ft-long in the southerly direction and 3,200 ft wide. The other island was installed about 61,000 ft west of the channel and was 15,000 ft long in the north-south dimension and 4,500 ft wide. See Figure 97.

Reef2. A long-shore reef anchored to the western tip of Point Au Fer Island and extending a total of 56,500 ft mainly along the 8-ft depth contour was installed in the existing model condition with 24-ft-deep channel. The reef crossed the channel at station 512+00 with a gap in the reef of 1,200 ft. See Figure 98.

Reef3. Compound long-shore reefs anchored to the western tip of Point Au Fer Island were installed in the existing model condition with 24-ft-deep channel. An inshore reef was similar to Reef2 but only 32,300 ft long and. The offshore reef extended a total of 48,800 ft at angle of about 70 degrees to the channel and roughly followed the 10 ft depth contour. The reefs crossed the channel at stations 512+00 and 582+00 ft with gaps in the reefs of 1,200 ft. See Figure 99.

RJ4. A reef-jetty combination with a reef similar to the offshore part of the *Reef3* plan and a pair of 8,600-ft-long jetties seaward was installed into the existing model condition with 24-ft-deep channel. The jetties were located between channel stations 573+00 and 659+00 ft and the distance between the jetties was 1,200 ft. See Figure 100.

Reef4. A long-shore reef anchored to the western tip of Point Au Fer Island and extending a total of 55,600 ft mainly along the 10-ft depth contour was installed in the existing model condition with 38-ft-deep channel. The reef crossed the channel at station 582+00 with a thick section extending 8,700 ft inshore on the west side of the channel and 2,600 ft on east side of the channel. The gap in the reef was 400 ft. See Figure 101.

Reef5. A long-shore reef identical to *Reef4* plan anchored to the western tip of Point Au Fer Island and extending a total of 55,600 ft mainly along the 10-ft depth contour was installed in the existing model condition with 38-ft-deep channel. The reef crossed the channel at station 582+00 with a thick section extending 4,600 ft on east side of the channel. The gap in the reef was 1,200 ft. See Figure 102.

RJ8. A reef-jetty combination and a closure for Oyster Bayou were installed into the existing model condition with 38-ft-deep channel. The reef extended 31,800 ft total mostly on the west side of the channel in 10- to 12-ft water depths and connected to two jetties at about channel station 604+00 ft. The jetties were about 11,700 ft long and the distance between them was 800 ft. Oyster Bayou just east of Point Au Fer Island was closed with a dam at the coastline and a dike slightly offshore. See Figure 103.

Model sediment and salinity results at ERDC and channel stations for *Jetty1-3* plans are presented in Tables 20 and 21. Station locations are shown in Figure 2. *Jetty3* and *Jetty4* (the single jetty) plans are compared to each other and to the base in Table 22. The *Jetty4* simulation used a shorter time step because of increased channel current magnitudes and only three stations are available for comparison in Table 22. Table 22 also contains maximum and root-mean-square (rms) surface current magnitude U_s for two channel stations. Shoal profile plots for *Jetty1-4* are presented in Figures 104 to 107.

Jetty pairs reduced shoaling progressively with longer lengths. Also, shoal distributions were moved progressively seaward with longer lengths. Jetty pairs maintained channel flows along their jettied lengths. Channel velocities were increased (Table 22) and made uniform over their jettied lengths instead of decreasing seaward. Salinities and salinity stratification within jettied channels greatly decreased – conditions expected to decrease channel shoaling. Salinities outside the jetties were also reduced by their blocking affect on east/west coastal flow. Bay outflow was trained parallel to, instead of crossing, the channel, especially to the west of the channel. The success of the single jetty (*Jetty4*), that reduced shoal volume almost as much as the equal-length jetty pair (*Jetty3*), might indicate that blocking of the east/west coastal flow was the most important factor in reducing channel shoaling. However, *Jetty4* had channel-salinity effects opposite from the other jetty plans, and channel salinities actually increased (and yet salinity stratification greatly decreased) as compared to the base condition. Apparently, the down-current lee of *Jetty4* to the west of the channel created conditions where freshwater flow was drawn from the channel.

Sediment and salinity results for *RJ5-7* are presented in Tables 23 and 24. Shoal profile plots for *RJ5-7* are presented in Figures 108 to 110. Results for *RJ5-7* plans were surprising in that the shoal-reducing effectiveness of the *Jetty3* plan was decreased by the addition of reef-like lateral dikes. These results indicate that there is an optimum amount of jettied channel flow. *Jetty1-3* plans were apparently closer to that optimum. *RJ5-7* plans had greater jettied channel flow (lower channel salinities) because of the lateral dikes. The result was that more sediment was delivered to the seaward end of the jetties and greater channel deposition occurred in this area.

Some of these results can be seen in plots of the averages over the simulation year of the model depth-averaged TSM fields (saved at 3 hr intervals, n=2880). Base-condition results for the vicinity of the 38-ft channel (with existing conditions) are shown in Figure 111. The comparable results for *Jetty3* and *RJ5* plans are shown in Figures 112 and 113. The effects of the plans on the TSM field alongside and seaward of the structures can be seen in these plots.

Results for *Reef2*, *Reef3*, and *RJ4* plans are presented in Table 25 and 26 for sediment and salinity. Results for *Reef4*, *Reef5*, and *RJ8* plans are presented in Table 27 and 28 for sediment and salinity. Shoal profile plots are presented in Figures 114 to 116 for *Reef2-3* and *RJ4*, and in Figures 117 to 119 for *Reef4-5* and *RJ8*.

Planform variations in *Reef2-3* and *RJ4* and results indicated that, like the *Jetty1-3* plans, longer structures and those that moved bay outflow further from the channel were most effective. Reef plans worked as expected, diverting bay outflow from the vicinity of the channel, increasing salinities and decreasing TSM levels in and around the channel shoal location (see Tables 25 to 28). The *Reef2* plan was most effective. For this plan, TSM levels at the ERDC stations were similar to those for the low river-inflow sensitivity test. Reefs that angled across the channel were less effective apparently because they deflected the coastal flow seaward to the area seaward of ERDC stations and the shoal peak location (about station 800+00). Plan *RJ4* had a concentrated shoal at this location (see Figure 116).

Examples of these results are shown in the time and depth averaged TSM fields presented in Figures 120 to 122 for the 24-ft channel and existing conditions (the base), *Reef2* plan, and *RJ4* plan, respectively. The model predicts that *Reef2* was more effective than *RJ4* at reducing TSM in the critical area of the channel.

Shoal volume time-history plots are presented in Figure 123 for *Jetty1-2*, in Figure 124 for *Jetty3-4*, in Figure 125 *RJ5-7*, in Figure 126 for *Reef2-3* and *RJ4*, and in Figure 127 for *Reef4-5* and *RJ8*. Like the production run results, structural alternative shoal-volume time histories displayed slow or no growth during dredging periods and steady-state shoal volumes established before the end of the simulation year. The exception was the *Reef2* plan that had improved dredging effectiveness and reduced shoal volume growth after dredging - too slow to reach a steady-state volume by the end of the simulation year.

Shoaling Indices

To gauge the economic effect of possible project changes, three shoal-change indices were developed and calculated from model results to quantify the effects various plans would have on project economics. Model simulations started with a bare, empty channel. Model dredging was preprogrammed to occur over 90 to 110 day periods (depending on channel depth) beginning at day 120 of simulations. A dredging error was defined as the difference between the preprogrammed volume and the volume actually available to be

removed during simulations. The shoal had ample time to reform after the dredging period.

Final Shoal Volume index is the shoal volume at the end of the simulated year normalized by the base shoal volume less 1.0. This assumes that maintenance would be performed on an annual basis and that dredging for the subsequent year would depend on this final shoal volume.

Two Dredgings index assumed that maintenance would be performed twice a year as implied in the model simulations. Although only one dredging cycle was simulated, the model started with an empty channel, implying a second dredging cycle at the beginning of the year. The quantity dredged would equal the final shoal volume plus the amount dredged from the channel in the model adjusted by the amount remaining in the channel after dredging (what should have been dredged). This two-dredging volume was then normalized by the base volume and 1.0 subtracted.

Average Shoaling Rate index assumes that overall project economics depends on the length of time the project is operational during the year as well as on the dredging amount. The average shoaling rate is related to how fast the channel shoal reforms after dredging and how long it takes for the shoal to intrude into the project prism. Instantaneous shoaling rate is dependent on wind and river inflow conditions. Over simulated time, a linear trend is apparent in the model results up to the point when the final shoal volume is approached. The average shoaling rate was calculated as the dredged volume (since dredging affected shoal volume) plus 90 percent of the final shoal volume, and this quantity was divided by the time it took for the shoal to grow to 90 percent of its final volume. (Even though brief shoal-volume spikes sometimes reached 90 percent of the final during dredging, the time after dredging was used in the index.) As with the other indices, the change index was calculated by normalizing the average shoaling rate by the base value and subtracting 1.0.

Shoal-change indices were calculated for some of the sensitivity test runs. The indices are not perfectly correlated – meaning that the indices contain distinct information about model response. Sensitivity test shoal indices for existing model condition with 24- and 38-ft-deep channels are presented in Table 29. The Season wind scenario reversed the wind seasonality in runs while the Uniform wind scenario randomly sequenced weekly wind periods over the yearlong simulations. Low and high wind-wave shear stress τ sensitivity tests had 0.75 and 1.25 times the base wind-wave shear stress applied to the bed. The biggest difference among the three indices was between *Final Shoal Volume* and A*verage Shoaling Rate* indices (mean difference 0.130, root-mean-square rms difference 0.186, n=8). The next biggest difference was between *Final Shoal Volume* and *Two Dredgings* indices (mean difference 0.088, rms difference 0.125, n=8). The closest indices were *Two Dredgings* and A*verage Shoaling Rate* (mean difference 0.040, rms difference 0.084, n=8). Comparing indices in Table 29 by channel depth, the corresponding indices tracked within 10 percent (rms difference = 0.090, n=12), indicating the deeper channel was slightly more sensitive to these test parameters.

Shoal-change indices were calculated for production and structural alternative test runs and presented in Table 30. For many of the model test plans, shoal change indices are close to one another. In some cases, differences were caused by changes in the rate of shoal formation. For example, *Reef2* had a much slower average shoal rate index when compared to the final shoal volume index. Thus, annual dredging would be less affected (-24 percent) than would the time required for the shoal to reform (-47 percent).

Operational economics are also affected by the distribution of shoal material in the channel. Field channel centerline information from three condition surveys taken 17 June 2002 and 2 and 19 July 2002 were averaged and then volumes were extracted for the four survey reaches (each about 23,000 ft long). These results should be representative of pre-dredge conditions and are presented in Table 31. Also presented in Table 31 are select model results with 24-ft and 38-ft channel depths. Final-shoal model results are for the *Reef2* and *Jetty4* plans and for corresponding base runs. Field information, 24-ft channel, and 38-ft channel base runs all display a shoal distribution peak in the second survey reach. The 38-ft channel *Jetty4* plan, however, had 73 percent of the shoal volume displaced seaward of the existing channel.

PART VII: SUMMARY AND CONCLUSIONS

A three-dimensional numerical hydrodynamic and fluid / settled mud model has been developed and applied for the Lower Atchafalaya River Bar Channel located in south-central coastal Louisiana. The resulting model is known as CH3DZ-FM and is based on the CH3DZ hydrodynamics computer code. The numerical model contains in excess of 20,000 computational cells. A one-year simulation with a time step of 45 seconds requires 60 hours of computational time on a personal computer with a 2 GHz Pentium processor.

Validation of the hydrodynamics revolved around (1) employing data from an ERDC field study conducted in 2001-2002 and from LSU's BAYWATCH stations, and (2) demonstrating that the hydrodynamic computations respond properly to freshwater inflows and episodic events associated with the passing of weather fronts. A yearlong simulation from 1 September 2001 through 31 August 2002 was made. After the hydrodynamics were considered validated, the fluid / settled mud computations were validated for the same simulation period. This validation revolved around ERDC suspended sediment data mainly from 2002 and shoal volumes and profiles as surveyed by MVN.

With both the hydrodynamics and fluid / settled mud computations reproducing observed processes and data well, CH3DZ-FM was then applied to assess the impact on the formation of fluid mud in the bar channel due to channel deepening, structural alternatives such as reefs and jetties, and predicted bay conditions 50 years in the future. The same simulation period of 1 September 2001 to 31 August 2002 was used in all scenarios.

Production model runs included 24-, 30-, and 38-ft-deep channels with existing conditions and conditions expected 50 years into the future. Channel depth was found to have a strong effect on channel shoaling. Three metrics were used to compare shoaling results: *Final Shoal Volume*, *Two Dredgings*, and *Average Shoaling Rate* change indices. The existing and future condition final shoal volume results were not statistically different (paired t-test p-value=0.38). Both 30-ft and 38-ft channel depths had all three shoal-change indices significantly higher than for the 24-ft channel depth case. The intermediate 30 ft channel depth had relatively high shoaling, nearly as much shoaling as the 38 ft channel and shoal change indices for these two channel depths were not statistically different. Averages of existing and future condition final shoal volume increases for 30- and 38-ft-deep channels were 115 and 170 percent of the existing 24-ft-deep-channel shoal volume. The *Two Dredgings* and *Average Shoaling Rate* indices were similarly affected.

Salinity stratification and bottom salinities increased in the deepened channels, indicating decreased vertical mixing and increased gravitational circulation. Sediment trapping efficiency is deemed to have caused the channel shoaling increases. In some

estuarine situations, channel depth increases can cause only moderate density stratification and shoaling effects. However, a channel-depth breakpoint can occur at which density stratification reduces vertical mixing and shoaling increases dramatically.

Model sensitivity tests gauged model response to seasonal wind patterns, river and freshwater inflows, ocean suspended sediment boundary, wind-wave shear stress, bed initialization, and sediment parameters affecting bed-flow module. Sensitivity tests with different seasonal wind patterns show that dredging during the combination of high river inflow and high winds is not very effective. This was the situation for the base case. When inflow were high but winds low (Season scenario), dredging was most effective. When there was no seasonal wind trend (Uniform scenario), dredging effectiveness was intermediate to the other two cases.

Of the other sensitivity parameters, river inflow and wind-wave shear stress had greatest effects on shoaling results. Decreases in these conditions had larger effects than increases. Bed initialization tests indicated that the sediment source to the model channel did not depend on the erosion of older bed sediments. Reinitializing the bed should bring the bed sediment source closer to equilibrium with the imposed shear stress and other sedimentation conditions. Taken together, these sensitivity tests suggest that the main sediment source is output from the river inflows, both directly and indirectly as sediment is reworked and redistributed during wind-wave erosion events.

The sensitivity of model shoaling to channel depth change was much greater than for other parameters or conditions tested.

Structural alternative tests included 13 variations of jetty and artificial reef plans installed into the existing model condition. Jetties ranging from 75,000 to 118,500 ft were the largest structures tested. These jetties were installed into the model mesh with the 38-ft-deep channel and were most effective at reducing final shoal volumes (reductions of 30 to 62 percent relative to the 38-ft-deep base case) and other shoal-change indices (reductions of 32 to 65 percent). The jetties greatly reduced salinities in the channel as well as the salinities in areas adjacent to the channel. The jetties interrupted coastal flow and allowed build up of fresh- and brackish-water both between and outside of the jetties. Salinities outside the jetties were reduced most to the west of the channel. Jetties decreased salinity stratification between the jetties. Stratification seaward of the jetties was increased. Flow speeds increased appreciably in jettied channels.

Longer jetties caused channel flows to push shoaling distributions seaward. Shoal centroids were seaward of the ends of the jetties. A single jetty on the east side of the channel reduced shoaling by about the same amount as dual jetties of the same length (though maximum current speeds at the landward end of the jetty apparently increased appreciably as compared to base and the dual-jetty cases). Combination jetties and reefs *RJ5-7* did not perform as well as *Jetty3* because they increased jettied flows that caused increased sediment delivery and shoaling seaward of the jetties.

Artificial reefs were similar to long lateral dikes but intended to divert bay-water outflow away from the area of the channel rather than to train the flow in the channel. Most bay outflow is not carried in the channel. The longest artificial reef was 56,500 ft long and reduced final shoal volume by 24 percent. This reef reduced the average shoaling rate by 47 percent as compared to a 30 percent reduction found for the 75,000 ft jetties. This indicates that the reef structure was more effective at retarding shoal formation than jetties of a similar length. Seaward of reefs, TSM values decreased while channel salinities increased and salinity stratification decreased.

Most of the structural alternative test plans were smaller structures, some with relatively small-scale features. The intent was to find the lower limit to structure size that would appreciable reduce channel shoaling. Structures composed of smaller (shorter) reef and jetty combinations performed no better than the longer of the component parts. For example, the combination structure *RJ5* did not reduce shoal indices as well as the 75,000 ft jetty *Jetty3* that comprised its basic structure. Other small-scale structural appurtenances had little or no effect on shoaling (*Reef3* and *RJ4*, *Reef4* and *Reef5*).

A general conclusion from this study is that the 3D numerical hydrodynamic and fluid / settled mud model is a good representation of hydrodynamics and sedimentation processes in the LAR Bar Channel. This was demonstrated by illustrating that the model computes the proper response to basic processes and through comparisons of computed and observed variables such as water surface elevation, velocity, salinity, suspended sediment concentration, and bed thickness.

REFERENCES

Adams, C.E., Jr., Wells, J.T., and Coleman, J.M. (1982). “Sediment transport on the central Louisiana continental self: Implications for the developing Atchafalaya River Delta,” *Marine Science* 25, 133-148.

Alexander, M.P., Teeter, A.M., and Banks, G.E. (1997). "Development of an intrusive hydrographic survey system for fluid mud channels," Technical Report DRP-97-1, U.S. Army Engineer Waterways Experiment Station, Vicksburg, MS.

Bloss, S., Lehfeldt, R., and Patterson, J. (1988). “Modeling turbulent transport in a stratified estuary,” *J. of Hydraulic Engrg.* 114(9), 1113-33.

Bunch, B.W., Cerco, C.F., Dortch, M.S., Johnson, B.H., and Kim, K.W. (2000). “Hydrodynamic and water quality model study of San Juan Estuary,” ERDC TR-00-1, Engineer Research and Development Center, Vicksburg, MS.

DiMarco, S.F., and Reid, R.O. (1998). "Characterization of the principal tidal current constituents on the Texas-Louisiana shelf," *J. Geophys. Res.* 103(C2), 3093-3109.

Donnell, B.P., Letter, J.V., and Teeter, A.M. (1991). “The Atchafalaya River Delta, Report 11, Two-dimensional modeling,” Technical Report HL-82-15, U.S. Army Engineer Waterways Experiment Station, Vicksburg, MS.

Edinger, J., Brady, D., and Geyer, J. (1974). “Heat exchange and transport in the environment,” Report 14, Dept. of Geography and Environmental Engineering, Johns Hopkins University, Baltimore, MD.

Garratt, J. R. (1977). “Review of drag coefficients over oceans and continents,” *Monthly Weather Review* 105, 915-29.

GVI. (2003). “Value engineering report: Atchafalaya Bar Channel fluff and fluid mud study, Morgan City, Louisiana,” CEMVN-04-01, GeoVal, Inc., San Diego, CA.

Huh, O.K., Moeller, C.C., Menzel, W.P., Rouse, L.J., Jr., and Roberts, H.H. (1996). “Remote sensing of turbid coastal and estuarine waters: A method for multispectral water-type analysis,” *J. Coastal Res.* 12(4), 984-995.

Huh, O.K., Walker, N.D., and Moeller, C. (2001). "Sedimentation along the eastern Cheneir Plain coast: Down drift impact of a delta complex shift," *J. Coastal Res*. 17(1), 72-81.

Islam, M.A., and Karamisheva, R.D. (1998). "Initial settling rate/concentration relationship in zone settling," *J. Envir. Engrg.* 124, 1, 39-42.

Johnson, B. H. (1980). "VAHM – A Vertically Averaged Hydrodynamic Model using boundary-fitted coordinates," MP HL-80-3, U.S. Army Engineer Waterways Experiment Station, Vicksburg, MS.

Johnson, B.H., Heath, R.E., Hsieh, B.B., Kim, K.W., and Butler, H.L. (1991). "Development and verification of a three-dimensional numerical hydrodynamic, salinity, and temperature model of Chesapeake Bay," Technical Report HL-91-7, U.S. Army Engineer Waterways Experiment Station, Vicksburg, MS.

Johnson, B.H., Kim, K.W., Heath, R.E., Hsieh, B.B., and Butler, H.L. (1993). "Validation of a three-dimensional hydrodynamic model of Chesapeake Bay," *Journal of Hydraulic Engineering* 119(1), 2-20.

Johnson, B.H., Kim, K.W., Wang, H.V., Martin, B.L., and Heath, R.E. (1999). "Assessment of the impact of proposed dredged material placement islands in Upper Chesapeake Bay," Contract report to Maryland Environmental Service, Annapolis, MD.

Kemp, G.P. (1986). "Mud deposition at the shoreface: wave and sediment dynamics on the chenier plain of Louisiana," Ph.D. dissertation, Louisiana State University, Baton Rouge, LA.

Kim, K.W. and Johnson, B.H. (1998). "Assessment of channel deepening in the Delaware River and Bay," Technical Report CHL-98-29, U.S. Army Engineer Waterways Experiment Station, Vicksburg, MS.

Leonard, B. (1979). "A stable and accurate convection modeling procedure based on quadratic upstream interpolation," *Computer Methods in Applied Mechanics and Engineering* 19, 59-98.

Letter, J.V. (1982). "The Atchafalaya River Delta, Report 3: Extrapolation of delta growth," Technical Report HL-82-15, U.S. Army Engineer Waterways Experiment Station, Vicksburg, MS.

Letter and Powell (in preparation). “Development of a 2D numerical model to address Atchafalaya Bay Delta growth.”

Li, Y., and Mehta, A.J. (2001). “Fluid mud in the wave-dominated environment revisited,” in *Coastal and Estuarine Fine Sediment Processes*, W.H. McAnally and A.J. Mehta ed., Elsevier, NY, 79-93.

Mehta, A.J., and Kirby, R. (2001). “Muddy coast dynamics and stability,” *J. Coastal Res*., SI No. 27, 121-136.

Rodi, W. (1980). “Turbulence models and their application in hydraulics: A state of the art review,” IAHR, Delft, The Netherlands.

Sakakiyama, T., and Bijker, E.W. (1989). “Mass transport velocity in mud layer due to progressive waves,” *J. of Waterway, Port, Coastal, and Ocean Engrg*., ASCE, 115(5), 614-633.

Sheng, Y.P. (1986). “A three-dimensional mathematical model of coastal, estuarine, and lake currents using a boundary-fitted grid,” Report No. 585, A.R.A.P. Group of Titan Research and Technology, Princeton, NJ.

Teeter, A.M. (1992). "The viscous characteristics of channel-bottom muds," Technical Note DRP-1-07, U.S. Army Engineer Waterways Experiment Station, Vicksburg, MS.

Teeter, A.M. (2000). "Underflow spreading from an open-water pipeline disposal," ERDC TN-DOER-N7, U.S. Army Engineer Research and Development Center, Vicksburg, MS.

Teeter, A.M. (2002). "Sediment dispersion near a dredge pipeline discharge in Laguna Madre, Texas," ERDC TN-DOER-N16, U.S. Army Engineer Research and Development Center, Vicksburg, MS.

Teeter, A.M., and Pankow, W. (1989). “The Atchafalaya River Delta, Report 2, Field Data, Section 2: Settling characteristics of bay sediments,” Tech. Rpt. HL-82-15, U.S. Army Engineer Waterways Experiment Station, Vicksburg, MS.

Teeter, A.M., Brown, G.L., Alexander, M.P., Callegan, C.J., Sarruff, M.S., and McVan, D.C. (2002). “Wind-wave resuspension and circulation of sediment and dredged material

in Laguna Madre,Texas," U.S. Army Engineer Research and Development Center, Vicksburg, MS. (Draft)

Teeter, A.M., Fagerburg, T., Waller, T., Benson, H., Brister, D., and McAdory, R. (2003). "Factors affecting fluff and fluid mud accumulation in the Atchafalaya Bar Channel," U.S. Army Engineer Research and Development Center, Vicksburg, MS. (Final Draft)

Thomas, W.A., Heath, R.E., Stewart, J.P., and Clark, D.G. (1988). "The Atchafalaya River Delta, Report 5: The Atchafalaya River Delta quasi-two-dimensional model of delta growth and impacts on river stages," Technical Report HL-82-15, U.S. Army Engineer Waterways Experiment Station, Vicksburg, MS.

USACE. (1991). Tidal Hydraulics. EM 1110-2-1607, U.S. Army Corps of Engineers, Washington, DC.

USACE. (2002). "Mississippi River and tributaries, Atchafalaya Basin, Louisiana, Lower Atchafalaya Basin reevaluation study," Mississippi River Commission, Vicksburg, MS.

Van Heerden, I.L.I., and Kemp, G.P. (2000). "Recommendations for reduction of shoaling in the Atchafalaya River navigation bar channel," Final Report, Louisiana Sate University, Baton Rouge, LA.

Vinzon, S.B., and Paiva, A.M. (2002). "Modeling of sediment concentrations on the Amazon shelf," In J.C. Winterwerp and C. Kranenburg, Editors: *Fine sediment dynamics in the marine environment*. Elsevier, NY.

Wells, J.T. (1983). "Dynamics of coastal fluid muds in low-, moderate-, and high-tide-range environments," *Canadian J. of Fisheries, and Aquatic Sci*. 40 (supplement 1), 130-142.

Wells, J.T., and Coleman, J.M. (1981). "Periodic mudflat progradation, northeast coast of South America: A hypothesis," *J. Sedimentary Petrology* 51(4), 1069-1075.

Walker, N.D., and Hammack, A.B. (2000). "Impacts of winter storms on circulation and sediment transport: Atchafalaya-Vermilion Bay region, Louisiana, U.S.A.," *J. Coastal Res*. 16(4), 996-1010.

Westerink, J.J., Luettich, R.A., Baptista, A.M., Scheffner, N.W., and Farrar, P. (1992). "Tide and storm surge predictions using a finite element model," *J. of Hydraulic Engrg.* 118, 1373-90.

TABLE 1. Comparison of Water Depths from Various Sources at ERDC Stations

ERDC Station	GEODAS Depth, ft MLG	Grid Depth, ft MLG	MVN Depth, ft MLG	ERDC Depth, ft MTL (CI)
A	16	16	11	10.8 (10.2-11.5, n=8)
C	11.8	12	10	9.7 (9.5-10.2, n=9)
E	9.2	12	9	8.7 (7.9-9.5, n=7)

TABLE 2. Salinity Specification at Ocean Boundary, ppt

		Total River Flow, cfs		
Grid Point	Depth	75,000	150,000	300,000
UW	Surface	10	7	5
	Bottom	10	7	6
LW	Surface	30	27	21
	Bottom	34	31	25
LE	Surface	30	30	30
	Bottom	34	34	34
UE	Surface	5	3	0
	Bottom	5	3	0

TABLE 3. Distribution of Freshwater Inflow	
Inflow Point	Distribution
Atchafalaya River	87.3% of Observed Flow at Morgan City
Wax Lake	100% of Observed Flow at Calumet
Jaws	Charenton Flow + (2/3)(8.7% of Morgan City Flow)
West Vermilion Bay	(1/3)(8.7% of Morgan City Flow)
Vermilion River	100% of Observed Flow at Lafayette

TABLE 4. Layer Characteristics of the Sediment Bed						
		At the Top of Layer				
Layer Index	*Hso*, cm	*Cs*, kg/m^3	τ_{ce}, Pa	*M*, g/m^2/sec	τ_y, Pa	*Wh*, mm/sec
0	6.2	51	Fluid Mud Entrainment Regime		0.04	7.76
1	9.7	74			0.12	5.68
2	15.7	109			0.44	3.47
3	32.5	159	0.06	0.350	1.52	1.64
4	57.7	232	0.15	0.228	5.27	0.49
5	110.5	339	0.38	0.087	18.4	0.06
6	156.0	495	0.98	0.016	64.3	0.0001

TABLE 5. Validation Comparison to TSM and Salinity ERDC Data at Specific Times

		TSM, mg/l		Salinity, ppt	
Station (Field n)	Percentile	Field	Model	Field	Model
A (n=100)	5	16	46	1.40	6.22
	16	26	74	2.94	14.7
	50	58	177	15.3	27.5
	84	158	463	24.1	31.9
	95	627	766	27.1	32.1
B (n=49)	5	22	48	11.2	11.3
	16	32	65	14.5	18.1
	50	71	155	21.6	25.0
	84	155	478	27.2	31.9
	95	304	776	29.7	32.0
C (n=59)	5	37	39	7.44	1.22
	16	58	72	12.6	8.98
	50	111	123	19.0	24.9
	84	298	313	25.4	31.4
	95	427	783	29.1	31.7
E (n=70)	5	28	64	0.23	0.01
	16	58	94	0.73	0.30
	50	104	212	4.44	11.6
	84	231	559	16.5	24.2
	95	576	2066	23.6	27.7
F (n=74)	5	48	40	1.57	0.10
	16	68	65	3.74	1.03
	50	185	124	12.2	14.3
	84	976	331	23.2	26.2
	95	1401	769	26.7	28.9

TABLE 6. Validation Comparison to TSM and Salinity ERDC Data for All Model Hourly Values (n=8610)

		TSM, mg/l		Salinity, ppt	
Station (Field n)	Percentile	Field	Model	Field	Model
A (n=219)	16	27	36	8.05	17.1
	50	74	91	18.5	31.6
	84	256	287	26.7	32.4
	95	845	853	28.0	33.3
B (n=116)	16	25	37	13.7	17.4
	50	81	91	21.1	31.7
	84	199	288	27.7	32.5
	95	513	836	28.7	33.3
C (n=98)	16	35	26	15.5	6.89
	50	97	71	21.7	28.5
	84	310	228	26.9	32.2
	95	427	890	28.5	33.1
D (n=96)	16	35	30	10.2	8.12
	50	80	81	19.6	29.1
	84	187	272	26.8	32.3
	95	292	1113	27.8	33.1
E (n=164)	16	39	48	1.41	0.63
	50	93	136	10.0	16.6
	84	212	467	22.5	30.3
	95	400	2656	26.2	32.5
F (n=158)	16	49	35	3.78	0.81
	50	133	93	12.5	17.4
	84	602	315	23.4	30.3
	95	1074	1719	26.6	32.5

TABLE 7. Production Run Sediment Results for 24- to 38-ft Channels with Existing and Future Conditions						
Channel Depth, ft	24		30		38	
Condition, Existing/Future	E	F	E	F	E	F
TSM Stations, mg/l (std) **A**	92 (2.8)	88 (2.8)	89 (2.3)	84 (2.8)	86 (2.7)	82 (2.7)
B	91 (2.8)	88 (2.7)	89 (2.7)	85 (2.7)	87 (2.7)	83 (2.7)
C	71 (2.9)	71 (3.0)	70 (2.8)	68 (2.9)	67 (2.8)	66 (3.0)
D	81 (3.0)	80 (3.2)	80 (3.0)	77 (3.1)	77 (2.9)	76 (3.1)
E	137 (3.1)	140 (2.9)	135 (3.0)	134 (2.9)	129 (3.1)	136 (2.9)
F	94 (3.0)	94 (3.1)	94 (2.9)	91 (3.0)	94 (2.8)	95 (2.8)
CS TSM, mg/l (std) 480	266 (1.8)	316 (1.6)	282 (1.7)	310 (1.5)	297 (1.6)	297 (1.6)
630	149 (2.8)	173 (2.7)	153 (2.7)	165 (2.7)	177 (2.4)	178 (2.4)
762	142 (3.1)	146 (3.3)	138 (2.7)	136 (2.6)	141 (2.7)	141 (2.7)
884	124 (3.2)	124 (3.5)	121 (3.2)	118 (3.1)	125 (2.7)	125 (2.7)
1004	98 (3.2)	99 (3.2)	98 (3.0)	95 (2.9)	105 (2.8)	105 (2.8)
1200	80 (2.8)	80 (2.8)	82 (2.8)	79 (2.6)	89 (2.3)	89 (2.3)
1400	94 (2.9)	93 (2.9)	95 (2.7)	94 (2.7)	106 (3.0)	106 (3.0)
CS $\prod TSM / \overline{TSM}$ (std) 480	0.3 (1.7)	0.3 (1.6)	0.4 (1.6)	0.4 (1.5)	0.5 (1.5)	0.5 (1.5)
630	0.7 (0.9)	0.6 (1.1)	0.7 (1.1)	0.5 (1.3)	0.8 (1.1)	0.8 (1.1)
762	1.2 (0.6)	1.2 (0.6)	1.1 (0.6)	1.1 (0.6)	1.1 (0.7)	1.1 (0.7)
884	1.6 (0.5)	1.6 (0.5)	1.5 (0.5)	1.5 (0.4)	1.4 (0.4)	1.4 (0.4)
1004	1.7 (0.4)	1.9 (0.5)	1.6 (0.4)	1.6 (0.4)	1.5 (0.4)	1.5 (0.4)
1200	1.7 (0.3)	2.0 (0.4)	1.7 (0.5)	1.7 (0.3)	1.5 (0.3)	1.5 (0.3)
1400	2.1 (0.4)	2.2 (0.4)	2.3 (0.5)	2.3 (0.5)	1.8 (0.5)	1.8 (0.5)
Dredging Error, Mcyd	2.30	1.94	0.17	0.29	1.13	0.52
Total Dredging, Mcyd	6.7	7.06	10.33	10.21	12.55	13.16
Shoal Start Dredging, Mcyd	3.86	4.20	5.85	6.08	6.47	7.44
Shoal End Dredging, Mcyd	5.11	5.51	13.64	13.78	13.47	19.08
Shoal End Year, Mcyd	7.02	7.59	15.16	15.02	16.57	21.36

TABLE 8. Production Run Salinity Results for 24- to -38-ft Channel with Existing Conditions			
Channel Depth, ft	24	30	38
Condition Existing/Future	E	E	E
Salinity Sta., ppt (std) **A**	31.6 (0.5)	31.6 (0.5)	31.5 (0.5)
B	31.7 (0.5)	31.7 (0.5)	31.7 (0.5)
C	28.5 (0.9)	28.4 (0.9)	28.2 (0.9)
D	29.1 (0.8)	29.0 (0.8)	28.8 (0.9)
E	16.7 (1.8)	16.5 (1.8)	16.5 (1.8)
F	17.3 (1.7)	17.0 (1.7)	16.3 (1.8)
CS Salinity, ppt (std) 480	0.30 (82.)	0.25 (114)	0.84 (36.)
630	9.07 (3.2)	9.55 (3.2)	17.6 (1.8)
762	21.7 (1.4)	22.5 (1.4)	26.4 (1.0)
884	30.0 (0.6)	30.3 (0.6)	30.6 (0.4)
1004	31.7 (0.4)	31.8 (0.4)	31.8 (0.2)
1200	32.0 (0.2)	32.0 (0.2)	32.2 (0.1)
1400	32.0 (0.1)	32.1 (0.1)	32.1 (0.1)
CS ΠS, ppt (std) 480	0.00 (*)	0.00 (*)	0.04 (*)
630	0.81 (8.3)	0.76 (12.)	4.84 (2.8)
762	2.04 (3.0)	2.20 (3.1)	5.36 (2.4)
884	1.21 (5.1)	1.35 (4.7)	2.01 (6.7)
1004	0.54 (12.)	0.65 (9.4)	0.79 (16.)
1200	0.19 (29.)	0.21 (23.)	0.42 (23.)
1400	0.11 (30.)	0.14 (24.)	0.17 (29.)

TABLE 9. Production Run Salinity Results for 24- to 38-ft Channels with Future Conditions			
Channel Depth, ft	24	30	38
Condition Existing/Future	F	F	F
Salinity Sta., ppt (std) **A**	31.7 (0.5)	31.6 (0.5)	31.7 (0.5)
B	31.8 (0.5)	31.7 (0.5)	31.7 (0.5)
C	28.7 (0.9)	28.4 (0.9)	28.5 (0.9)
D	29.4 (0.9)	29.0 (0.8)	29.2 (0.9)
E	14.9 (2.0)	16.5 (1.8)	14.6 (2.0)
F	15.9 (1.9)	17.0 (1.7)	14.9 (2.0)
CS Salinity, ppt (std) 480	0.01 (*)	0.25 (*)	0.06 (*)
630	4.05 (7.2)	9.55 (3.2)	13.1 (2.4)
762	19.3 (1.6)	22.5 (1.4)	24.4 (1.3)
884	30.2 (0.8)	30.3 (0.6)	30.5 (0.6)
1004	31.8 (0.5)	31.8 (0.4)	31.8 (0.3)
1200	32.0 (0.3)	32.0 (0.2)	32.1 (0.2)
1400	32.0 (0.2)	32.1 (0.1)	32.1 (0.1)
CS ΠS, ppt (std) 480	0.00 (*)	0.00 (*)	0.00 (*)
630	0.21 (36.)	0.76 (12.)	3.66 (4.0)
762	1.56 (3.4)	2.20 (3.1)	3.58 (3.1)
884	0.81 (3.5)	1.35 (4.7)	1.24 (6.5)
1004	0.44 (8.7)	0.65 (9.4)	0.66 (14)
1200	0.13 (26)	0.21 (23.)	0.23 (29)
1400	0.22 (15)	0.14 (24.)	0.13 (30)

TABLE 10. Seasonal Wind Sensitivity Results for 24- and 38-ft Channels with Existing Conditions (See Text for Definitions)						
Channel Depth, ft	24			38		
Run State, Base/Test	B	Season	Uniform	B	Season	Uniform
TSM Stations, mg/l (std) **A**	92 (2.8)	72 (1.9)	79 (2.1)	86 (2.7)	72 (1.8)	78 (2.1)
B	91 (2.8)	73 (2.0)	80 (2.1)	87 (2.7)	72 (1.9)	79 (2.1)
C	71 (2.9)	62 (2.0)	67 (2.2)	67 (2.8)	61 (2.0)	65 (2.2)
D	81 (3.0)	71 (2.2)	77 (2.4)	77 (2.9)	70 (2.1)	75 (2.4)
E	137 (3.1)	153 (2.4)	148 (2.6)	129 (3.1)	147 (2.4)	144 (2.6)
F	94 (3.0)	106 (2.6)	103 (2.6)	94 (2.8)	108 (2.3)	105 (2.4)
CS TSM, mg/l (std) 480	266 (1.8)	285 (1.6)	277 (1.6)	297 (1.6)	300 (1.5)	296 (1.5)
630	149 (2.8)	188 (2.2)	177 (2.3)	177 (2.4)	180 (2.1)	182 (2.1)
762	142 (3.1)	154 (2.5)	152 (2.7)	141 (2.7)	130 (2.2)	135 (2.2)
884	124 (3.2)	102 (2.0)	112 (2.4)	125 (2.7)	95 (1.9)	104 (2.2)
1004	98 (3.2)	79 (1.9)	86 (2.2)	105 (2.8)	82 (1.9)	88 (2.0)
1200	80 (2.8)	73 (2.0)	76 (2.1)	89 (2.3)	78 (1.9)	80 (1.9)
1400	94 (2.9)	93 (2.3)	95 (2.6)	106 (3.0)	91 (2.0)	93 (2.0)
CS $\prod TSM / \overline{TSM}$ (std) 480	0.3 (1.7)	0.4 (1.5)	0.3 (1.6)	0.5 (1.5)	0.5 (1.4)	0.5 (1.3)
630	0.7 (0.9)	0.7 (0.8)	0.7 (0.9)	0.8 (1.1)	0.7 (1.0)	0.7 (1.0)
762	1.2 (0.6)	1.1 (0.5)	1.2 (0.5)	1.1 (0.7)	0.9 (0.8)	1.0 (0.7)
884	1.6 (0.5)	1.4 (0.3)	1.4 (0.3)	1.4 (0.4)	1.2 (0.4)	1.2 (0.4)
1004	1.7 (0.4)	1.5 (0.2)	1.5 (0.2)	1.5 (0.4)	1.3 (0.3)	1.3 (0.3)
1200	1.7 (0.3)	1.7 (0.2)	1.7 (0.2)	1.5 (0.3)	1.4 (0.3)	1.3 (0.3)
1400	2.1 (0.4)	2.2 (0.4)	2.2 (0.4)	1.8 (0.5)	1.5 (0.2)	1.6 (0.3)
Dredging Error, Mcyd	2.30	4.56	3.60	1.13	5.93	2.68
Total Dredging, Mcyd	6.7	4.44	5.40	12.55	7.75	11.00
Shoal Start Dredging, Mcyd	3.86	3.59	3.71	6.47	7.03	7.39
Shoal End Dredging, Mcyd	5.11	0.65	1.70	13.47	4.68	7.92
Shoal End Year, Mcyd	7.02	5.82	6.13	16.57	11.96	14.78

TABLE 11. River Inflow *Qr* Sensitivity Results for 24- and 38-ft Channels with Future Conditions (See Text for Definitions)						
Channel Depth, ft	24			38		
Run State, Base/Test	B	High *Qr*	Low *Qr*	B	High *Qr*	Low *Qr*
TSM Stations, mg/l (std) **A**	88 (2.8)	79 (3.6)	62 (2.6)	82 (2.7)	120 (3.1)	61 (2.5)
B	88 (2.7)	122 (3.0)	63 (2.5)	83 (2.7)	119 (3.0)	62 (2.5)
C	71 (3.0)	92 (3.2)	44 (2.2)	66 (3.0)	90 (3.1)	42 (2.2)
D	80 (3.2)	105 (3.3)	50 (2.4)	76 (3.1)	102 (3.2)	49 (2.4)
E	140 (2.9)	220 (2.2)	78 (3.0)	136 (2.9)	218 (2.1)	73 (3.0)
F	94 (3.1)	147 (2.6)	57 (2.9)	95 (2.8)	152 (2.3)	55 (2.8)
CS TSM, mg/l (std) 480	316 (1.6)	334 (1.1)	155 (2.6)	297 (1.6)	318 (1.4)	126 (2.9)
630	173 (2.7)	283 (1.6)	88 (2.7)	178 (2.4)	285 (1.7)	91 (2.6)
762	146 (3.3)	204 (2.6)	85 (2.7)	141 (2.7)	182 (2.4)	79 (2.4)
884	124 (3.5)	162 (3.5)	77 (2.3)	125 (2.7)	152 (3.0)	76 (2.2)
1004	99 (3.2)	126 (3.4)	67 (3.0)	105 (2.8)	139 (3.2)	72 (2.4)
1200	80 (2.8)	105 (3.2)	69 (2.7)	89 (2.3)	104 (2.5)	73 (2.4)
1400	93 (2.9)	103 (2.9)	91 (2.9)	106 (3.0)	101 (2.6)	91 (2.7)
CS $\prod TSM / \overline{TSM}$ (std) 480	0.3 (1.6)	0.3 (2.0)	0.3 (1.8)	0.5 (1.5)	0.3 (1.8)	0.4 (2.0)
630	0.6 (1.1)	0.4 (1.6)	0.8 (0.9)	0.8 (1.1)	0.4 (1.7)	0.9 (0.9)
762	1.2 (0.6)	1.0 (0.8)	1.2 (0.4)	1.1 (0.7)	0.7 (1.3)	1.1 (0.5)
884	1.6 (0.5)	1.5 (0.5)	1.5 (0.3)	1.4 (0.4)	1.3 (0.5)	1.2 (0.3)
1004	1.9 (0.5)	1.9 (0.8)	1.6 (0.3)	1.5 (0.4)	1.6 (0.6)	1.3 (0.2)
1200	2.0 (0.4)	2.3 (0.6)	1.7 (0.2)	1.5 (0.3)	1.6 (0.5)	1.4 (0.2)
1400	2.2 (0.4)	2.2 (0.4)	2.1 (0.4)	1.8 (0.5)	1.7 (0.5)	1.7 (0.4)
Dredging Error, Mcyd	1.94	1.76	2.63	0.52	0.62	1.97
Total Dredging, Mcyd	7.06	7.24	6.37	13.16	13.06	11.71
Shoal Start Dredging, Mcyd	4.20	4.81	3.33	7.44	9.26	6.42
Shoal End Dredging, Mcyd	5.51	6.31	4.00	19.08	21.13	12.36
Shoal End Year, Mcyd	7.59	8.06	5.34	21.36	22.87	14.31

TABLE 12. Freshwater Inflow *Qf* (Constant Sediment Input) Sensitivity Results for 24- and 38-ft Channels for Future Conditions						
Channel Depth, ft	24			38		
Run State, Base/Test	B	High *Qf*	Low *Qf*	B	High *Qf*	Low *Qf*
TSM Stations, mg/l (std) **A**	88 (2.8)	116 (3.1)	63 (2.5)	82 (2.7)	NA	62 (2.5)
B	88 (2.7)	115 (3.1)	64 (2.5)	83 (2.7)		63 (2.5)
C	71 (3.0)	84 (3.0)	46 (2.3)	66 (3.0)		45 (2.2)
D	80 (3.2)	95 (3.1)	53 (2.5)	76 (3.1)		52 (2.4)
E	140 (2.9)	171 (2.4)	94 (3.1)	136 (2.9)		90 (3.1)
F	94 (3.1)	125 (2.5)	65 (3.0)	95 (2.8)		64 (2.9)
CS TSM, mg/l (std) 480	316 (1.6)	243 (1.2)	226(3.8)	297 (1.6)		195 (4.1)
630	173 (2.7)	216 (1.7)	110 (3.0)	178 (2.4)		109 (3.1)
762	146 (3.3)	165 (2.6)	101 (3.0)	141 (2.7)		92 (2.7)
884	124 (3.5)	146 (3.4)	81 (2.4)	125 (2.7)		80 (2.2)
1004	99 (3.2)	132 (3.5)	68 (2.7)	105 (2.8)		73 (2.3)
1200	80 (2.8)	99 (3.0)	69 (2.7)	89 (2.3)		74 (2.4)
1400	93 (2.9)	101 (2.9)	90 (2.9)	106 (3.0)		91 (2.6)
CS $\prod TSM / \overline{TSM}$ (std) 480	0.3 (1.6)	0.3 (2.1)	0.4 (1.8)	0.5 (1.5)		0.4 (1.6)
630	0.6 (1.1)	0.4 (1.7)	0.9 (0.7)	0.8 (1.1)		0.9 (0.9)
762	1.2 (0.6)	0.9 (0.9)	1.3 (0.4)	1.1 (0.7)		1.1 (0.5)
884	1.6 (0.5)	1.6 (0.5)	1.5 (0.2)	1.4 (0.4)		1.2 (0.2)
1004	1.9 (0.5)	1.8 (0.5)	1.5 (0.2)	1.5 (0.4)		1.3 (0.2)
1200	2.0 (0.4)	2.0 (0.4)	1.7 (0.2)	1.5 (0.3)		1.4 (0.2)
1400	2.2 (0.4)	2.3 (0.4)	2.1 (0.5)	1.8 (0.5)		1.7 (0.4)
Dredging Error, Mcyd	1.94	1.81	2.73	0.52	1.44	1.19
Total Dredging, Mcyd	7.06	7.19	6.27	13.16	12.24	12.49
Shoal Start Dredging, Mcyd	4.20	4.60	3.58	7.44	8.67	7.02
Shoal End Dredging, Mcyd	5.51	5.78	4.28	19.08	20.23	14.43
Shoal End Year, Mcyd	7.59	7.34	6.35	21.36	NA	16.96

TABLE 13. Salinity Results for *Qf* and *Qr* (*Q*) Sensitivity Tests for 24- and 38-ft Channels with Future Conditions							
Channel Depth, ft		24			38		
Run State, Base/Test		B	High *Q*	Low *Q*	B	High *Q*	Low *Q*
Salinity Sta., ppt (std)	**A**	31.7 (0.5)	30.1 (0.8)	32.0 (0.3)	31.7 (0.5)	29.8 (0.8)	32.0 (0.3)
	B	31.8 (0.5)	30.5 (0.7)	32.0 (0.2)	31.7 (0.5)	30.2 (0.8)	32.0 (0.2)
	C	28.7 (0.9)	21.8 (1.4)	31.5 (0.5)	28.5 (0.9)	20.8 (1.5)	31.5 (0.5)
	D	29.4 (0.9)	23.4 (1.3)	31.6 (0.4)	29.2 (0.9)	22.3 (1.4)	31.6 (0.4)
	E	14.9 (2.0)	3.20 (8.4)	26.3 (1.0)	14.6 (2.0)	3.24 (8.2)	26.4 (0.9)
	F	15.9 (1.9)	4.26 (6.4)	26.8 (0.9)	14.9 (2.0)	3.93 (6.7)	26.5 (0.9)
CS Salinity, ppt (std)	480	0.01 (*)	0.0 (*)	4.14 (6.5)	0.06 (*)	0.00 (*)	12.9 (2.4)
	630	4.05 (7.2)	0.06 (*)	26.1 (1.1)	13.1 (2.4)	0.91 (*)	26.3 (0.8)
	762	19.3 (1.6)	5.83 (5.3)	29.4 (0.7)	24.4 (1.3)	14.5 (2.2)	31.3 (0.2)
	884	30.2 (0.8)	25.5 (1.2)	31.9 (0.3)	30.5 (0.6)	26.1 (1.0)	32.0 (0.1)
	1004	31.8 (0.5)	30.8 (0.7)	32.1 (0.2)	31.8 (0.3)	30.8 (0.5)	32.2 (0.1)
	1200	32.0 (0.3)	31.9 (0.4)	32.2 (0.1)	32.1 (0.2)	32.0 (0.1)	32.2 (0.1)
	1400	32.0 (0.2)	31.9 (0.2)	32.1 (0.1)	32.1 (0.1)	32.1 (0.1)	32.2 (0.1)
CS $\sqcap S$, ppt (std)	480	0.00 (*)	0.0 (*)	0.00(*)	0.00 (*)	0.0 (*)	4.10 (3.3)
	630	0.21 (36)	0.0 (*)	2.47 (5.2)	3.66 (4.0)	0.0 (*)	5.64 (2.9)
	762	1.56 (3.4)	0.81 (9.0)	1.91 (3.4)	3.58 (3.1)	3.38 (4.0)	5.01 (3.3)
	884	0.81 (3.5)	1.18 (2.8)	0.61 (9.9)	1.24 (6.5)	1.68 (4.5)	0.93 (13)
	1004	0.44 (8.7)	0.98 (4.3)	0.24 (16)	0.66 (14)	1.38 (6.7)	0.40 (18)
	1200	0.13 (26)	0.34 (13)	0.15 (21)	0.23 (29)	0.52 (19)	0.22 (16)
	1400	0.22 (15)	0.19 (24)	0.05 (32)	0.13 (30)	0.21 (31)	0.09 (20)

TABLE 14. Ocean Suspended Sediment Boundary Condition Sensitivity Results for 24- and 38-ft Channels with Existing and Future Conditions						
Channel Depth, ft	24			38		
Condition, Existing/Future	E			F		
Run State, Base/Test	B	T High	T Low	B	T High	T Low
TSM Stations, mg/l (std) **A**	92 (2.8)	92 (2.7)	89 (2.9)	82 (2.7)	88 (2.6)	84 (2.8)
B	91 (2.8)	93 (2.7)	89 (2.9)	83 (2.7)	88 (2.6)	85 (2.8)
C	71 (2.9)	71 (2.8)	70 (2.9)	66 (3.0)	68 (2.8)	67 (2.9)
D	81 (3.0)	82 (2.9)	81 (3.0)	76 (3.1)	78 (2.9)	76 (3.0)
E	137 (3.1)	136 (3.1)	135 (3.1)	136 (2.9)	130 (3.0)	129 (3.0)
F	94 (3.0)	94 (3.0)	93 (3.0)	95 (2.8)	94 (2.8)	93 (2.8)
CS TSM, mg/l (std) 480	266 (1.8)	266 (1.8)	266 (1.8)	297 (1.6)	280 (1.7)	280 (1.7)
630	149 (2.8)	150 (2.8)	150 (2.8)	178 (2.4)	161 (2.5)	161 (2.5)
762	142 (3.1)	142 (3.1)	141 (3.1)	141 (2.7)	131 (2.4)	129 (2.4)
884	124 (3.2)	126 (3.2)	123 (3.3)	125 (2.7)	117 (2.5)	115 (2.6)
1004	98 (3.2)	100 (3.2)	97 (3.3)	105 (2.8)	98 (2.4)	95 (2.6)
1200	80 (2.8)	83 (2.6)	77 (2.9)	89 (2.3)	86 (2.1)	81 (2.4)
1400	94 (2.9)	96 (2.8)	82 (3.3)	106 (3.0)	101 (2.2)	87 (2.8)
CS $\prod TSM / \overline{TSM}$ (std) 480	0.3 (1.7)	0.3 (1.7)	0.3 (1.7)	0.5 (1.5)	0.4 (1.6)	0.4 (1.7)
630	0.7 (0.9)	0.7 (0.9)	0.7 (0.9)	0.8 (1.1)	0.7 (1.1)	0.7 (1.1)
762	1.2 (0.6)	1.2 (0.5)	1.2 (0.6)	1.1 (0.7)	1.0 (0.7)	1.0 (0.7)
884	1.6 (0.5)	1.6 (0.5)	1.6 (0.5)	1.4 (0.4)	1.3 (0.3)	1.3 (0.4)
1004	1.7 (0.4)	1.7 (0.4)	1.6 (0.4)	1.5 (0.4)	1.4 (0.3)	1.4 (0.3)
1200	1.7 (0.3)	1.7 (0.3)	1.7 (0.3)	1.5 (0.3)	1.4 (0.3)	1.4 (0.2)
1400	2.1 (0.4)	2.1 (0.5)	2.1 (0.6)	1.8 (0.5)	1.6 (0.3)	1.7 (0.4)
Dredging Error, Mcyd	2.30	2.25	2.33	0.52	1.20	1.16
Total Dredging, Mcyd	6.7	6.75	6.67	13.16	12.48	12.52
Shoal Start Dredging, Mcyd	3.86	3.90	3.82	7.44	7.94	7.26
Shoal End Dredging, Mcyd	5.11	5.12	5.02	19.08	18.11	16.31
Shoal End Year, Mcyd	7.02	7.09	6.88	21.36	21.53	19.13

TABLE 15. Wind-Wave Shear Stress // Sensitivity Sediment Results for 24- and 38-ft Channels with Existing Conditions (See Text for Definitions)						
Channel Depth, ft	24			38		
Run State, Base/Test	B	Low //	High //	B	Low //	High //
TSM Stations, mg/l (std) **A**	92 (2.8)	70 (2.5)	113 (2.9)	82 (2.7)	67 (2.5)	107 (2.8)
B	91 (2.8)	70 (2.5)	113 (2.9)	83 (2.7)	67 (2.5)	107 (2.8)
C	71 (2.9)	57 (2.7)	82 (2.9)	66 (3.0)	54 (2.8)	78 (2.9)
D	81 (3.0)	65 (2.9)	97 (3.0)	76 (3.1)	62 (2.9)	92 (2.9)
E	137 (3.1)	120 (3.1)	152 (3.0)	136 (2.9)	113 (3.2)	144 (3.0)
F	94 (3.0)	82 (3.1)	104 (2.9)	95 (2.8)	82 (2.8)	104 (2.7)
CS TSM, mg/l (std) 480	266 (1.8)	263 (1.8)	267 (1.7)	297 (1.6)	278 (1.7)	284 (1.6)
630	149 (2.8)	142 (2.9)	163 (2.6)	178 (2.4)	150 (2.7)	172 (2.4)
762	142 (3.1)	122 (2.8)	160 (3.3)	141 (2.7)	107 (2.6)	144 (2.4)
884	124 (3.2)	98 (2.7)	151 (3.6)	125 (2.7)	89 (2.5)	138 (2.8)
1004	98 (3.2)	75 (2.7)	127 (3.7)	105 (2.8)	75 (2.3)	119 (2.8)
1200	80 (2.8)	67 (2.1)	100 (3.4)	89 (2.3)	70 (2.0)	99 (2.4)
1400	94 (2.9)	82 (2.3)	111 (3.1)	106 (3.0)	81 (2.0)	109 (2.9)
CS $\prod TSM / \overline{TSM}$ (std) 480	0.3 (1.7)	0.3 (1.7)	0.3 (1.7)	0.5 (1.5)	0.4 (1.6)	0.4 (1.5)
630	0.7 (0.9)	0.7 (1.0)	0.7 (0.9)	0.8 (1.1)	0.7 (1.1)	0.7 (1.1)
762	1.2 (0.6)	1.2 (0.6)	1.2 (0.6)	1.1 (0.7)	1.0 (0.8)	1.0 (0.7)
884	1.6 (0.5)	1.5 (0.4)	1.7 (0.5)	1.4 (0.4)	1.2 (0.4)	1.4 (0.4)
1004	1.7 (0.4)	1.6 (0.3)	1.9 (0.6)	1.5 (0.4)	1.3 (0.3)	1.5 (0.4)
1200	1.7 (0.3)	1.7 (0.2)	1.8 (0.4)	1.5 (0.3)	1.4 (0.2)	1.4 (0.2)
1400	2.1 (0.4)	2.1 (0.4)	2.3 (0.4)	1.8 (0.5)	1.5 (0.2)	1.8 (0.5)
Dredging Error, Mcyd	2.30	3.13	1.87	0.52	4.11	0.41
Total Dredging, Mcyd	6.7	5.87	7.13	13.16	9.57	13.27
Shoal Start Dredging, Mcyd	3.86	3.09	4.59	7.44	5.92	9.39
Shoal End Dredging, Mcyd	5.11	3.54	5.45	19.08	11.70	22.26
Shoal End Year, Mcyd	7.02	5.49	7.58	21.36	13.60	25.18

TABLE 16. Bed Re-Initialization Sensitivity Sediment Results for 24- and 38-ft Channels with Future Conditions (See Text for Definitions)						
Channel Depth, ft	24			38		
Run State, Base/Test	B	T I	T II	B	T I	T II
TSM Stations, mg/l (std) **A**	88 (2.8)	126 (2.9)	130 (2.8)	82 (2.7)	116 (2.8)	124 (2.8)
B	88 (2.7)	126 (2.8)	132 (2.8)	83 (2.7)	117 (2.8)	125 (2.8)
C	71 (3.0)	88 (2.7)	87 (2.6)	66 (3.0)	83 (2.7)	83 (2.6)
D	80 (3.2)	103 (2.8)	103 (2.7)	76 (3.1)	97 (2.8)	98 (2.7)
E	140 (2.9)	156 (2.5)	148 (2.4)	136 (2.9)	152 (2.5)	147 (2.5)
F	94 (3.1)	106 (2.7)	101 (2.6)	95 (2.8)	109 (2.5)	106 (2.4)
CS TSM, mg/l (std) 480	316 (1.6)	311 (1.6)	281 (1.3)	297 (1.6)	303 (1.6)	286 (1.4)
630	173 (2.7)	185 (2.5)	172 (2.1)	178 (2.4)	187 (2.4)	181 (2.0)
762	146 (3.3)	163 (2.9)	154 (2.6)	141 (2.7)	145 (2.4)	142 (2.2)
884	124 (3.5)	160 (3.2)	158 (3.1)	125 (2.7)	145 (2.7)	147 (2.6)
1004	99 (3.2)	144 (3.4)	148 (3.2)	105 (2.8)	132 (2.8)	143 (3.0)
1200	80 (2.8)	108 (3.2)	113 (3.0)	89 (2.3)	100 (2.5)	113 (2.8)
1400	93 (2.9)	106 (3.0)	118 (3.1)	106 (3.0)	103 (2.6)	115 (2.7)
CS $\prod TSM / \overline{TSM}$ (std) 480	0.3 (1.6)	0.4 (1.4)	0.3 (1.4)	0.5 (1.5)	0.5 (1.6)	0.4 (1.6)
630	0.6 (1.1)	0.7 (1.0)	0.6 (1.1)	0.8 (1.1)	0.6 (1.2)	0.6 (1.3)
762	1.2 (0.6)	1.3 (0.5)	1.2 (0.5)	1.1 (0.7)	1.0 (0.7)	1.0 (0.8)
884	1.6 (0.5)	1.7 (0.5)	1.7 (0.4)	1.4 (0.4)	1.4 (0.4)	1.4 (0.4)
1004	1.9 (0.5)	2.0 (0.5)	2.0 (0.5)	1.5 (0.4)	1.5 (0.4)	1.7 (0.6)
1200	2.0 (0.4)	2.4 (0.6)	2.4 (0.5)	1.5 (0.3)	1.6 (0.4)	1.6 (0.4)
1400	2.2 (0.4)	2.3 (0.4)	2.3 (0.4)	1.8 (0.5)	1.7 (0.4)	1.8 (0.5)
Dredging Error, Mcyd	1.94	1.65	1.63	0.52	0.33	0.41
Total Dredging, Mcyd	7.06	7.35	7.37	13.16	13.35	13.27
Shoal Start Dredging, Mcyd	4.20	5.90	6.18	7.44	10.74	12.26
Shoal End Dredging, Mcyd	5.51	6.36	6.77	19.08	21.79	22.60
Shoal End Year, Mcyd	7.59	8.34	8.39	21.36	23.93	24.62

TABLE 17. Bed Flow Module Sensitivity Sediment Results for 24-ft Channel with Existing Conditions (See Text for Details)					
Condition	Base	Improved COBDFLW	Increased FM Layer Thickness	Decreased Surface Density	Changed FM Layer Thickness
TSM Stations, mg/l (std) **A**	92 (2.8)	102 (2.9)	79 (2.9)	65 (3.1)	73 (3.0)
B	91 (2.8)	103 (2.8)	78 (2.9)	66 (3.0)	73 (3.0)
C	71 (2.9)	80 (2.7)	63 (3.0)	55 (3.2)	60 (3.1)
D	81 (3.0)	92 (2.9)	73 (3.2)	64 (3.3)	70 (3.2)
E	137 (3.1)	152 (2.7)	127 (3.2)	118 (3.3)	123 (3.3)
F	94 (3.0)	102 (2.7)	86 (3.2)	77 (3.3)	82 (3.2)
CS TSM, mg/l (std) 480	266 (1.8)	278 (1.5)	266 (1.9)	271 (1.8)	269 (1.8)
630	149 (2.8)	163 (2.4)	141 (2.9)	127 (3.3)	135 (3.1)
762	142 (3.1)	156 (2.9)	131 (3.4)	118 (3.7)	126 (3.6)
884	124 (3.2)	142 (3.5)	112 (3.6)	95 (3.8)	104 (3.7)
1004	98 (3.2)	113 (3.4)	86 (3.5)	71 (3.6)	79 (3.5)
1200	80 (2.8)	84 (3.0)	69 (3.0)	55 (3.2)	64 (3.0)
1400	94 (2.9)	91 (3.0)	72 (3.3)	68 (3.3)	75 (3.1)
CS $\prod TSM / \overline{TSM}$ (std) 480	0.3 (1.7)	0.27 (1.6)	0.30 (1.7)	0.33 (1.6)	0.30 (1.7)
630	0.7 (0.9)	0.66 (0.9)	0.73 (0.9)	0.77 (0.8)	0.75 (0.9)
762	1.2 (0.6)	1.22 (0.6)	1.25 (0.6)	1.30 (0.6)	1.28 (0.6)
884	1.6 (0.5)	1.72 (0.5)	1.65 (0.5)	1.65 (0.5)	1.65 (0.5)
1004	1.7 (0.4)	2.03 (0.5)	1.75 (0.4)	1.74 (0.4)	1.76 (0.4)
1200	1.7 (0.3)	2.09 (0.4)	2.07 (0.4)	2.06 (0.4)	2.51 (0.5)
1400	2.1 (0.4)	2.20 (0.4)	2.12 (0.7)	2.25 (0.4)	2.23 (0.4)
Dredging Error, Mcyd	2.30	1.78	1.78	1.48	1.72
Total Dredging, Mcyd	6.7	7.22	7.22	7.52	7.28
Shoal Start Dredging, Mcyd	3.86	3.97	4.13	4.04	4.19
Shoal End Dredging, Mcyd	5.11	5.35	5.51	6.10	5.63
Shoal End Year, Mcyd	7.02	7.55	7.69	8.04	7.72

TABLE 18. Sediment Parameter Sensitivity Sediment Results for 24-ft Channel with Existing Conditions (See Text for Details)					
Condition	Base with *TUY1* = 16,320 Pa	*TUY1* = 24,480 Pa	*TUY1* = 8,120 Pa	*Ws* Salt Factor Reduced	Wh_O = 7.5e-6 m/sec
TSM Stations, mg/l (std) **A**	69 (3.1)	73 (3.0)	69 (3.1)	72 (3.0)	74 (3.0)
B	72 (2.9)	73 (3.0)	73 (3.0)	72 (3.0)	73 (3.0)
C	60 (3.1)	60 (3.1)	60 (3.1)	59 (3.1)	60 (3.1)
D	70 (3.3)	69 (3.3)	70 (3.3)	69 (3.2)	70 (3.3)
E	123 (3.3)	122 (3.3)	123 (3.3)	125 (3.4)	123 (3.3)
F	82 (3.2)	82 (3.2)	82 (3.2)	81 (3.2)	82 (3.2)
CS TSM, mg/l (std) 480	266 (1.8)	262 (1.9)	269 (1.9)	333 (1.8)	264 (1.9)
630	134 (3.0)	136 (3.1)	135 (3.1)	141 (4.3)	137 (3.0)
762	126 (3.5)	125 (3.5)	126 (3.6)	129 (4.2)	124 (3.7)
884	104 (3.7)	104 (3.6)	106 (3.7)	104 (3.8)	106 (3.8)
1004	75 (3.4)	79 (3.5)	75 (3.4)	79 (3.5)	81 (3.5)
1200	55 (3.1)	64 (3.1)	56 (3.1)	63 (3.1)	64 (3.0)
1400	68 (3.4)	68 (3.4)	71 (3.3)	68 (3.4)	68 (3.3)
CS $\prod TSM / \overline{TSM}$ (std) 480	0.31 (1.6)	0.33 (1.6)	0.35 (1.5)	0.48 (1.2)	0.32 (1.6)
630	0.75 (0.9)	0.75 (0.8)	0.74 (0.8)	0.88 (0.6)	0.75 (0.8)
762	1.27 (0.6)	1.27 (0.6)	1.27 (0.6)	1.37 (0.5)	1.27 (0.6)
884	1.65 (0.5)	1.64 (0.5)	1.68 (0.5)	1.69 (0.5)	1.68 (0.5)
1004	1.67 (0.3)	1.74 (0.4)	1.71 (0.3)	1.77 (0.4)	1.86 (0.5)
1200	1.85 (0.4)	2.09 (0.4)	1.86 (0.4)	2.08 (0.4)	2.35 (0.5)
1400	2.16 (0.6)	2.15 (0.6)	2.18 (0.5)	2.17 (0.6)	2.15 (0.6)
Dredging Error, Mcyd	1.45	1.79	1.45	1.79	0.75
Total Dredging, Mcyd	7.55	7.21	7.55	7.21	8.25
Shoal Start Dredging, Mcyd	4.09	4.08	4.13	4.37	4.34
Shoal End Dredging, Mcyd	6.42	5.53	6.67	5.85	7.05
Shoal End Year, Mcyd	8.17	7.83	8.35	8.15	8.50

TABLE 19. Curved Channel Sensitivity Sediment Results for 38-ft Channels with Existing Conditions (See Text for Description)		
Channel Depth, ft	38	
Base/Plan Test	B	Curved Channel
TSM Stations, mg/l (std) **A**	86 (2.7)	86 (2.7)
B	87 (2.7)	87 (2.7)
C	67 (2.8)	68 (2.8)
D	77 (2.9)	78 (2.9)
E	129 (3.1)	132 (3.0)
F	94 (2.8)	95 (2.8)
CS TSM, mg/l (std) 480	297 (1.6)	282 (1.7)
630	177 (2.4)	164 (2.5)
762	141 (2.7)	131 (2.4)
884	125 (2.7)	116 (2.5)
1004	105 (2.8)	96 (2.5)
1200	89 (2.3)	83 (2.2)
1400	106 (3.0)	94 (2.6)
CS $\prod TSM / \overline{TSM}$ (std) 480	0.5 (1.5)	0.41 (1.6)
630	0.8 (1.1)	0.67 (1.1)
762	1.1 (0.7)	0.99 (0.7)
884	1.4 (0.4)	1.29 (0.3)
1004	1.5 (0.4)	1.43 (0.3)
1200	1.5 (0.3)	1.38 (0.2)
1400	1.8 (0.5)	1.72 (0.3)
Dredging Error, Mcyd	1.13	1.77
Total Dredging, Mcyd	12.55	11.91
Shoal Start Dredging, Mcyd	6.47	6.34
Shoal End Dredging, Mcyd	13.47	13.33
Shoal End Year, Mcyd	16.57	16.88

TABLE 20. Channel-side Jetty Structure Sediment Results for *Jetty1-3* Plans with 38-ft Channels and Exisitng Conditions				
Base/Plan Test	B	*Jetty1*	*Jetty2*	*Jetty3*
TSM Stations, mg/l (std) **A**	86 (2.7)	90 (2.2)	91 (2.1)	106 (2.2)
B	87 (2.7)	72 (2.9)	70 (3.0)	77 (3.2)
C	67 (2.8)	76 (2.3)	80 (2.1)	77 (2.4)
D	77 (2.9)	74 (3.2)	70 (3.2)	79 (3.2)
E	129 (3.1)	151 (2.3)	147 (2.2)	157 (2.4)
F	94 (2.8)	89 (2.7)	83 (2.7)	93 (2.7)
CS TSM, mg/l (std) 480	297 (1.6)	210 (2.1)	199 (2.0)	225 (2.0)
630	177 (2.4)	203 (2.2)	192 (2.1)	216 (2.1)
762	141 (2.7)	196 (2.5)	192 (2.3)	219 (2.2)
884	125 (2.7)	192 (2.8)	178 (2.9)	210 (2.6)
1004	105 (2.8)	168 (3.4)	160 (3.2)	185 (3.1)
1200	89 (2.3)	136 (4.3)	142 (3.6)	145 (4.7)
1400	106 (3.0)	117 (5.2)	126 (4.0)	93 (2.5)
CS $\prod TSM / \overline{TSM}$ (std) 480	0.5 (1.5)	0.3 (1.9)	0.29 (1.8)	0.33 (1.9)
630	0.8 (1.1)	0.5 (1.5)	0.39 (1.5)	0.45 (1.6)
762	1.1 (0.7)	0.7 (1.1)	0.64 (1.0)	0.66 (1.3)
884	1.4 (0.4)	0.9 (1.0)	0.87 (0.9)	0.96 (1.0)
1004	1.5 (0.4)	1.1 (0.9)	1.05 (0.8)	1.18 (0.8)
1200	1.5 (0.3)	1.3 (0.8)	1.22 (0.8)	1.25 (0.7)
1400	1.8 (0.5)	1.3 (0.8)	1.32 (0.8)	1.53 (0.3)
Dredging Error, Mcyd	1.13	8.32	8.72	6.51
Total Dredging, Mcyd	12.55	5.36	4.96	7.17
Shoal Start Dredging, Mcyd	6.47	5.32	4.29	6.00
Shoal End Dredging, Mcyd	13.47	7.20	4.44	10.03
Shoal End Year, Mcyd	16.57	9.30	6.34	11.61

TABLE 21. Salinity Results for *Jetty1-3* Structures with 38-ft Channels and Existing Conditions					
Condition Existing/Plan		E	*Jetty1*	*Jetty2*	*Jetty3*
Salinity Sta., ppt (std)	**A**	31.5 (0.5)	15.2 (1.3)	13.13 (1.5)	20.10 (1.0)
	B	31.7 (0.5)	25.6 (0.6)	27.27 (0.5)	25.30 (0.7)
	C	28.2 (0.9)	8.86 (2.3)	9.46 (2.1)	11.33 (2.1)
	D	28.8 (0.9)	19.9 (1.3)	22.90 (1.1)	19.53 (1.3)
	E	16.5 (1.8)	4.66 (3.7)	6.42 (3.2)	4.62 (4.2)
	F	16.3 (1.8)	14.0 (2.0)	17.75 (1.7)	13.50 (2.0)
CS Salinity, ppt (std)	480	0.84 (36.)	1.80 (15.)	2.08 (12.)	1.93 (14.)
	630	17.6 (1.8)	3.02 (9.5)	2.88 (9.1)	2.89 (10.)
	762	26.4 (1.0)	3.30 (8.9)	3.36 (8.2)	3.41 (8.9)
	884	30.6 (0.4)	3.80 (7.8)	4.08 (7.1)	4.16 (7.5)
	1004	31.8 (0.2)	4.46 (6.7)	4.66 (6.3)	6.50 (4.8)
	1200	32.2 (0.1)	6.22 (4.9)	6.12 (4.8)	14.94 (2.1)
	1400	32.1 (0.1)	12.3 (2.5)	8.16 (3.6)	31.89 (0.1)
CS ΔS, ppt (std)	480	0.04 (*)	-0.03 (*)	-0.06 (38.)	-0.01 (*)
	630	4.84 (2.8)	0.00 (*)	0.00 (*)	0.00 (*)
	762	5.36 (2.4)	0.05 (*)	0.05 (58.)	0.07 (79.)
	884	2.01 (6.7)	0.17 (22.)	0.20 (17.)	0.13 (25.)
	1004	0.79 (16.)	0.29 (12.)	0.39 (9.2)	0.17 (17.)
	1200	0.42 (23.)	0.34 (10.)	0.59 (5.8)	0.20 (12.)
	1400	0.17 (29.)	0.40 (8.7)	0.65 (6.3)	0.71 (8.2)

TABLE 22. Sediment, Salinity, and Channel Current Results for Dual and Single Jetty Plans *Jetty3-4* with 38-ft Channels and Existing Conditions				
Base/Plan Test		B	Dual Short Jetties (*Jetty3*)	Single Short Jetty (*Jetty4*)
CS TSM, mg/l (std)	480	297 (1.6)	225 (2.0)	270 (1.7)
	630	177 (2.4)	216 (2.1)	249 (1.8)
	762	141 (2.7)	219 (2.2)	222 (2.0)
CS $\Pi TSM / \overline{TSM}$ (std)	480	0.5 (1.5)	0.33 (1.9)	0.41 (1.7)
	630	0.8 (1.1)	0.45 (1.6)	0.33 (1.9)
	762	1.1 (0.7)	0.66 (1.3)	0.29 (2.1)
CS Salinity, ppt (std)	480	0.84 (36.)	1.93 (14.)	25.56 (1.2)
	630	17.6 (1.8)	2.89 (10.)	27.32 (1.1)
	762	26.4 (1.0)	3.41 (8.9)	28.82 (1.0)
CS ΠS, ppt (std)	480	0.04 (*)	-0.01 (*)	0.14 (15.)
	630	4.84 (2.8)	0.00 (*)	0.28 (5.5)
	762	5.36 (2.4)	0.07 (79.)	0.38 (2.7)
CS $(U_S)_{max}$, cm/sec	600	180	193	168
	762	118	185	142
CS $(U_S)_{rms}$, cm/sec	600	34.9	54.9	28.9
	762	26.0	53.2	22.6
Dredging Error, Mcyd		1.13	6.51	5.82
Total Dredging, Mcyd		12.55	7.17	7.86
Shoal Start Dredging, Mcyd		6.47	6.00	6.67
Shoal End Dredging, Mcyd		13.47	10.03	10.28
Shoal End Year, Mcyd		16.57	11.61	11.80

TABLE 23. Sediment Results for Jetty/Reef Structures *RJ5-7* with 38-ft Channels and Exisitng Conditions				
Base/Plan Test	B	*RJ5*	*RJ6*	*RJ7*
TSM Stations, mg/l (std) **A**	86 (2.7)	97 (2.0)	133 (2.4)	139 (2.2)
B	87 (2.7)	43 (2.9)	43 (3.0)	34 (2.8)
C	67 (2.8)	59 (2.4)	91 (2.3)	92 (2.3)
D	77 (2.9)	30 (2.6)	30 (2.6)	27 (2.7)
E	129 (3.1)	29 (2.8)	214 (1.8)	210 (1.8)
F	94 (2.8)	25 (2.5)	25 (2.5)	22 (2.9)
CS TSM, mg/l (std) 480	297 (1.6)	281 (1.7)	274 (1.8)	266 (1.8)
630	177 (2.4)	268 (1.8)	252 (2.0)	248 (2.0)
762	141 (2.7)	262 (2.0)	236 (2.3)	241 (2.2)
884	125 (2.7)	242 (2.2)	206 (2.7)	220 (2.5)
1004	105 (2.8)	218 (2.6)	176 (3.4)	204 (2.7)
1200	89 (2.3)	182 (3.4)	153 (4.3)	187 (3.7)
1400	106 (3.0)	83 (2.8)	87 (2.9)	100 (3.0)
CS $\prod TSM / \overline{TSM}$ (std) 480	0.5 (1.5)	0.56 (1.5)	0.56 (1.6)	0.56 (1.6)
630	0.8 (1.1)	0.66 (1.3)	0.58 (1.5)	0.58 (1.6)
762	1.1 (0.7)	0.82 (1.1)	0.70 (1.2)	0.71 (1.4)
884	1.4 (0.4)	0.99 (1.0)	0.95 (1.1)	0.97 (1.1)
1004	1.5 (0.4)	1.14 (0.8)	1.16 (0.8)	1.10 (0.9)
1200	1.5 (0.3)	1.16 (0.8)	1.21 (0.7)	1.30 (0.7)
1400	1.8 (0.5)	1.65 (0.4)	1.69 (0.4)	1.75 (0.6)
Dredging Error, Mcyd	1.13	5.05	4.86	3.82
Total Dredging, Mcyd	12.55	8.63	8.82	9.86
Shoal Start Dredging, Mcyd	6.47	6.71	6.87	7.21
Shoal End Dredging, Mcyd	13.47	11.31	12.02	12.83
Shoal End Year, Mcyd	16.57	13.28	14.07	14.56

TABLE 24. Salinity Results for Reef/Jetty Structures *RJ5-7* with 38-ft Channels and Exisitng Conditions					
Condition Existing/Plan		E	*RJ5*	*RJ6*	*RJ7*
Salinity Sta., ppt (std)	**A**	31.5 (0.5)	21.47 (1.0)	20.29 (1.1)	19.04 (1.2)
	B	31.7 (0.5)	28.37 (0.5)	28.69 (0.5)	29.11 (0.3)
	C	28.2 (0.9)	14.58 (1.6)	10.48 (2.3)	10.49 (2.4)
	D	28.8 (0.9)	27.64 (0.5)	27.78 (0.5)	28.61 (0.3)
	E	16.5 (1.8)	11.21 (1.8)	1.98 (8.2)	1.91 (8.7)
	F	16.3 (1.8)	26.98 (0.5)	27.09 (0.5)	28.07 (0.4)
CS Salinity, ppt (std)	480	0.84 (36.)	0.07 (*)	0.16 (*)	0.18 (*)
	630	17.6 (1.8)	0.14 (*)	0.26 (95.)	0.28 (89.)
	762	26.4 (1.0)	0.21 (*)	0.42 (70.)	0.38 (79.)
	884	30.6 (0.4)	0.38 (80.)	0.83 (38.)	0.63 (50.)
	1004	31.8 (0.2)	2.55 (12.)	4.39 (7.2)	2.64 (12.)
	1200	32.2 (0.1)	11.88 (2.7)	14.39 (2.2)	12.94 (2.5)
	1400	32.1 (0.1)	31.68 (0.2)	31.81 (0.2)	31.78 (0.2)
CS ΔS, ppt (std)	480	0.04 (*)	-0.01 (*)	-0.02 (*)	-0.03 (*)
	630	4.84 (2.8)	-0.01 (*)	-0.02 (*)	-0.02 (*)
	762	5.36 (2.4)	-0.01 (*)	-0.01 (*)	-0.01 (*)
	884	2.01 (6.7)	0.0 (*)	0.01 (*)	0.0 (*)
	1004	0.79 (16.)	0.07 (49.)	0.15 (27.)	0.08 (47.)
	1200	0.42 (23.)	0.12 (17.)	0.15 (14.)	0.21 (11.)
	1400	0.17 (29.)	0.39 (11.)	0.49 (10.)	1.04 (5.4)

TABLE 25. Sediment Results for Reef Structures *Reef2-3* and *RJ4* with 24-ft Channels and Existing Conditions				
Channel Depth, ft	24			
Condition, Existing/Test	E	*Reef2*	*Reef3*	*RJ4*
TSM Stations, mg/l (std) **A**	92 (2.8)	67 (2.8)	72 (2.6)	74 (3.0)
B	91 (2.8)	65 (2.6)	70 (2.7)	71 (2.8)
C	71 (2.9)	45 (2.7)	53 (3.0)	53 (2.9)
D	81 (3.0)	49 (2.7)	57 (3.1)	58 (3.0)
E	137 (3.1)	87 (2.9)	94 (3.3)	103 (2.7)
F	94 (3.0)	64 (2.9)	68 (3.2)	77 (2.7)
CS TSM, mg/l (std) 480	266 (1.8)	163 (2.7)	171 (2.8)	204 (2.1)
630	149 (2.8)	95 (2.5)	110 (3.0)	130 (2.4)
762	142 (3.1)	89 (2.8)	103 (3.2)	111 (2.7)
884	124 (3.2)	80 (2.6)	93 (3.1)	94 (3.1)
1004	98 (3.2)	74 (3.0)	80 (3.1)	82 (3.3)
1200	80 (2.8)	71 (2.7)	73 (2.8)	73 (2.9)
1400	94 (2.9)	91 (2.9)	92 (2.9)	92 (2.9)
CS $\prod TSM / \overline{TSM}$ (std) 480	0.3 (1.7)	0.24 (3.4)	0.32 (2.4)	0.25 (2.6)
630	0.7 (0.9)	0.40 (1.7)	0.44 (1.8)	0.49 (2.2)
762	1.2 (0.6)	1.18 (0.6)	1.26 (0.6)	0.91 (1.0)
884	1.6 (0.5)	1.54 (0.3)	1.58 (0.4)	1.59 (0.4)
1004	1.7 (0.4)	1.63 (0.3)	1.63 (0.3)	1.76 (0.4)
1200	1.7 (0.3)	1.73 (0.3)	1.75 (0.3)	1.77 (0.3)
1400	2.1 (0.4)	2.19 (0.4)	2.18 (0.4)	2.22 (0.4)
Dredging Error, Mcyd	2.30	4.22	3.87	4.97
Total Dredging, Mcyd	6.7	4.78	5.13	4.03
Shoal Start Dredging, Mcyd	3.86	1.82	2.06	3.85
Shoal End Dredging, Mcyd	5.11	3.73	4.43	5.66
Shoal End Year, Mcyd	7.02	5.33	6.20	6.16

TABLE 26. Salinity Results for Reef Structures *Reef2-3* and *RJ4* with 24-ft Channels and Existing Conditions					
Channel Depth, ft		24			
Condition Existing/Plan		E	*Reef2*	*Reef3*	*RJ4*
Salinity Sta., ppt (std)	**A**	31.6 (0.5)	32.0 (0.5)	32.0 (0.5)	31.97 (0.5)
	B	31.7 (0.5)	32.0 (0.4)	32.0 (0.5)	32.00 (0.5)
	C	28.5 (0.9)	31.6 (0.7)	31.3 (0.8)	31.33 (0.7)
	D	29.1 (0.8)	31.7 (0.6)	31.6 (0.7)	31.65 (0.7)
	E	16.7 (1.8)	23.2 (1.2)	24.0 (1.2)	23.95 (1.2)
	F	17.3 (1.7)	23.5 (1.2)	24.6 (1.2)	24.59 (1.2)
CS Salinity, ppt (std)	480	0.30 (82.)	4.26 (6.0)	2.85 (8.5)	2.85 (8.5)
	630	9.07 (3.2)	10.0 (2.5)	7.92 (3.2)	7.92 (3.2)
	762	21.7 (1.4)	29.3 (0.7)	29.3 (0.8)	29.29 (0.8)
	884	30.0 (0.6)	31.9 (0.4)	31.8 (0.4)	31.80 (0.4)
	1004	31.7 (0.4)	32.1 (0.3)	32.0 (0.3)	32.05 (0.3)
	1200	32.0 (0.2)	32.1 (0.2)	32.1 (0.2)	32.12 (0.2)
	1400	32.0 (0.1)	32.1 (0.1)	32.0 (0.1)	32.05 (0.1)
CS ΠS, ppt (std)	480	0.00 (*)	0.69 (18.)	0.28 (20.)	0.28 (20.5)
	630	0.81 (8.3)	0.20 (20.)	0.15 (27.)	0.15 (27.0)
	762	2.04 (3.0)	2.42 (3.8)	1.58 (4.8)	1.58 (4.8)
	884	1.21 (5.1)	0.4 (22.)	0.44 (16.)	0.44 (15.7)
	1004	0.54 (12.)	0.21 (40.)	0.20 (41.)	0.20 (40.6)
	1200	0.19 (29.)	0.13 (43.)	0.13 (43.)	0.13 (42.6)
	1400	0.11 (30.)	0.14 (23.)	0.15 (22.)	0.15 (21.6)

TABLE 27. Sediment Results for Reefs *Reef4-5* and Reef/Jetty *RJ8* with 38-ft Channels and Existing Conditions				
Channel Depth, ft	38			
Condition, Existing/Test	New Base	*Reef4*	*Reef5*	*RJ8*
TSM Stations, mg/l (std) **A**	86 (2.7)	66 (2.7)	65 (2.7)	76 (2.6)
B	86 (2.7)	63 (2.6)	63 (2.6)	75 (2.6)
C	67 (2.8)	44 (2.7)	44 (2.6)	60 (2.7)
D	77 (2.9)	49 (2.7)	49 (2.6)	70 (2.9)
E	128 (3.1)	91 (3.0)	86 (2.8)	89 (2.0)
F	92 (2.8)	70 (2.9)	66 (2.7)	99 (2.5)
CS TSM, mg/l (std) 480	278 (1.6)	171 (2.7)	162 (2.4)	263 (1.7)
630	156 (2.4)	131 (2.8)	100 (2.5)	161 (2.6)
762	127 (2.6)	84 (2.9)	79 (2.8)	134 (3.0)
884	114 (2.5)	79 (2.5)	78 (2.4)	101 (2.5)
1004	96 (2.5)	76 (2.6)	75 (2.6)	86 (2.4)
1200	82 (2.3)	74 (2.4)	74 (2.4)	78 (2.4)
1400	94 (2.7)	91 (2.4)	90 (2.4)	93 (2.8)
CS $\prod TSM / \overline{TSM}$ (std) 480	0.38 (1.5)	0.46 (1.6)	0.38 (1.7)	0.36 (1.8)
630	0.65 (1.2)	0.45 (1.3)	0.48 (1.5)	0.81 (1.3)
762	0.99 (0.7)	1.00 (0.8)	0.97 (0.8)	1.08 (0.8)
884	1.27 (0.3)	1.25 (0.3)	1.24 (0.2)	1.23 (0.3)
1004	1.40 (0.3)	1.35 (0.2)	1.33 (0.2)	1.36 (0.2)
1200	1.48 (0.3)	1.38 (0.2)	1.37 (0.2)	1.39 (0.2)
1400	1.78 (0.4)	1.66 (0.3)	1.65 (0.3)	1.79 (0.5)
Dredging Error, Mcyd	0.04	1.54	2.12	1.64
Total Dredging, Mcyd	13.64	12.14	11.56	7.36
Shoal Start Dredging, Mcyd	7.14	6.18	6.15	6.35
Shoal End Dredging, Mcyd	18.68	13.12	12.89	13.22
Shoal End Year, Mcyd	21.85	15.74	15.07	17.30

TABLE 28. Salinity Results for Reefs *Reef4-5* and Reef/Jetty *RJ8* with 38-ft Channels and Existing Conditions					
Channel Depth, ft		38			
Condition Existing/Plan		New Base	*Reef4*	*Reef5*	*RJ8*
Salinity Sta., ppt (std)	**A**	31.54 (0.5)	33.58 (0.8)	33.58 (0.8)	31.53 (0.5)
	B	31.65 (0.5)	33.58 (0.9)	33.58 (0.9)	31.59 (0.5)
	C	28.25 (0.9)	33.34 (0.7)	33.35 (0.7)	28.14 (0.8)
	D	28.85 (0.8)	33.33 (0.7)	33.34 (0.7)	28.22 (0.8)
	E	16.63 (1.8)	32.84 (0.4)	32.90 (0.4)	18.70 (1.3)
	F	16.40 (1.8)	32.86 (0.4)	32.91 (0.4)	13.59 (1.9)
CS Salinity, ppt (std)	480	0.85 (36.)	6.92 (3.7)	10.12 (2.7)	4.01 (7.6)
	630	20.24 (1.6)	9.98 (2.7)	16.71 (1.6)	19.94 (1.6)
	762	26.76 (1.0)	30.63 (0.3)	30.88 (0.3)	22.71 (1.4)
	884	30.53 (0.4)	31.81 (0.2)	31.92 (0.2)	30.80 (0.3)
	1004	31.79 (0.3)	32.09 (0.1)	32.12 (0.1)	31.80 (0.2)
	1200	32.07 (0.1)	32.22 (0.1)	32.23 (0.1)	32.12 (0.1)
	1400	32.13 (0.1)	32.23 (0.1)	32.22 (0.1)	32.15 (0.1)
CS ΠS, ppt (std)	480	0.06 (*)	-0.05 (5.0)	-0.13 (4.2)	1.02 (13.)
	630	6.29 (2.5)	-0.01 (*)	-0.08 (7.8)	4.13 (2.7)
	762	5.44 (2.4)	1.62 (2.5)	0.84 (2.2)	3.84 (2.5)
	884	1.87 (6.2)	0.23 (2.7)	0.10 (2.1)	2.91 (4.8)
	1004	0.74 (14.)	0.09 (3.0)	0.05 (2.0)	0.78 (15.)
	1200	0.30 (23.)	0.05 (3.0)	0.02 (4.0)	0.29 (25.)
	1400	0.13 (28.)	0.01 (12.	-0.01 (-6.0)	0.15 (25.)

TABLE 29. Shoal Change Indices for Select Sensitivity Tests

Condition (Base)	Sensitivity Parameter	Channel Depth, ft	*Final Shoal Volume*	*Two Dredgings*	*Average Shoal Rate*
Existing (24 E)	Base	24	0.00	0.00	0.00
"	Season Wind	"	-0.17	-0.42	-0.45
"	Uniform Wind	"	-0.13	-0.30	-0.40
"	Low //	"	-0.22	-0.21	-0.19
"	High //	"	0.08	0.07	0.07
Existing (38 E)	Base	38	0.00	0.00	0.00
"	Season Wind	"	-0.28	-0.43	-0.51
"	Uniform Wind	"	-0.11	-0.21	-0.37
"	Low //	"	-0.36	-0.35	-0.33
"	High //	"	0.17	0.13	0.12

TABLE 30. Shoal Change Indices for Production and Structural Alternative Tests

Condition (Base)*	Plan	Channel Depth, ft	*Final Shoal Volume*	*Two Dredgings*	*Average Shoal Rate*
Existing (24 E)	None	24	0.00	0.00	0.00
"	Deepened	30	1.16	1.08	0.99
"	"	38	1.36	1.26	1.14
Future (24 E)	None	24	0.08	0.07	0.05
"	Deepened	30	1.14	1.07	1.02
"	"	38	2.04	1.85	1.59
Existing (38 E)	*Jetty1*	38	-0.44	-0.49	-0.52
"	*Jetty2*	38	-0.62	-0.63	-0.65
"	*Jetty3*	38	-0.30	-0.32	-0.35
"	*Jetty4*	38	-0.30	-0.30	-0.32
"	*RJ5*	38	-0.20	-0.22	-0.24
"	*RJ6*	38	-0.15	-0.18	-0.21
"	*RJ7*	38	-0.12	-0.13	-0.12
Existing (24 E)	*Reef2*	24	-0.24	-0.27	-0.47
"	*Reef3*	24	-0.12	-0.16	-0.18
"	*RJ4*	24	-0.12	-0.16	-0.12
Existing (38 N)	*Reef4*	38	-0.28	-0.24	-0.22
"	*Reef5*	38	-0.31	-0.27	-0.26
"	*RJ8*	38	-0.21	-0.30	-0.34

* Base refers to the base run's channel depth and condition where E is existing, F is future, and N is new base.

TABLE 31. Field and Model Shoal Volume and Volume Distribution by Reach

	Shoal Volume, Mcyd (Fraction of Total)							
	Reach							
Source	475+00 to 705+00	705+00 to 935+00	935+00 to 1165+00	1165+00 to 1395+00	1395+00 to 1625+00	1625+00 to 1855+00	1855+00 to 2085+00	Total
Field 6/17/02-7/19/02 (n=3)	1.55 (0.19)	2.99 (0.37)	2.23 (0.27)	1.38 (0.17)				8.15 (1.0)
Model 24-ft with Existing	1.55 (0.22)	2.40 (0.34)	1.97 (0.28)	1.10 (0.16)				7.02 (1.0)
Model *Reef2* Plan w/ 24-ft	1.32 (0.25)	1.88 (0.35)	1.13 (0.21)	1.00 (0.19)				5.33 (1.0)
Model 38-ft with Existing	1.31 (0.08)	3.54 (0.21)	2.91 (0.18)	2.53 (0.15)	2.75 (0.17)	2.23 (0.13)	1.30 (0.08)	16.57 (1.0)
Model *Jetty4* Plan w/ 38-ft	0.70 (0.6)	0.37 (0.03)	0.63 (0.05)	1.53 (0.13)	3.84 (0.33)	2.99 (0.25)	1.74 (0.15)	11.80 (1.0)

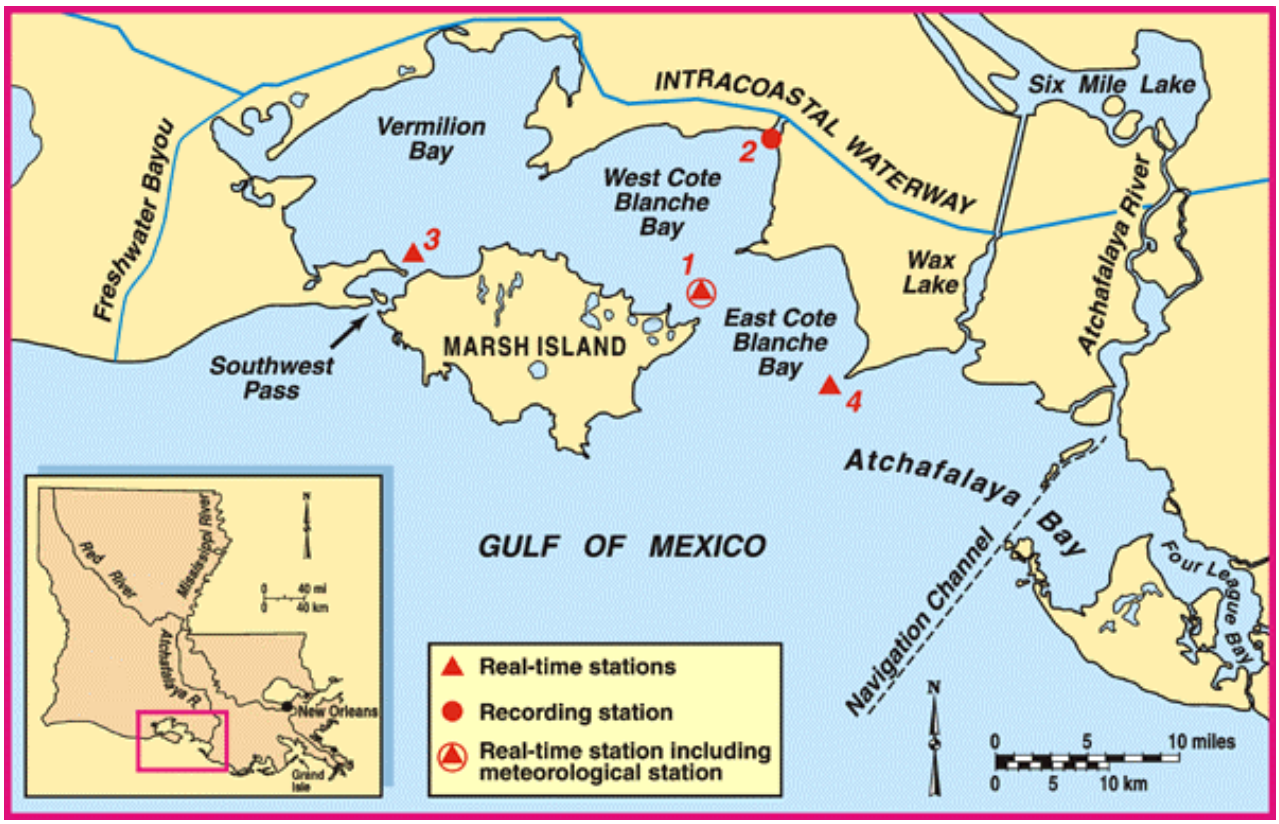

Figure 1. Atchafalaya Bay and Bar Channel (from the LSU BAYWATCH Program)

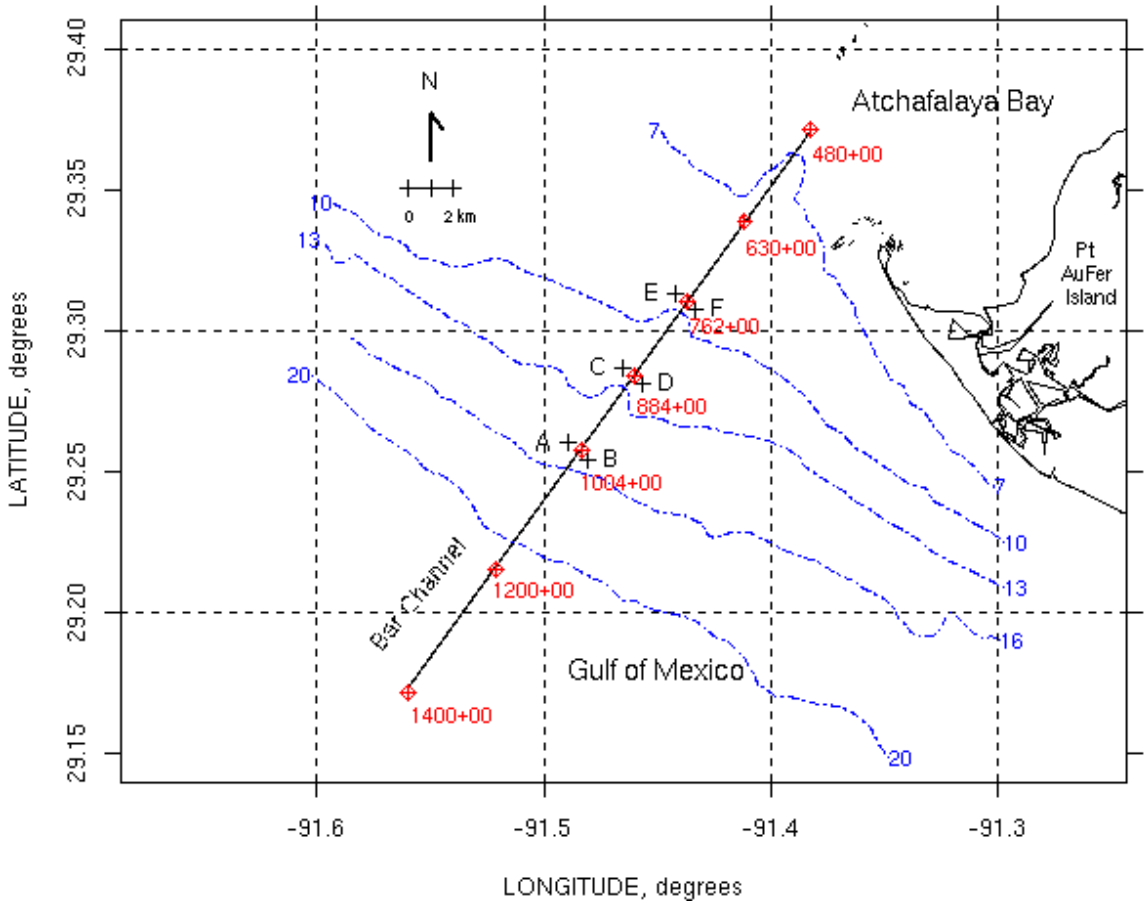

Figure 2. LAR Bar Channel with ERDC and channel stations and approximate depth contours in feet

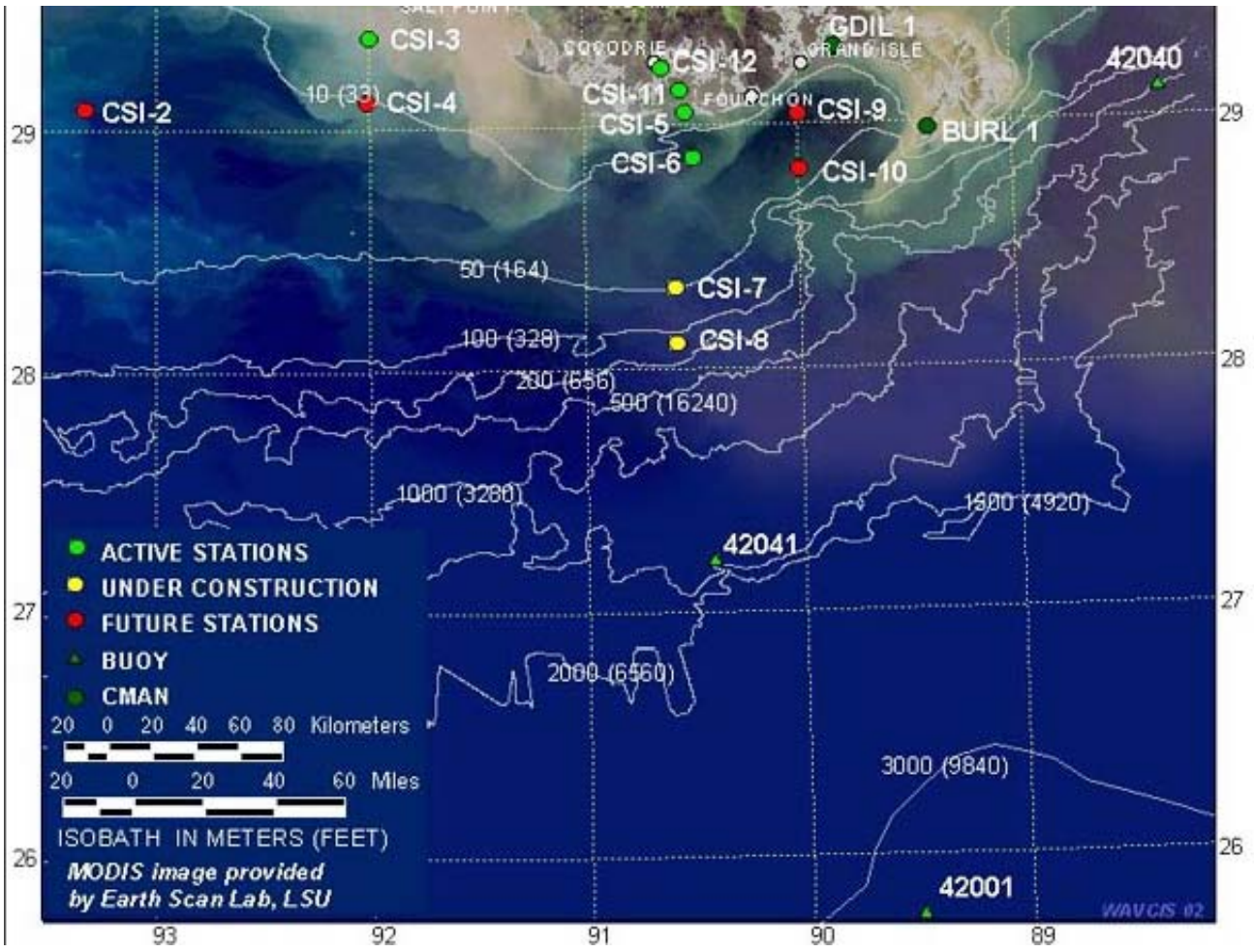

Figure 3. LSU WAVCIS stations

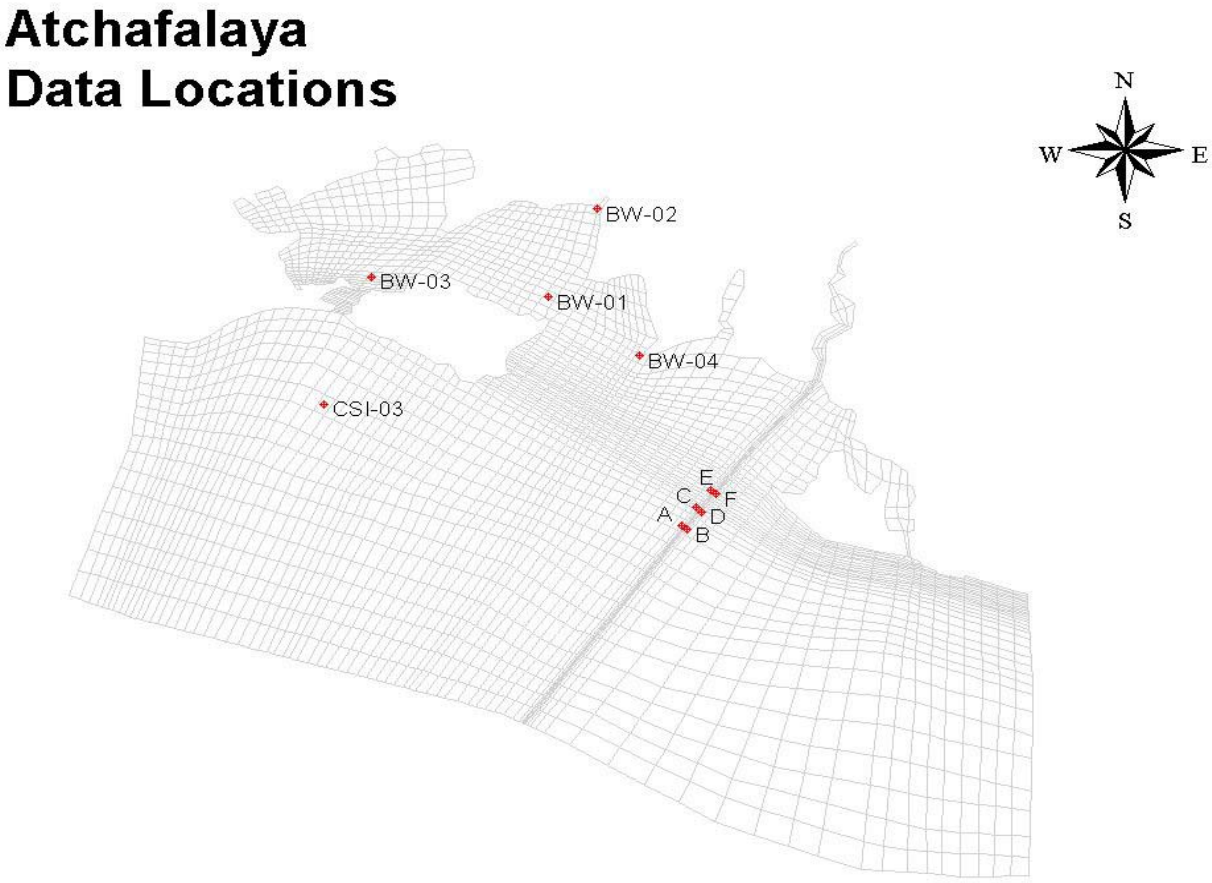

Figure 4. Interior data stations

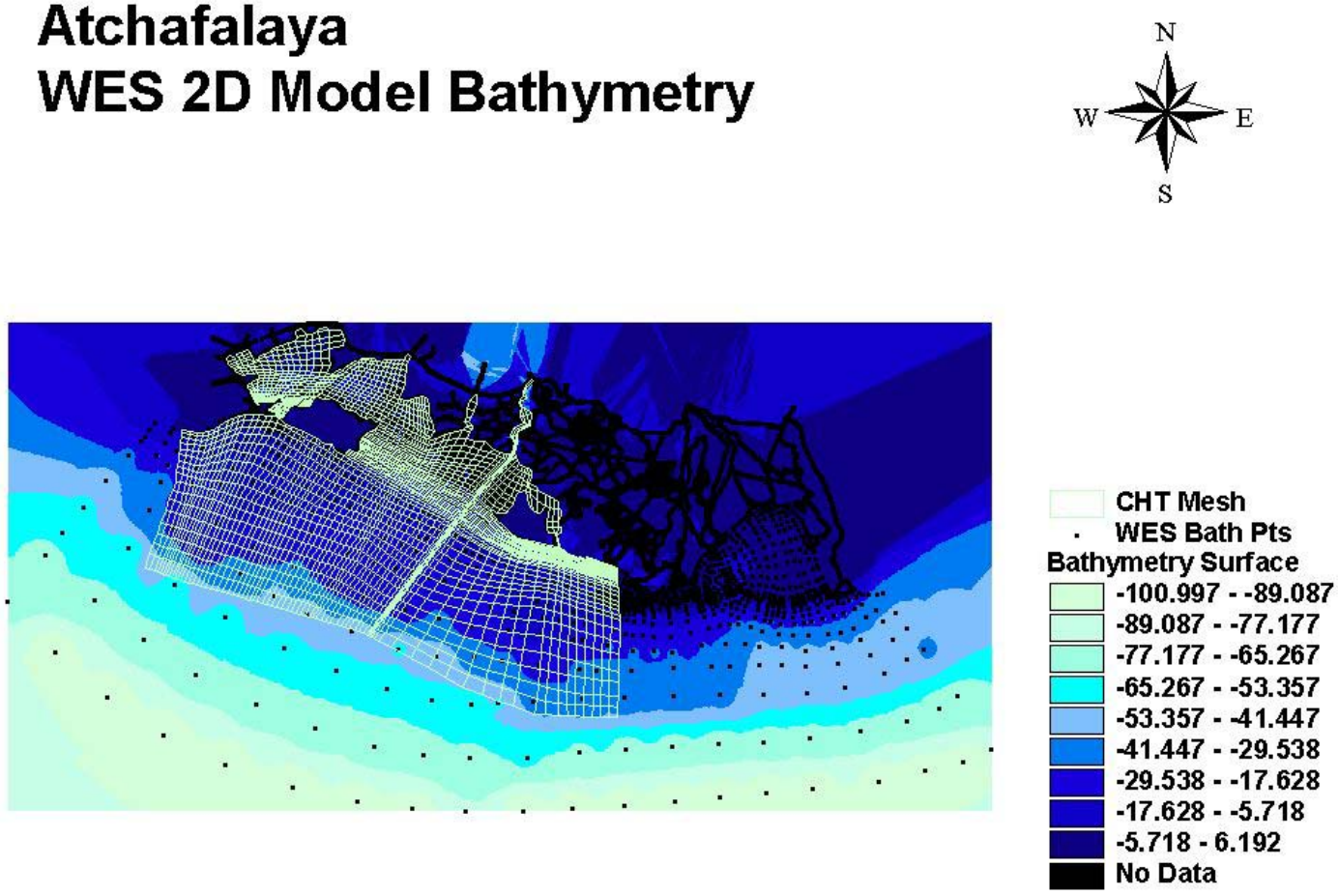

Figure 5. Bathymetry from WES 2D model

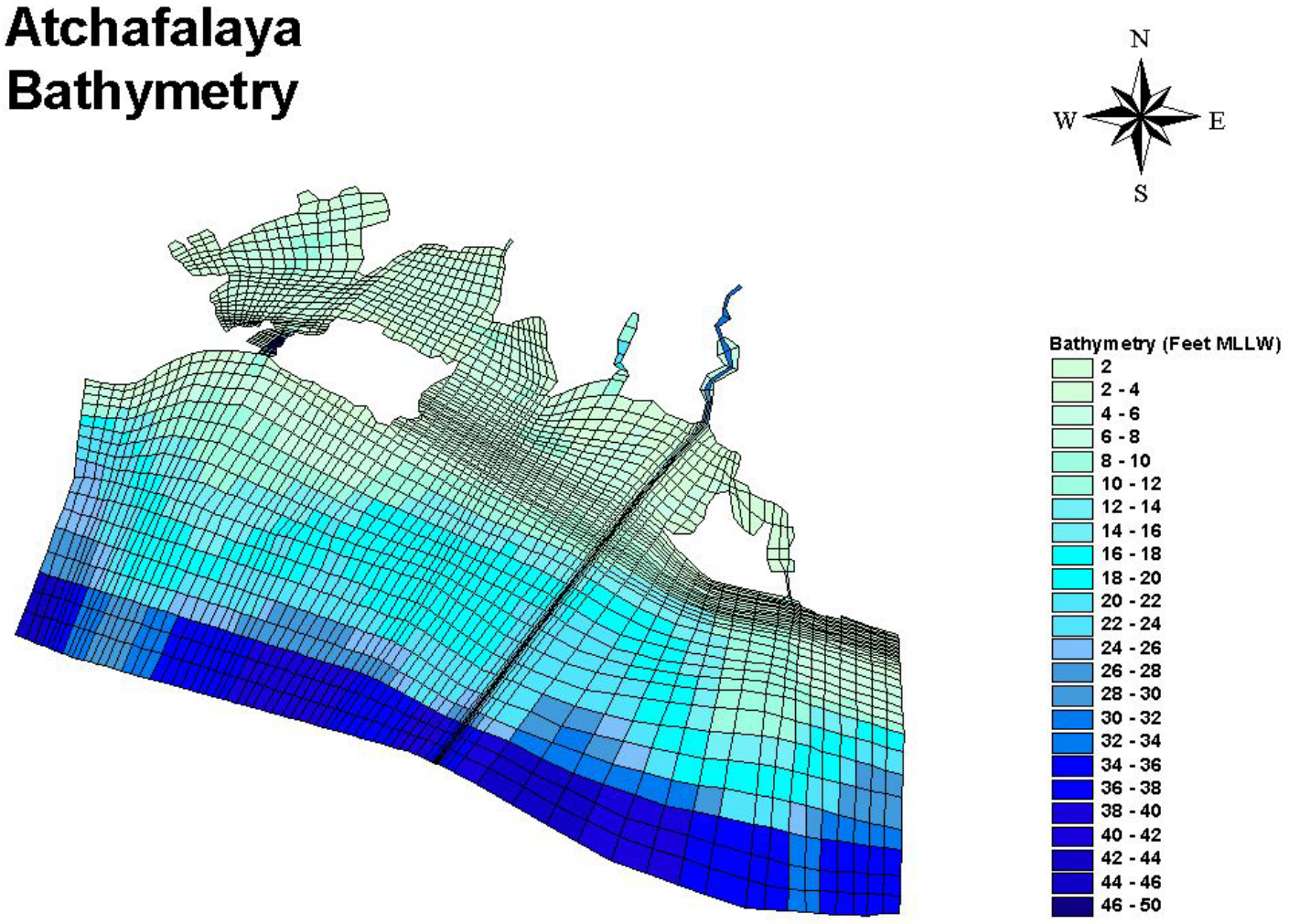

Figure 6. CH3D numerical planform grid with bathymetry

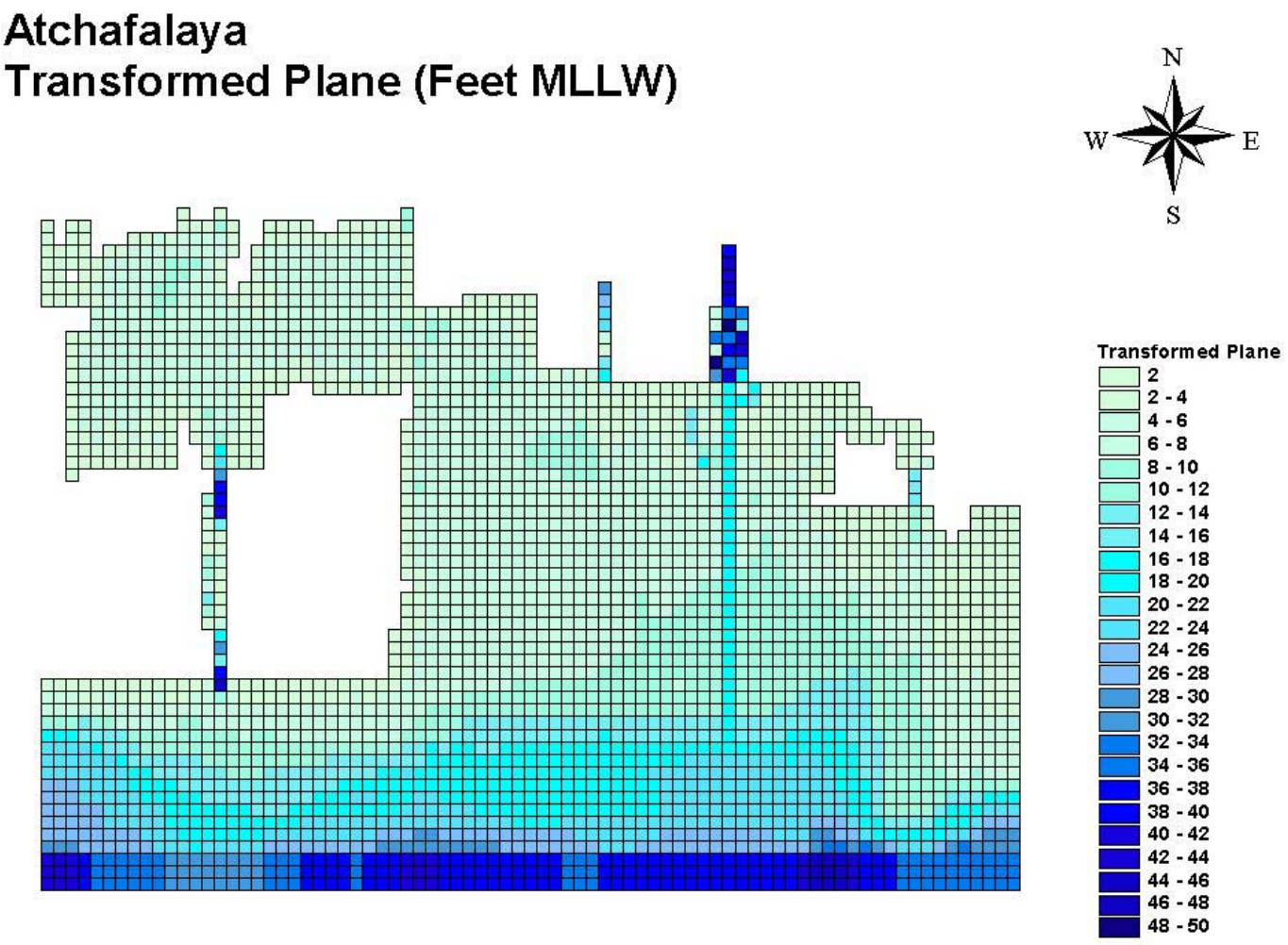

Figure 7. Transformed numerical grid

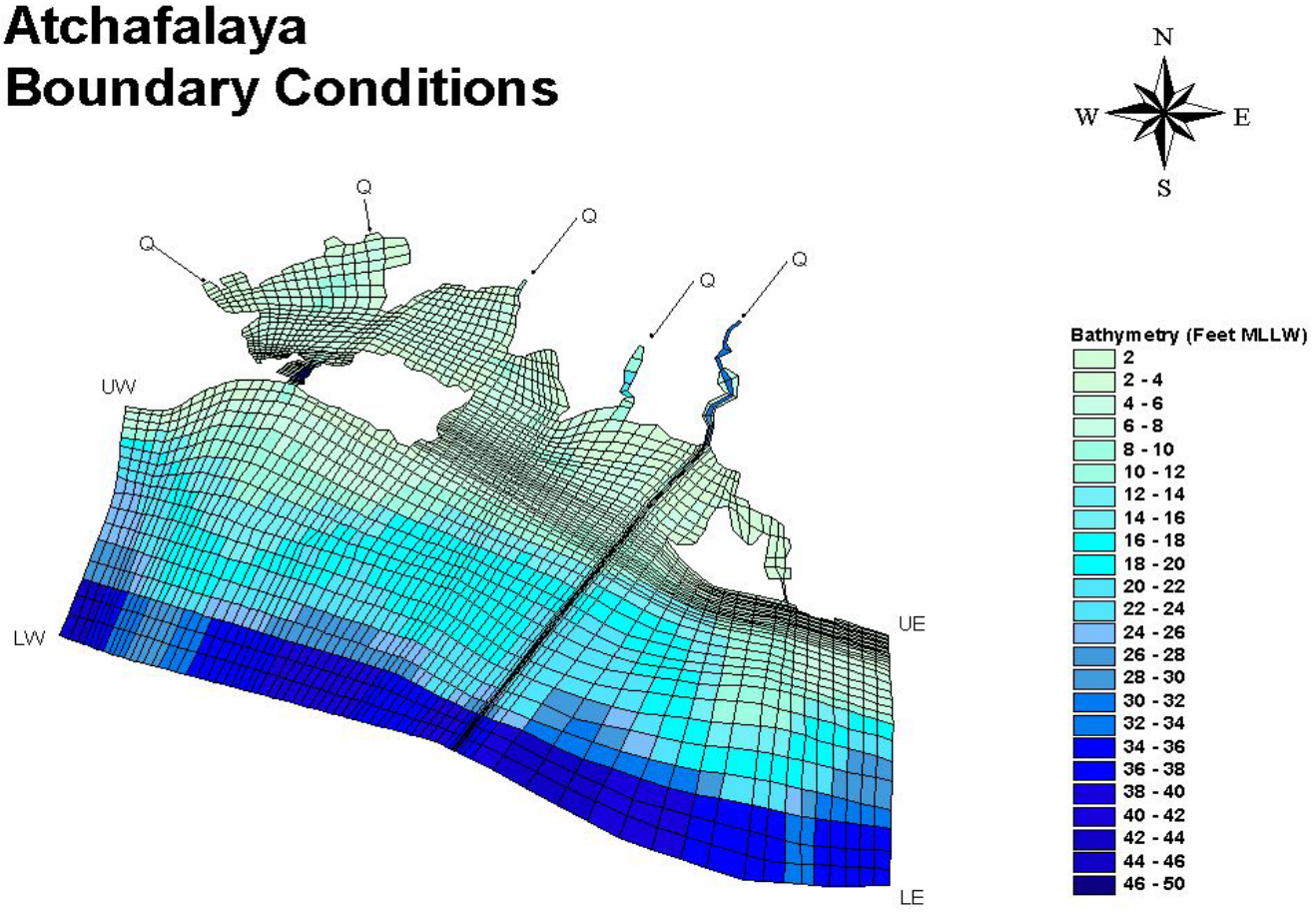

Figure 8. Location of boundary input data

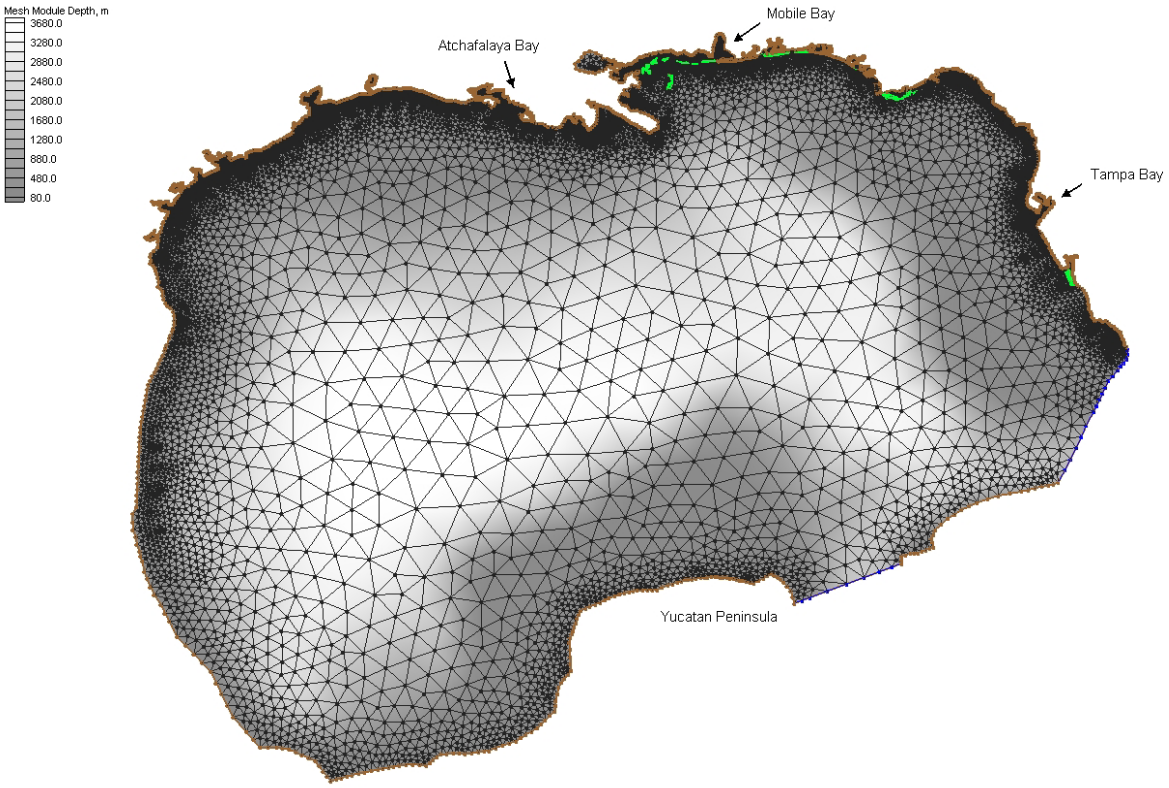

Figure 9. ADCIRC numerical grid

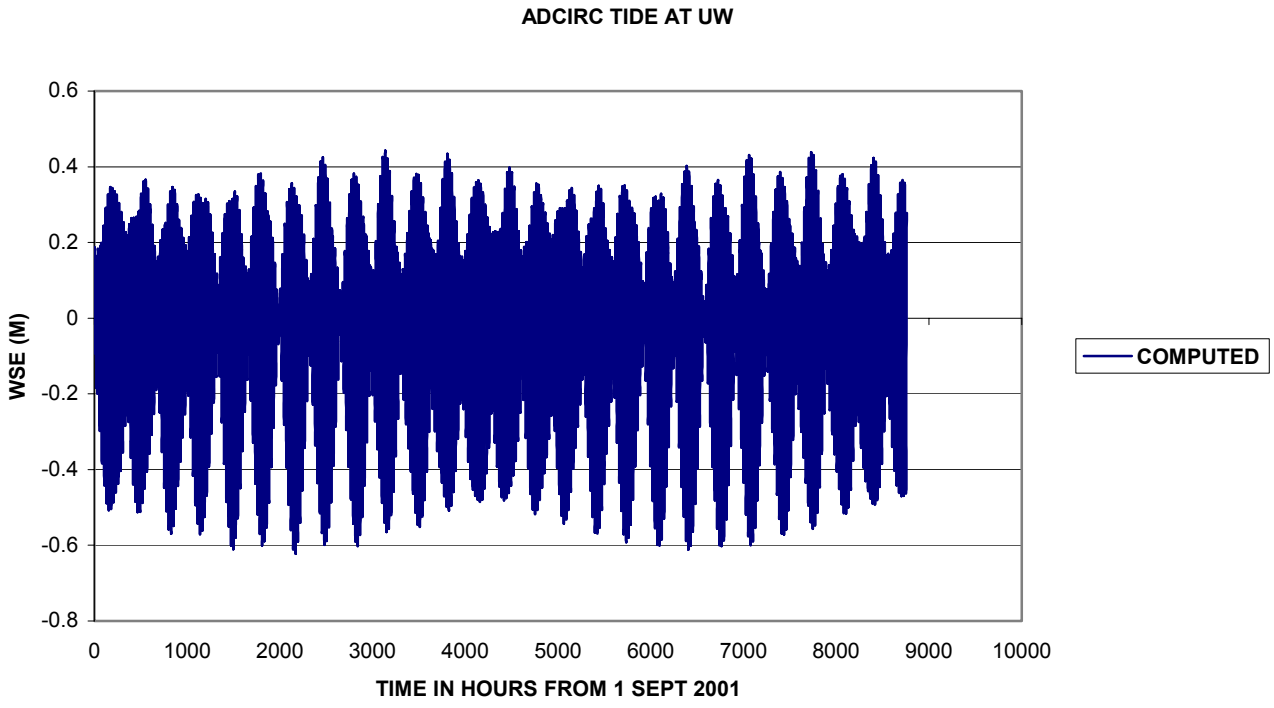

Figure 10. Astronomical tide at UW from ADCIRC

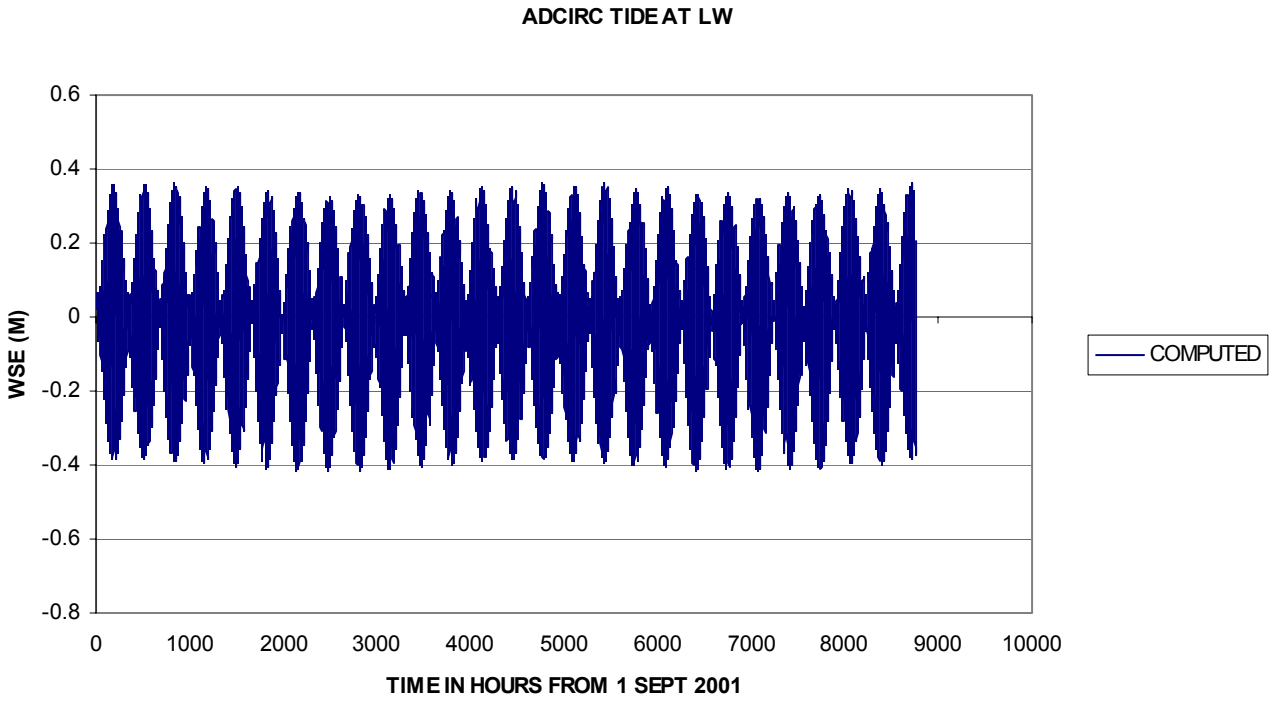

Figure 11. Astronomical tide at LW from ADCIRC

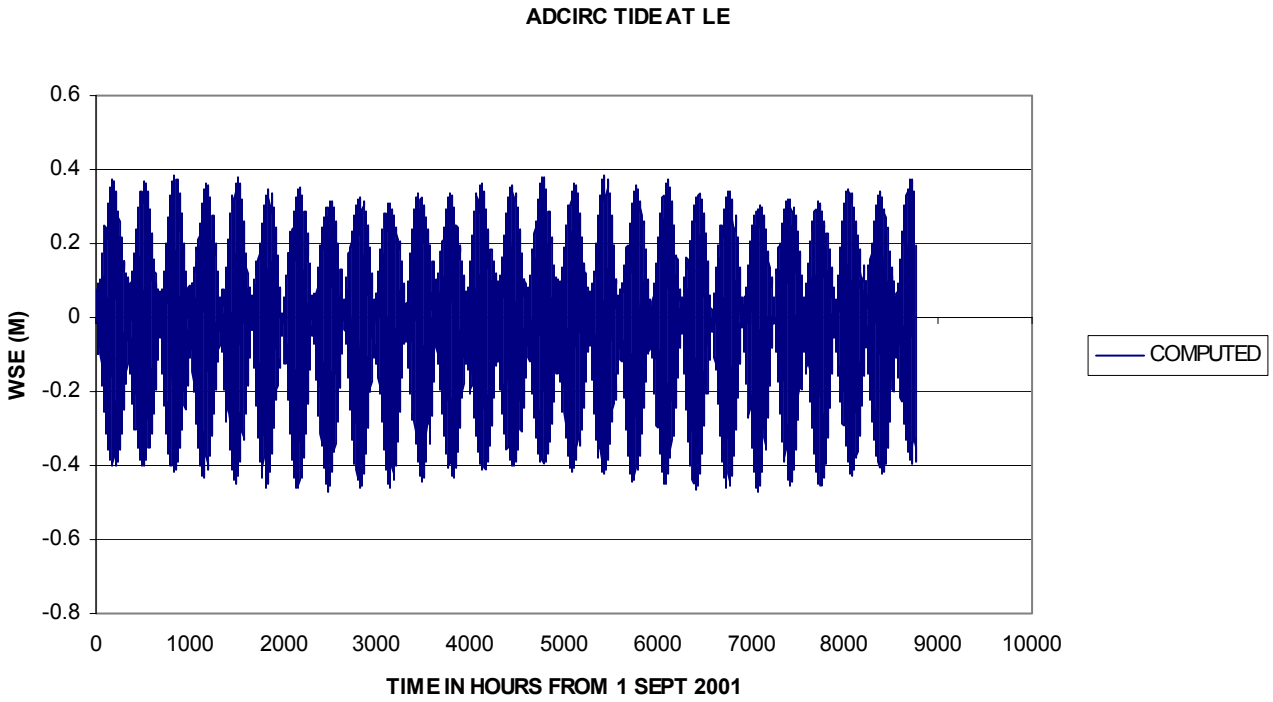

Figure 12. Astronomical tide at LE from ADCIRC

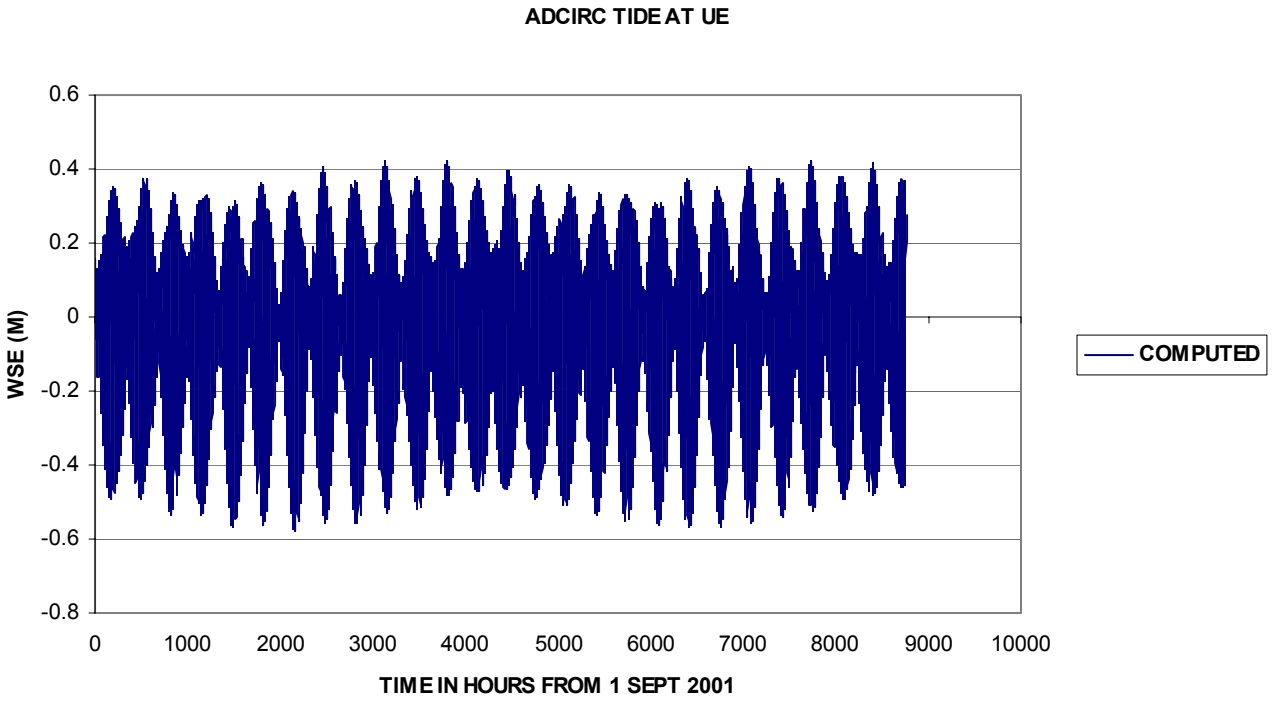

Figure 13. Astronomical tide at UE from ADCIRC

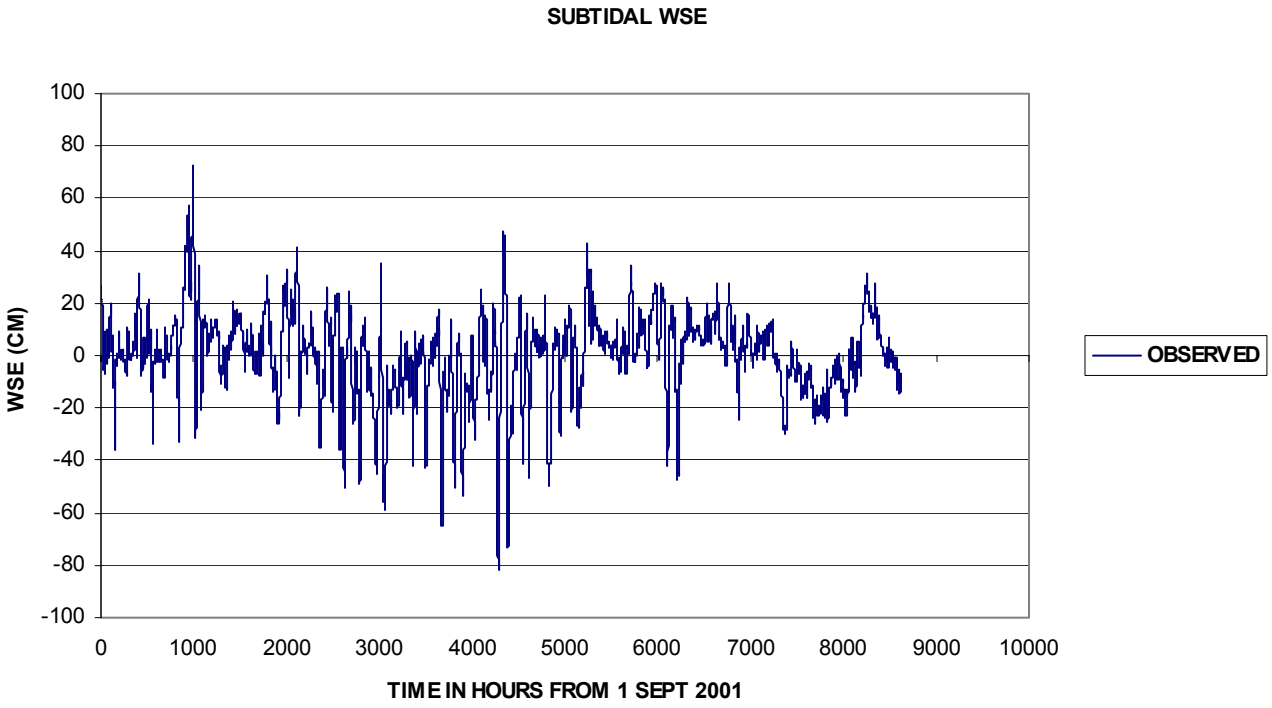

Figure 14. Subtidal component of WSE from BW-03

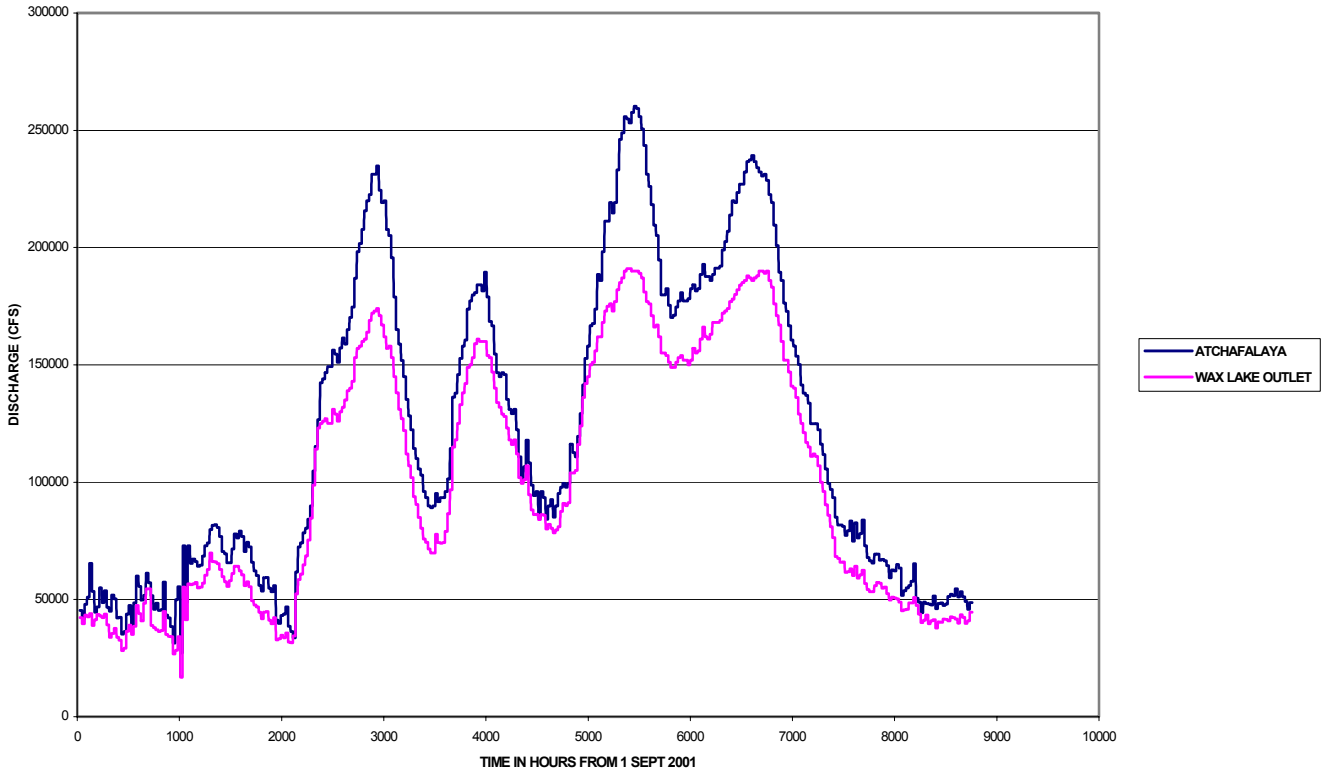

Figure 15. Major freshwater inflows

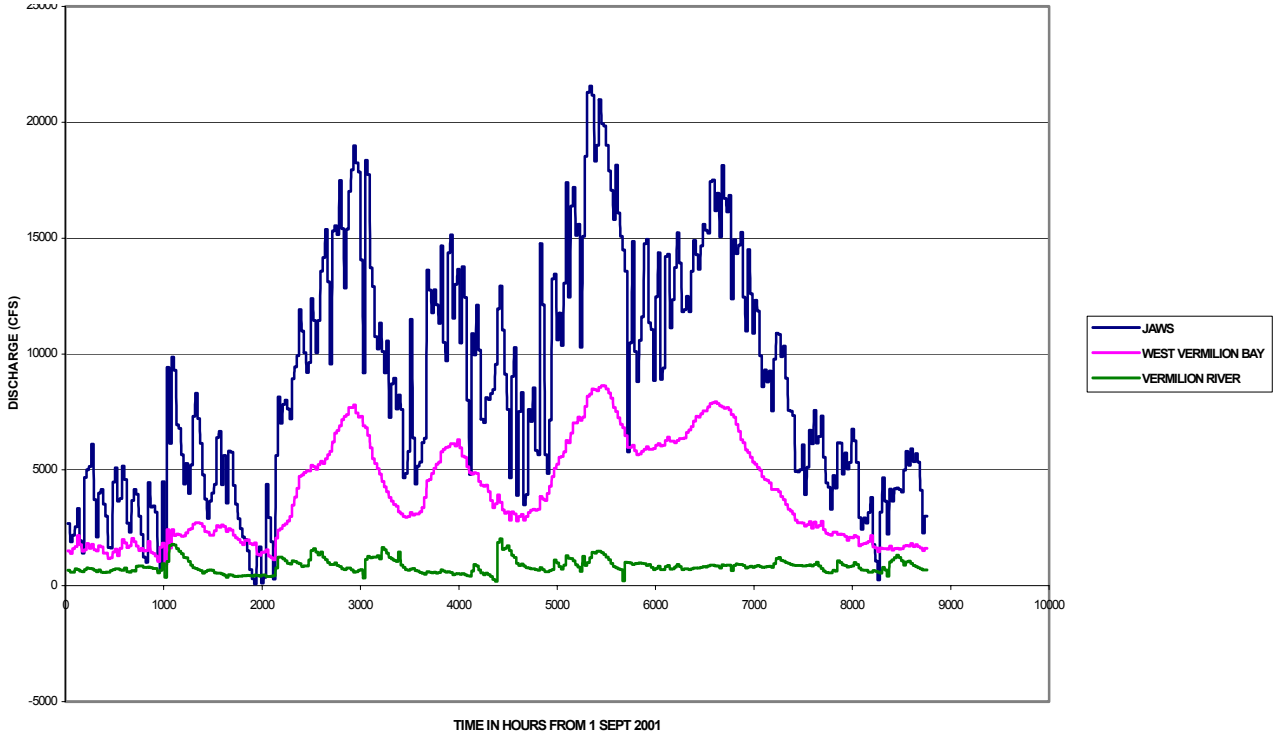

Figure 16. Minor freshwater inflows

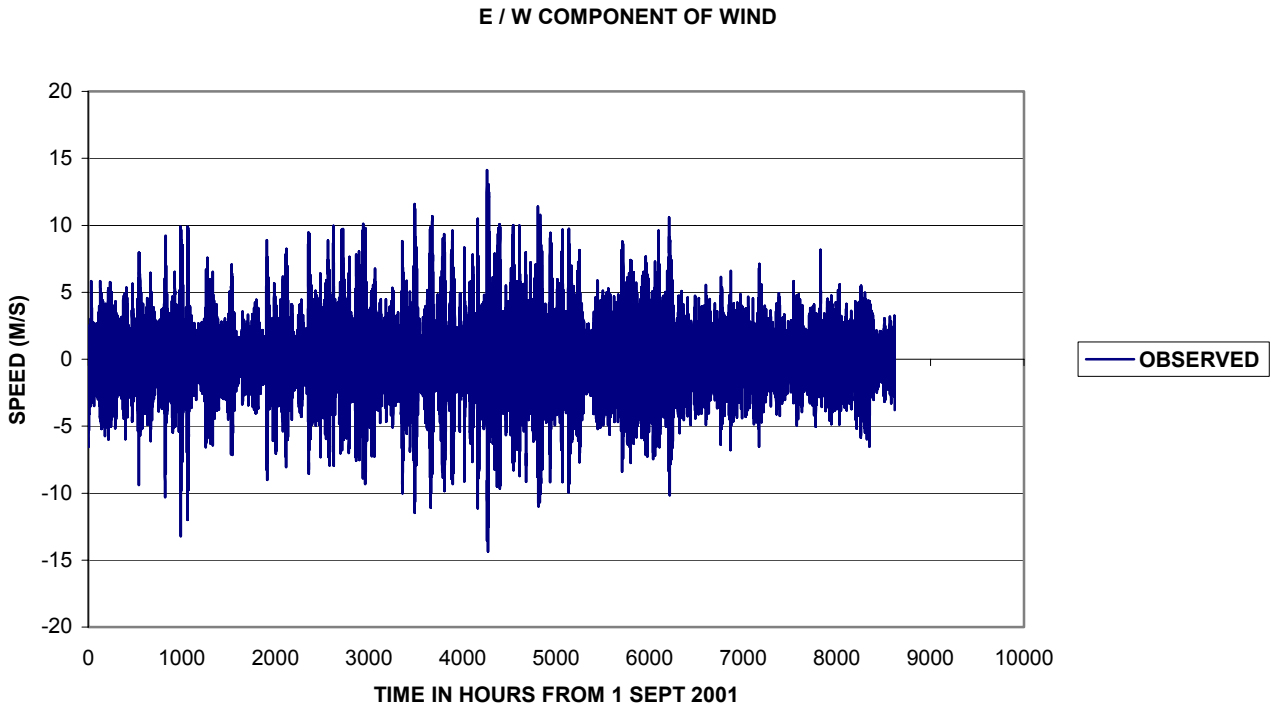

Figure 17. East / west component of wind field from BW-01

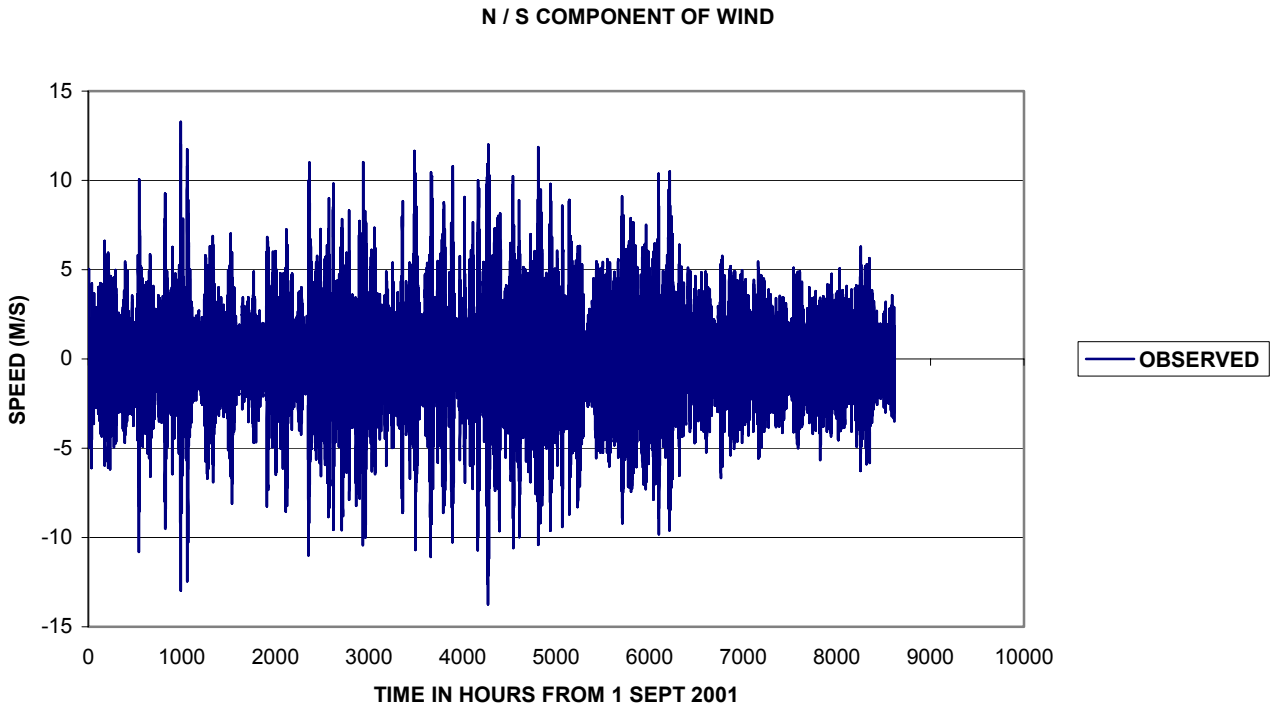

Figure 18. North / south component of wind from BW-01

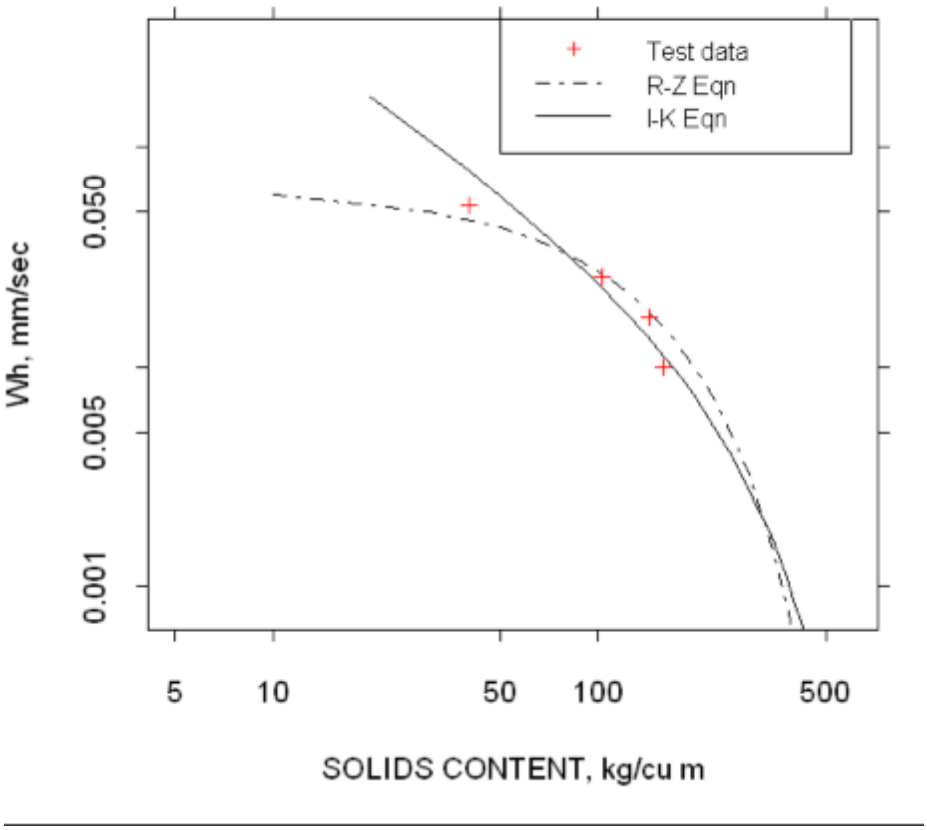

Figure 19. Fits of I-K and R-Z hindered settling equations to consolidation test data

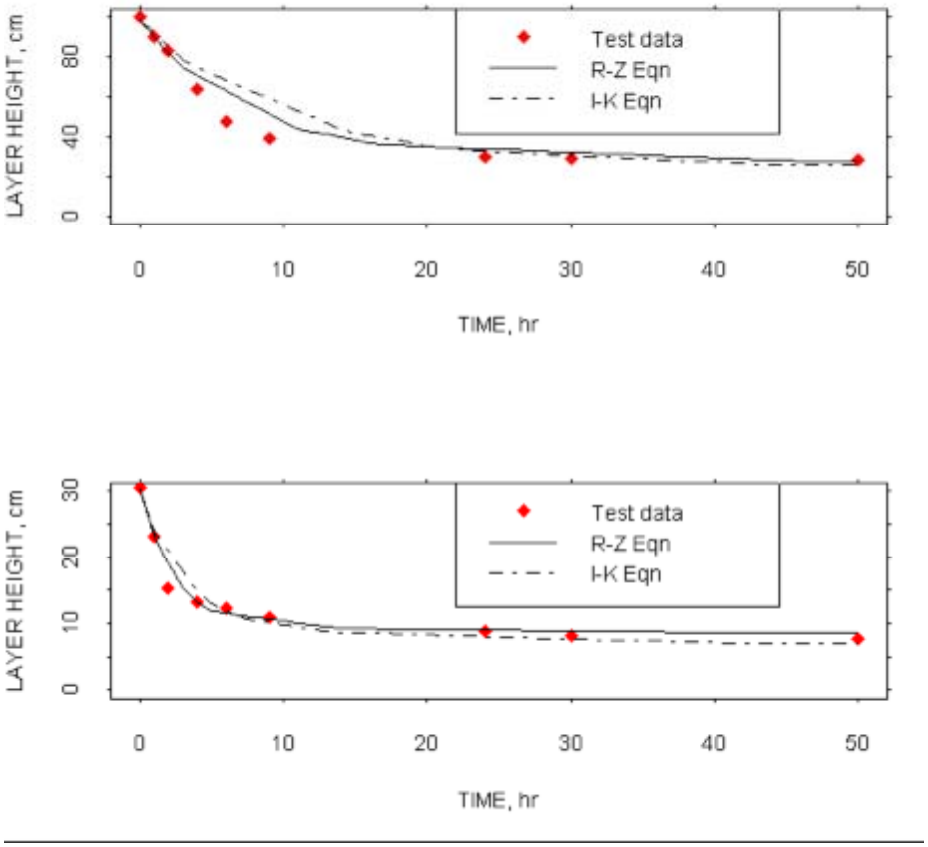

Figure 20. Simulation results for 144-kg/m^3 initial concentration starting with 30.5- and 100-cm-deep suspensions

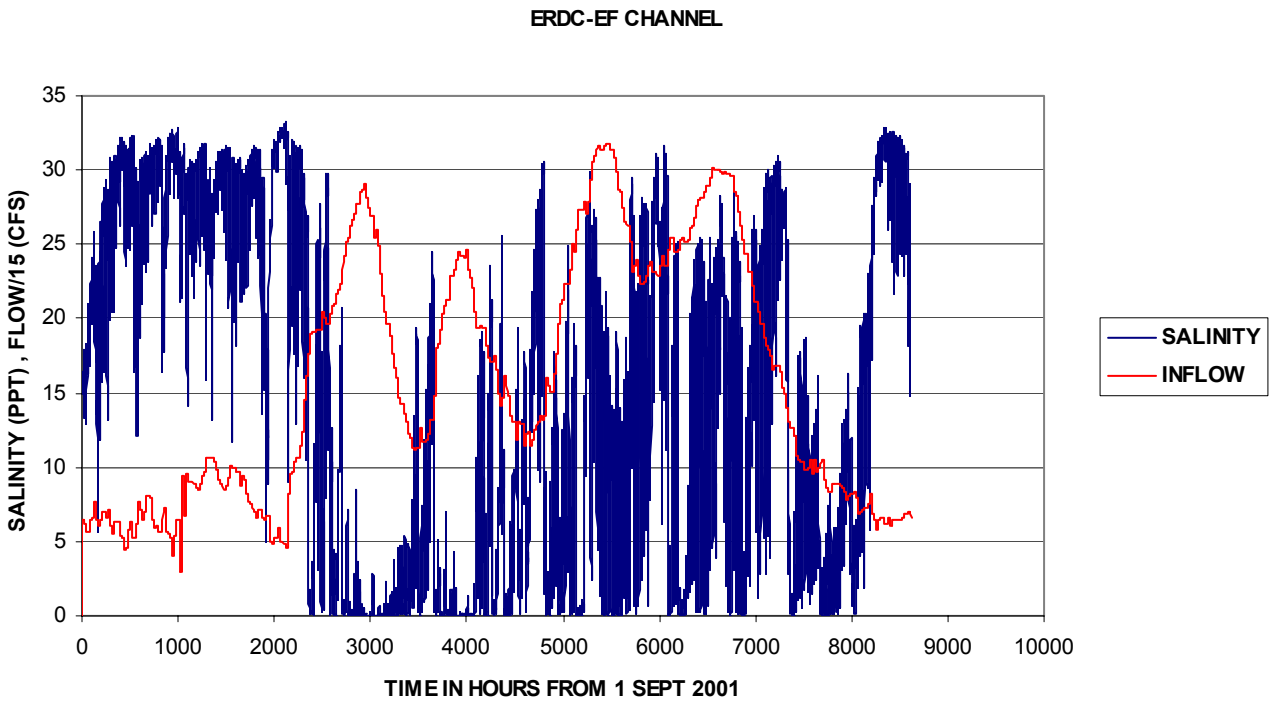

Figure 21. Impact of freshwater inflow on salinity

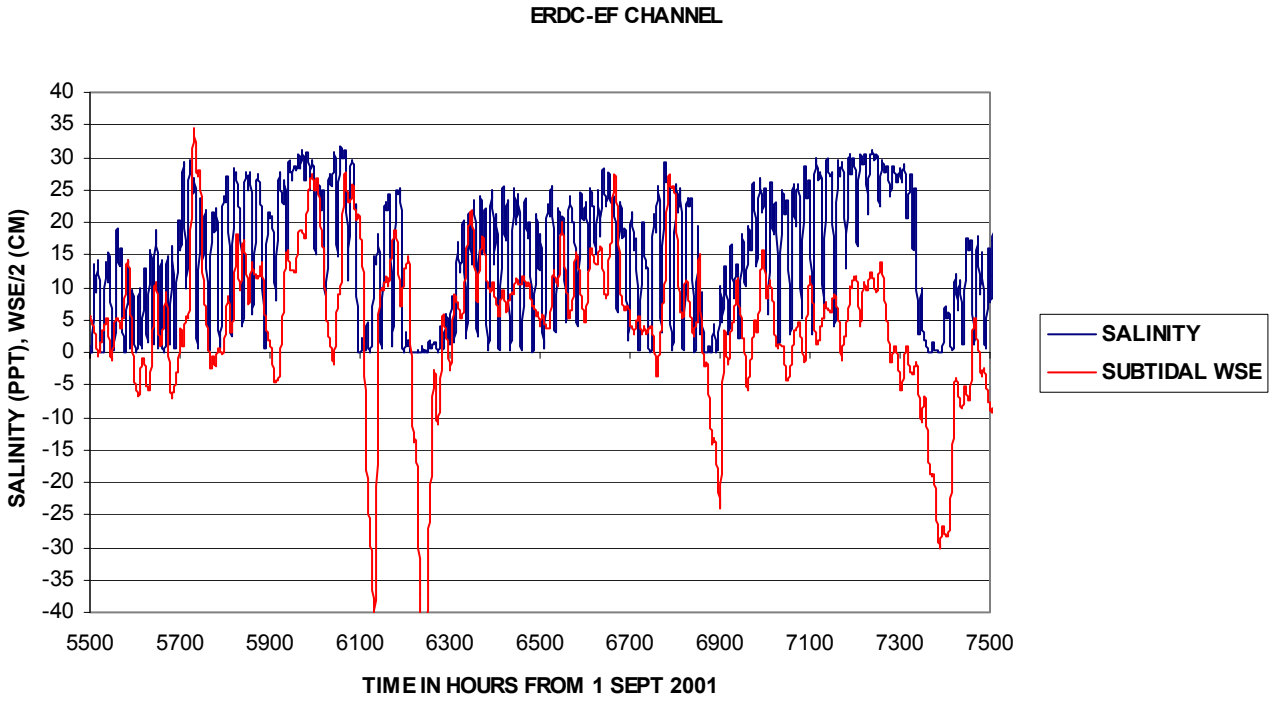

Figure 22. Impact of subtidal component of water surface on salinity

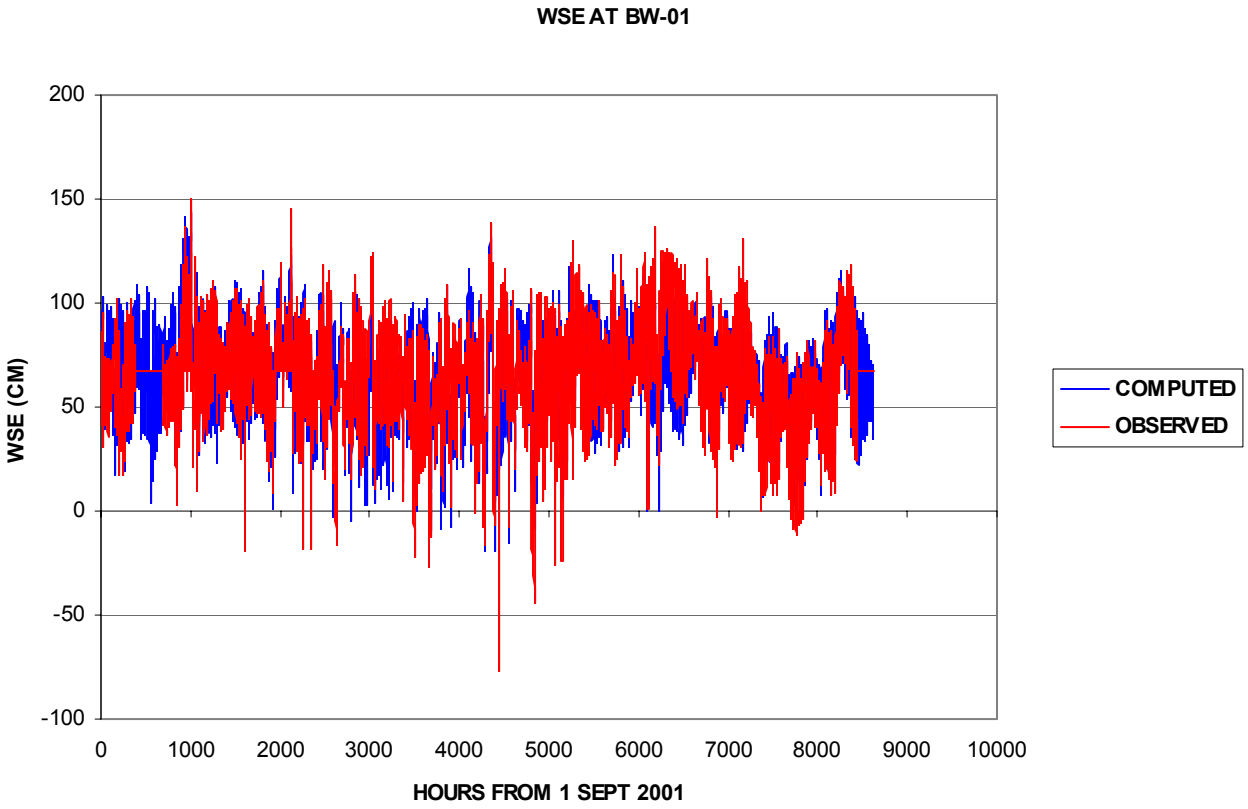

Figure 23. Observed versus computed WSE at BW-01

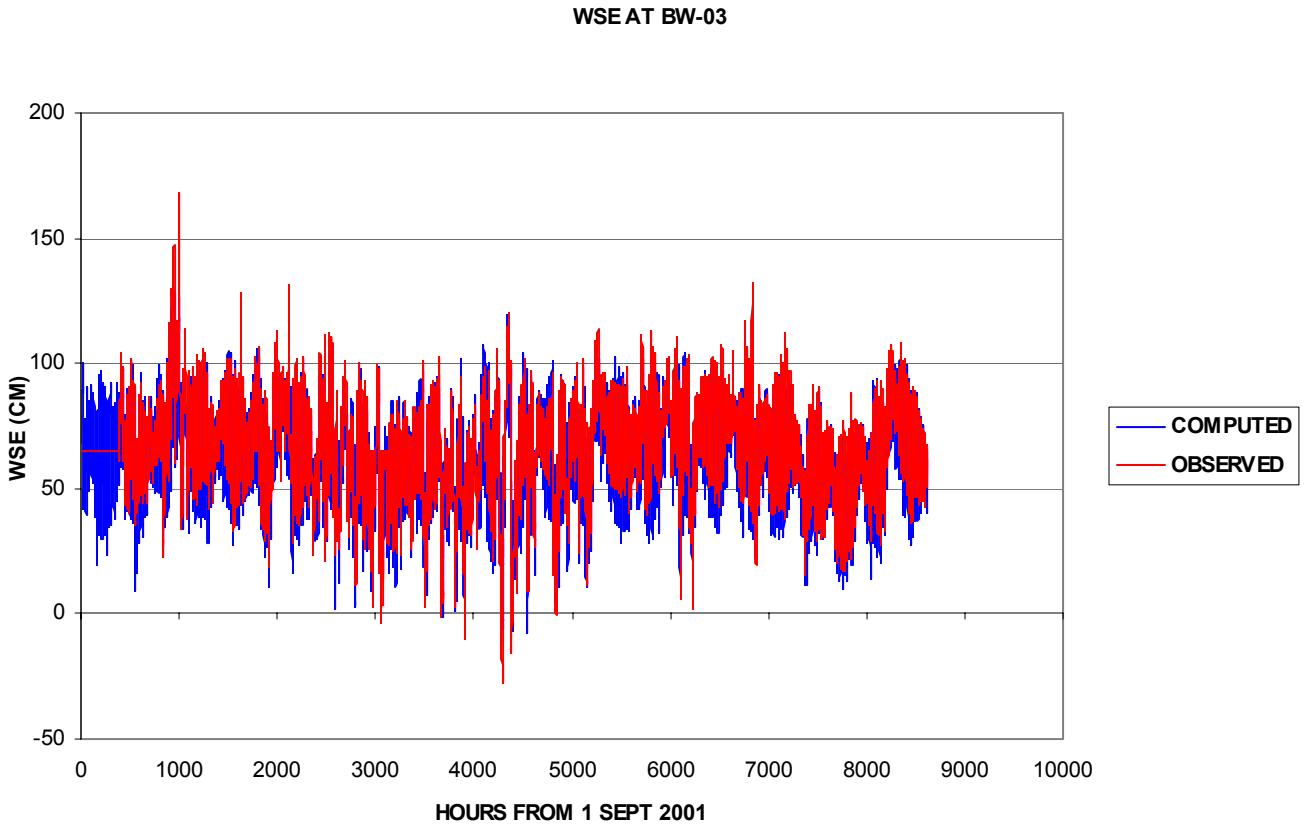

Figure 24. Observed versus computed WSE at BW-03

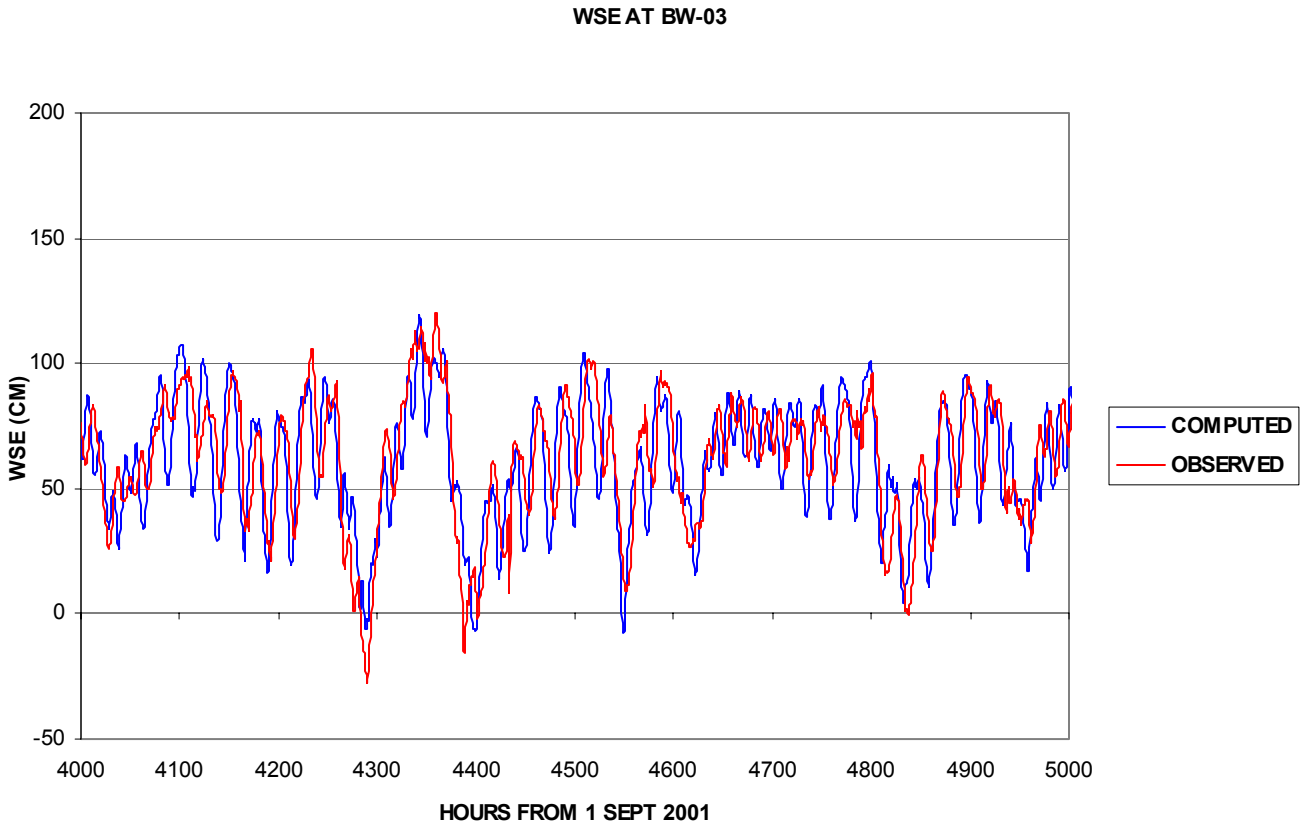

Figure 25. Blowup comparison of WSE at BW-03

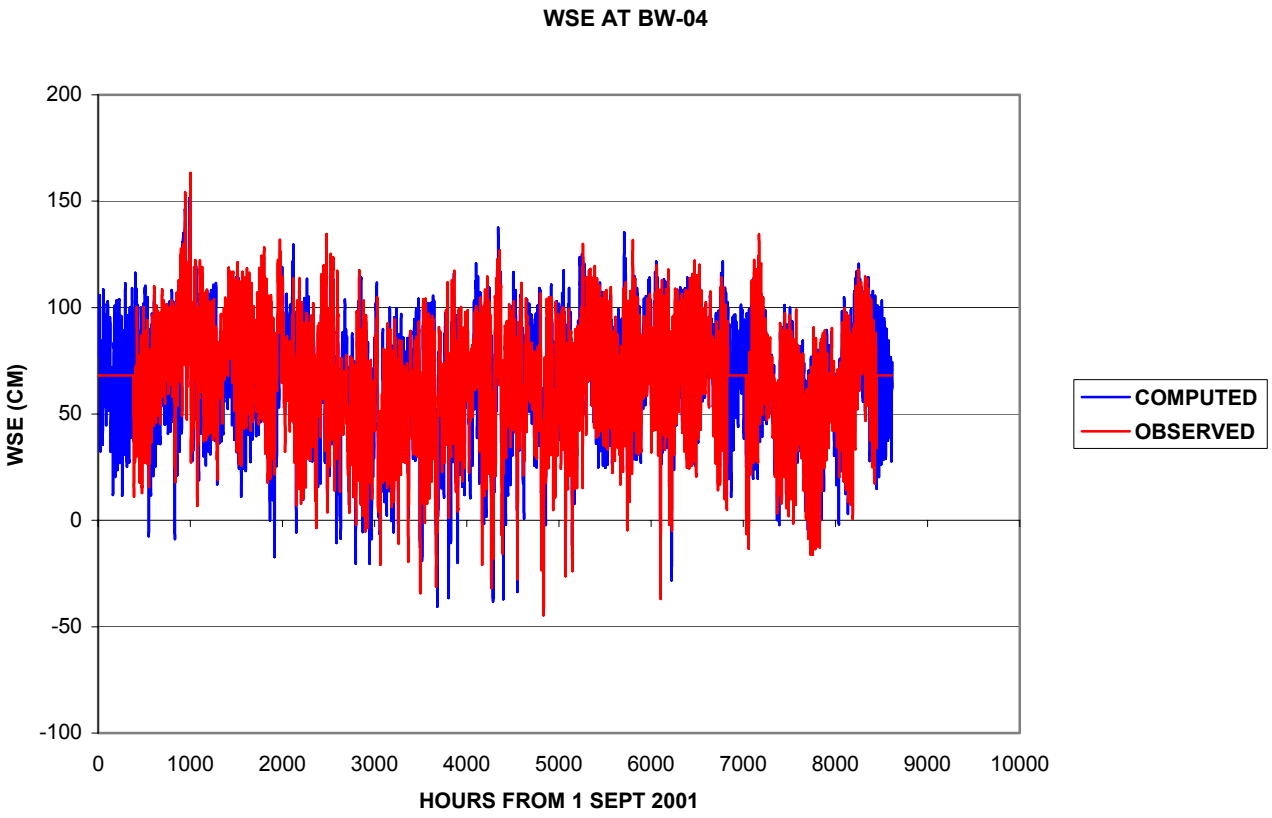

Figure 26. Observed versus computed WSE at BW-04

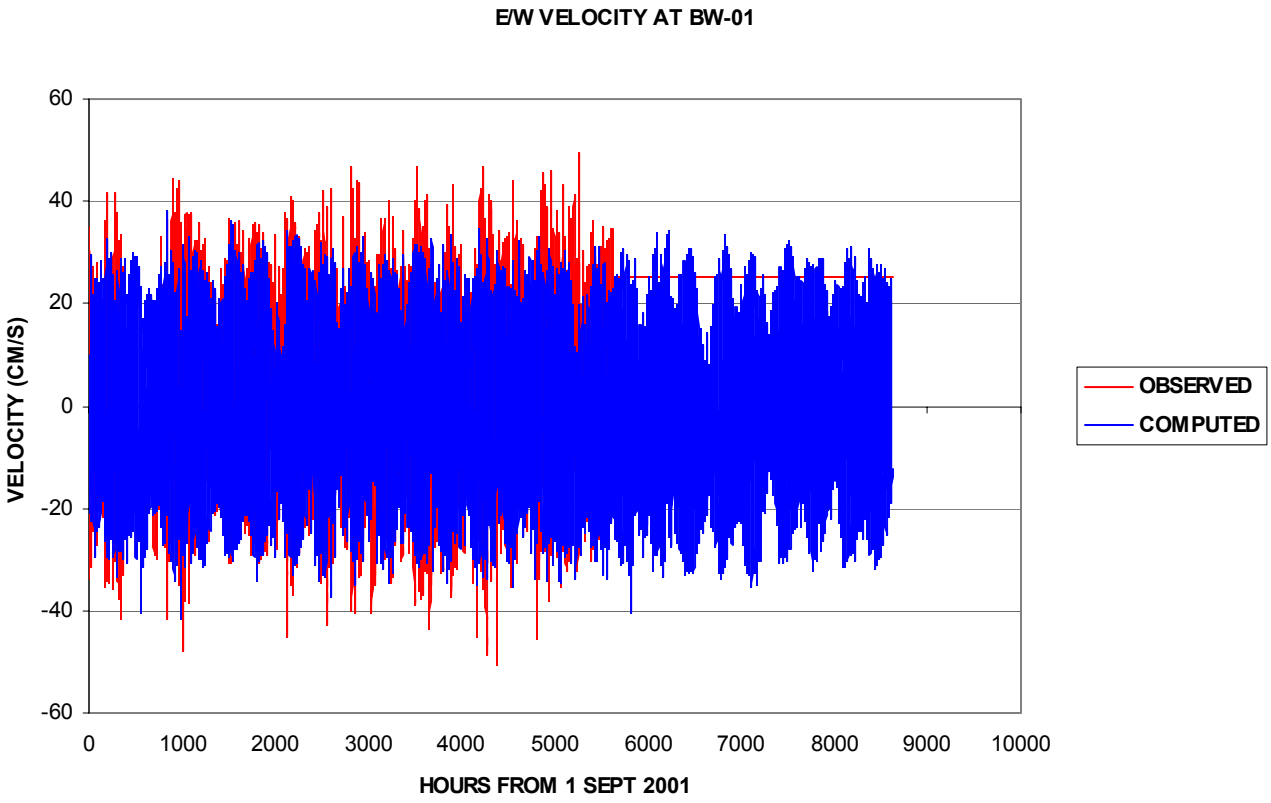

Figure 27. Comparison of east / west velocity component at BW-01

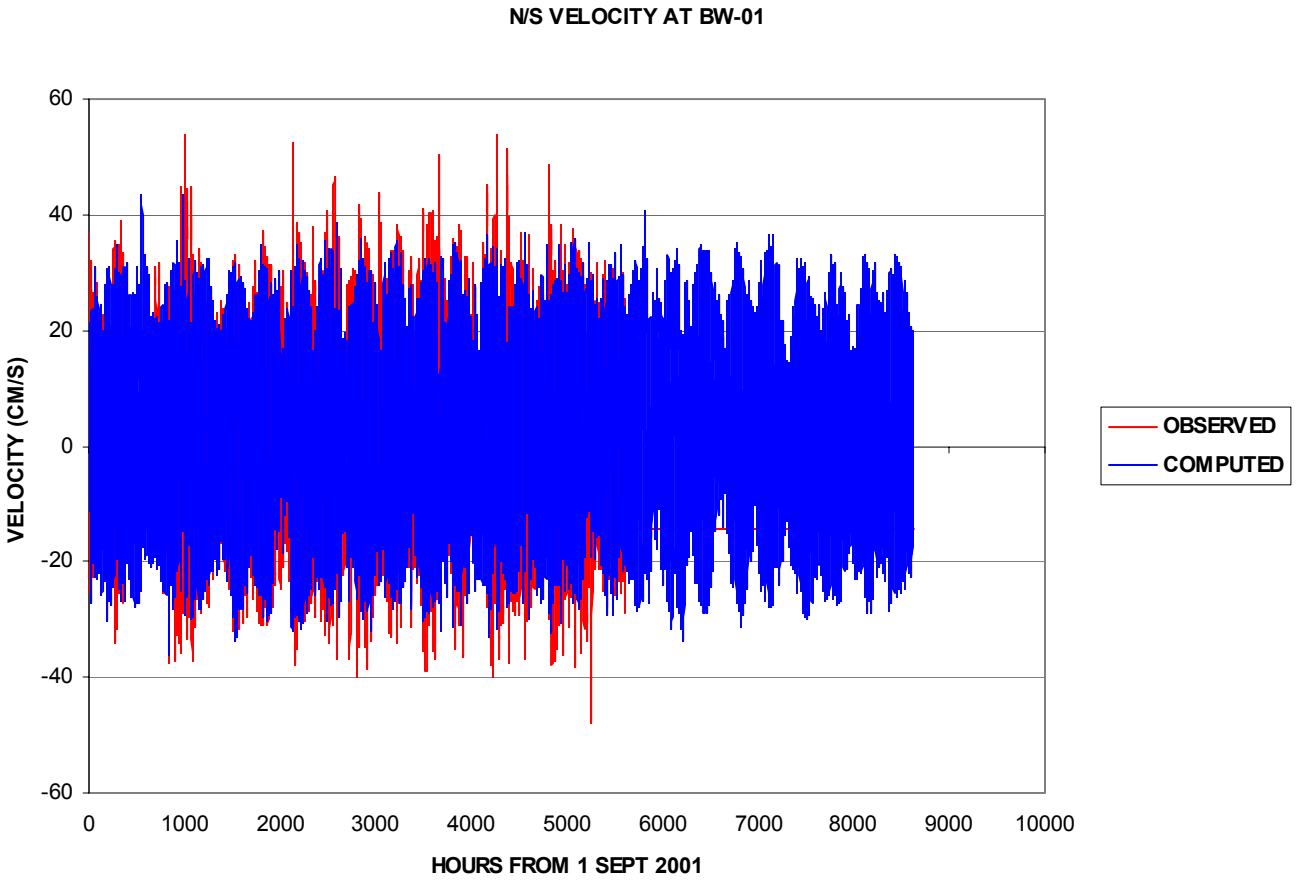

Figure 28. Comparison of north / south component of velocity at BW-01

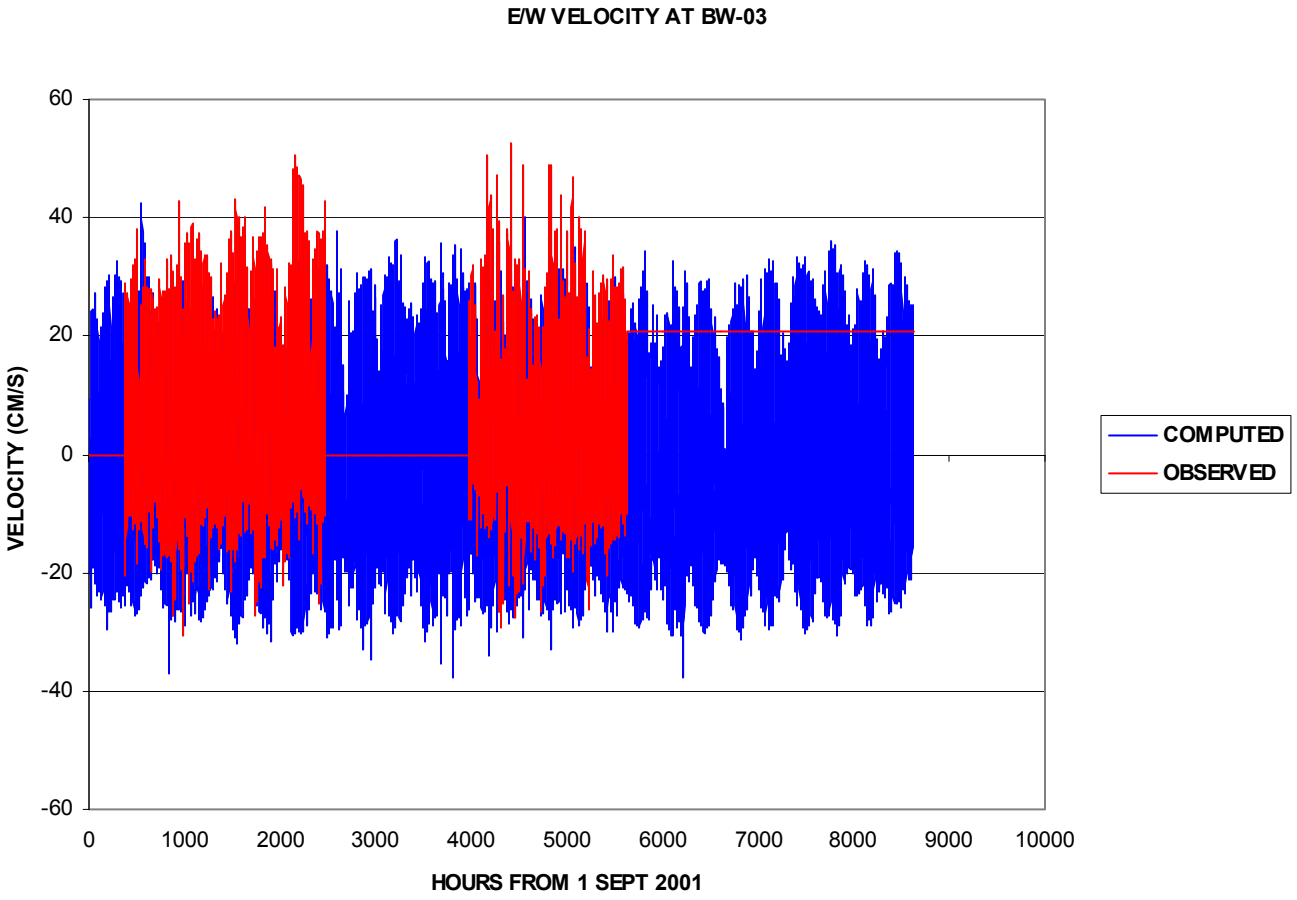

Figure 29. Comparison of east / west component of velocity at BW-03

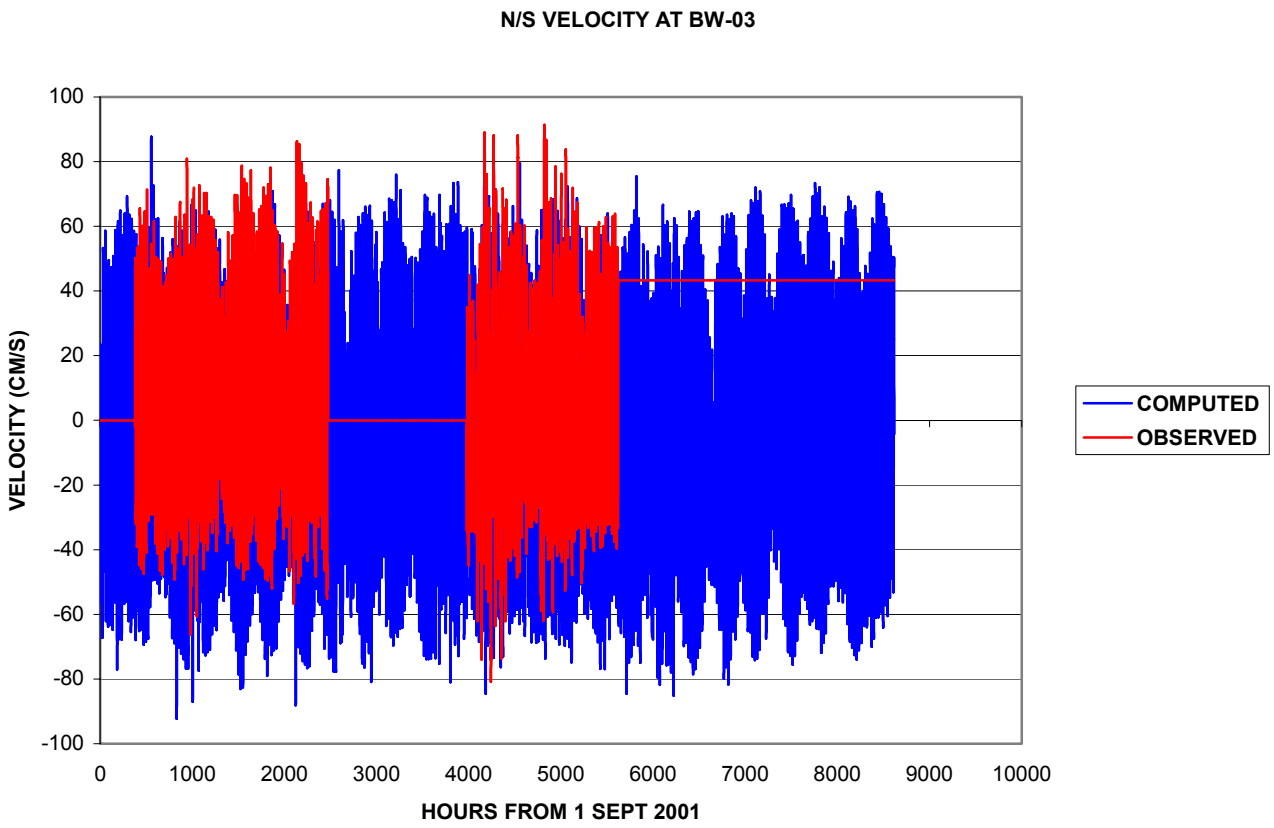

Figure 30. Comparison of north / south component of velocity at BW-03

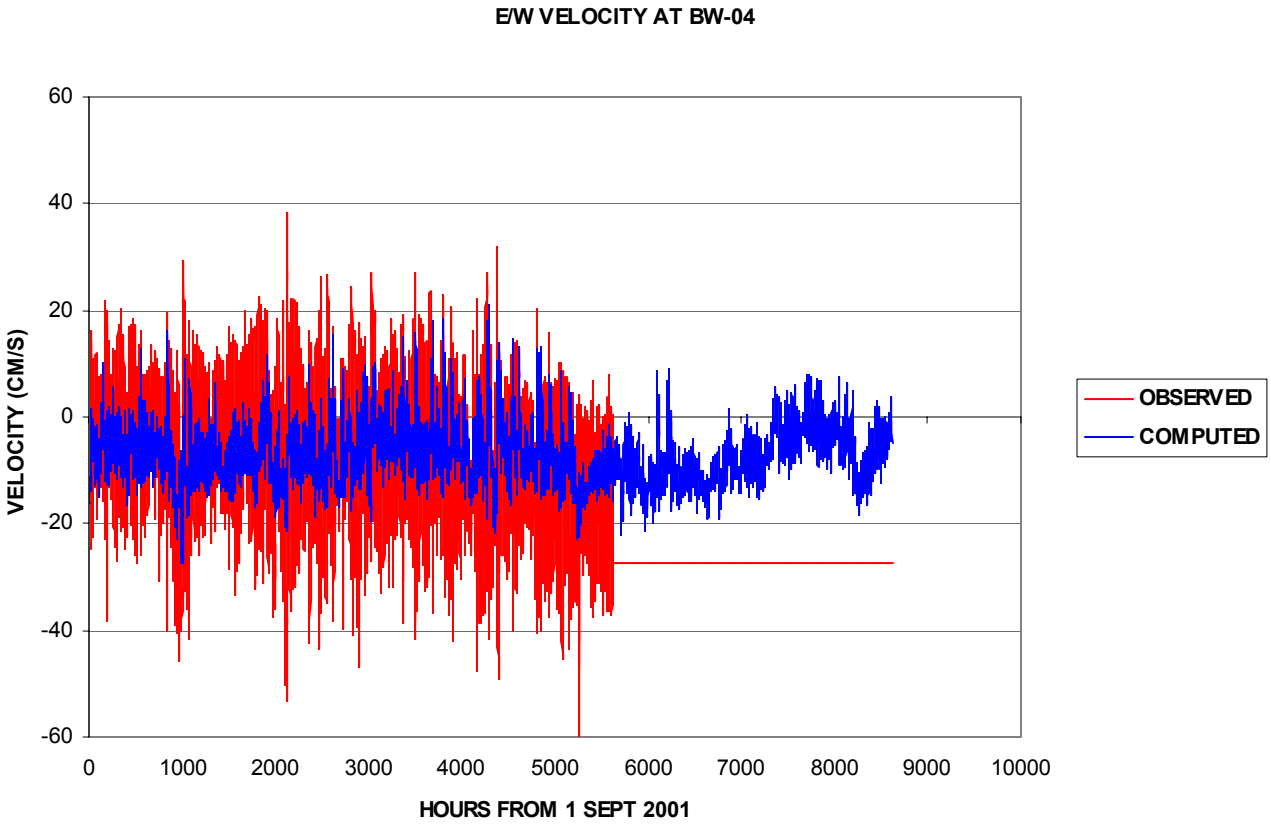

Figure 31. Comparison of east / west component of velocity at BW-04

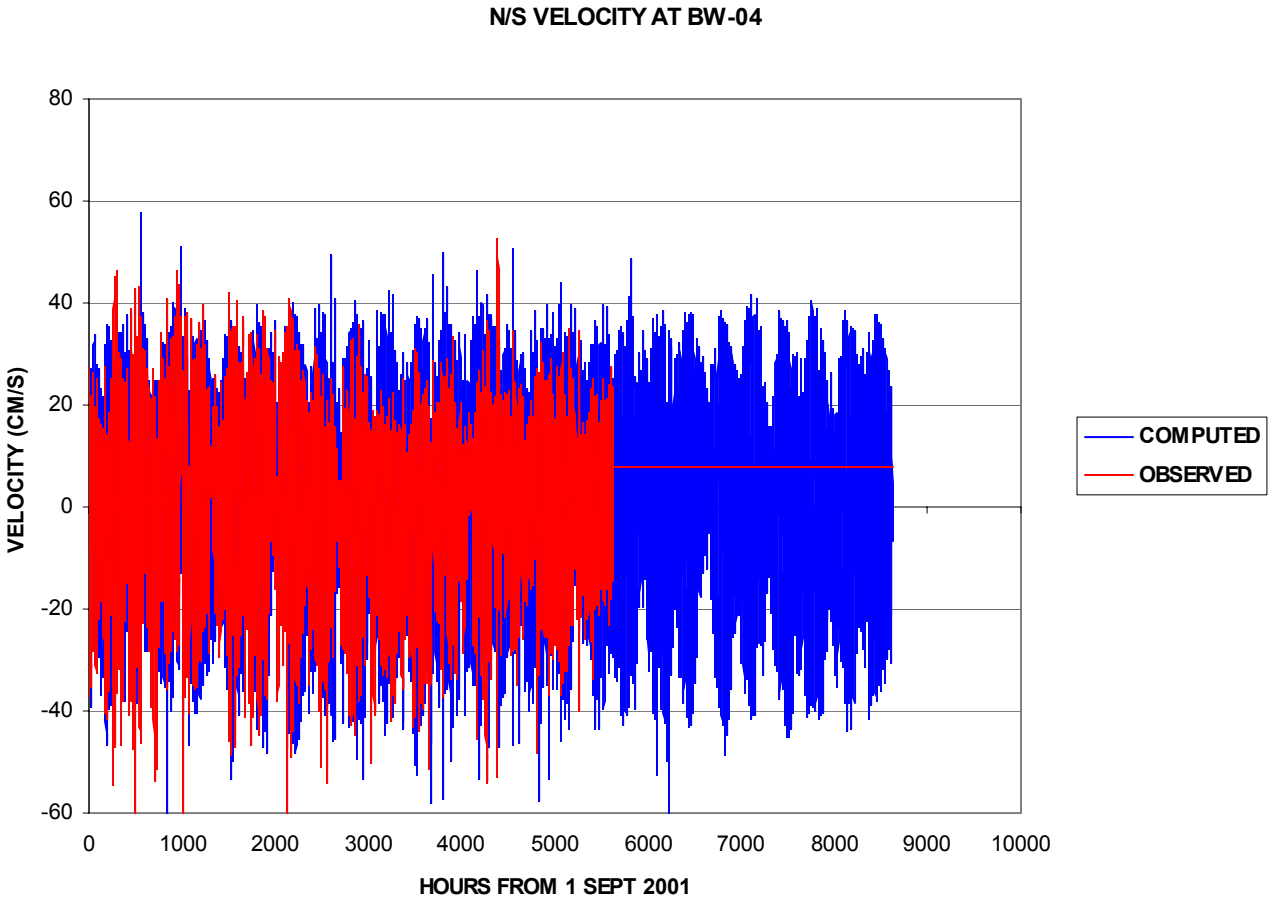

Figure 32. Comparison of north / south component of velocity at BW-04

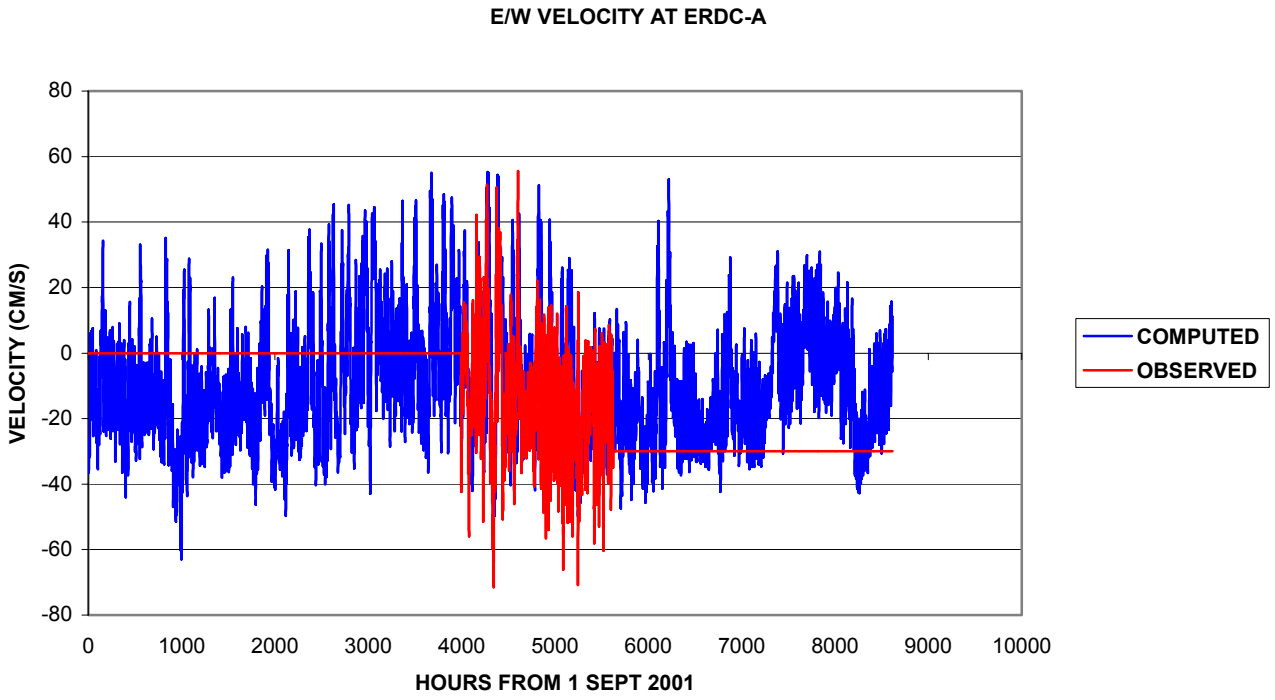

Figure 33. Comparison of east / west component of velocity at ERDC-A

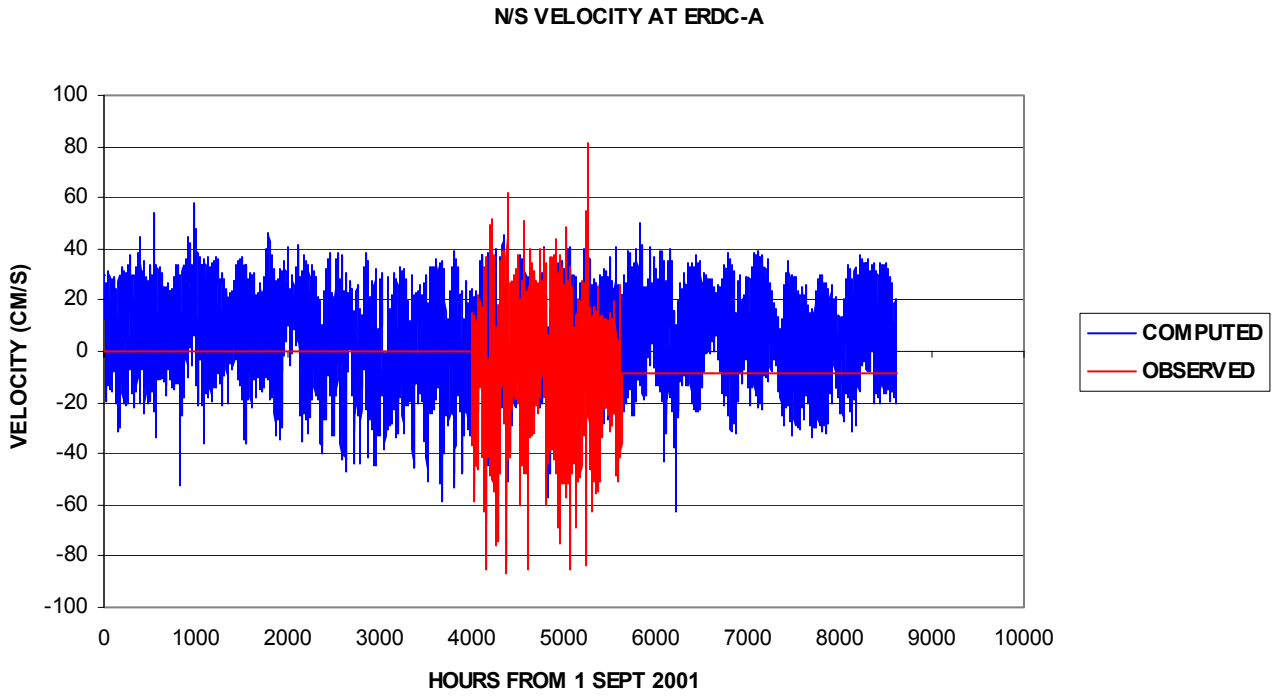

Figure 34. Comparison of north / south component of velocity at ERDC-A

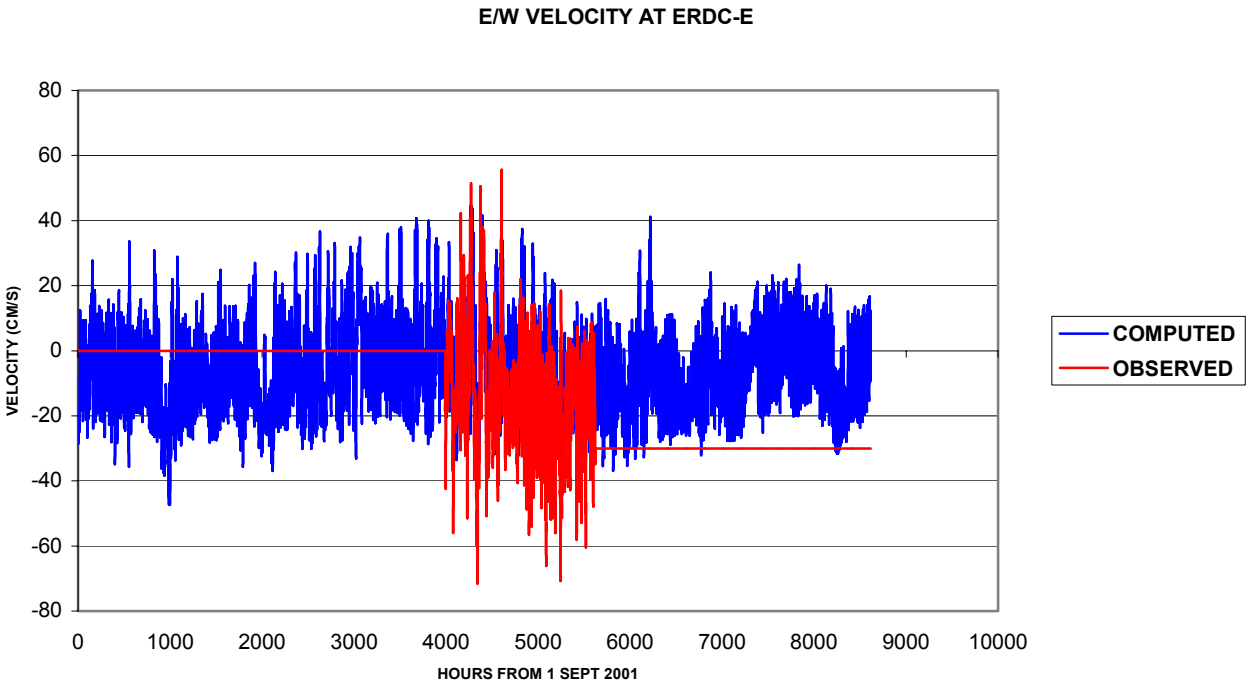

Figure 35. Comparison of east / west component of velocity at ERDC-E

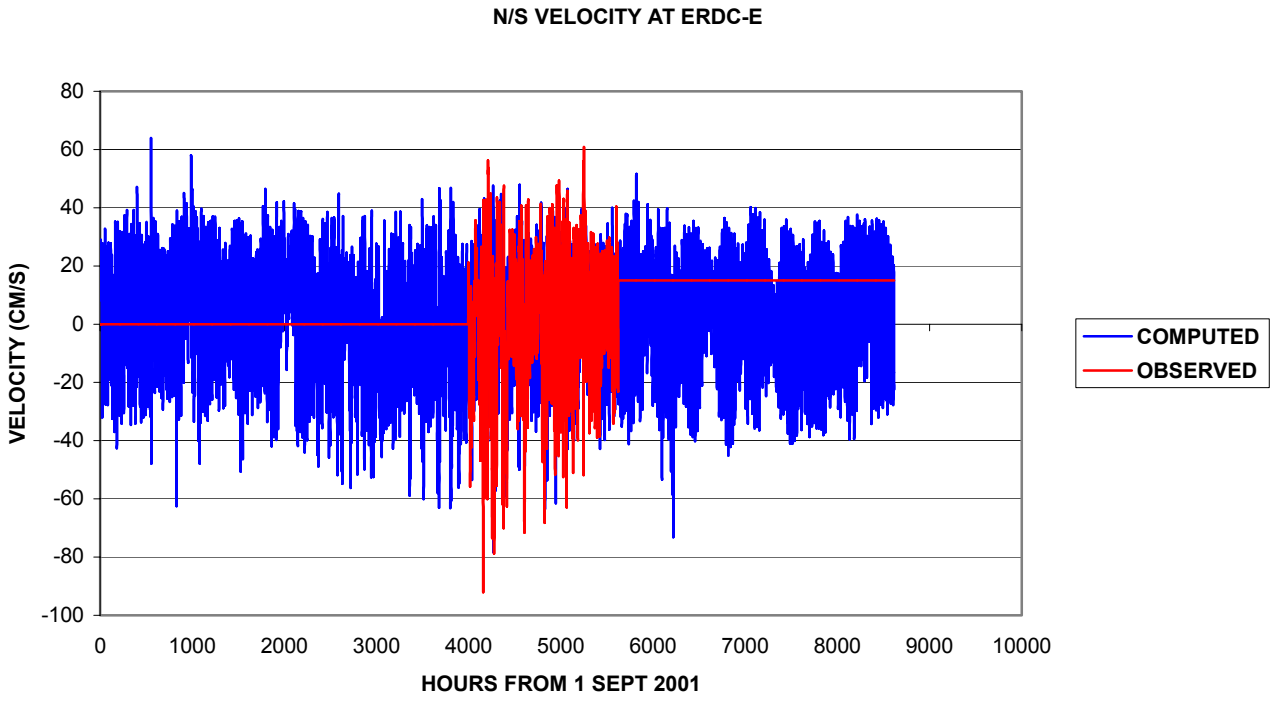

Figure 36. Comparison of north / south component of velocity at ERDC-E

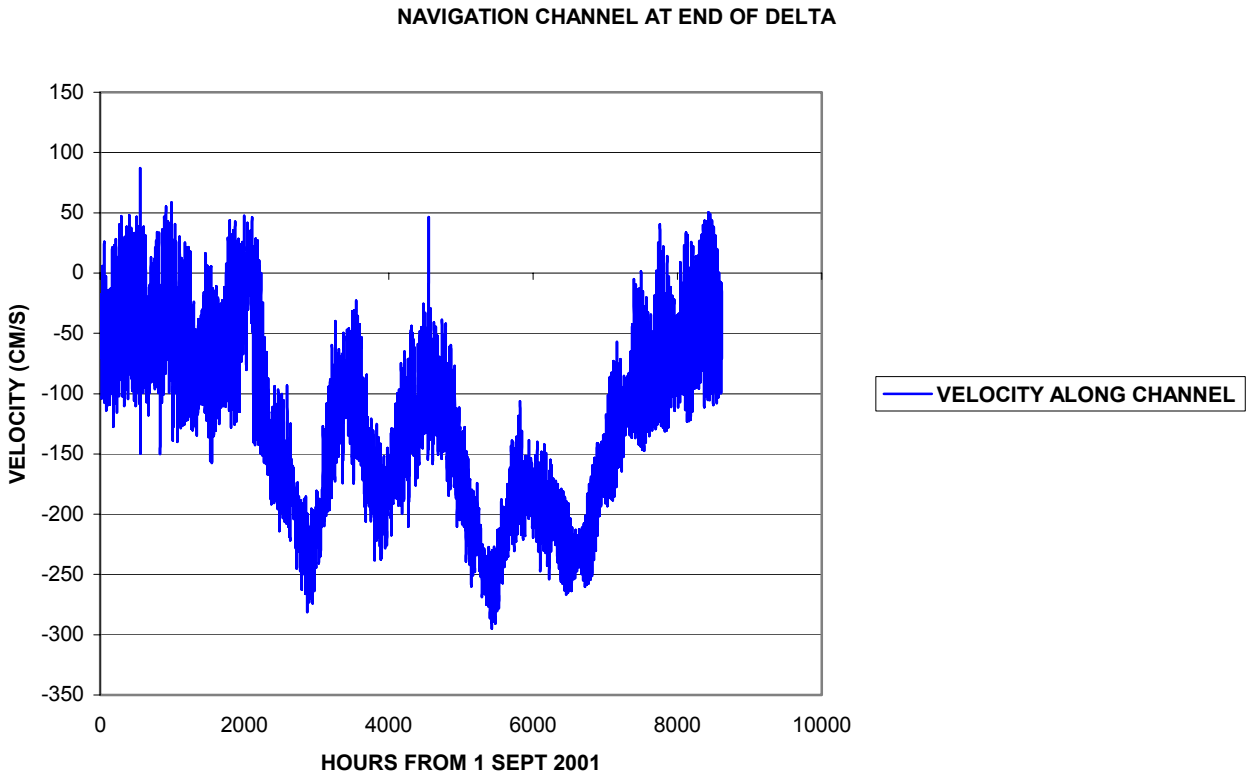

Figure 37. Computed velocity in channel at end of delta

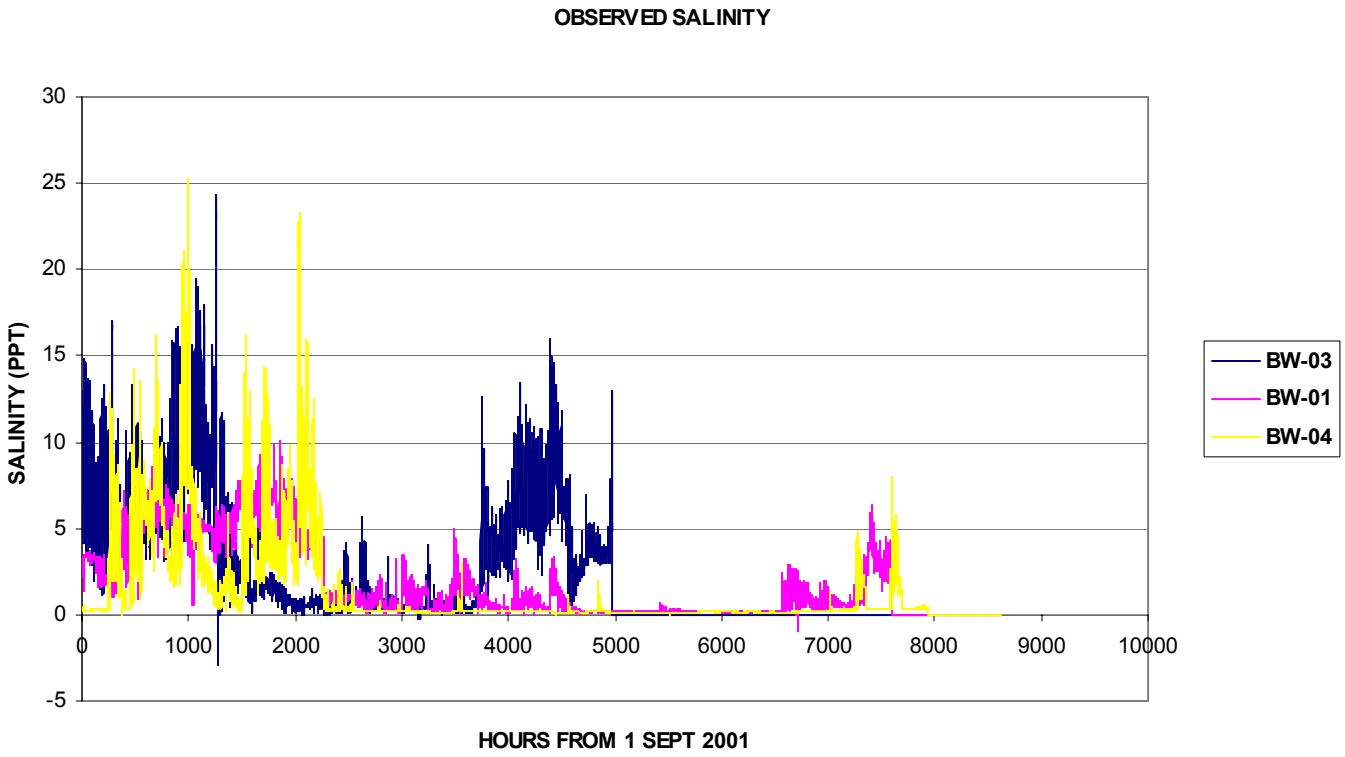

Figure 38. Observed salinity at BAYWATCH stations

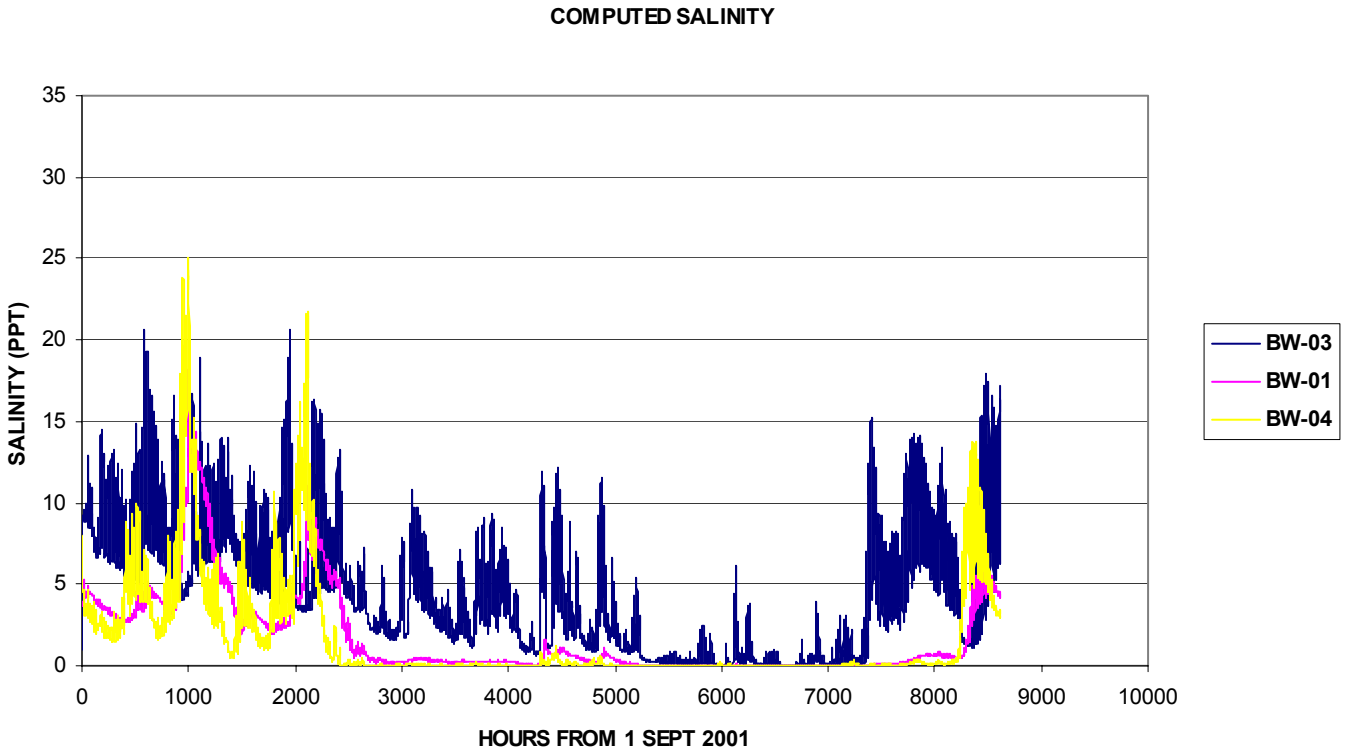

Figure 39. Computed salinity at BAYWATCH stations

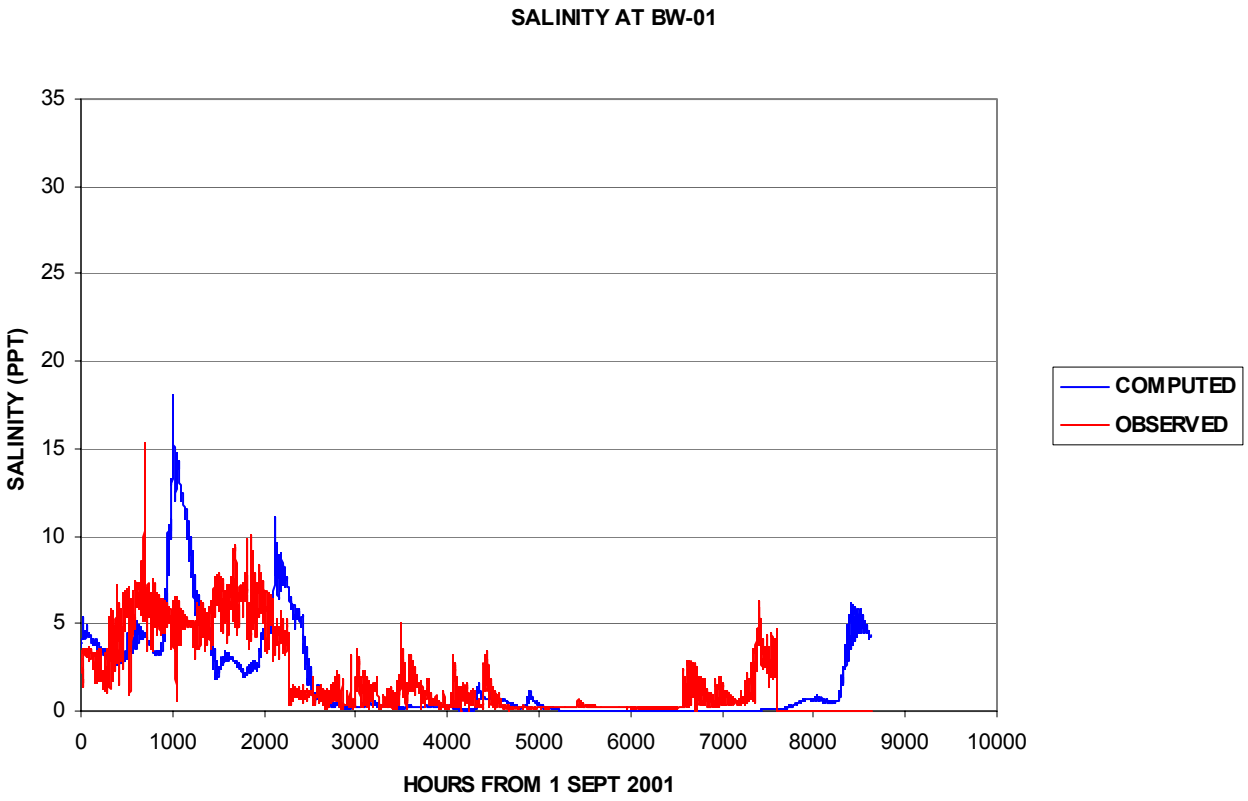

Figure 40. Observed versus computed salinity at BW-01

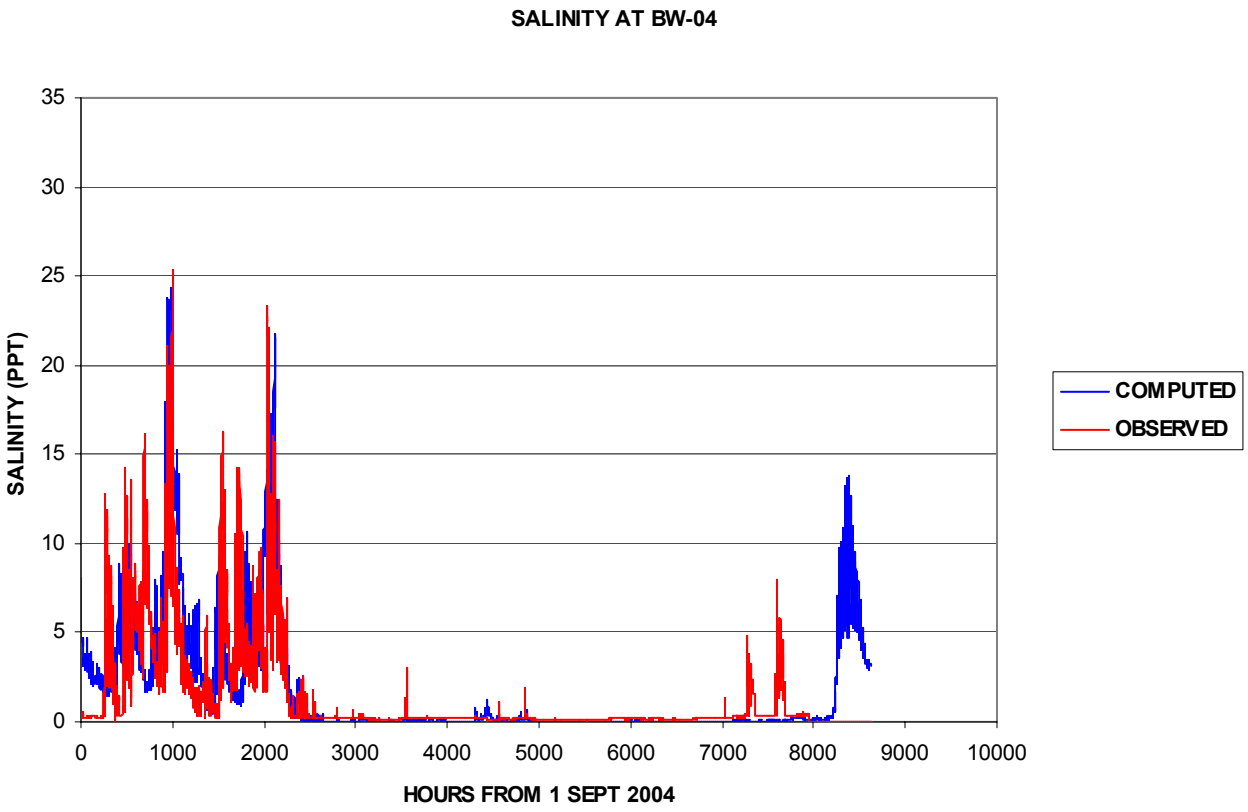

Figure 41. Observed versus computed salinity at BW-04

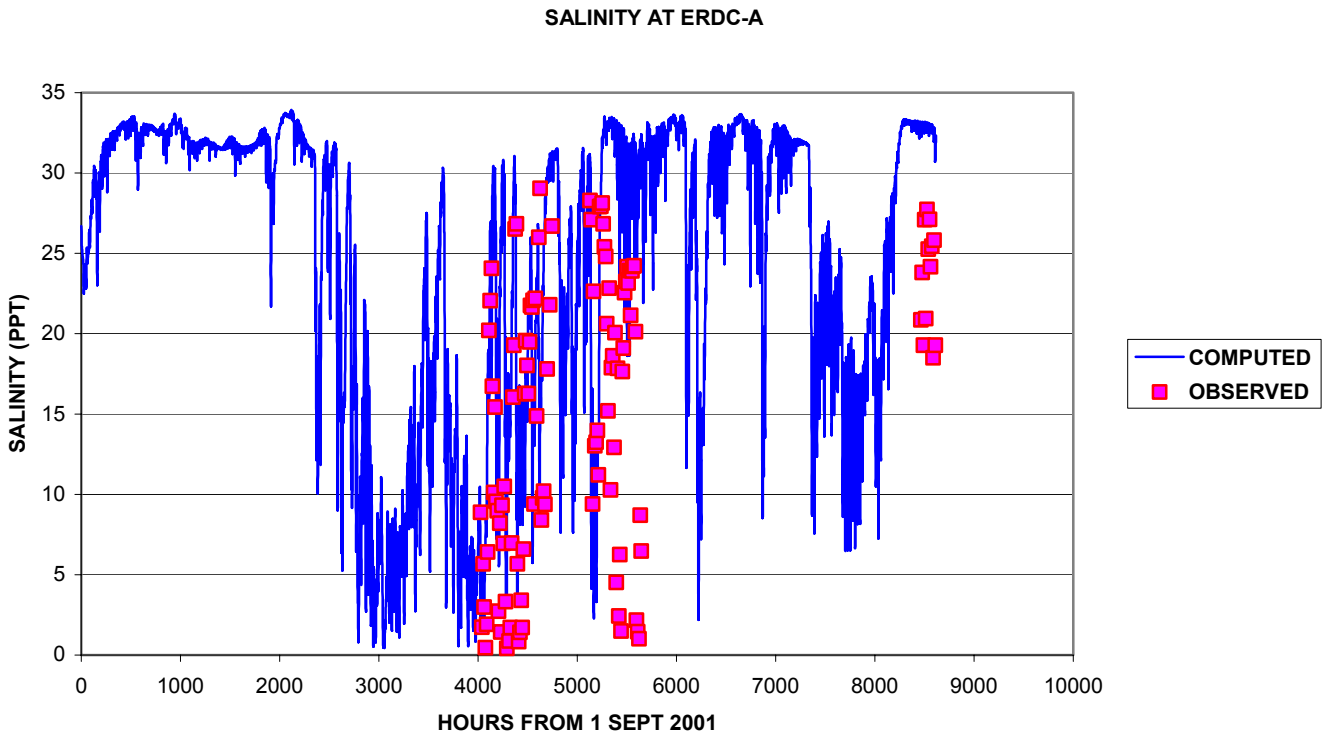

Figure 42. Observed versus computed salinity at ERDC-A

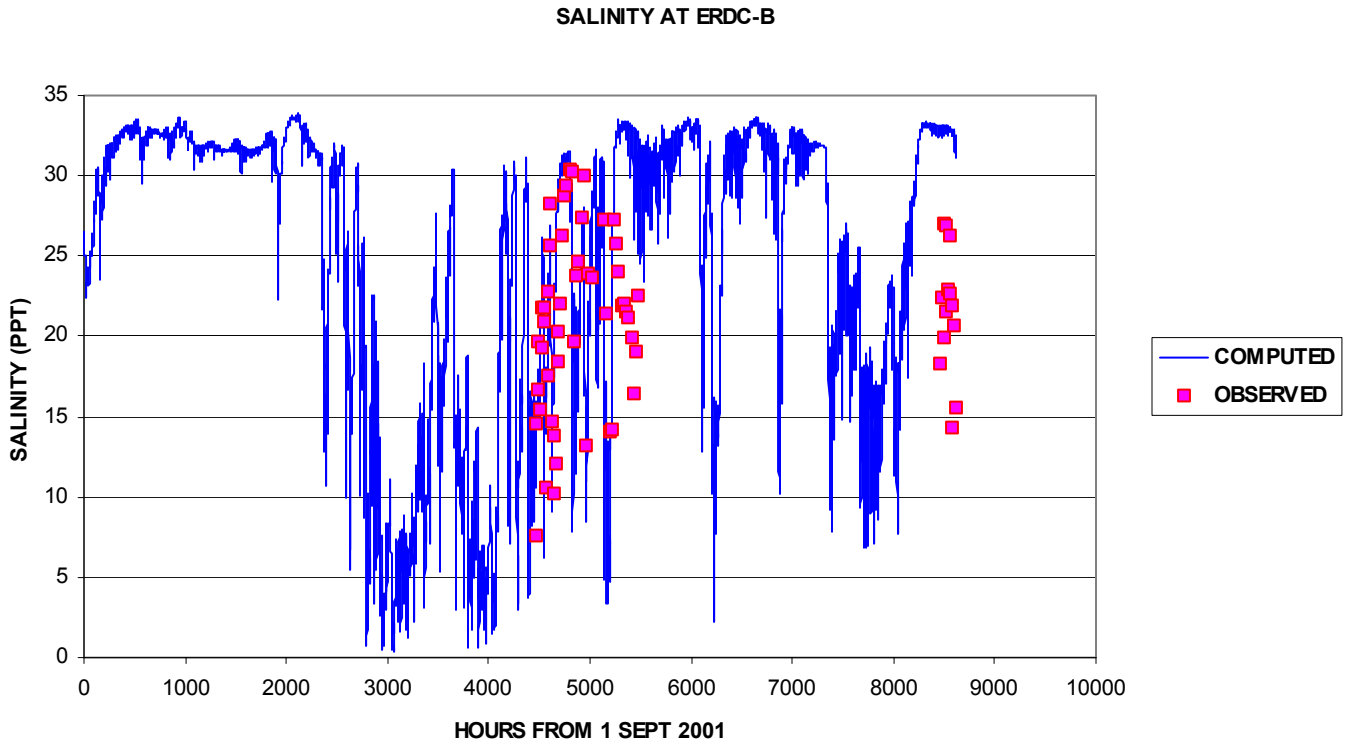

Figure 43. Observed versus computed salinity at ERDC-B

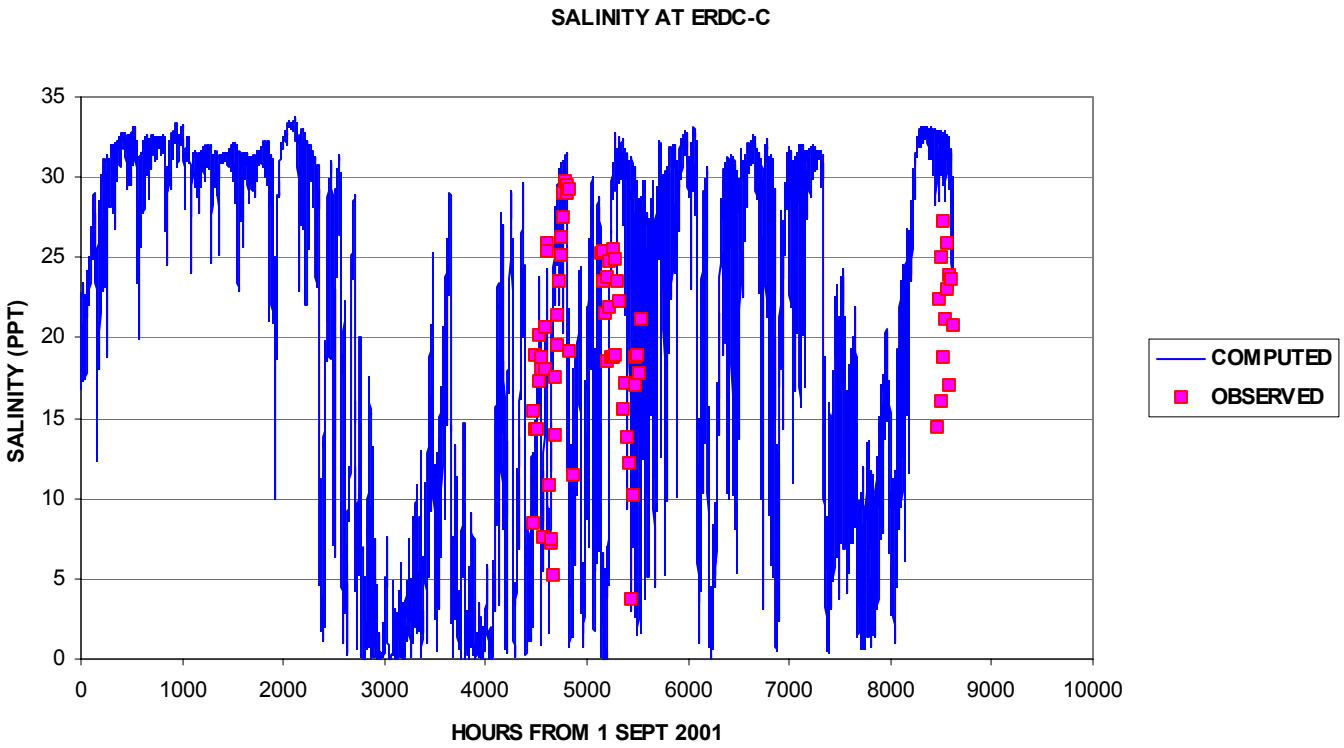

Figure 44. Observed versus computed salinity at ERDC-C

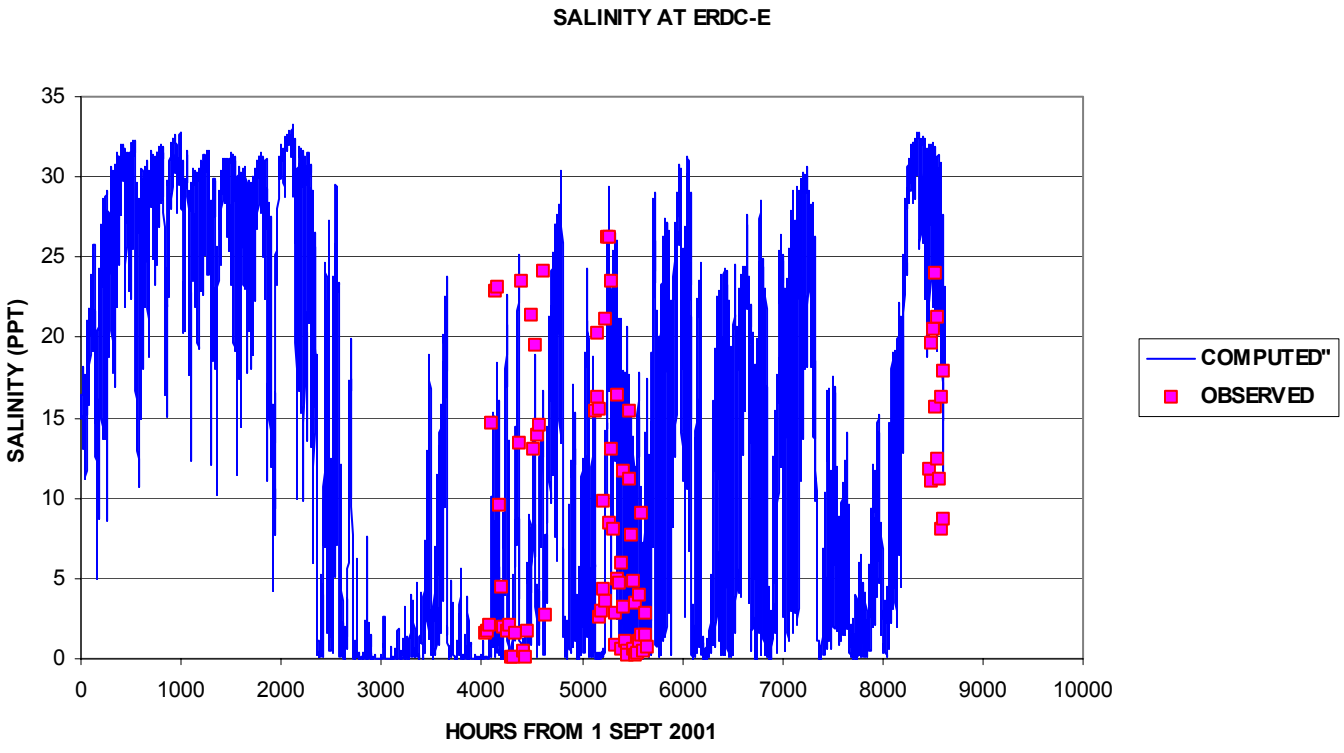

Figure 45. Observed versus computed salinity at ERDC-E

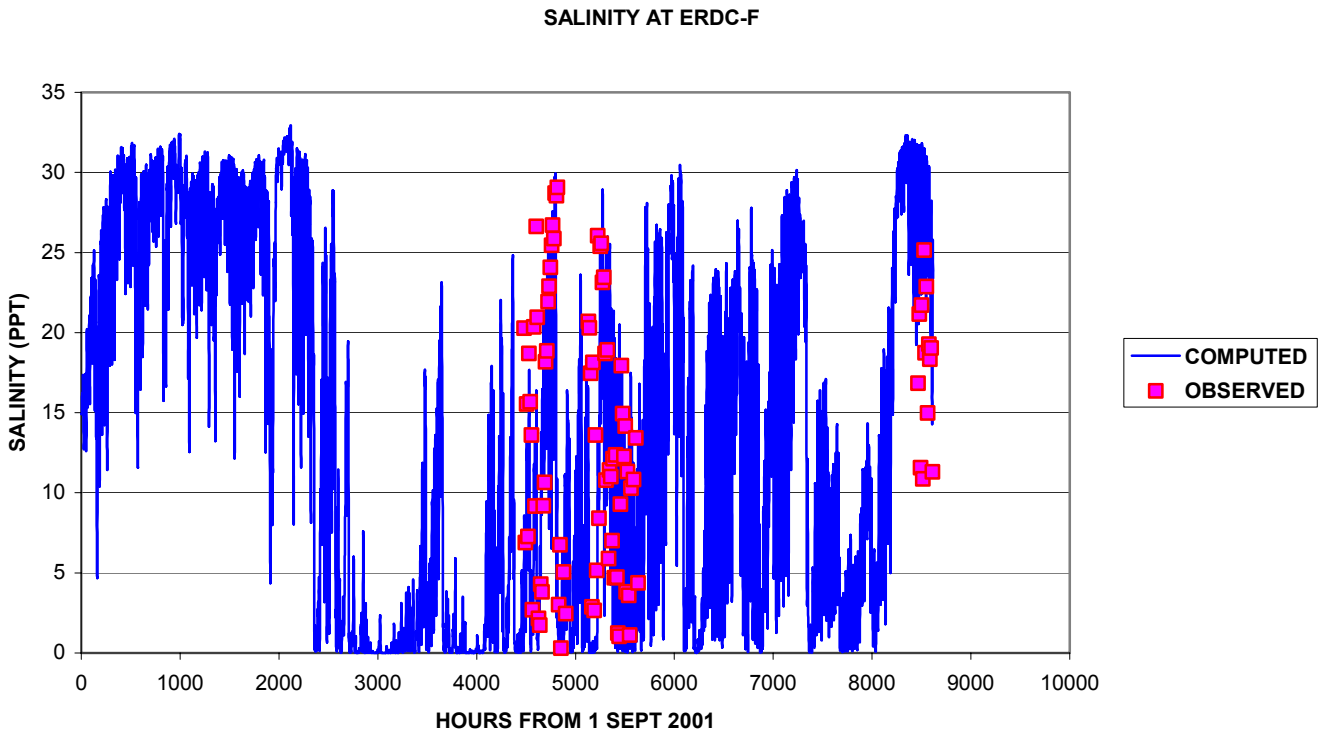

Figure 46. Observed versus computed salinity at ERDC-F

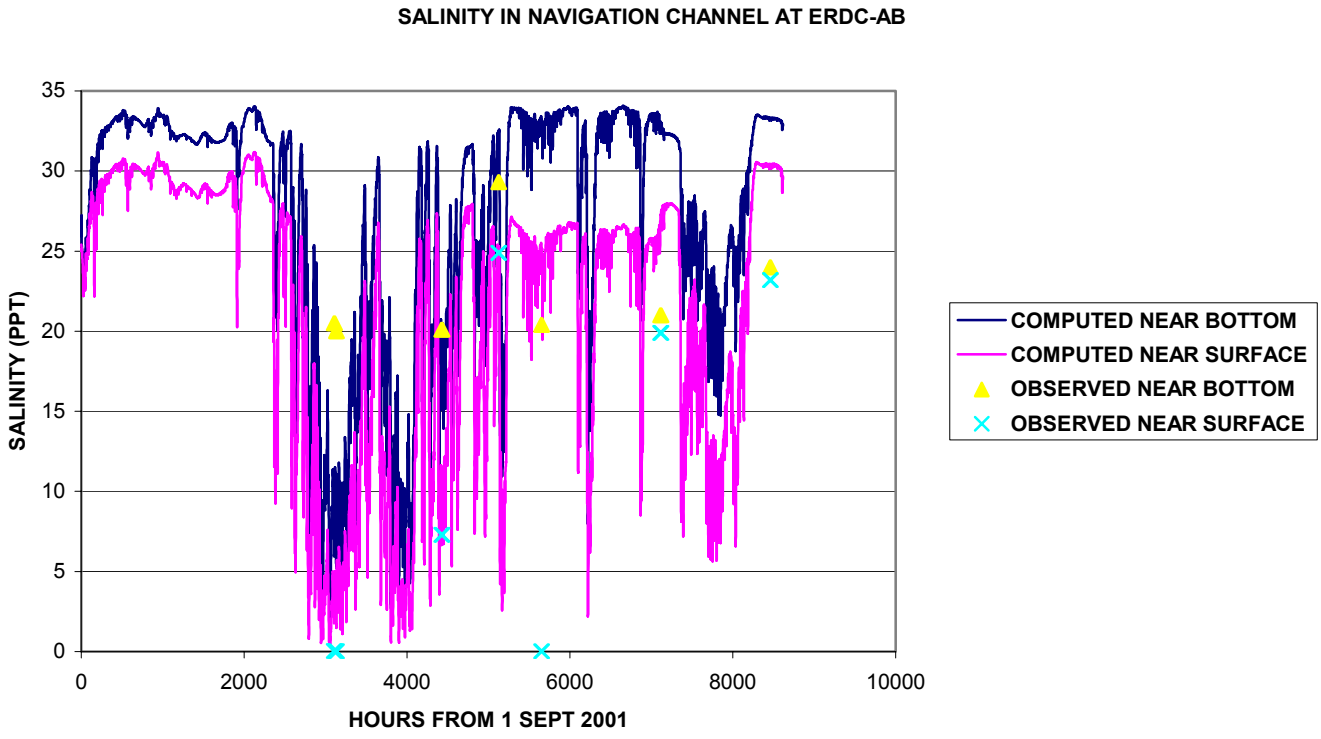

Figure 47. Comparison of near surface / near bottom salinity at ERDC-AB

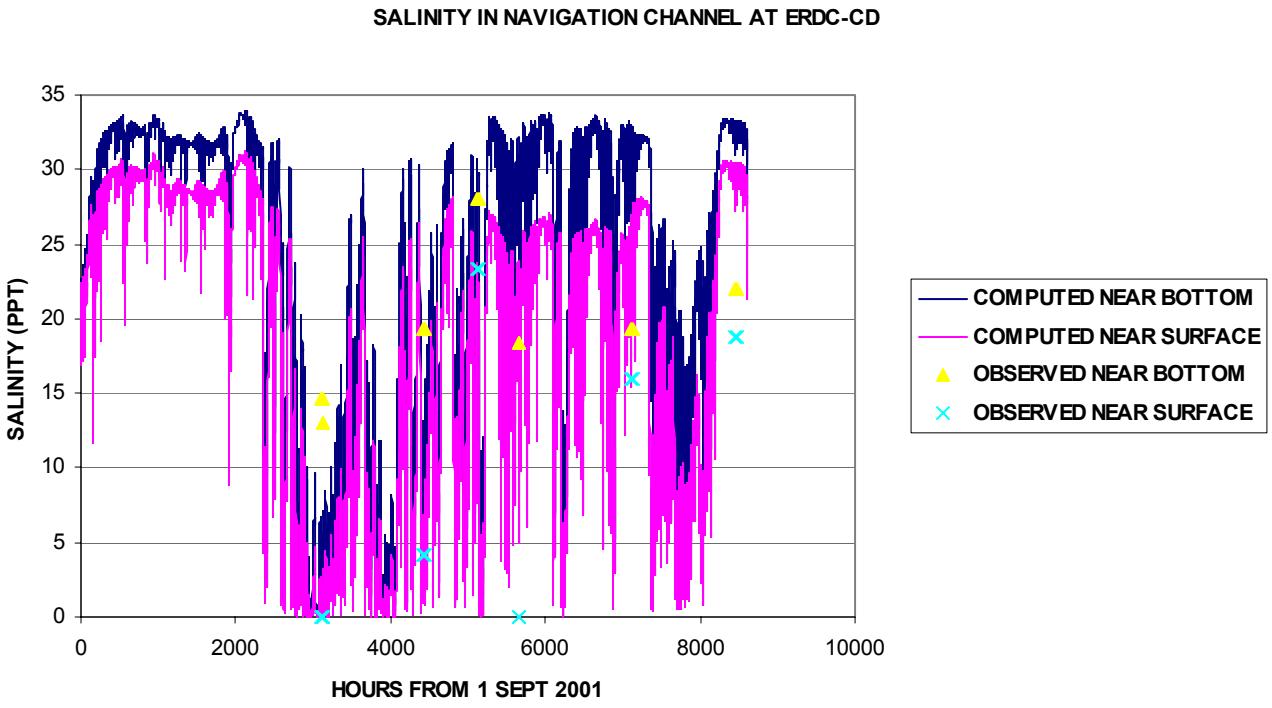

Figure 48. Comparison of near surface / near bottom salinity at ERDC-CD

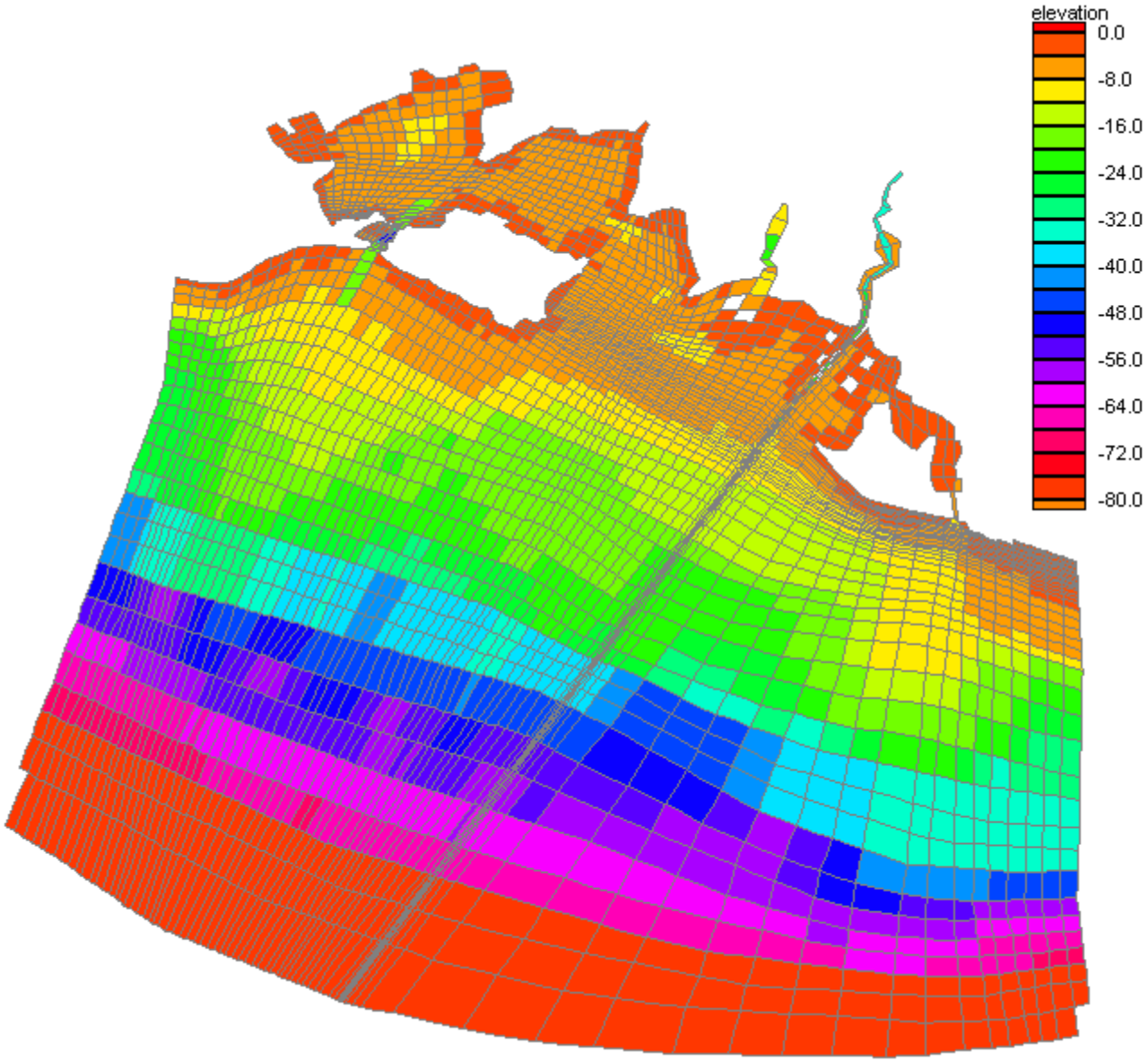

Figure 49. Extended CH3D numerical planform grid

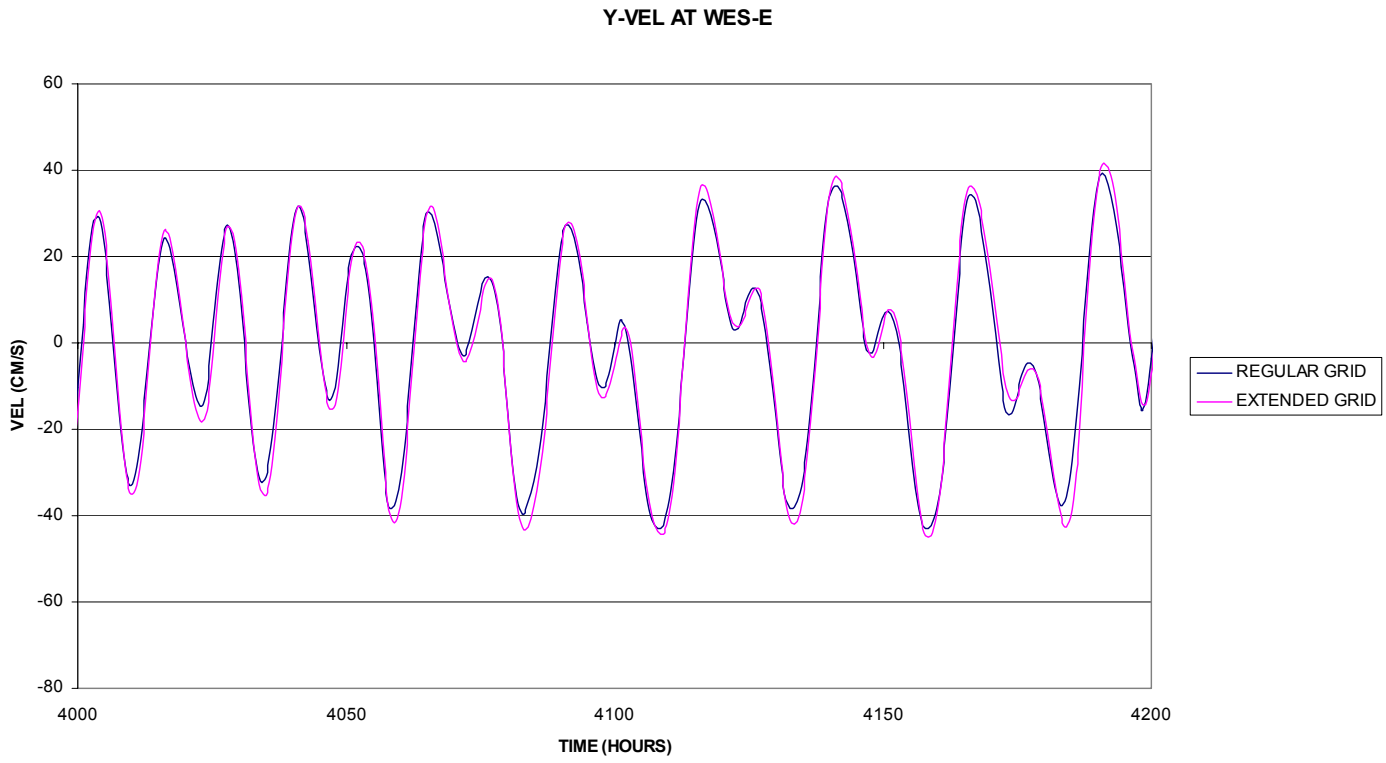

Figure 50. Impact of extended grid on Y component of velocity at ERDC-E

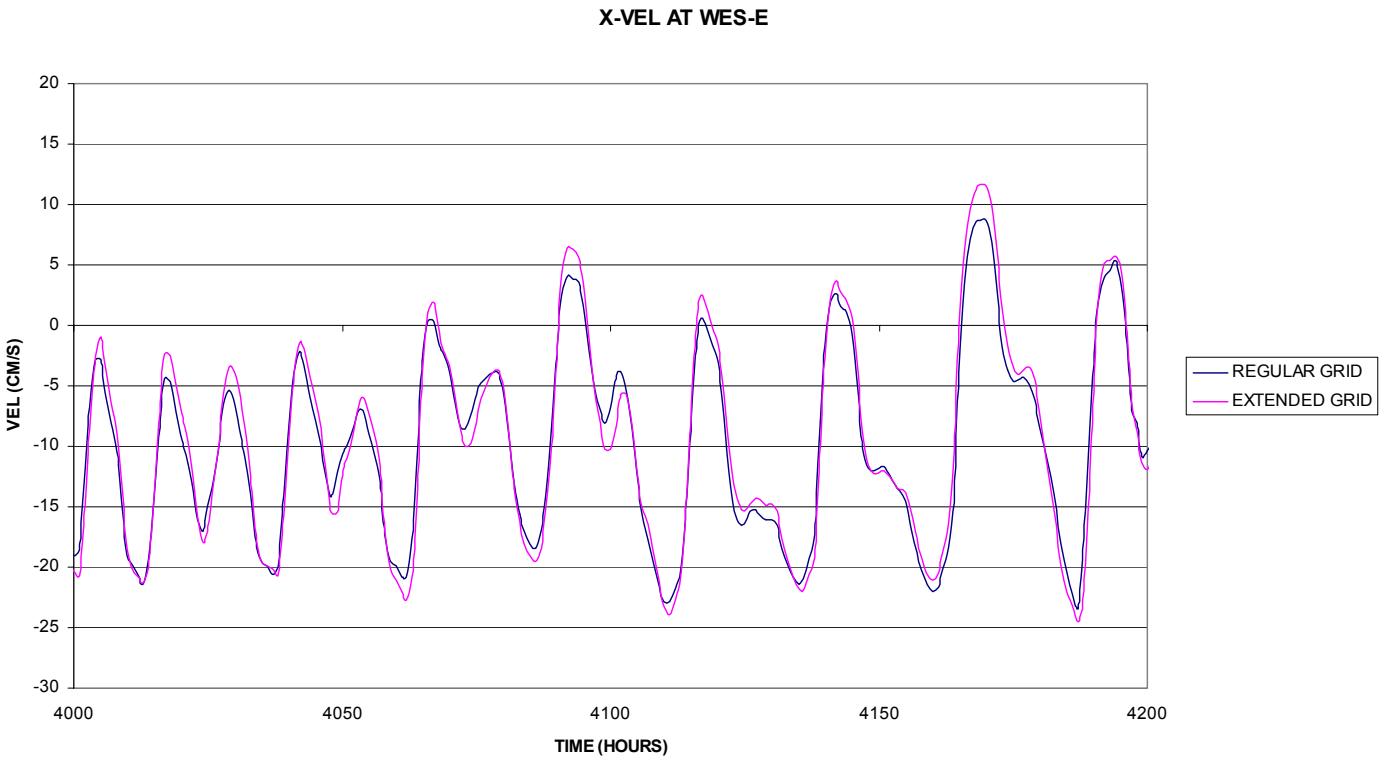

Figure 51. Impact of extended grid on X component of velocity at ERDC-E

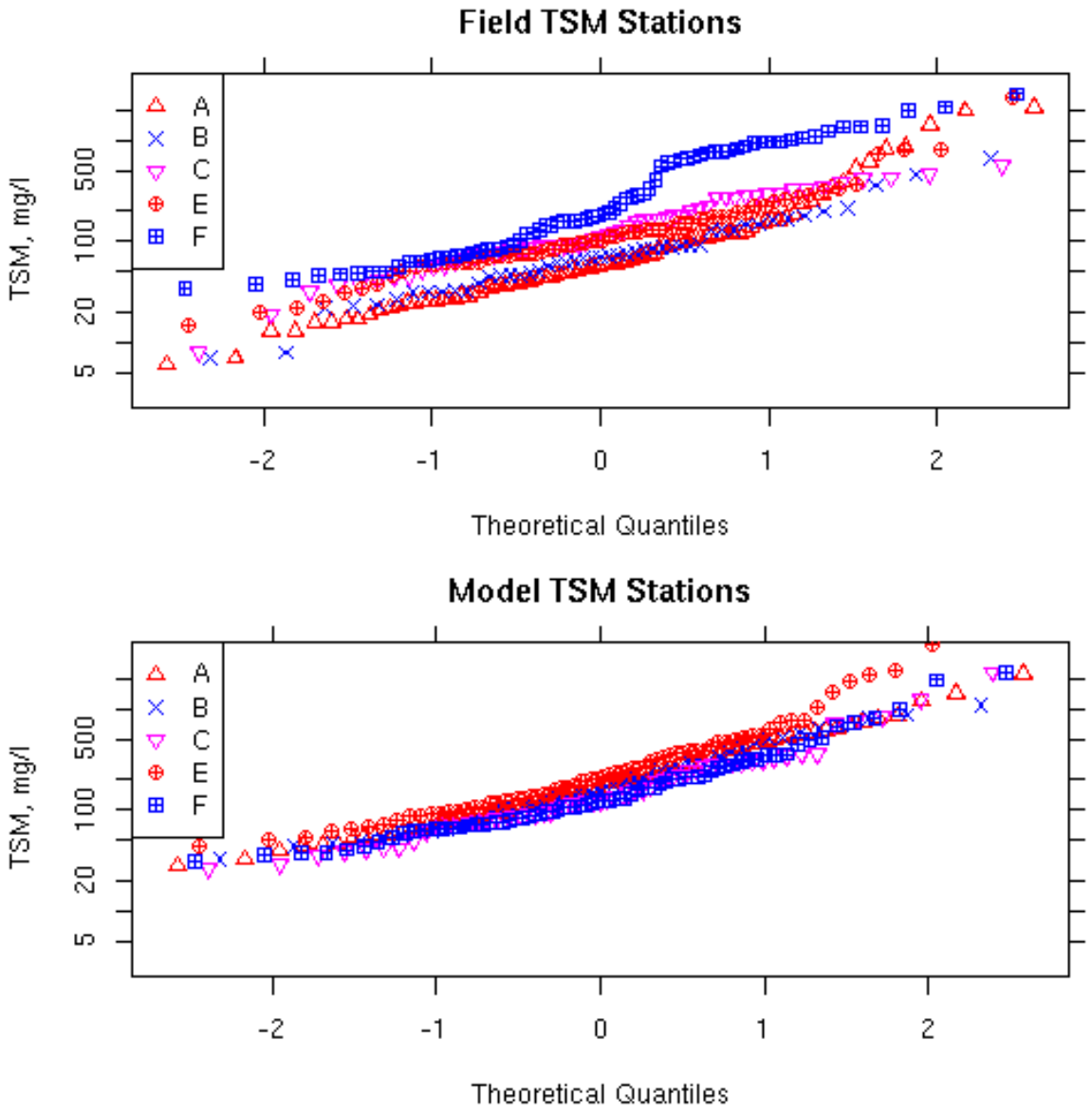

Figure 52. Comparison of point-to-point field and model TSM statistical distributions

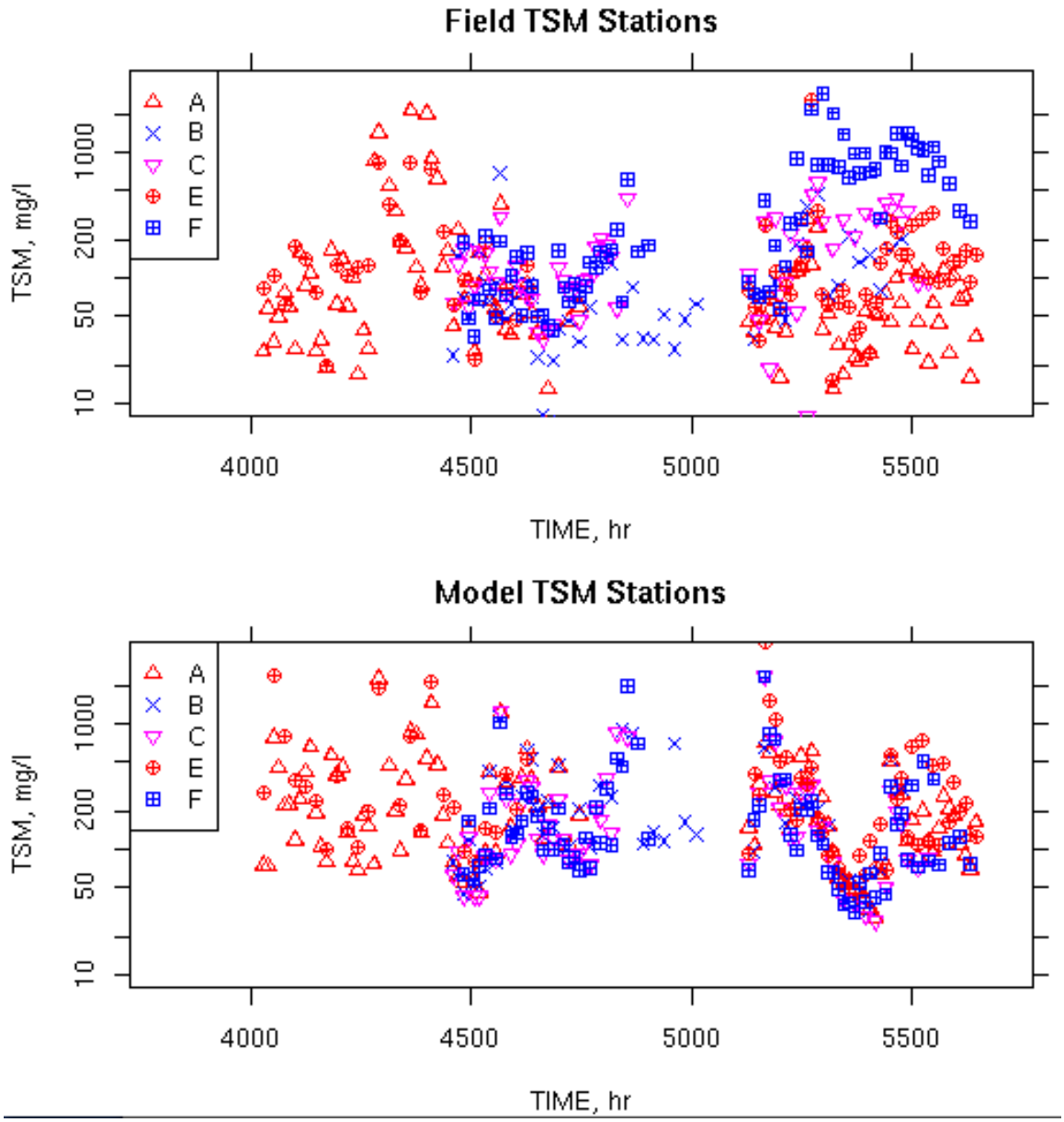

Figure 53. Validation comparison of field and model TSM time-series at ERDC stations

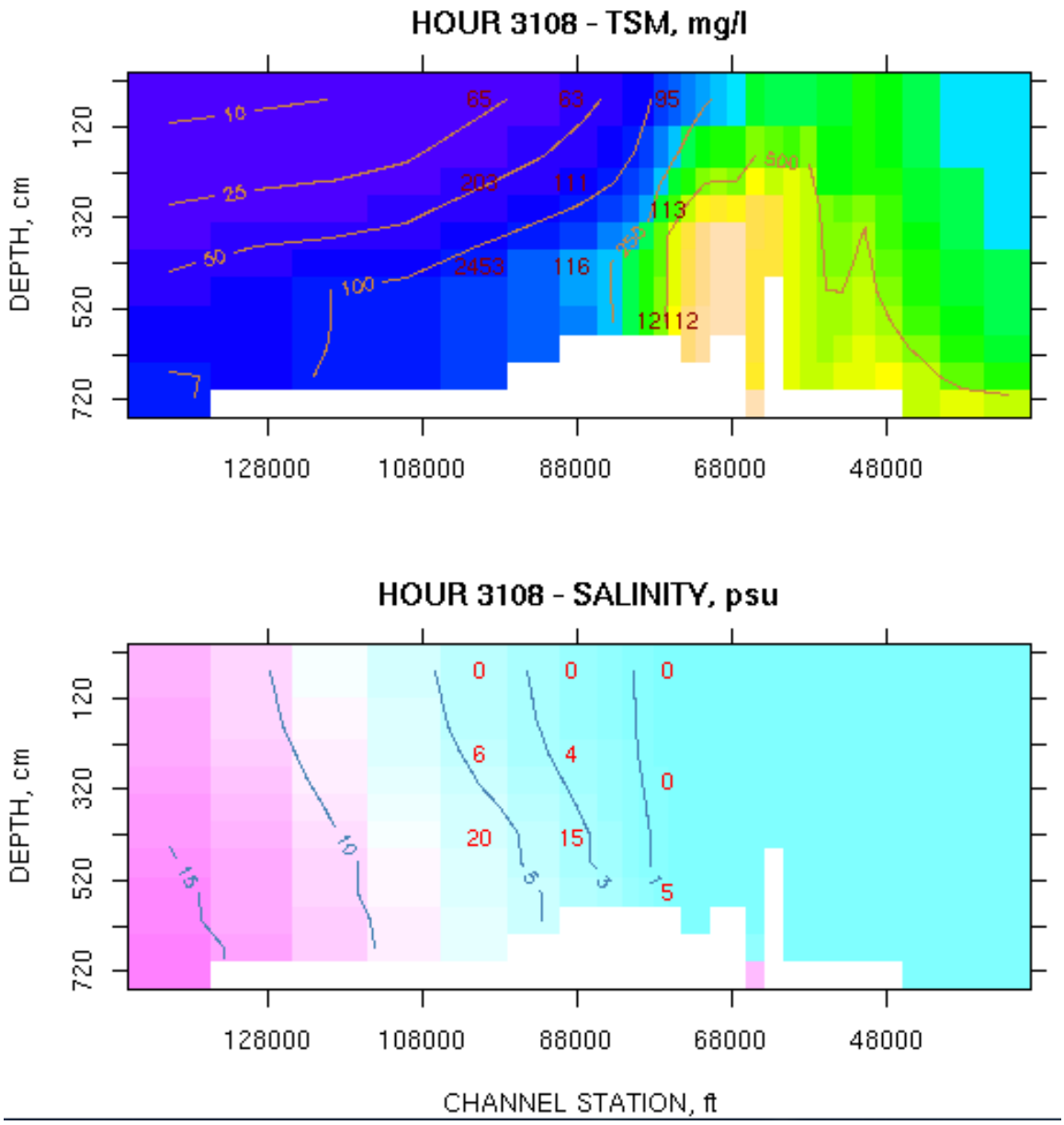

Figure 54. Channel profile snapshot comparisons of field (point values) and model (isopleths and shading) TSM and salinity at hour 3,108

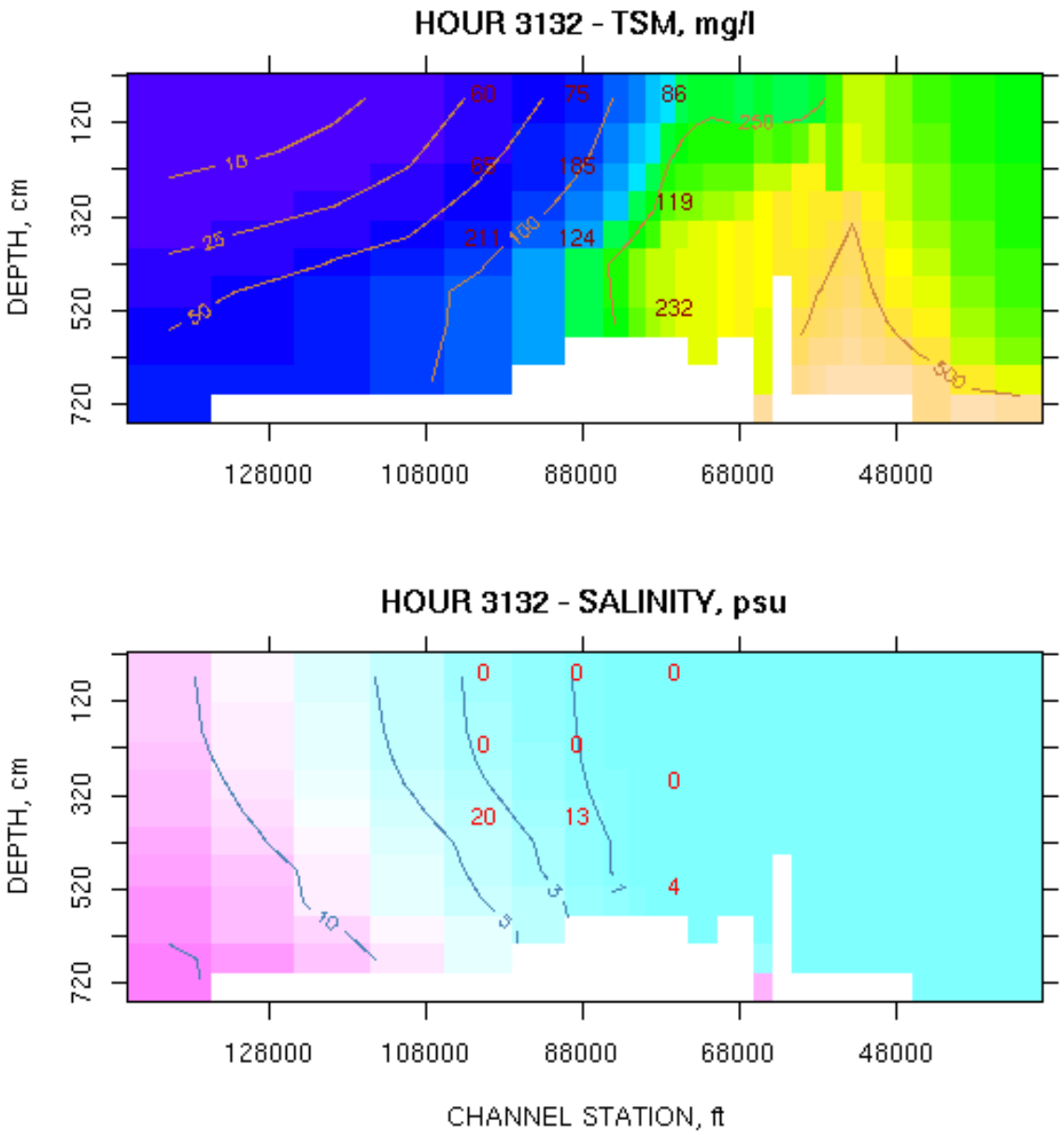

Figure 55. Channel profile snapshot comparisons of field (point values) and model (isopleths and shading) TSM and salinity at hour 3,132

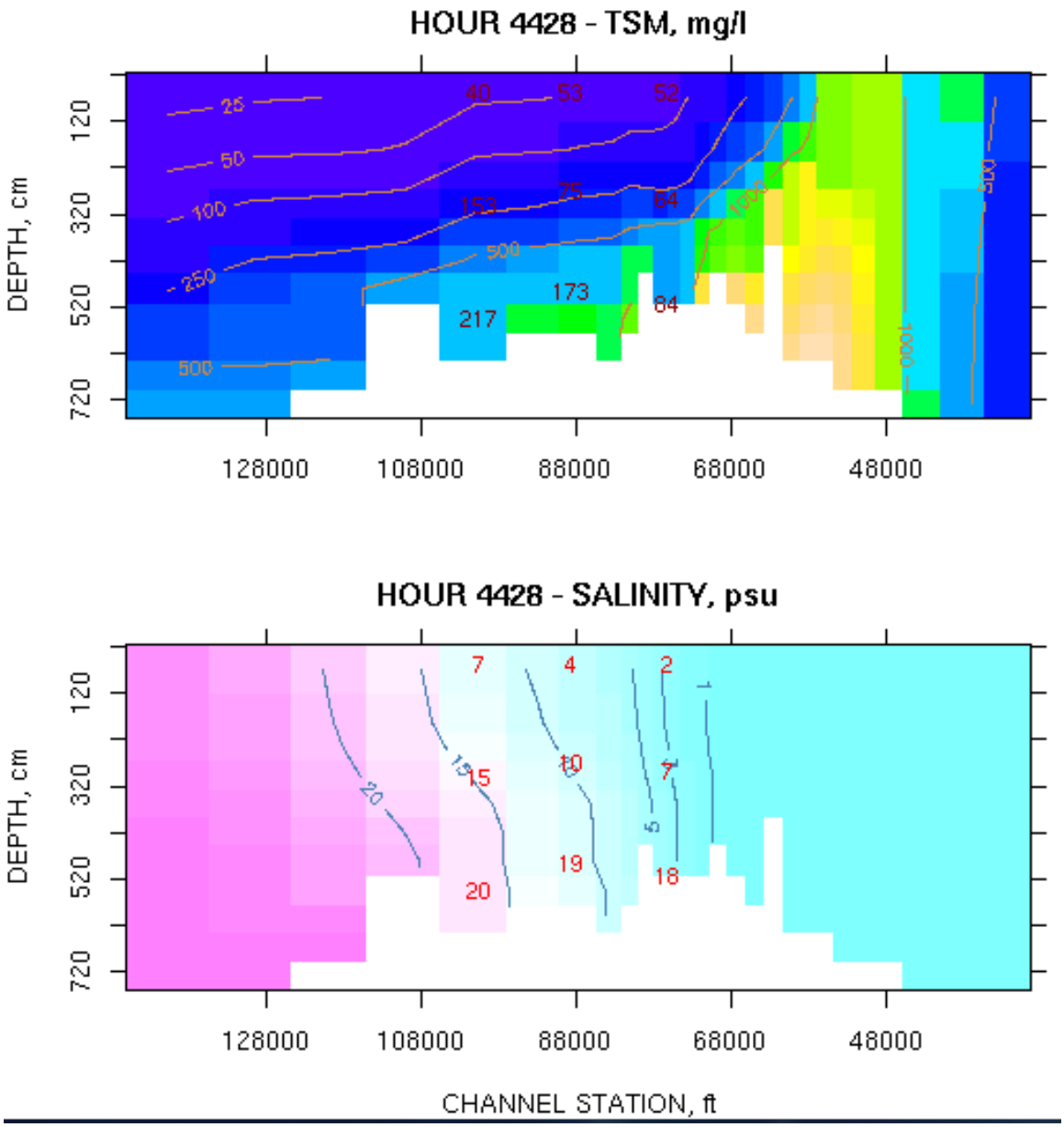

Figure 56. Channel profile snapshot comparisons of field (point values) and model (isopleths and shading) TSM and salinity at hour 4,428

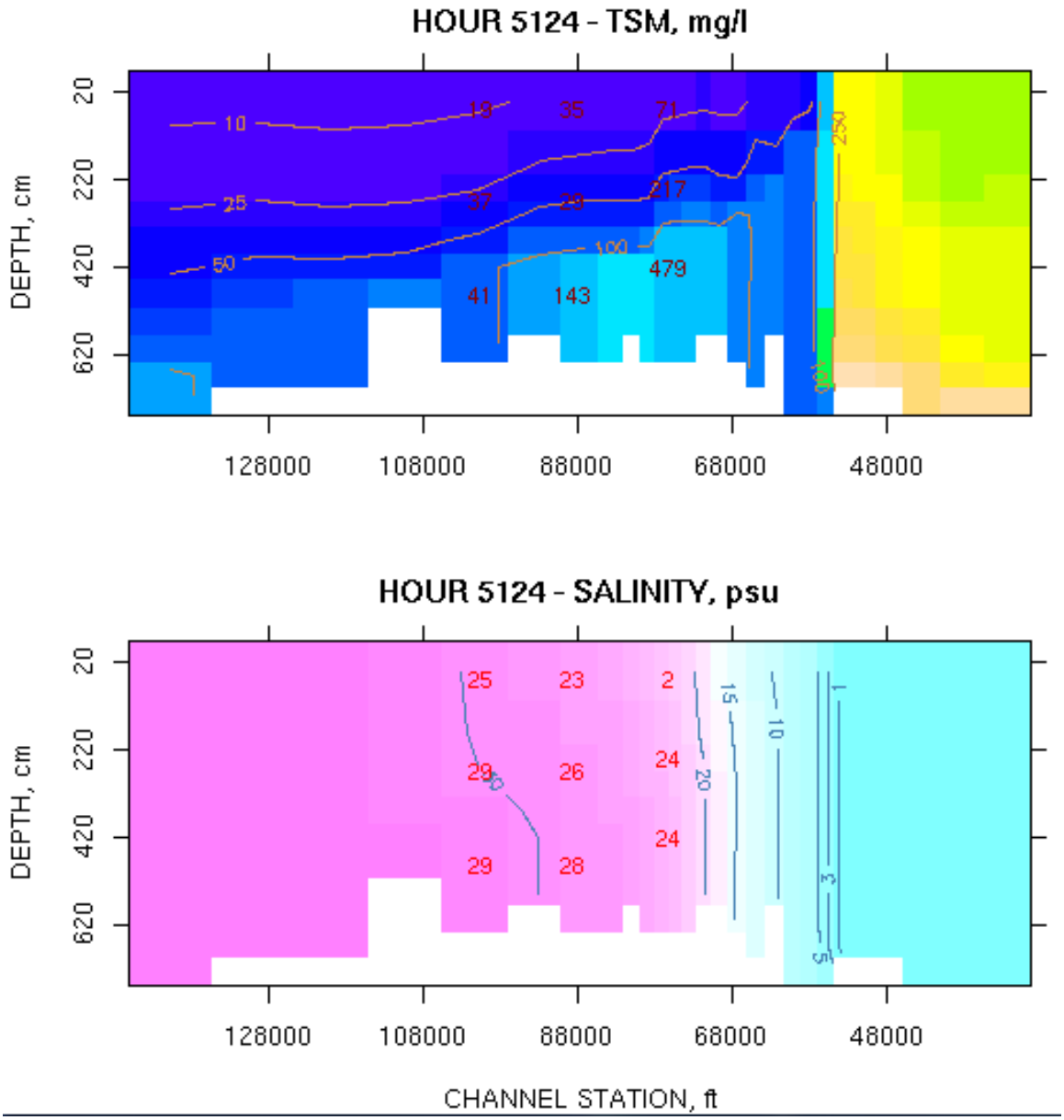

Figure 57. Channel profile snapshot comparisons of field (point values) and model (isopleths and shading) TSM and salinity at hour 5,124

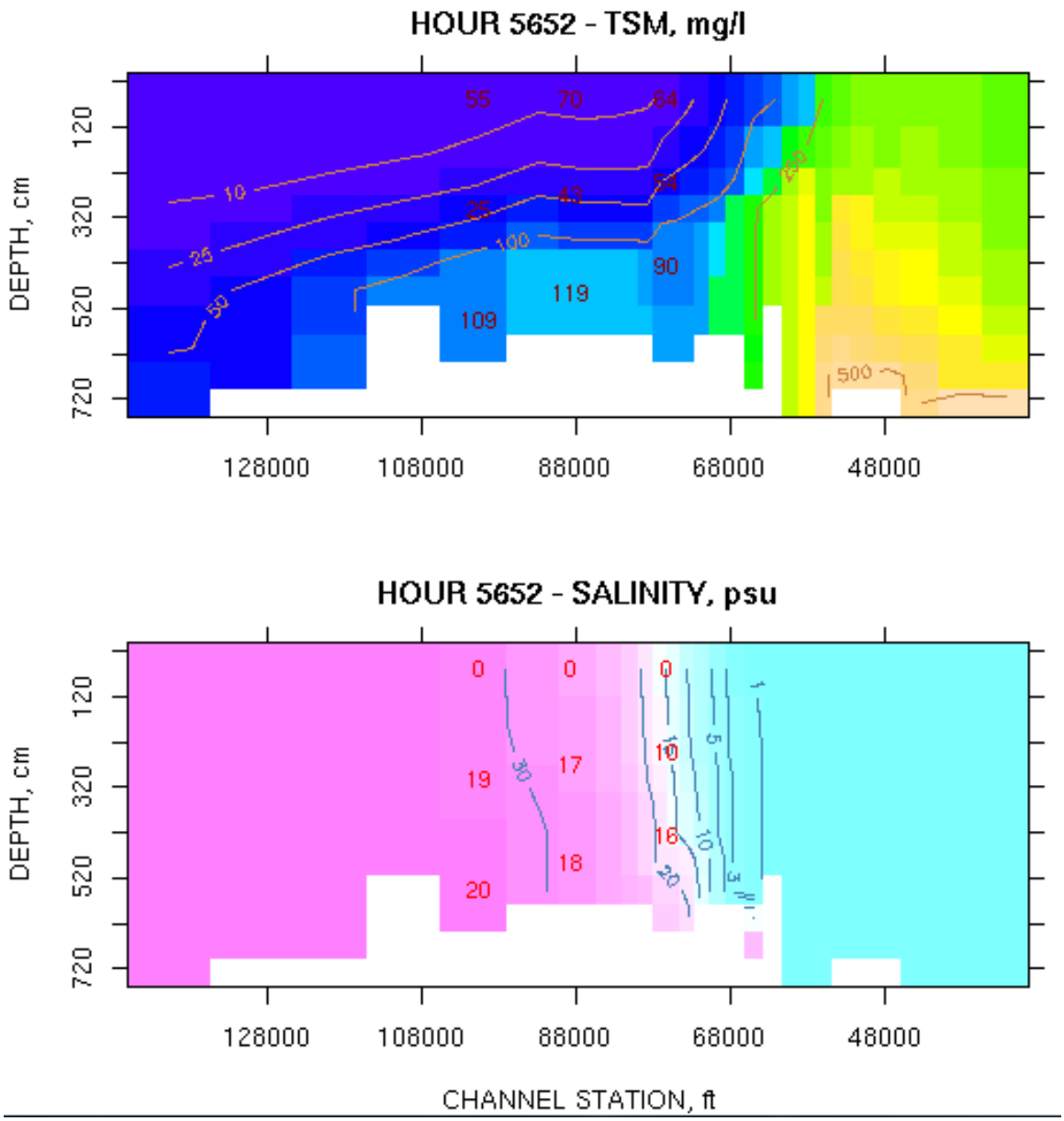

Figure 58. Channel profile snapshot comparisons of field (point values) and model (isopleths and shading) TSM and salinity at hour 5,652

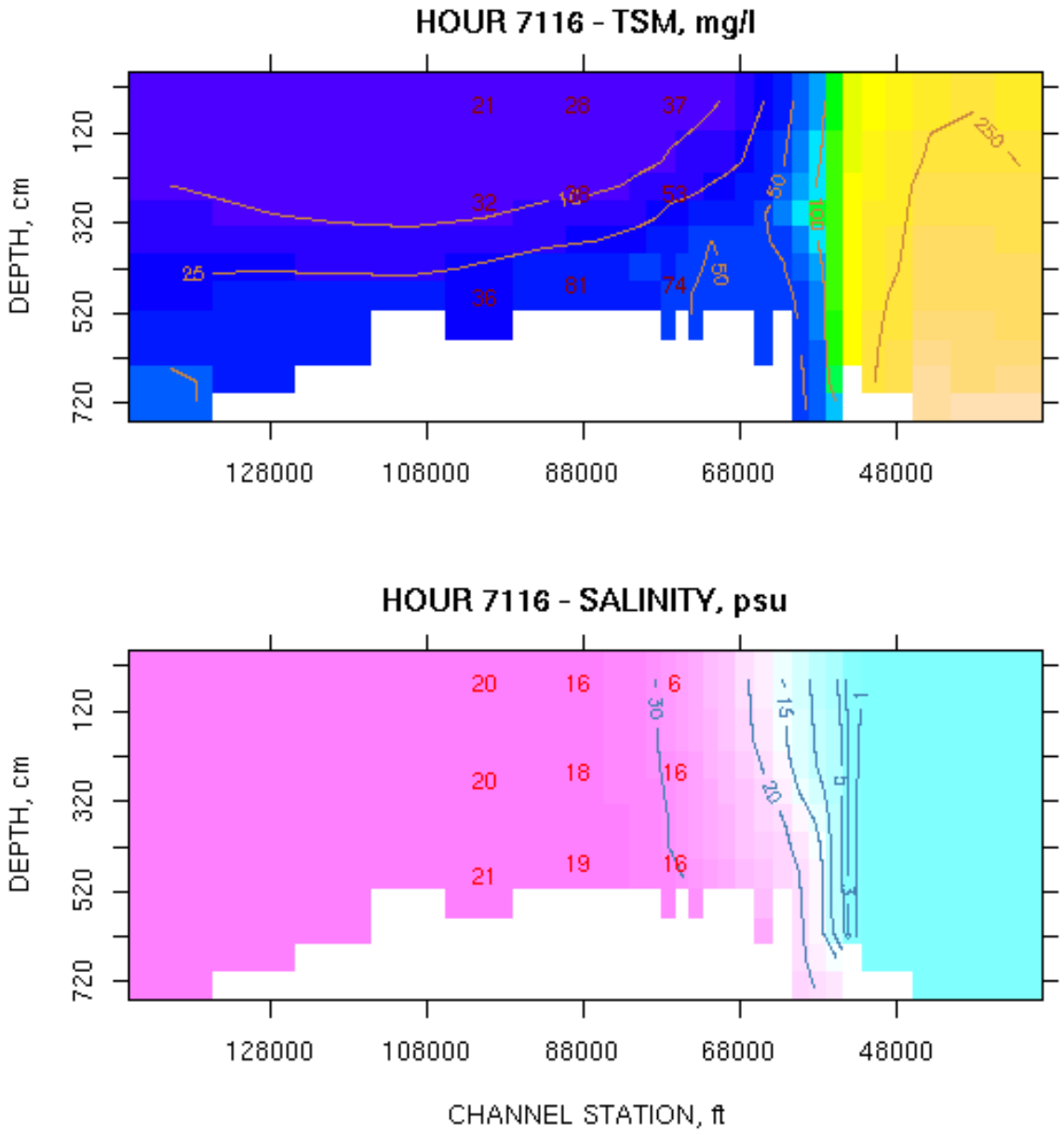

Figure 59. Channel profile snapshot comparisons of field (point values) and model (isopleths and shading) TSM and salinity at hour 7,116

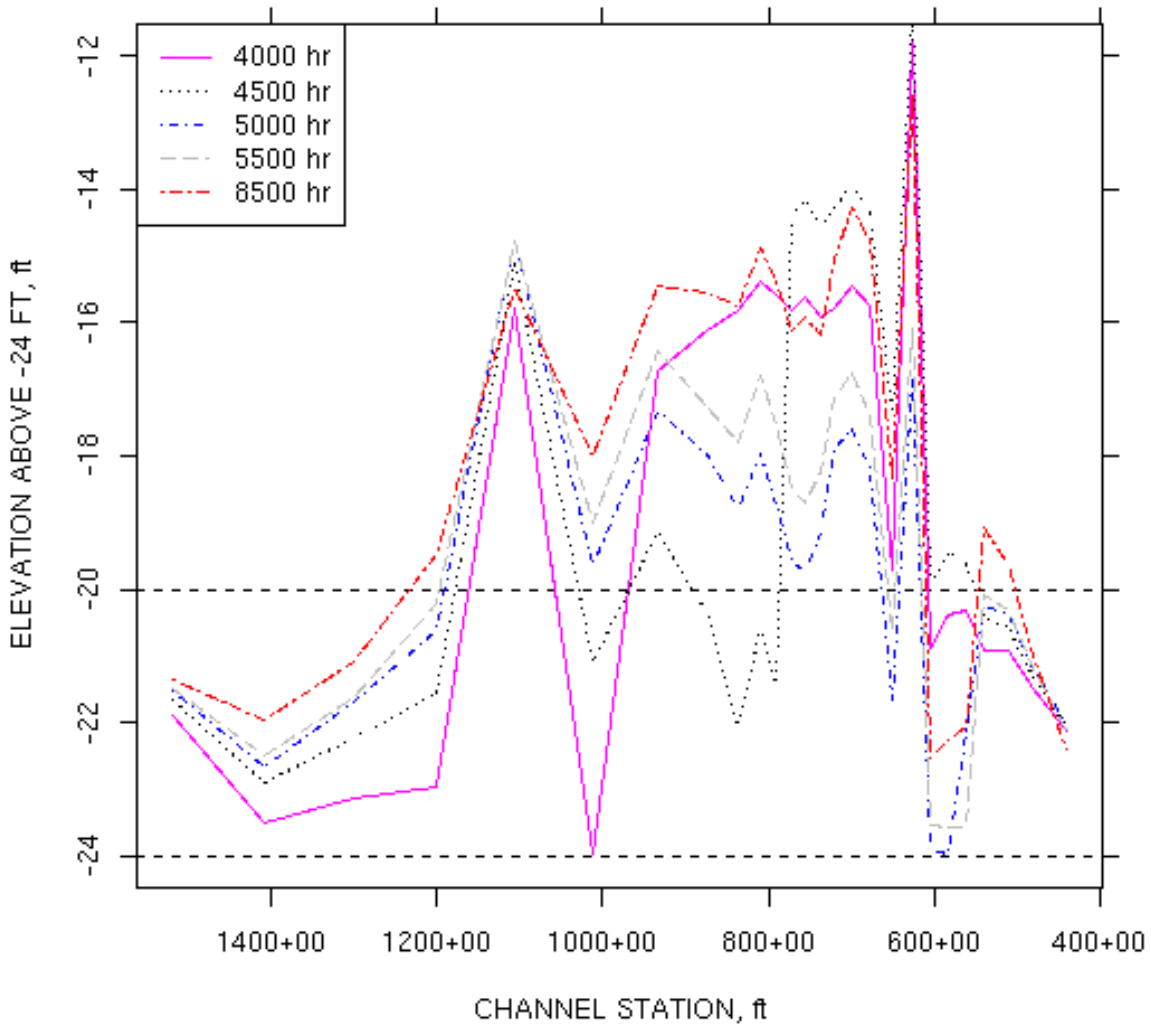

Figure 60. Validation shoal profiles at select hours during and after dredging

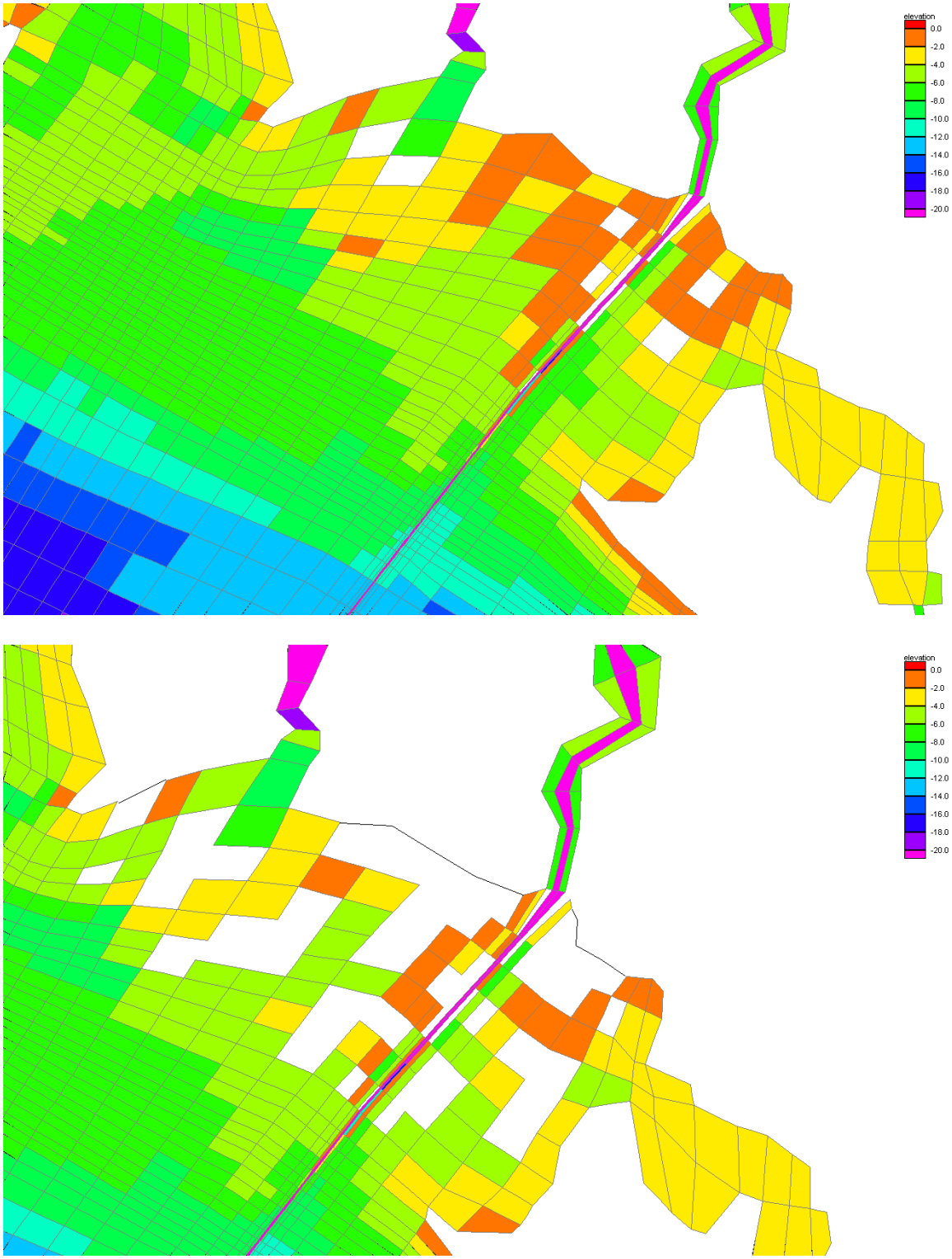

Figure 61. Existing (top) and future (bottom) bay grid configurations

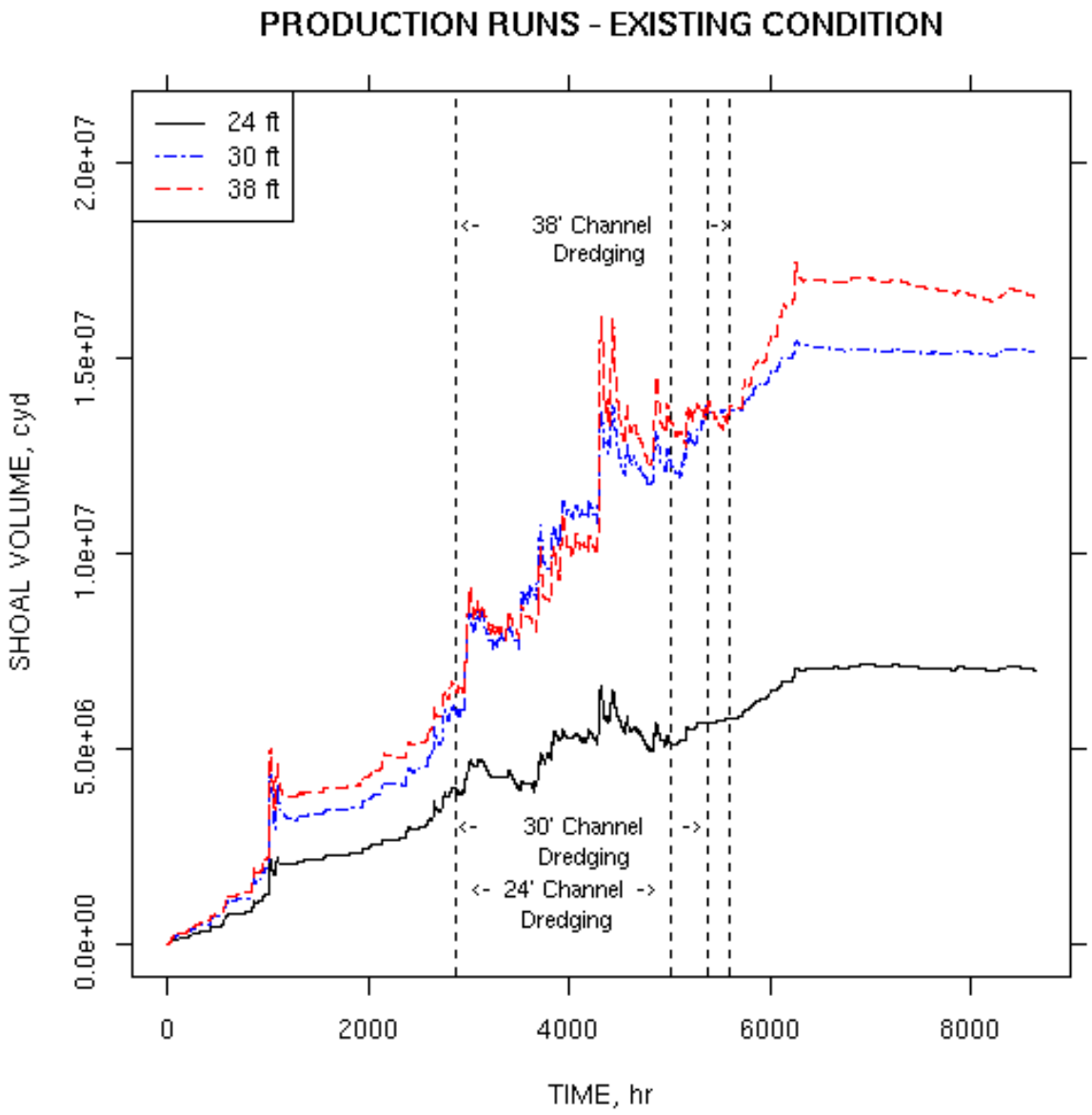

Figure 62. Shoal history comparison for production runs with existing conditions

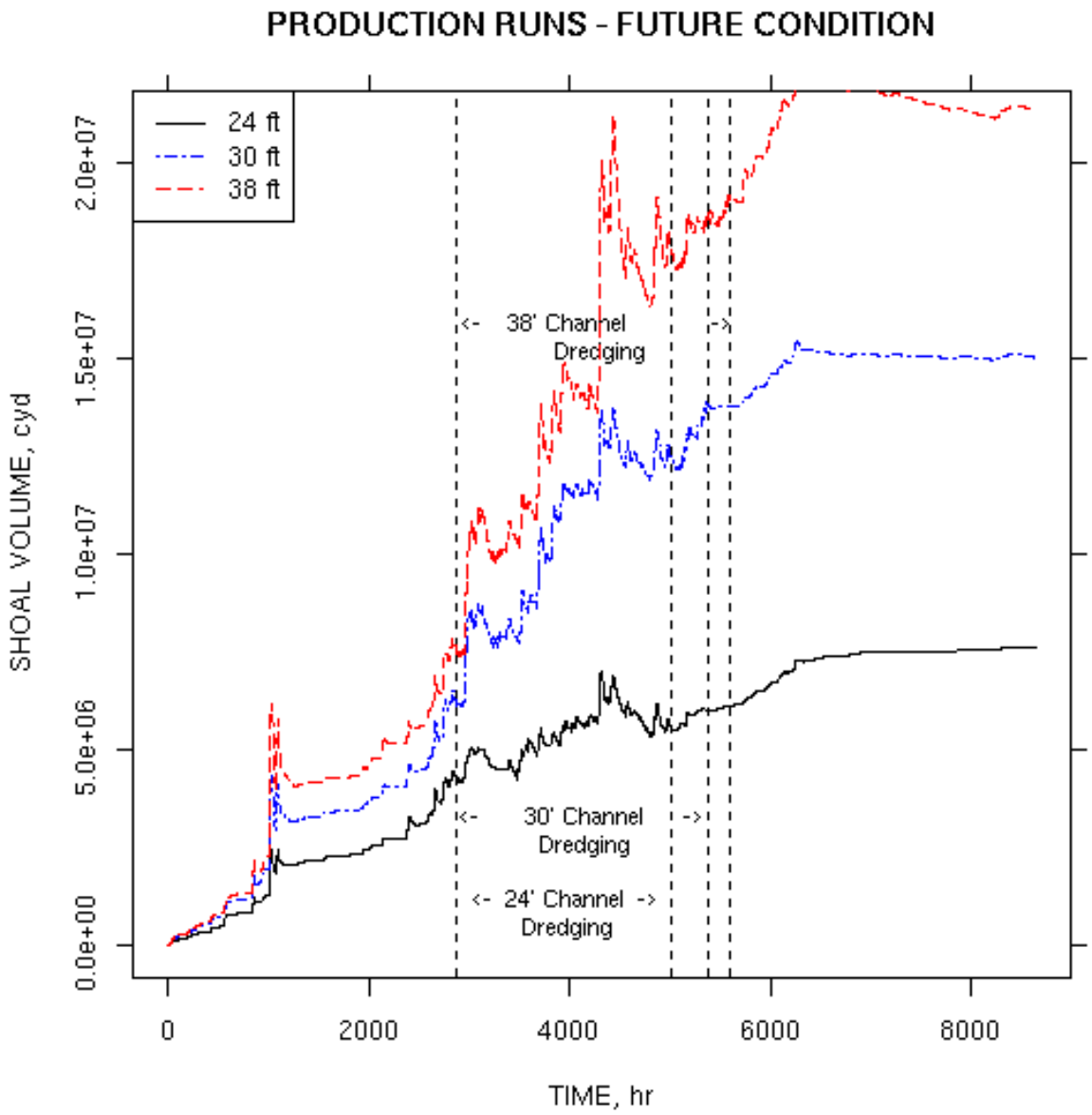

Figure 63. Shoal history comparison for production runs with future conditions

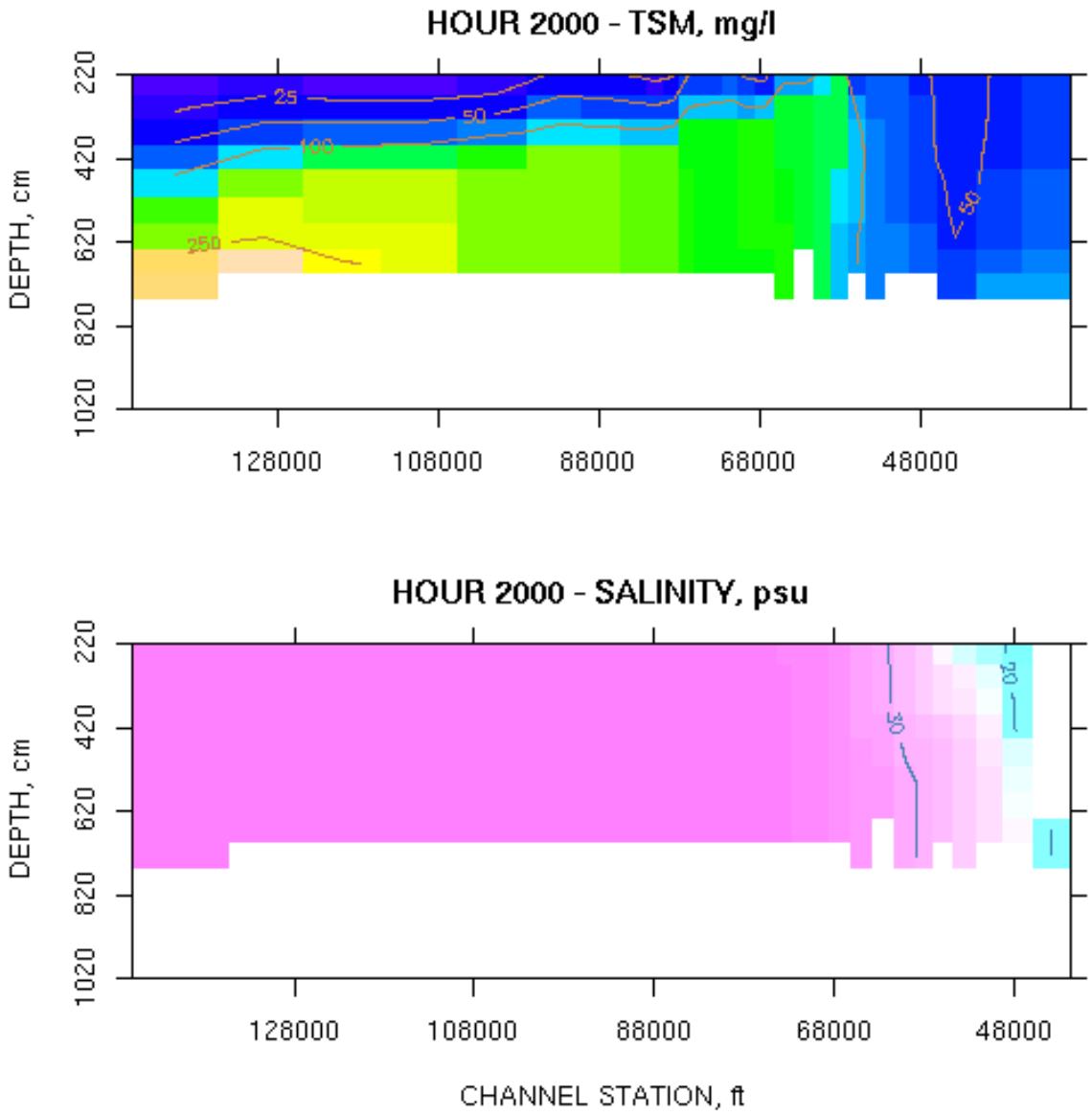

Figure 64. Channel profile snapshots of TSM and salinity for 24 ft existing channel at hour 2,000

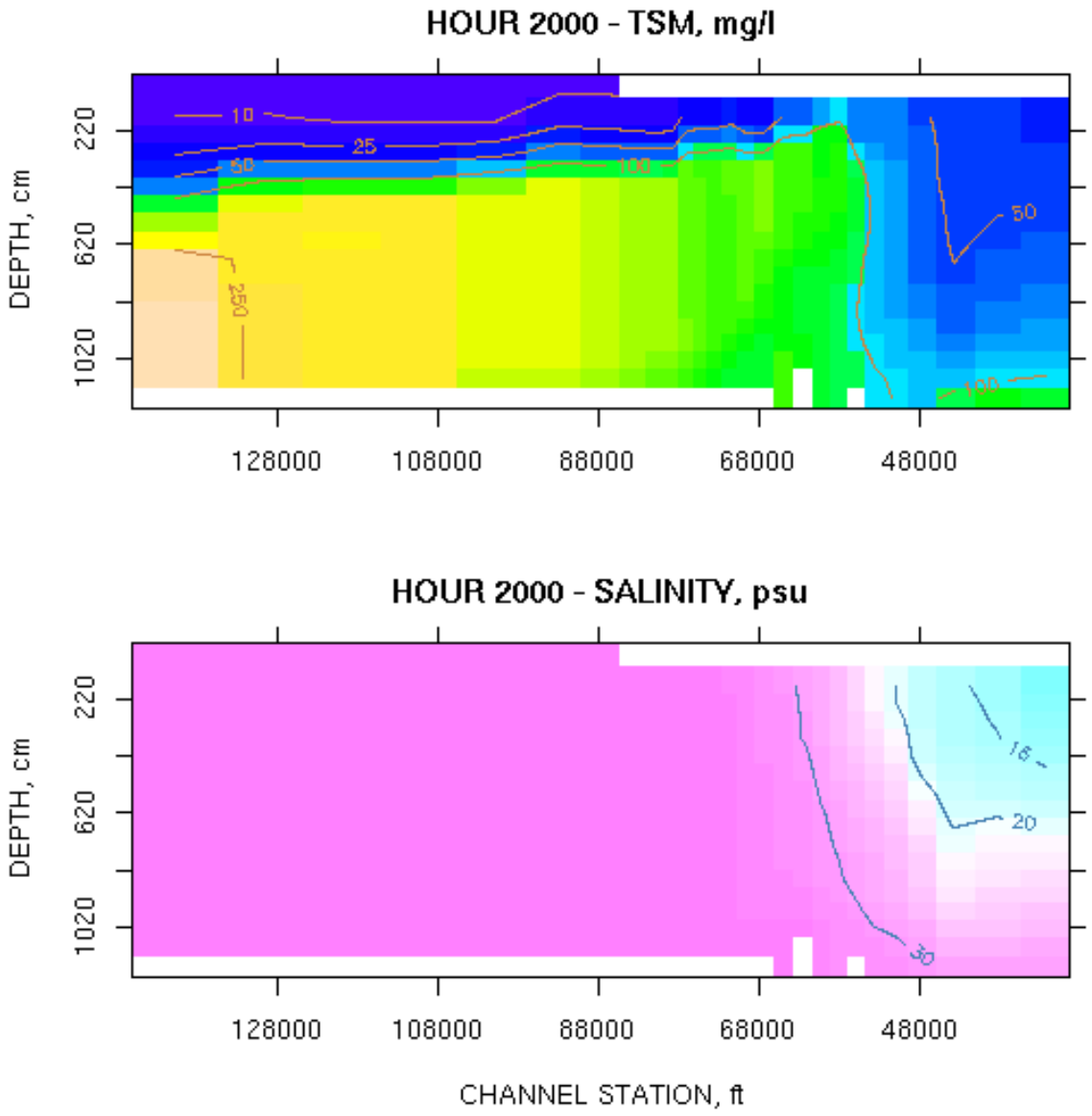

Figure 65. Channel profile snapshots of TSM and salinity for 38 ft existing channel at hour 2,000

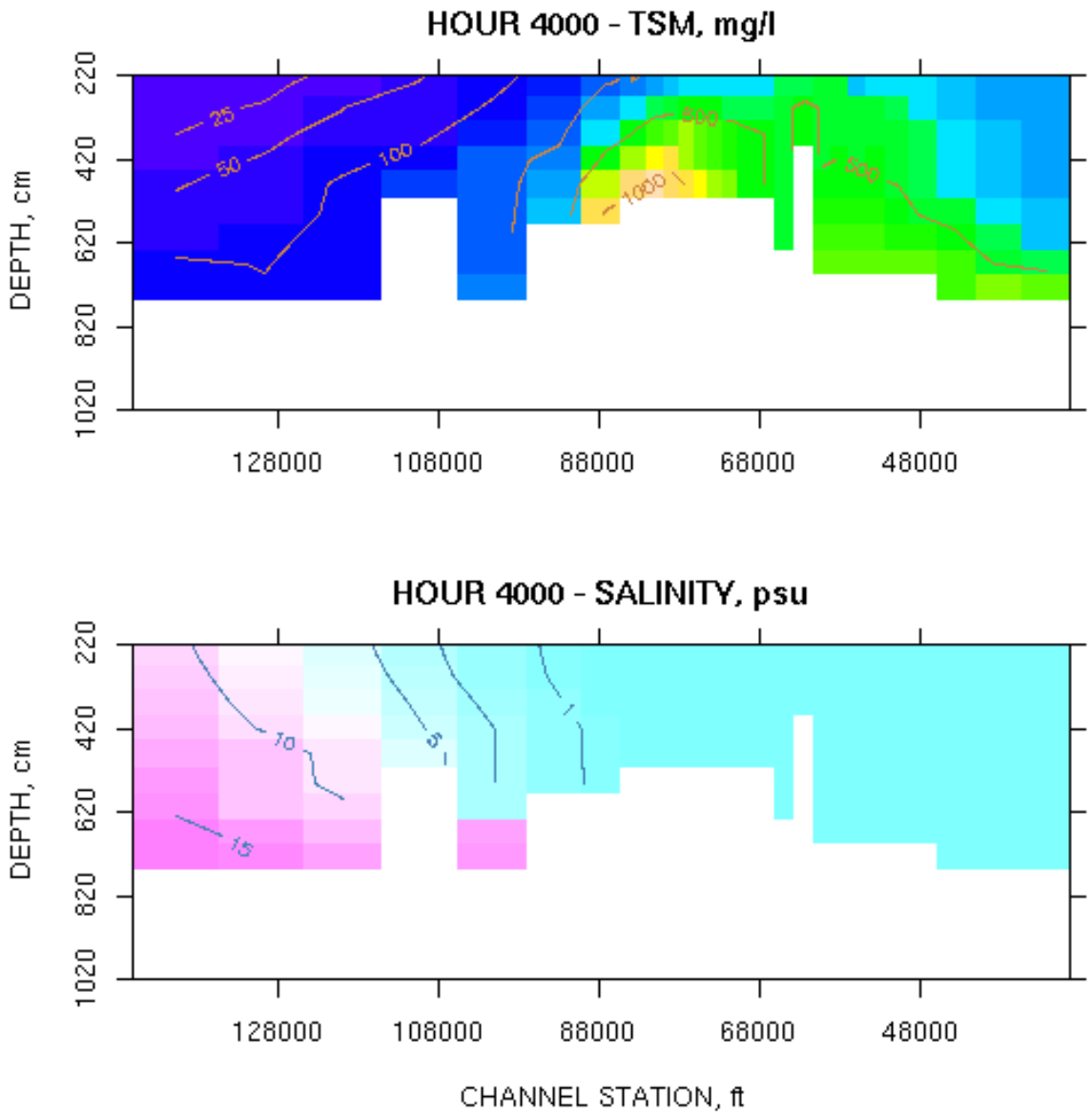

Figure 66. Channel profile snapshots of TSM and salinity for 24 ft existing channel at hour 4,000

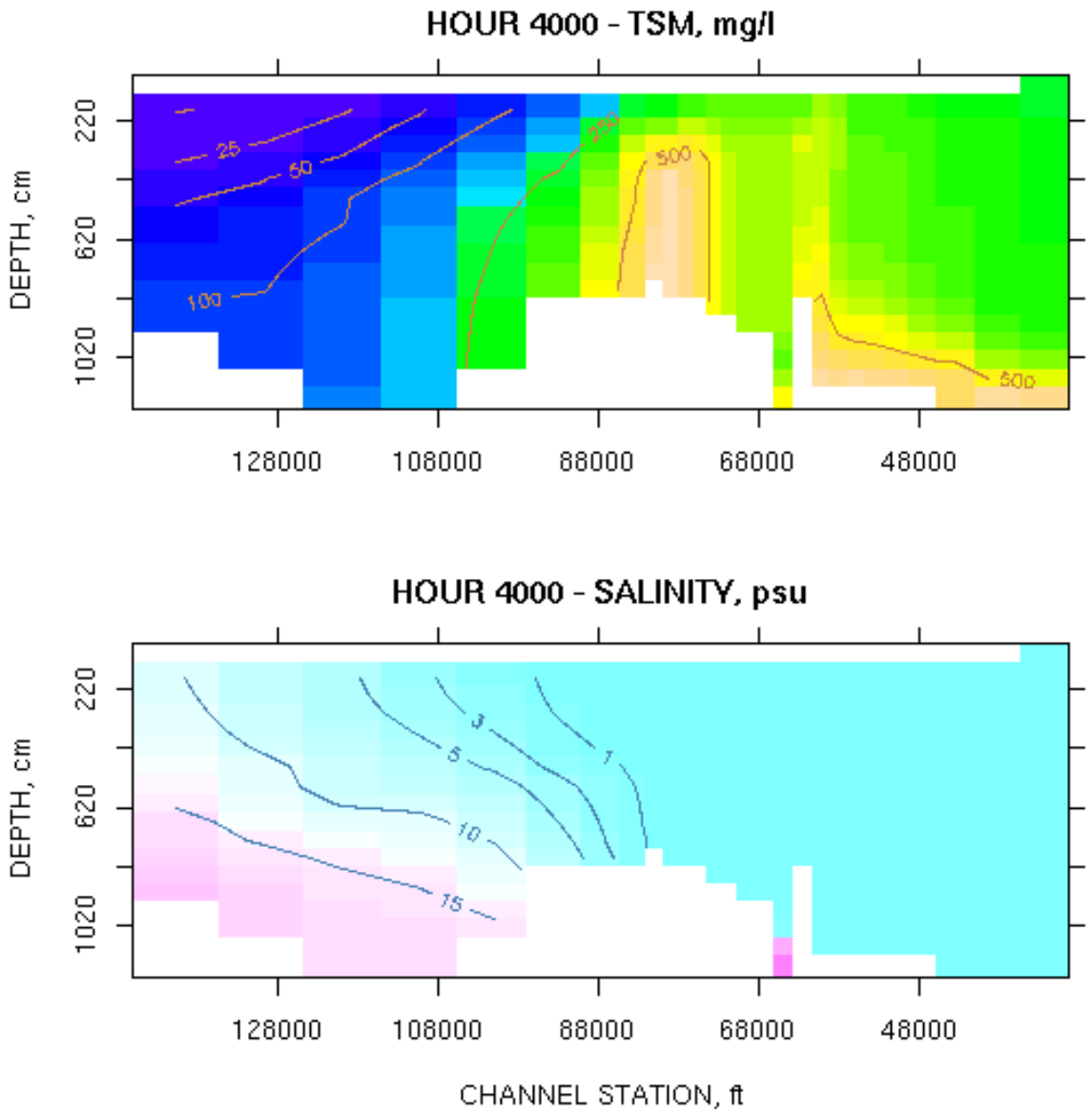

Figure 67. Channel profile snapshots of TSM and salinity for 38 ft existing channel at hour 4,000

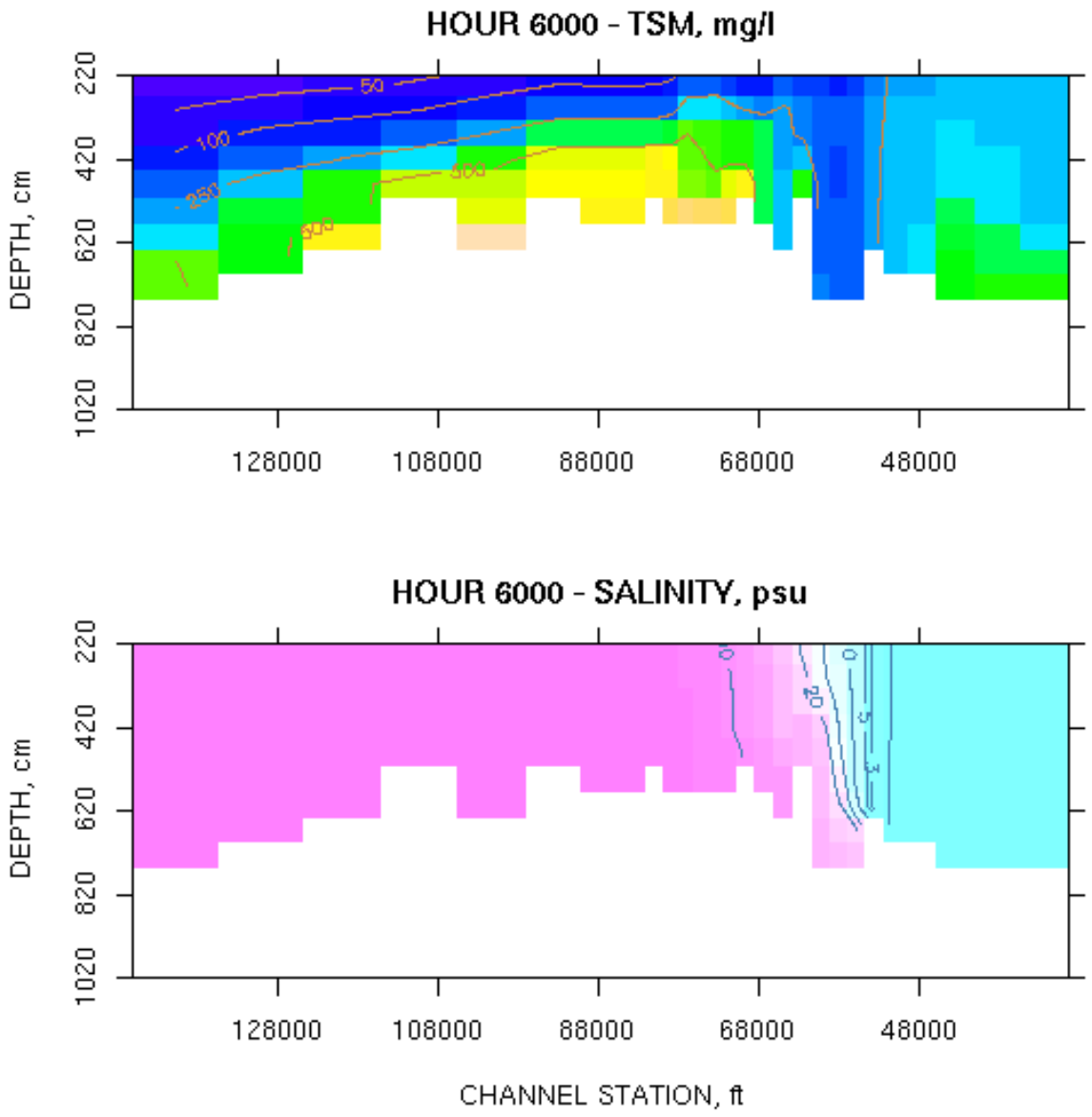

Figure 68. Channel profile snapshots of TSM and salinity for 24 ft existing channel at hour 6,000

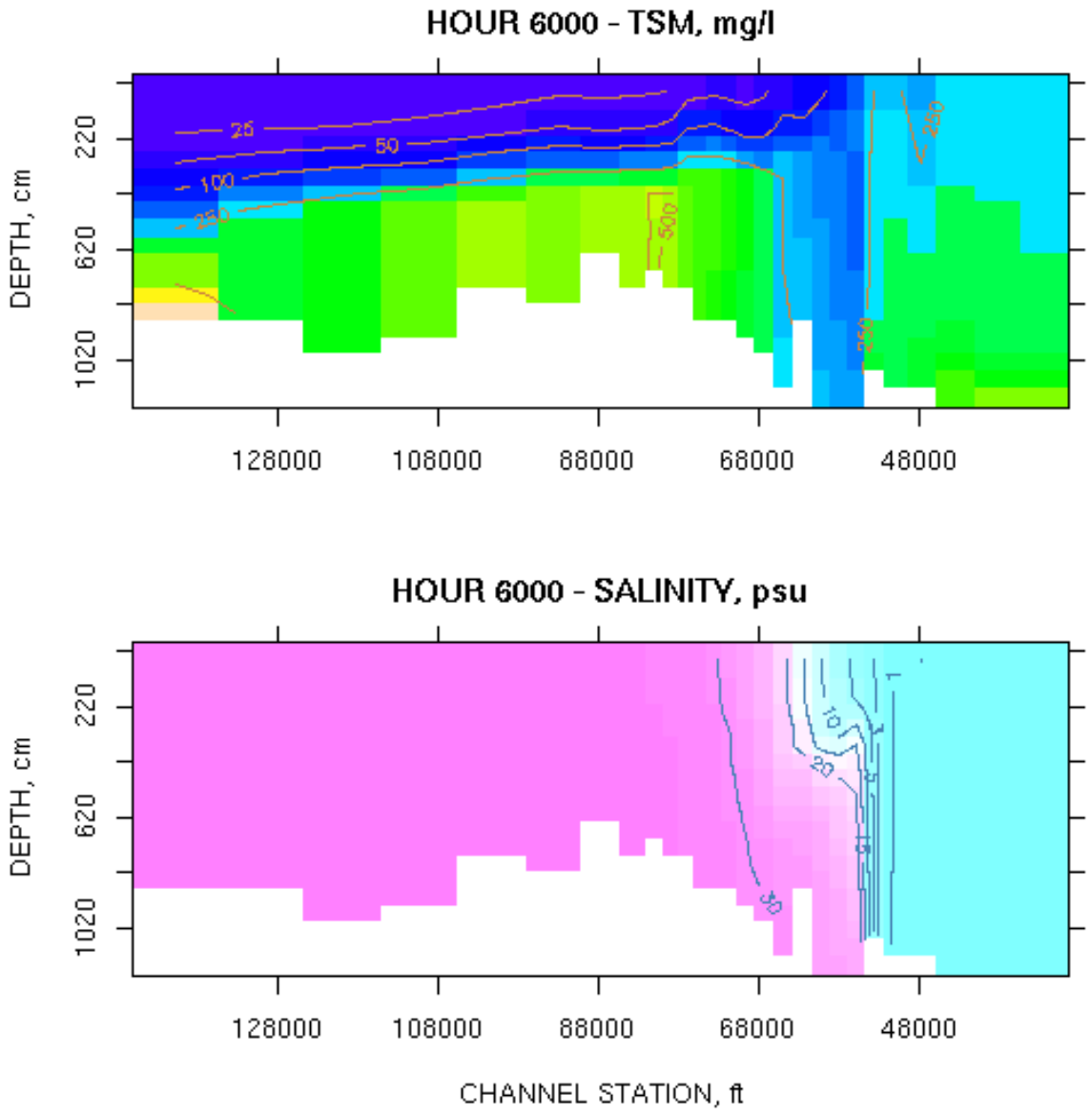

Figure 69. Channel profile snapshots of TSM and salinity for 38 ft existing channel at hour 6,000

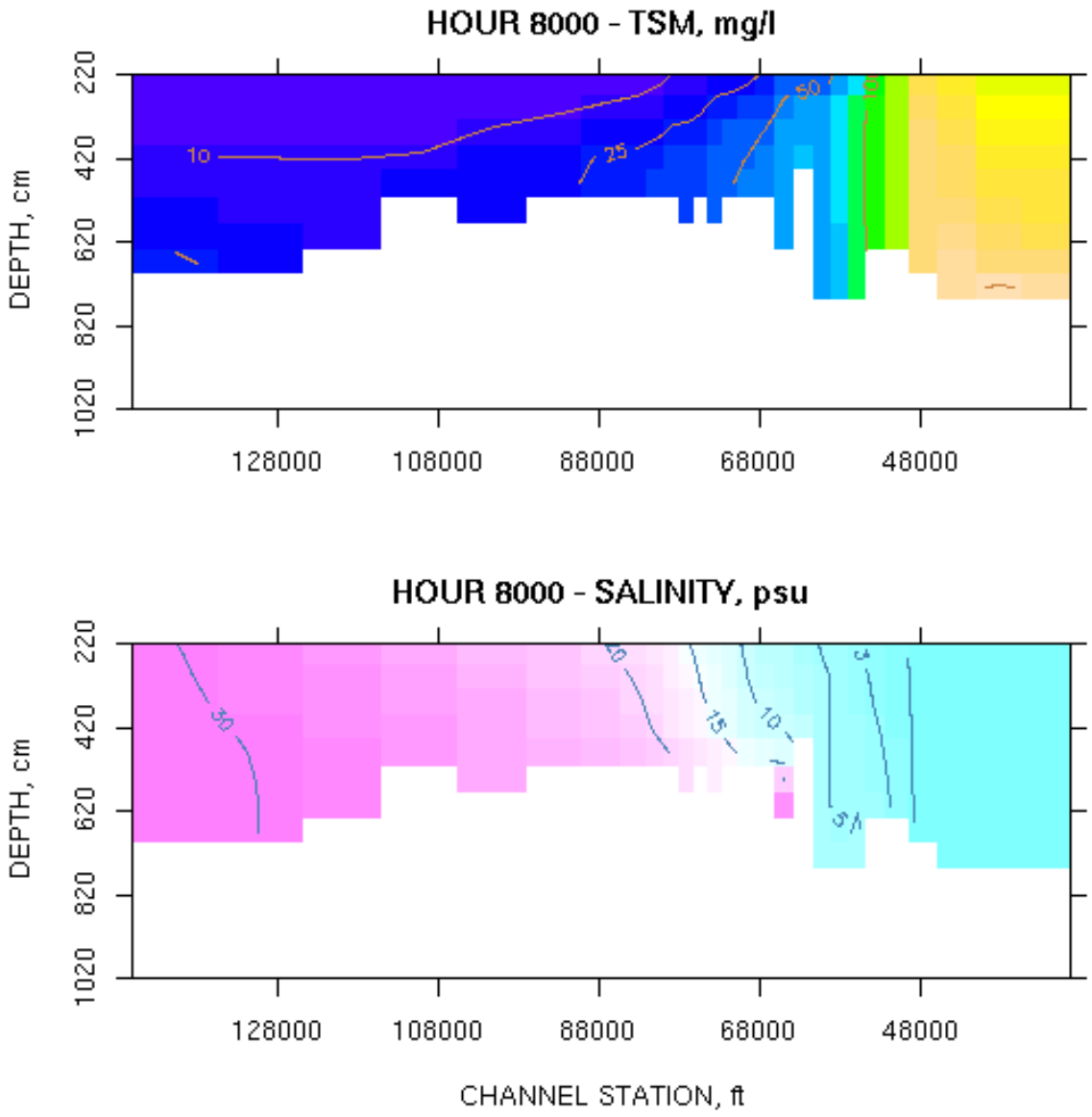

Figure 70. Channel profile snapshots of TSM and salinity for 24 ft existing channel at hour 8,000

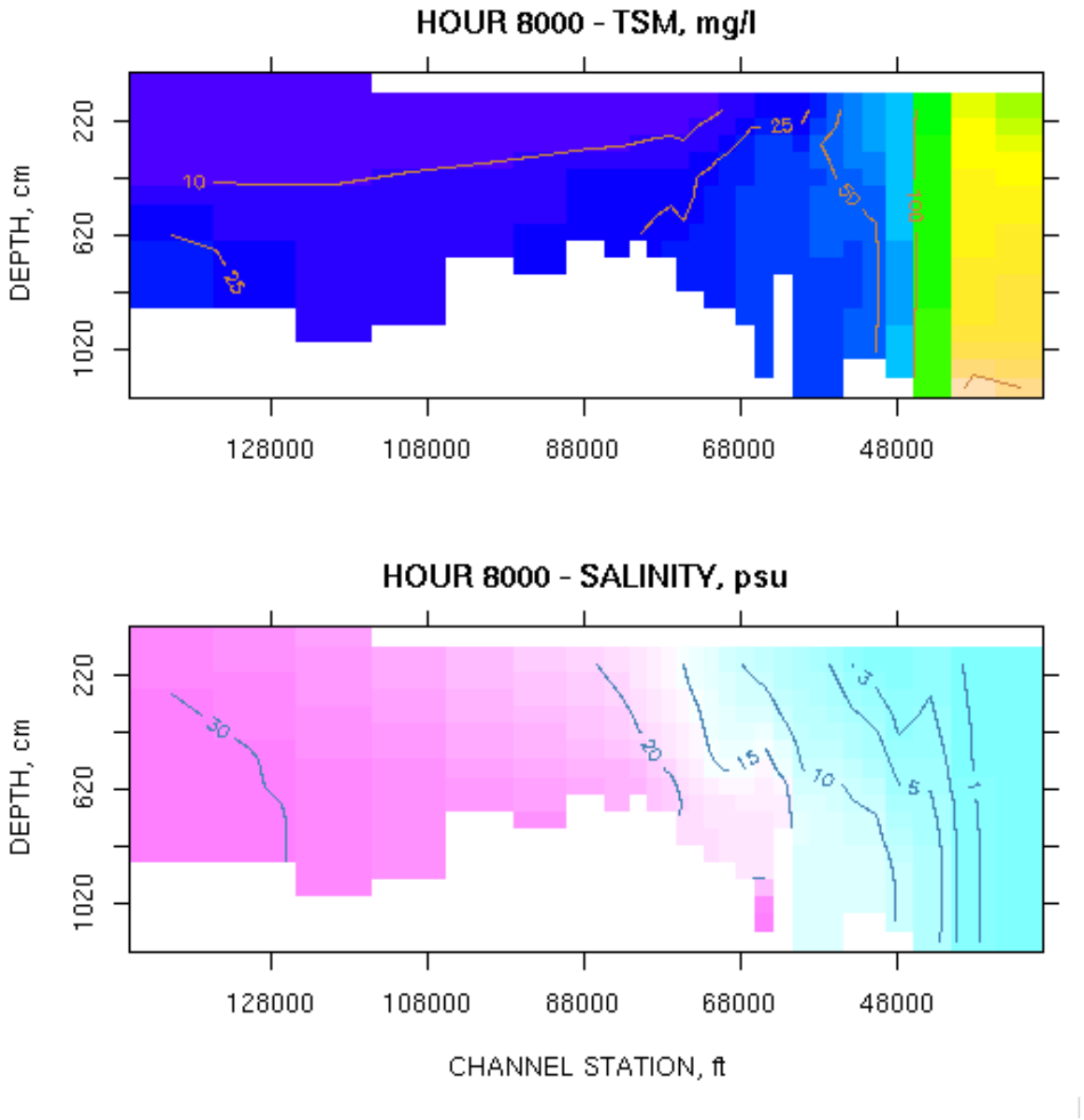

Figure 71. Channel profile snapshots of TSM and salinity for 38 ft existing channel at hour 8,000

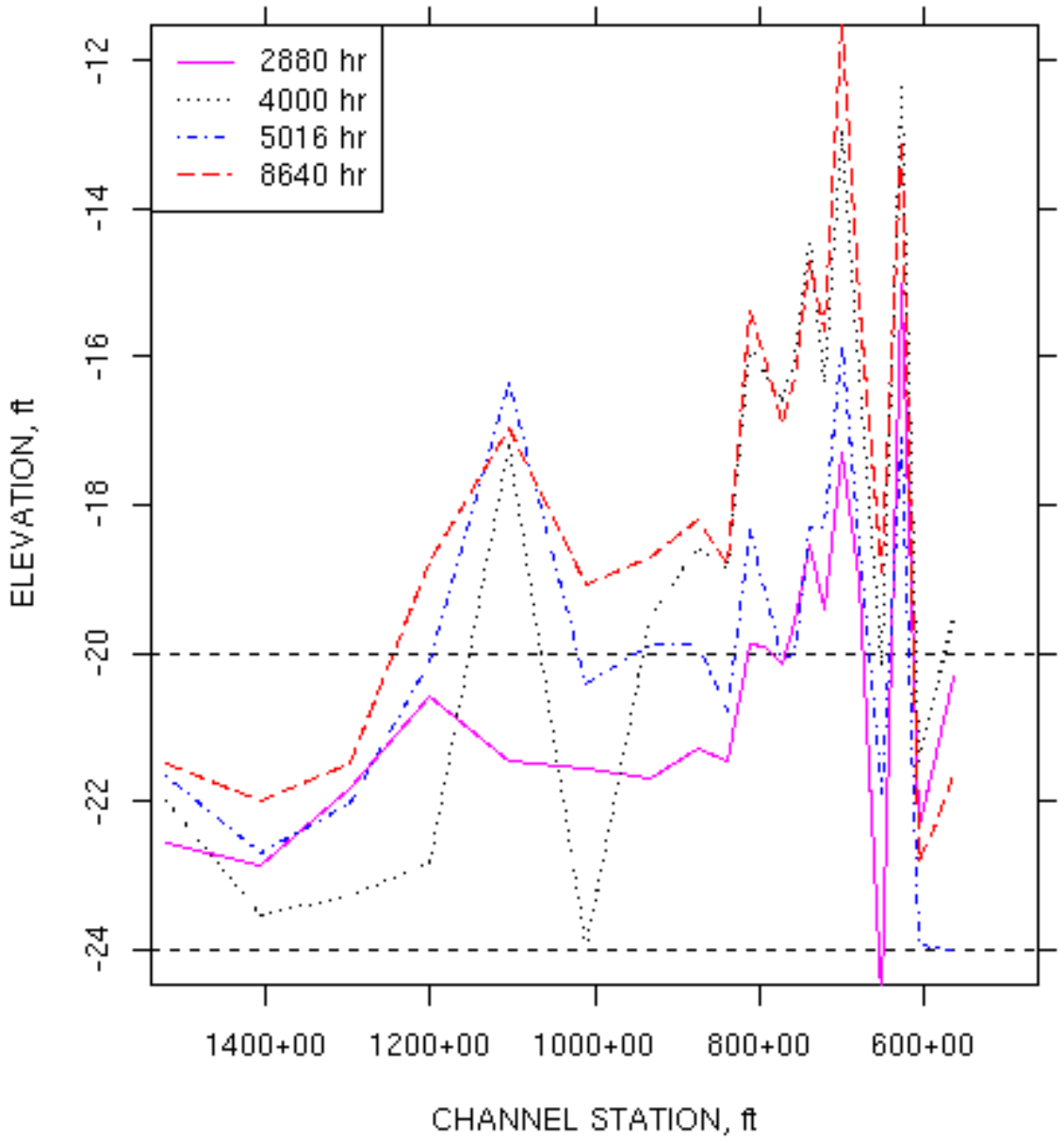

Figure 72. Shoal profiles for 24-ft-deep channel with existing conditions

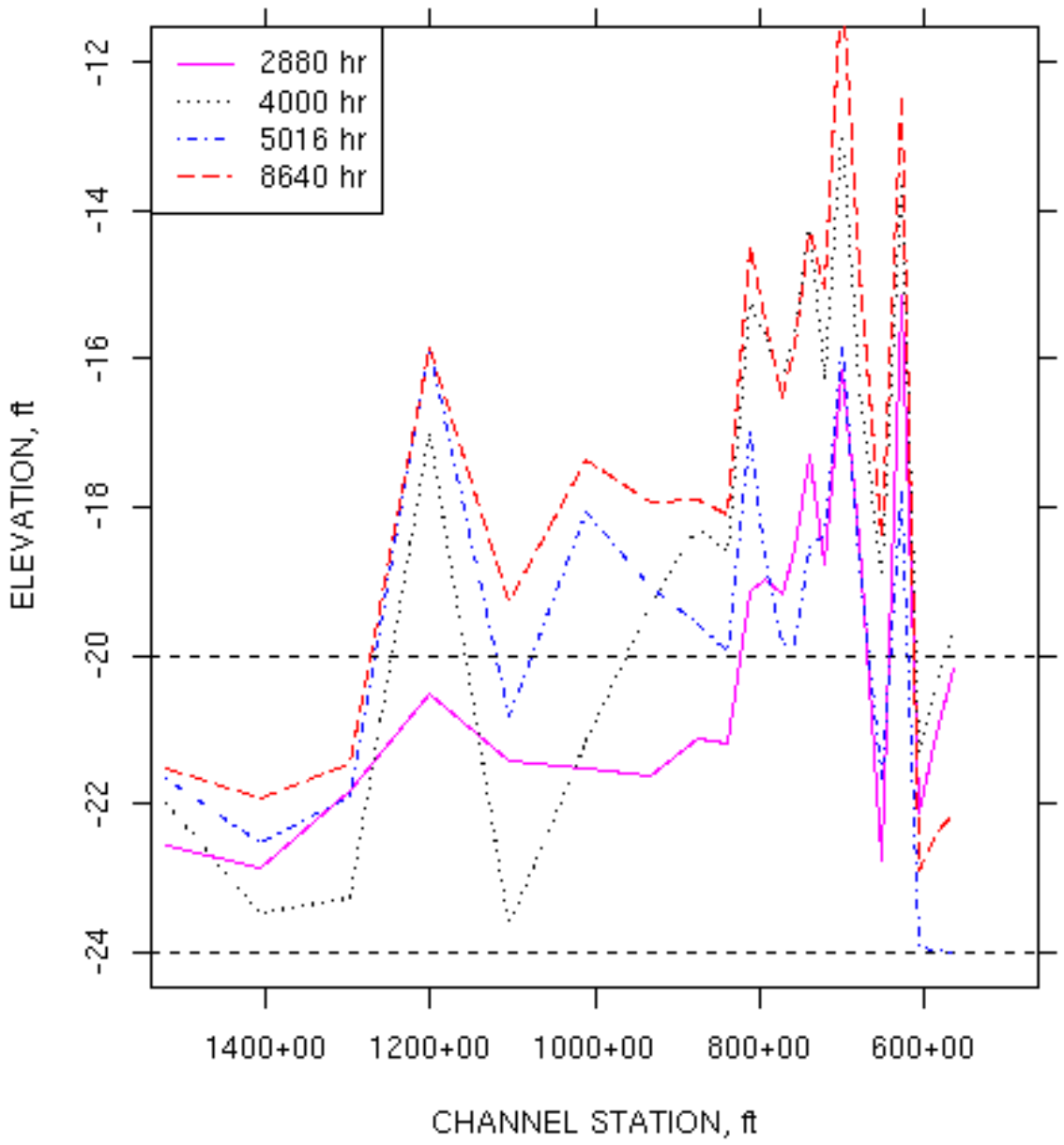

Figure 73. Shoal profiles for 24-ft-deep channel with future conditions

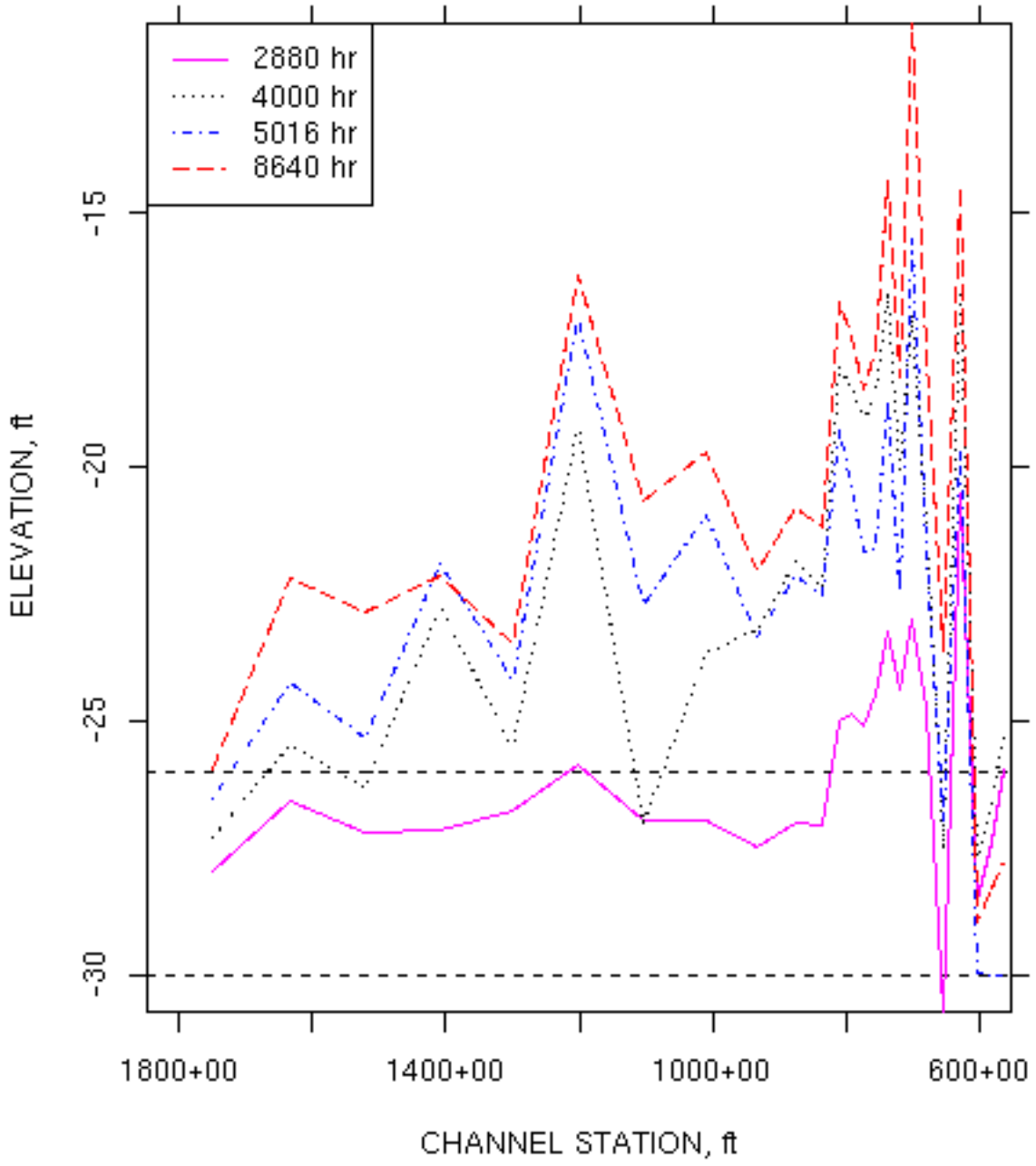

Figure 74. Shoal profiles for 30-ft-deep channel with existing conditions

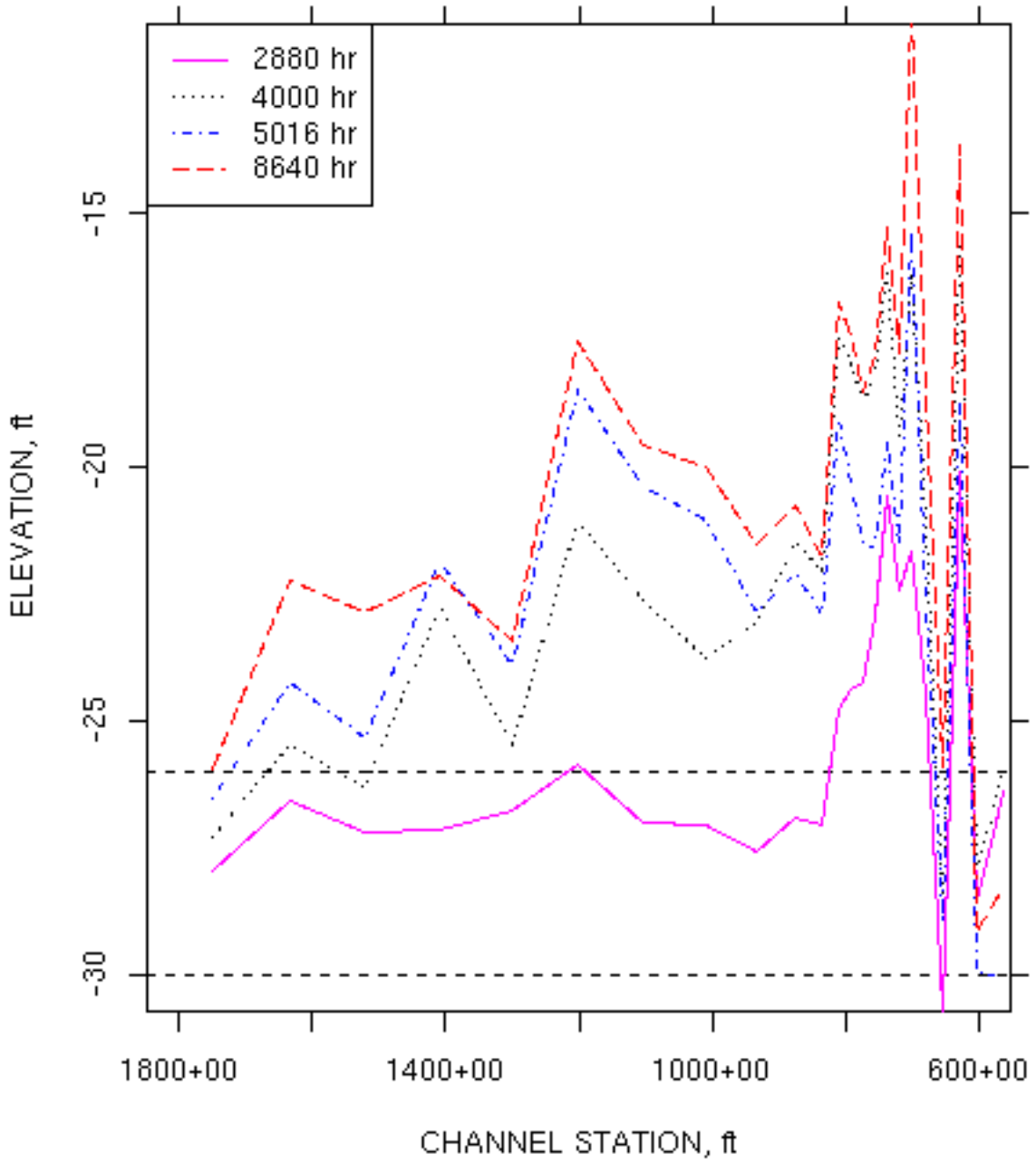

Figure 75. Shoal profiles for 30-ft-deep channel with future conditions

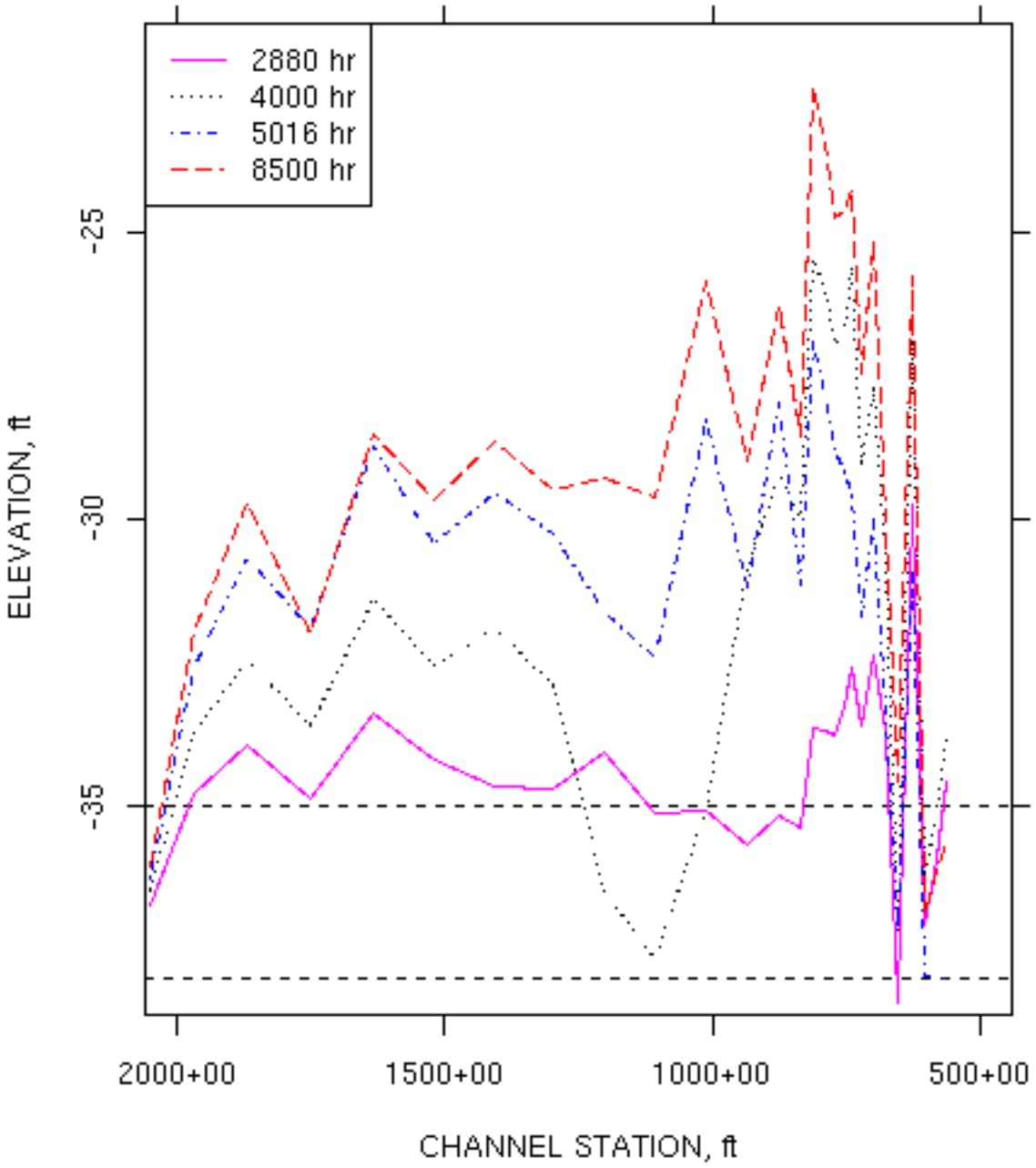

Figure 76. Shoal profiles for 38-ft-deep channel with existing conditions

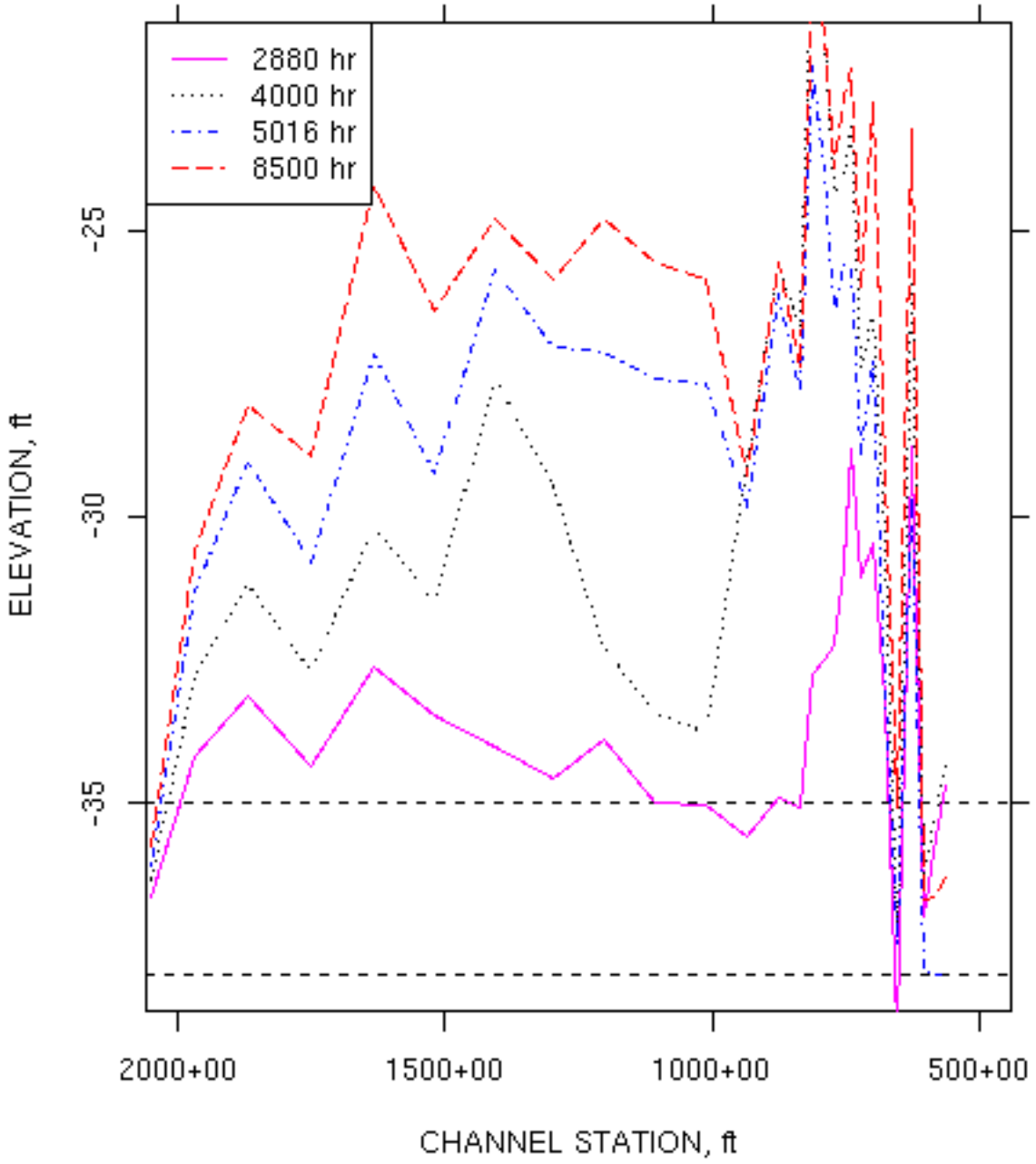

Figure 77. Shoal profiles for 38-ft-deep channel with future conditions

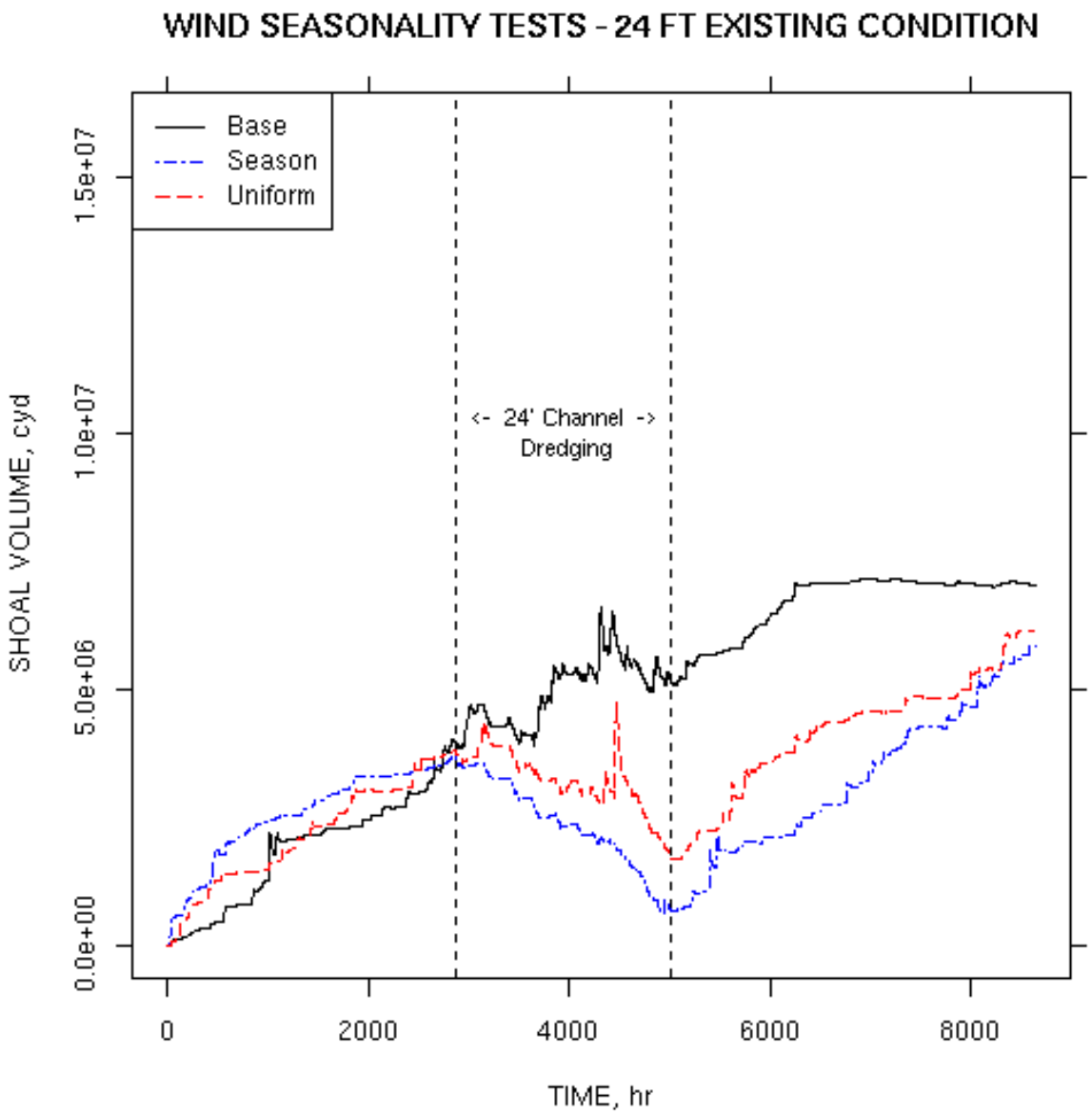

Figure 78. Wind-seasonality sensitivity test shoal histories with 24-ft-deep channels

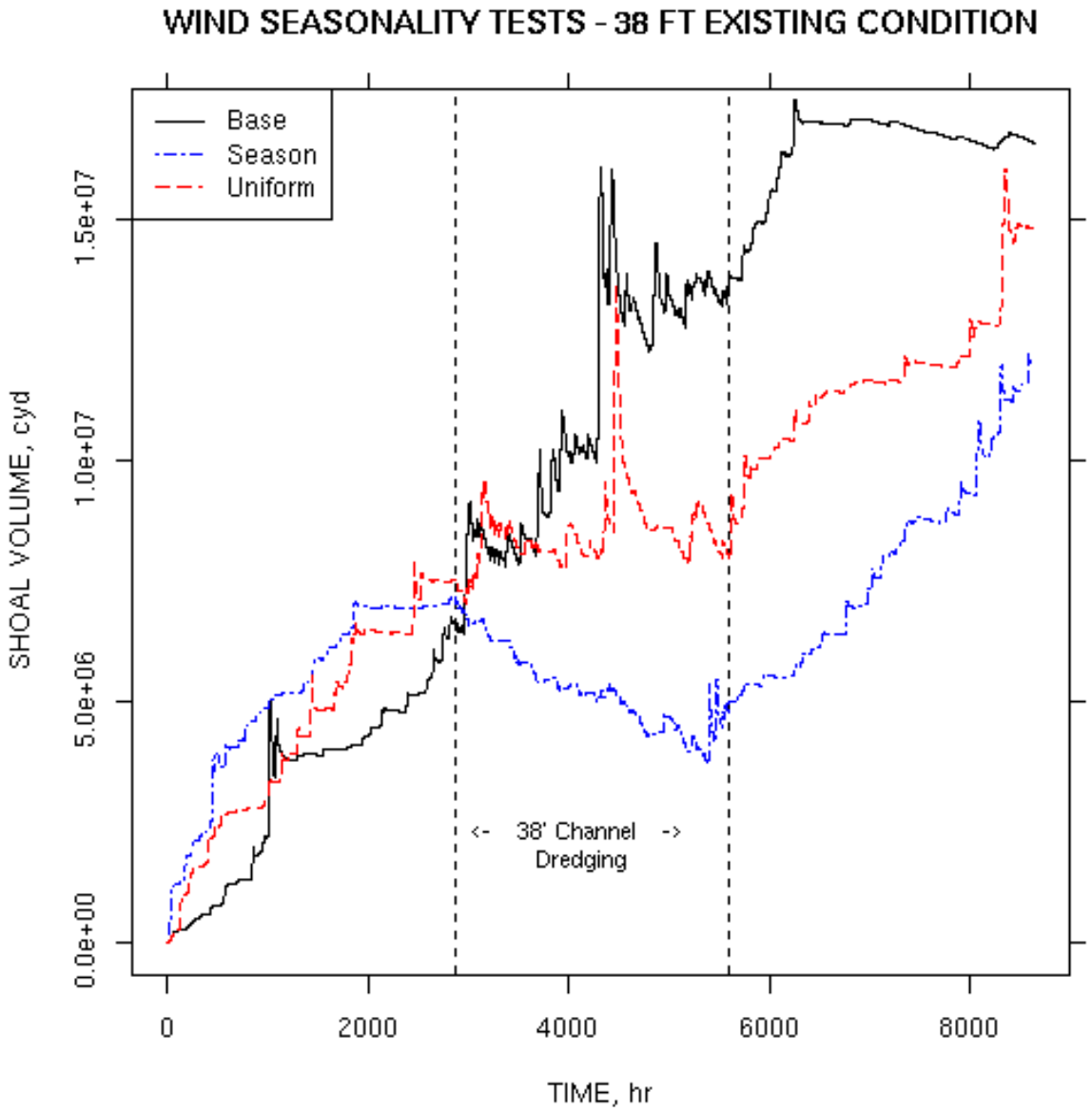

Figure 79. Wind-seasonality sensitivity test shoal histories with 38-ft-deep channels

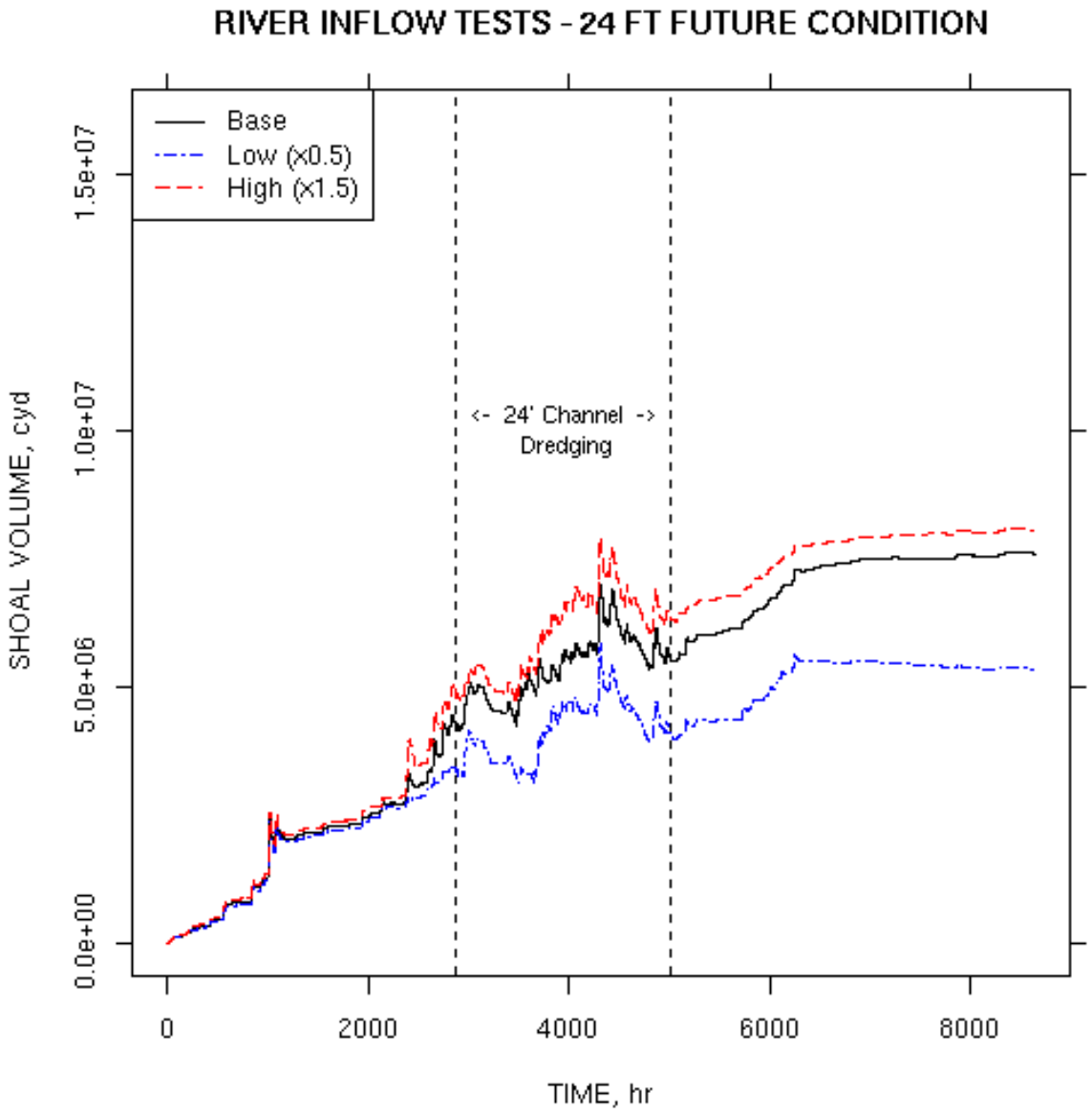

Figure 80. River inflow *Qr* sensitivity test shoal histories with 24-ft-deep channels

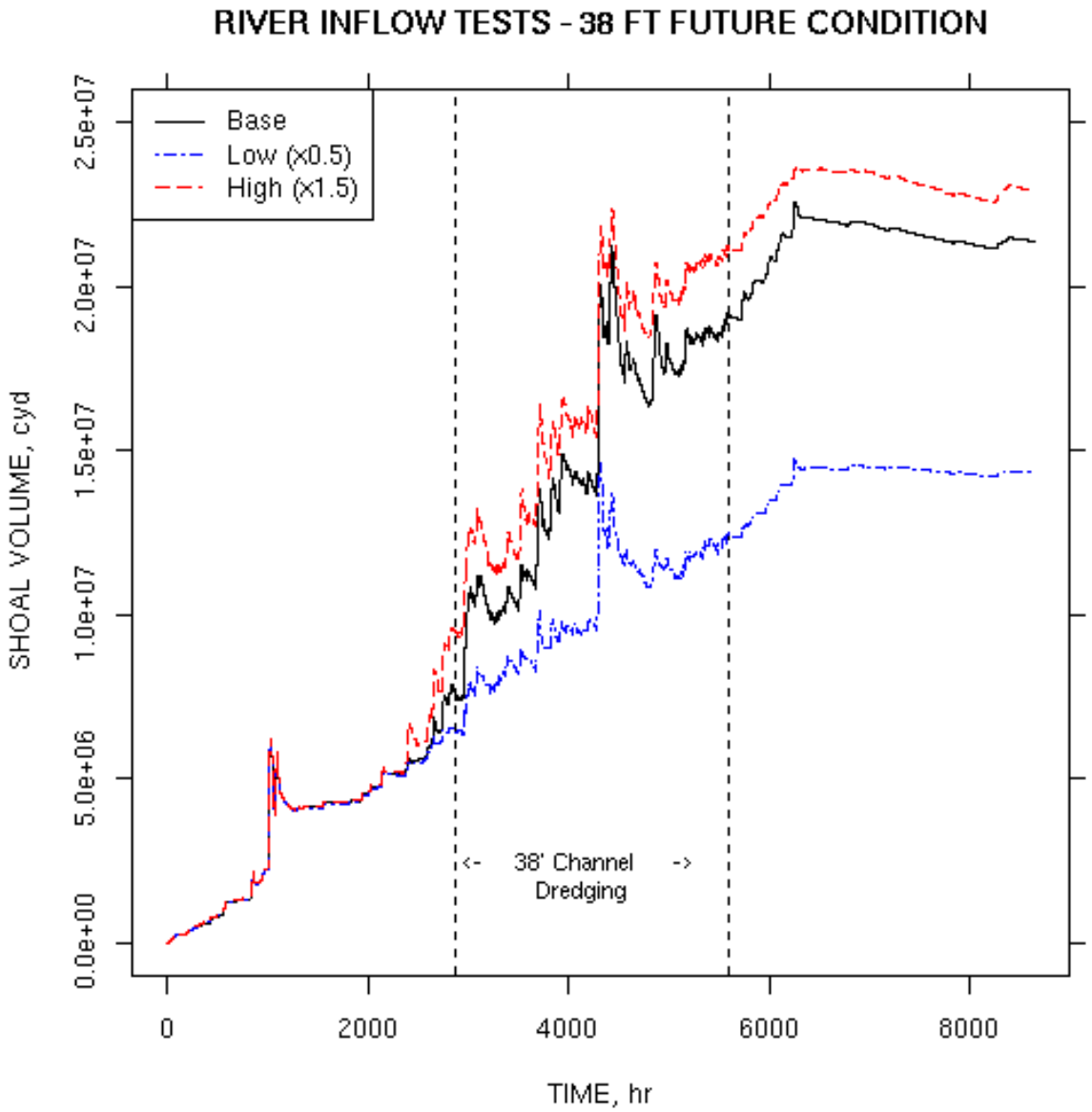

Figure 81. River inflow *Qr* sensitivity test shoal histories with 38-ft-deep channels

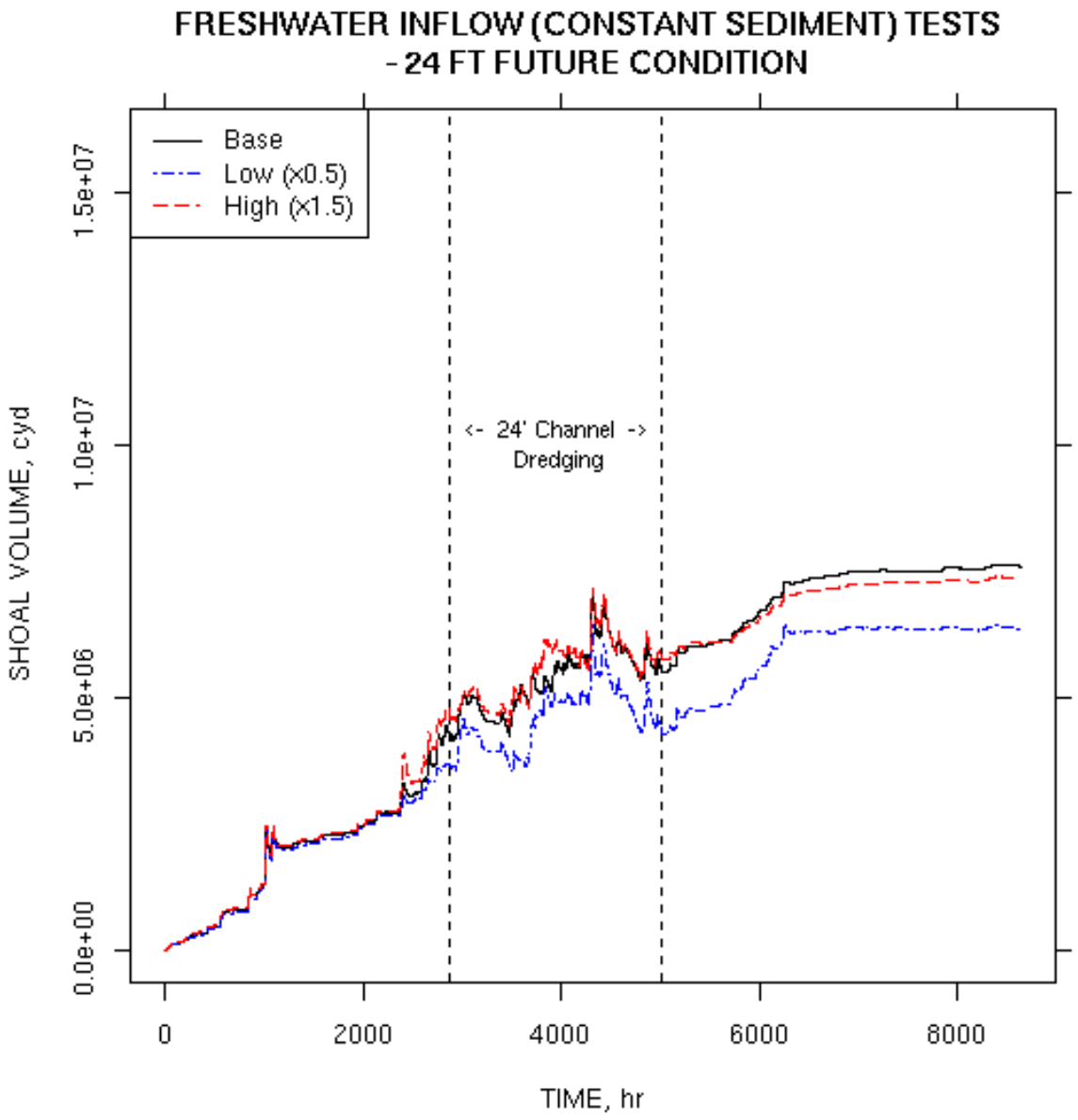

Figure 82. Freshwater inflow *Qf* sensitivity test shoal histories with 24-ft-deep channels

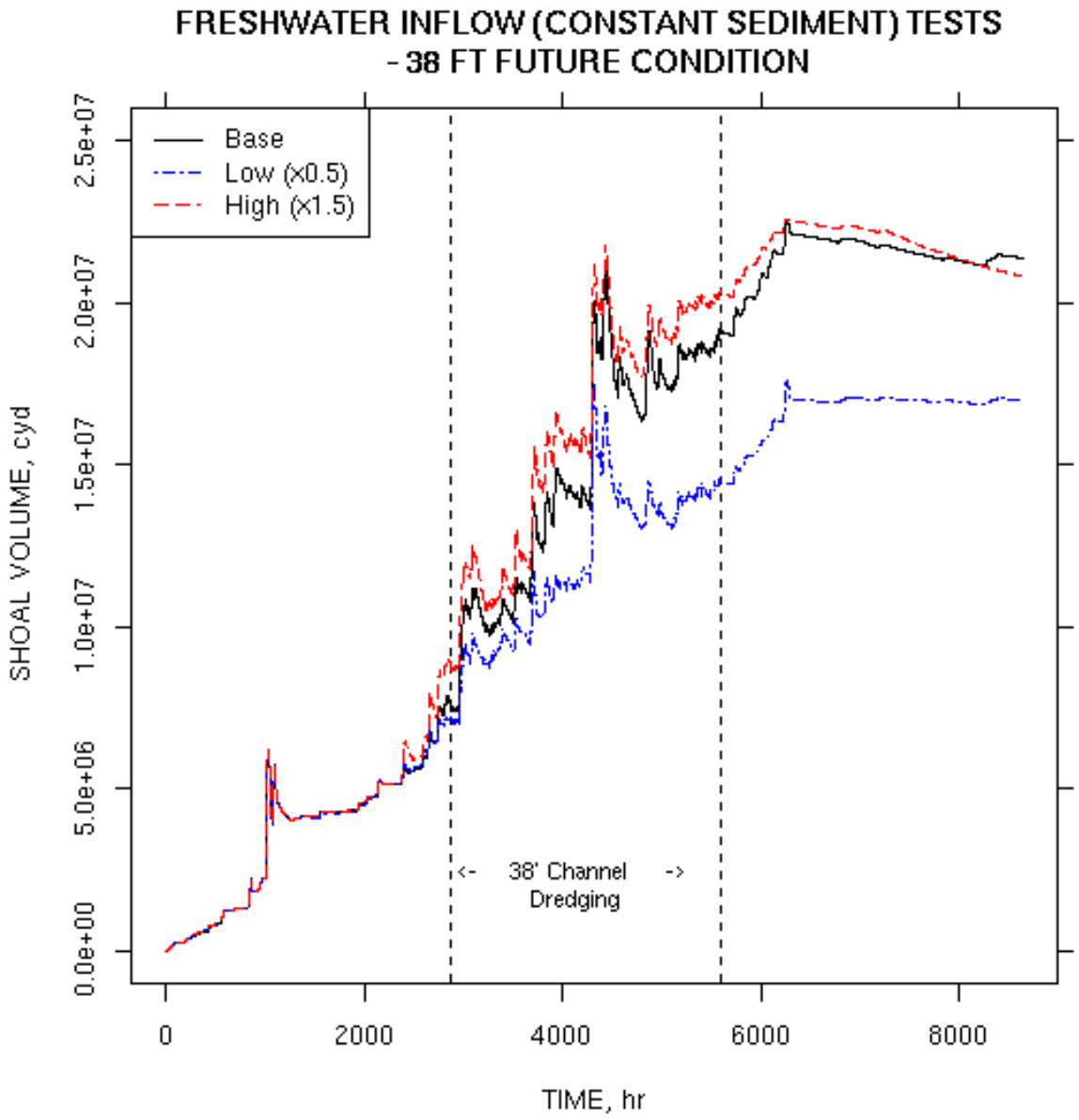

Figure 83. Freshwater inflow *Qf* sensitivity test shoal histories with 38-ft-deep channels

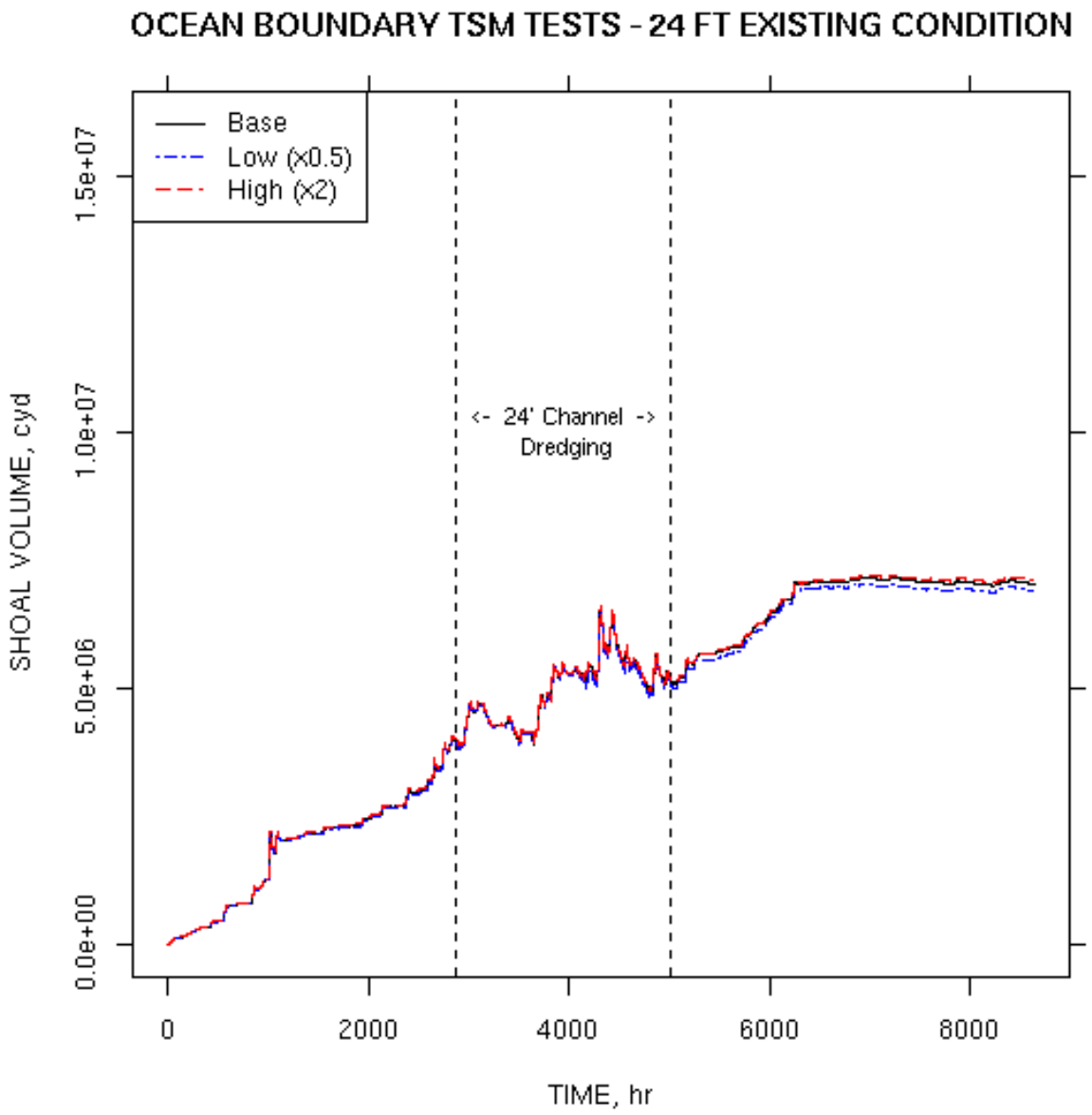

Figure 84. Ocean TSM boundary sensitivity test shoal histories with 24-ft-deep channels

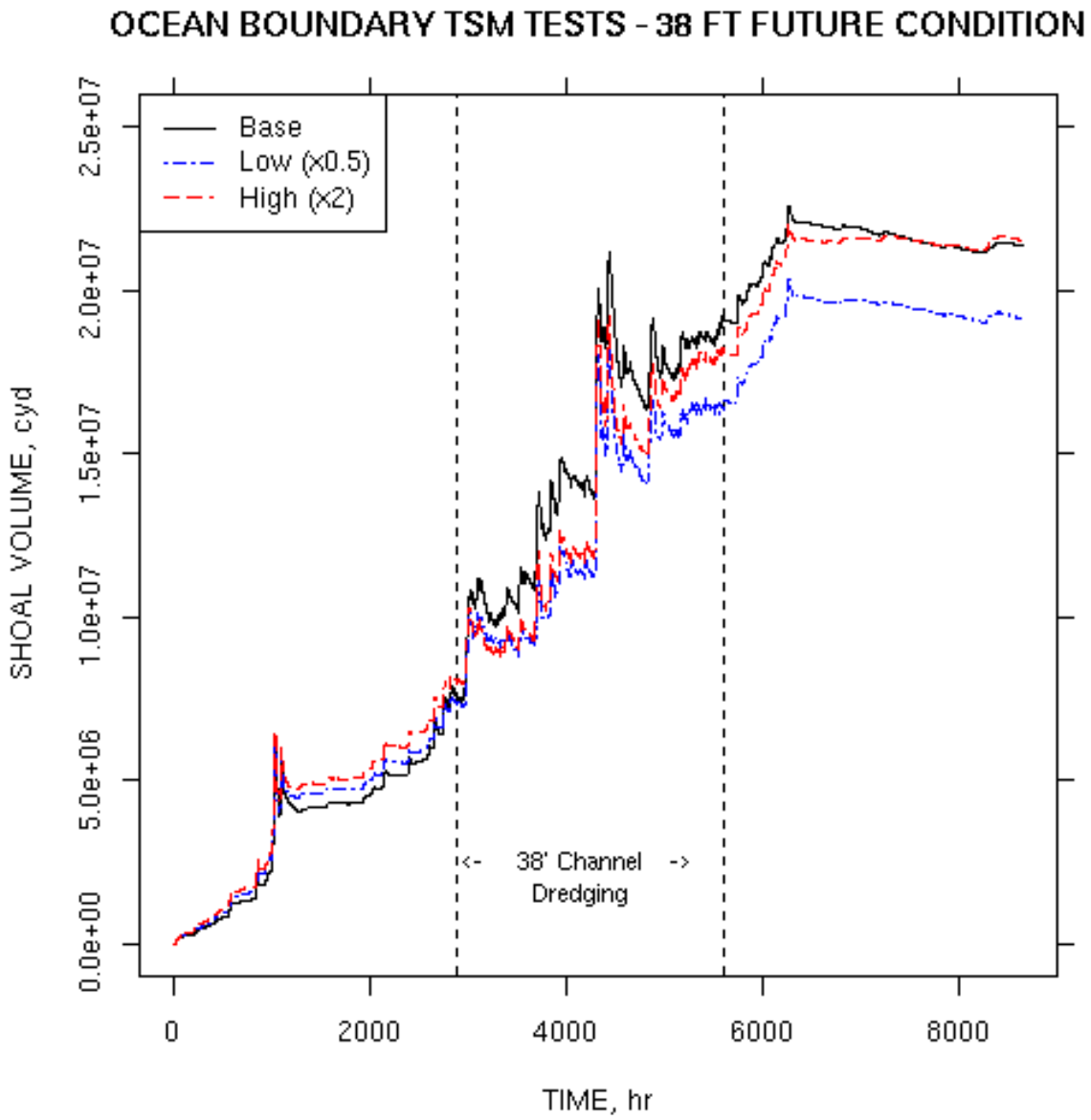

Figure 85. Ocean TSM boundary sensitivity test shoal histories with 38-ft-deep channels

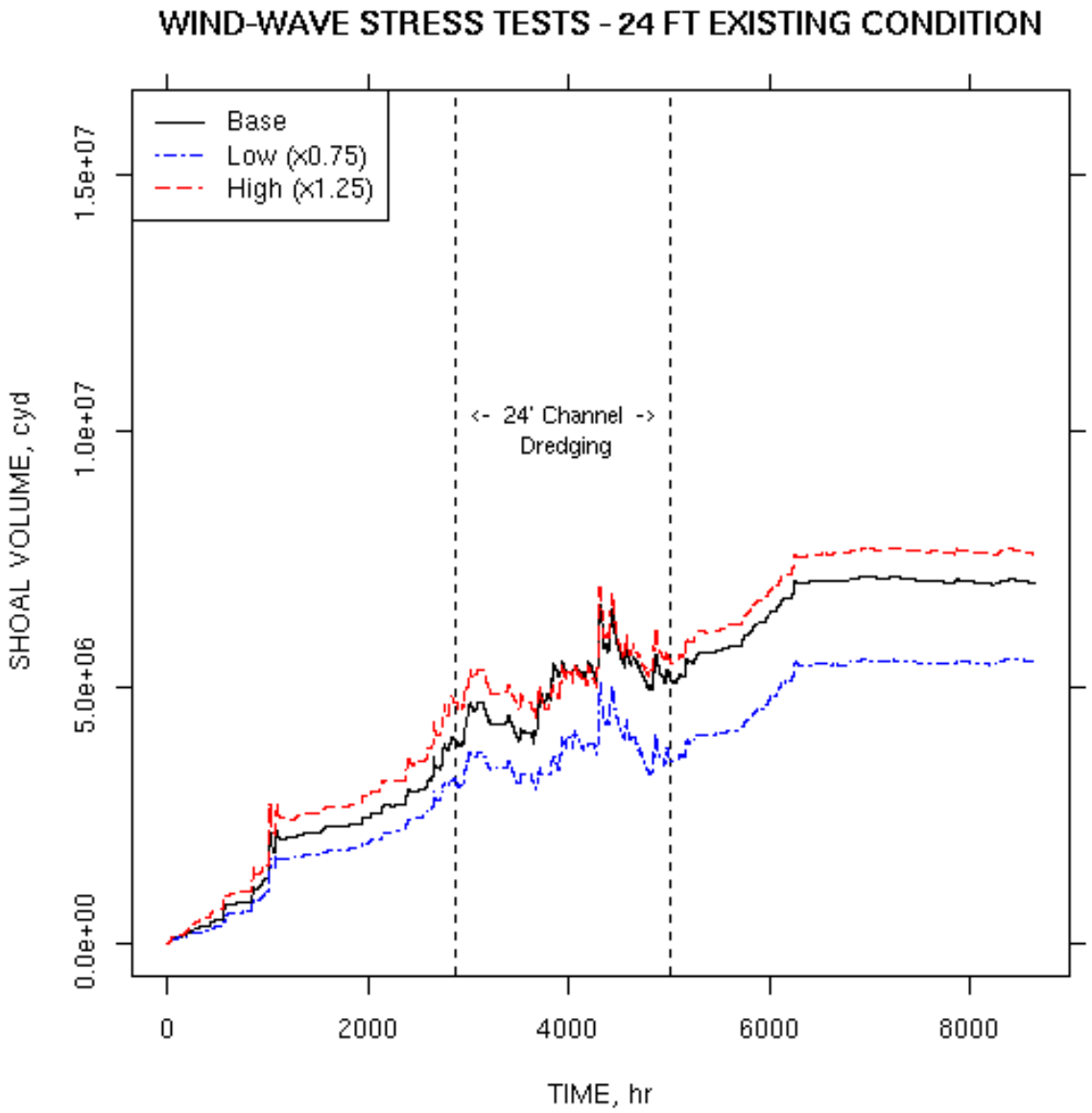

Figure 86. Wind-wave shear stress sensitivity test shoal histories for 24-ft-deep channels

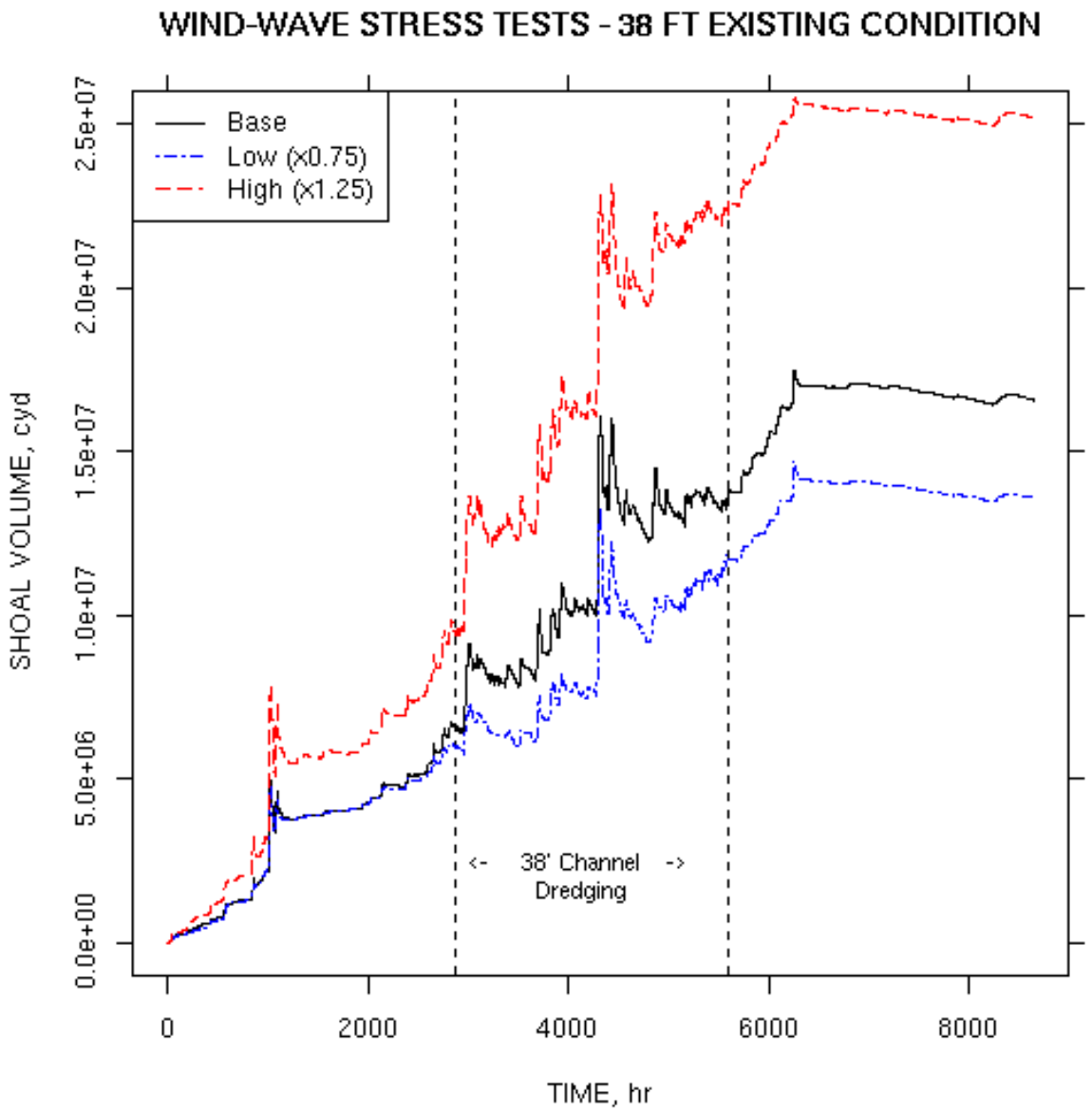

Figure 87. Wind-wave shear stress sensitivity test shoal histories for 38-ft-deep channels

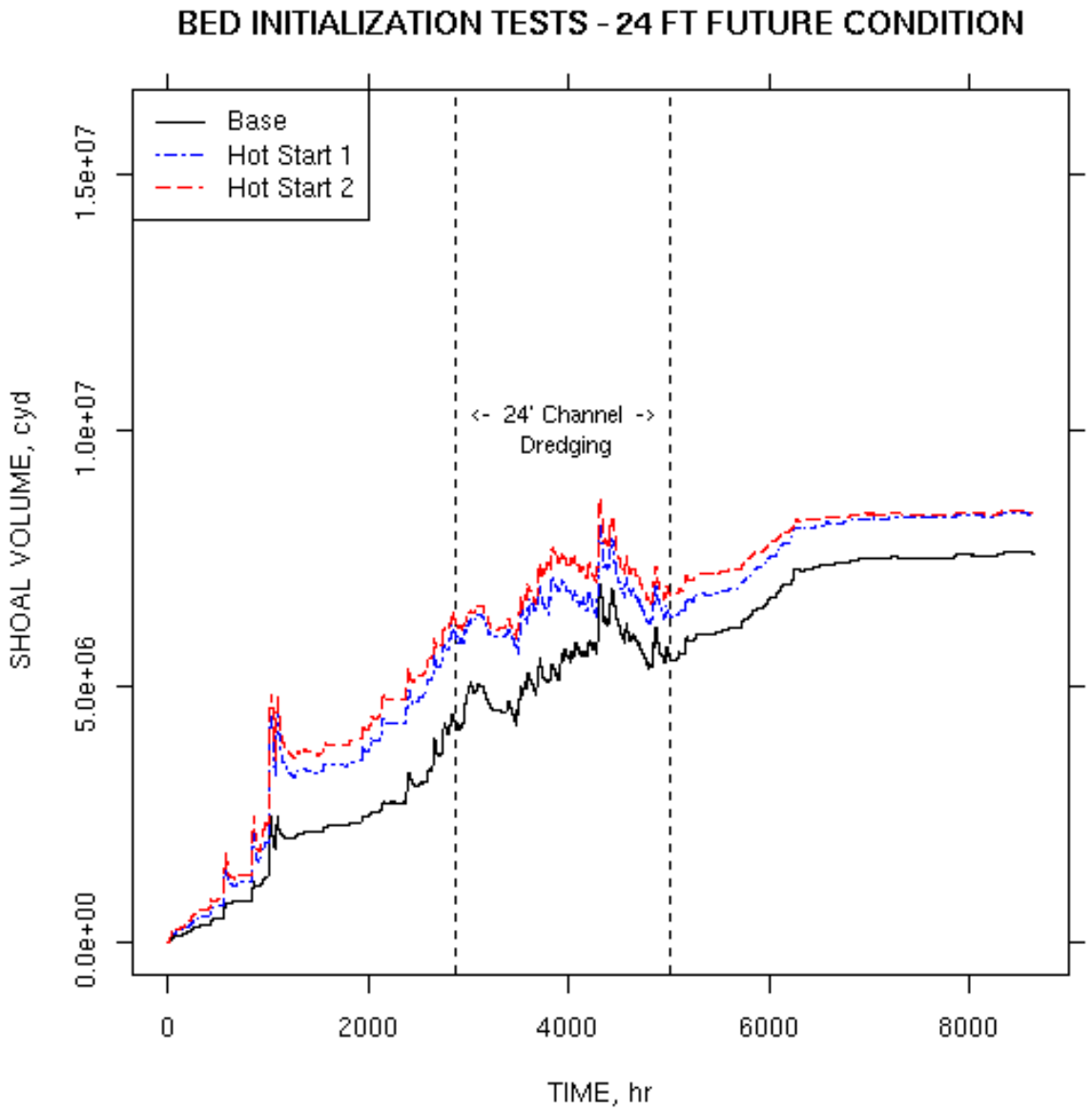

Figure 88. Bed re-initialization sensitivity test shoal histories for 24-ft-deep channels

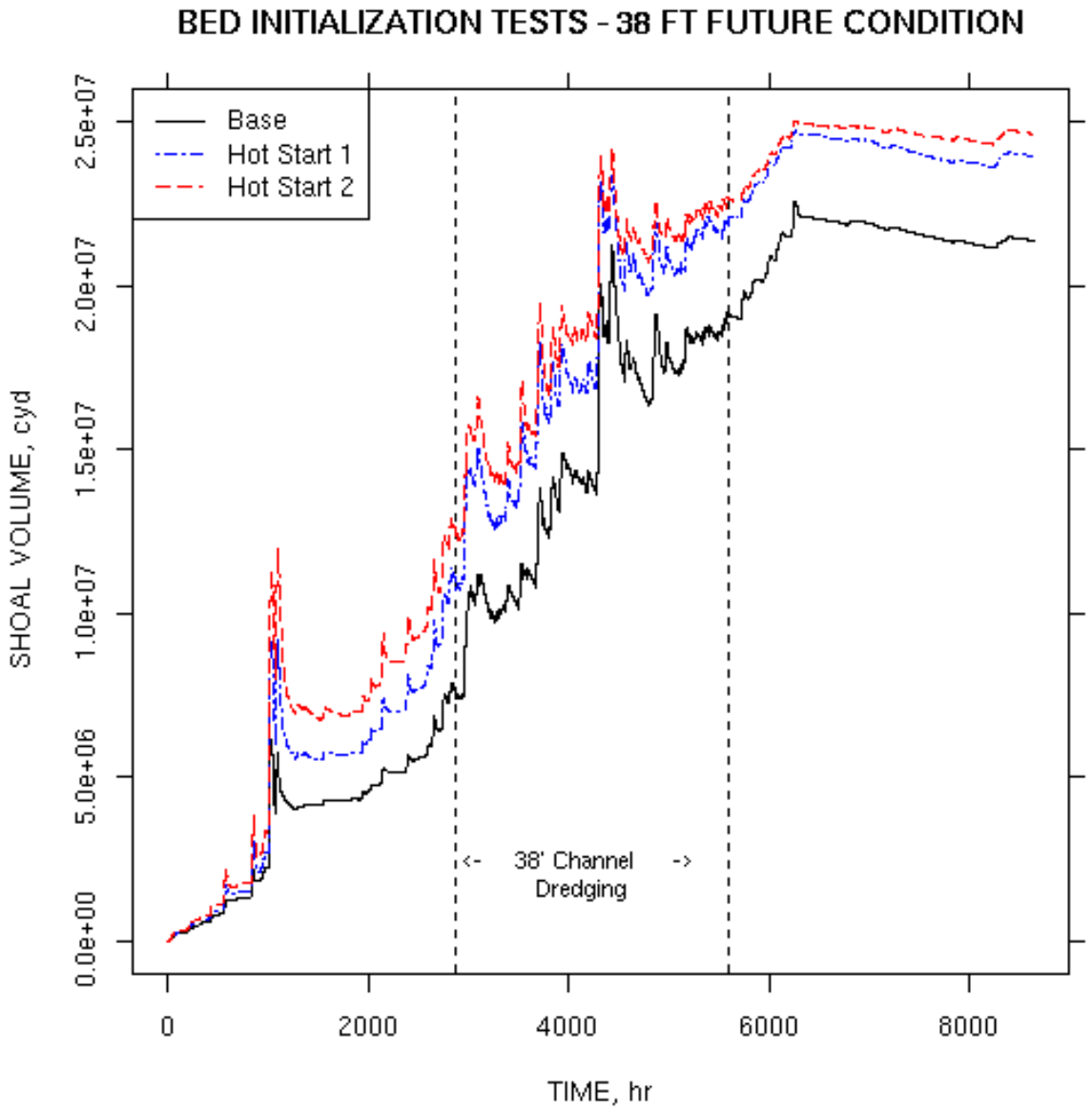

Figure 89. Bed re-initialization sensitivity test shoal histories for 38-ft-deep channels

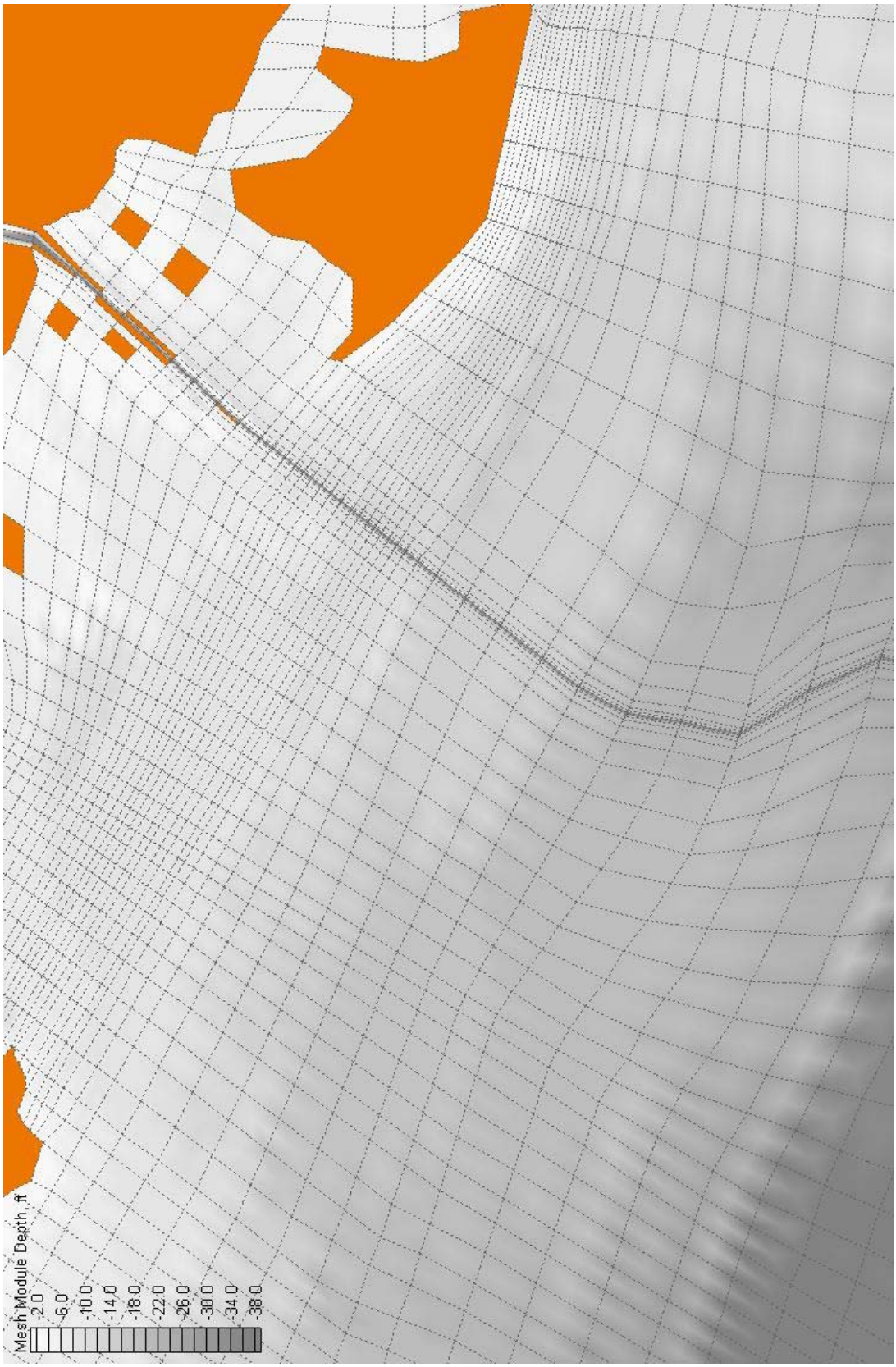

Figure 90. Curved channel grid used for sensitivity test

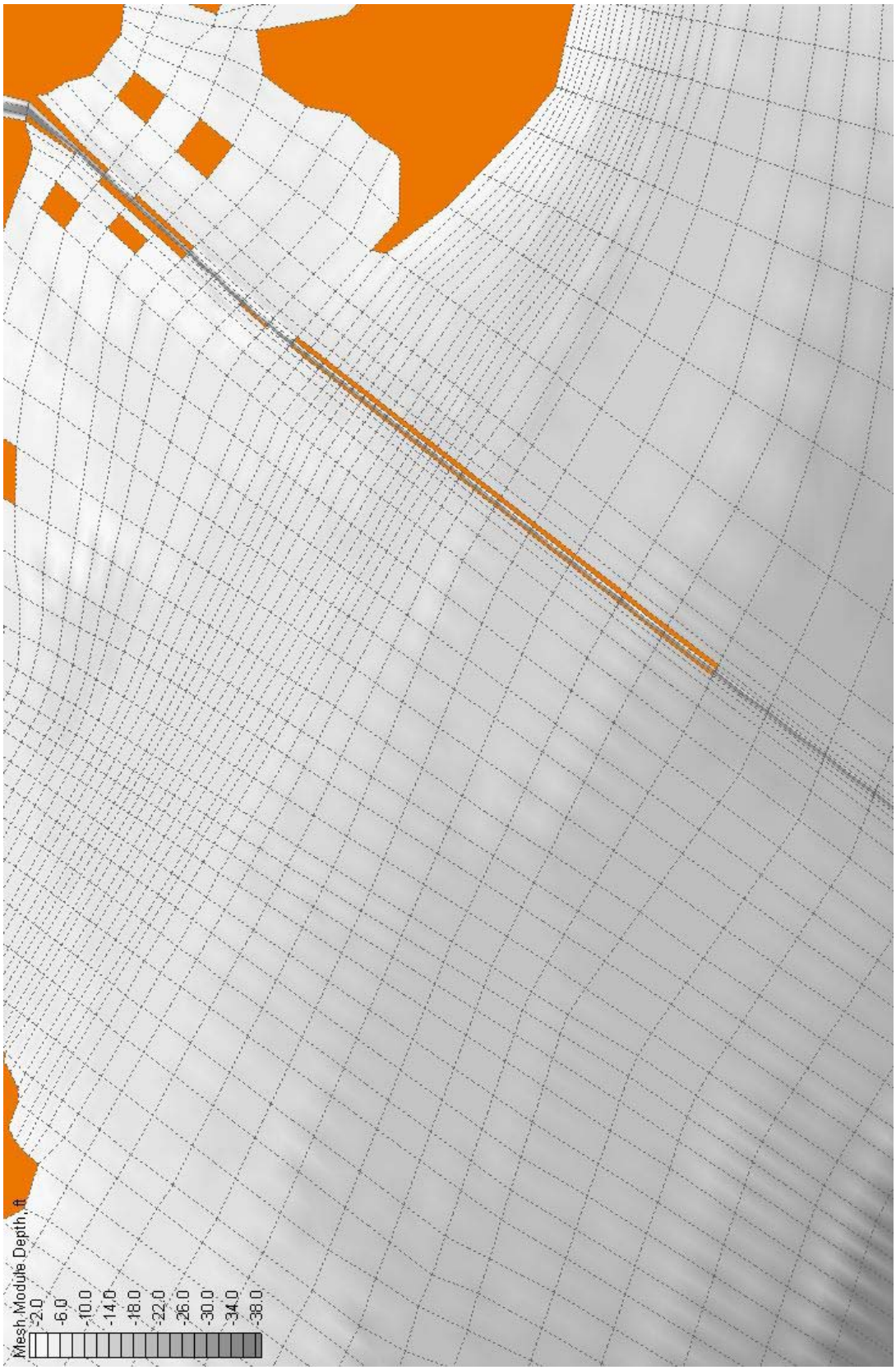

Figure 91. *Jetty1* plan configuration

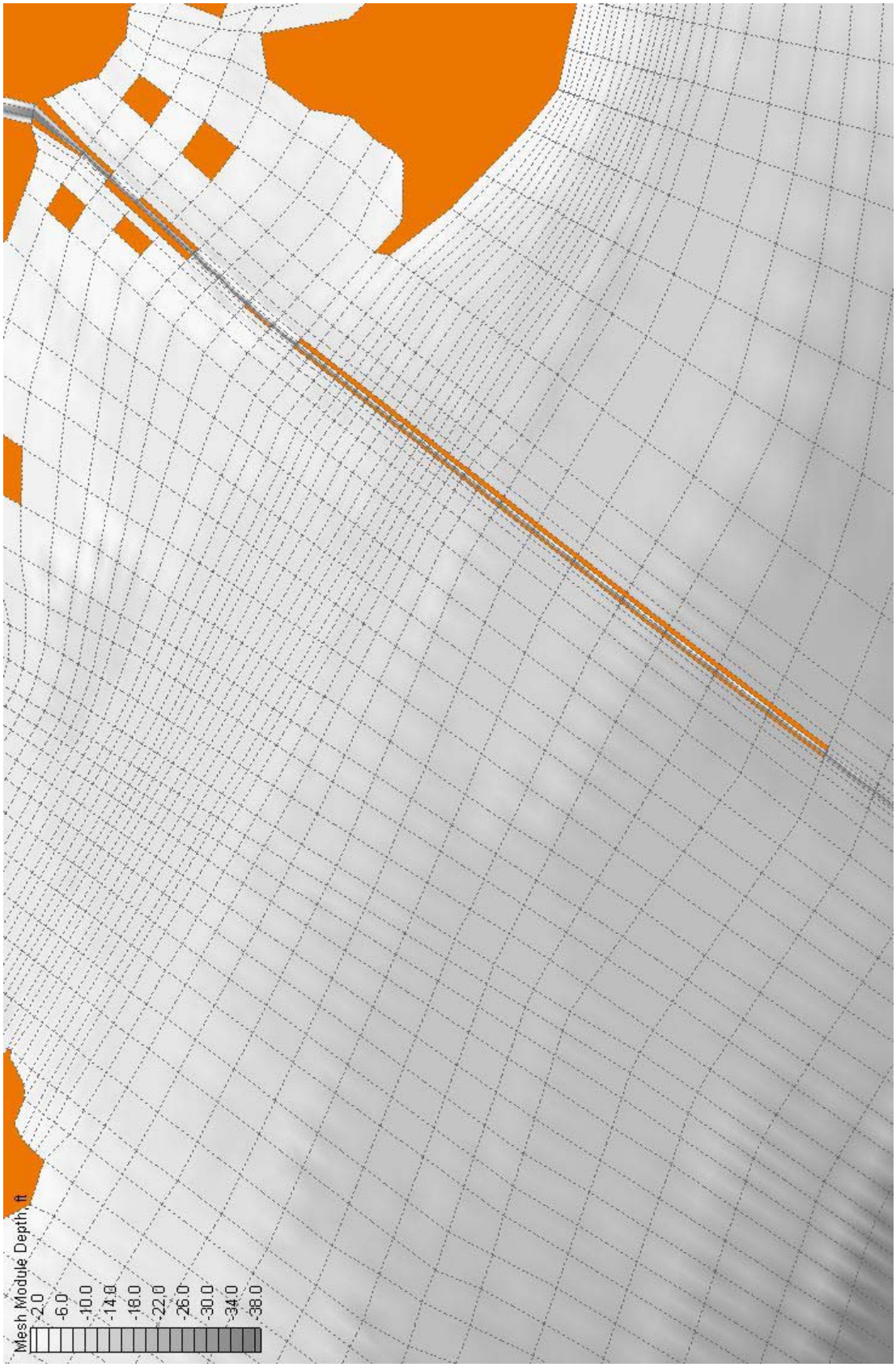

Figure 92. *Jetty2* plan configuration

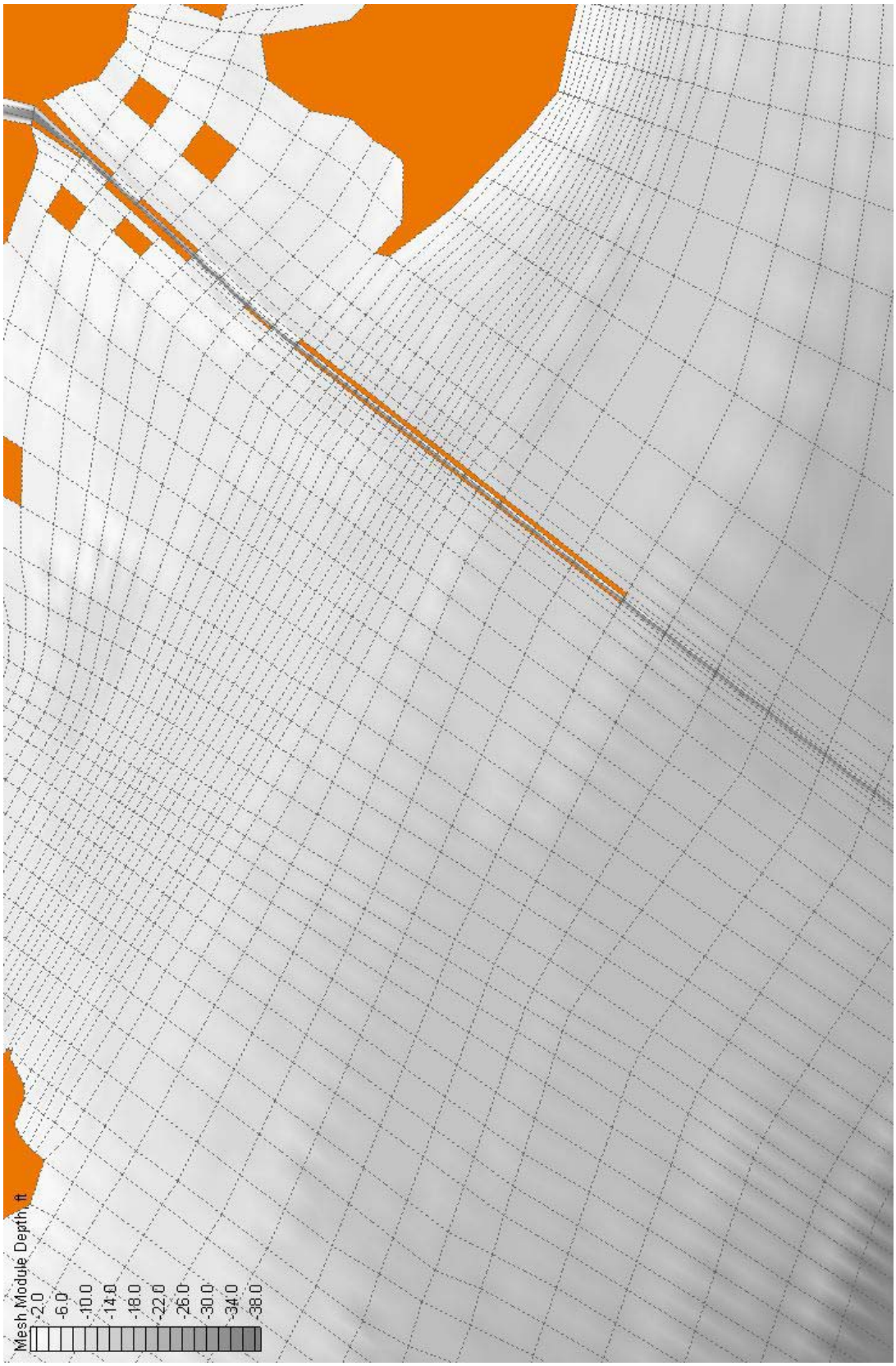

Figure 93. *Jetty3* plan configuration

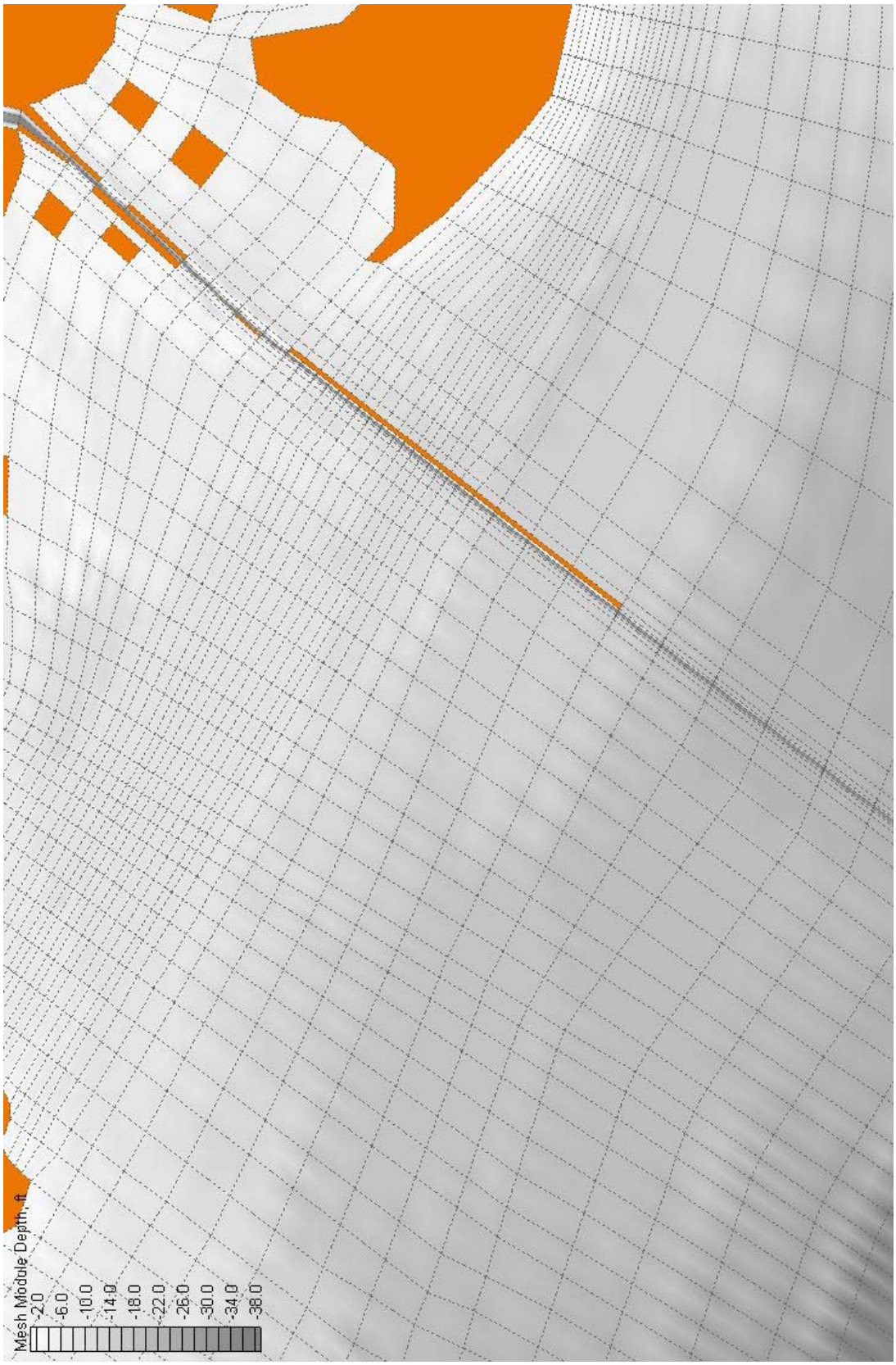

Figure 94. *Jetty4* plan configuration

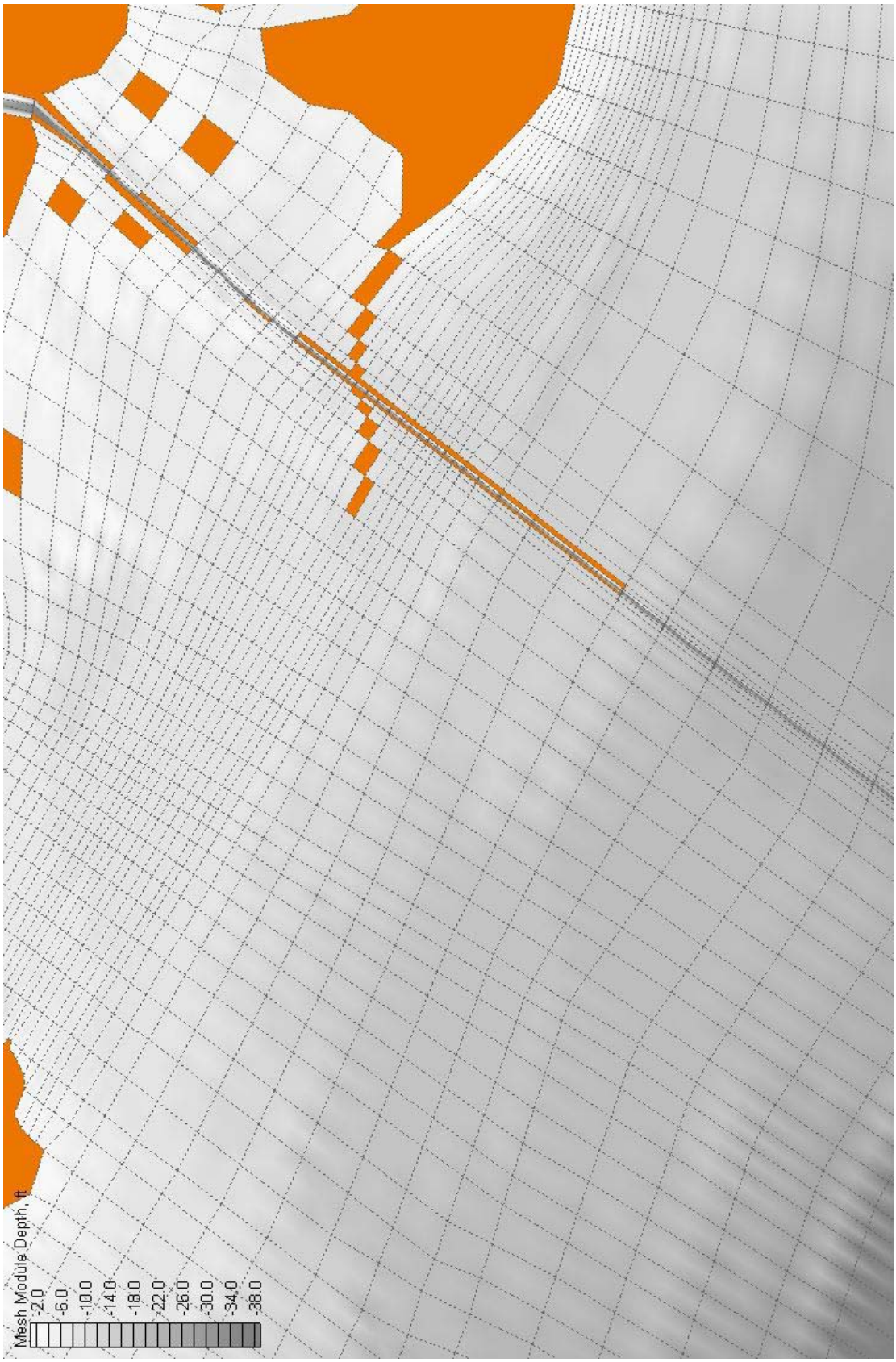

Figure 95. *RJ5* plan configuration

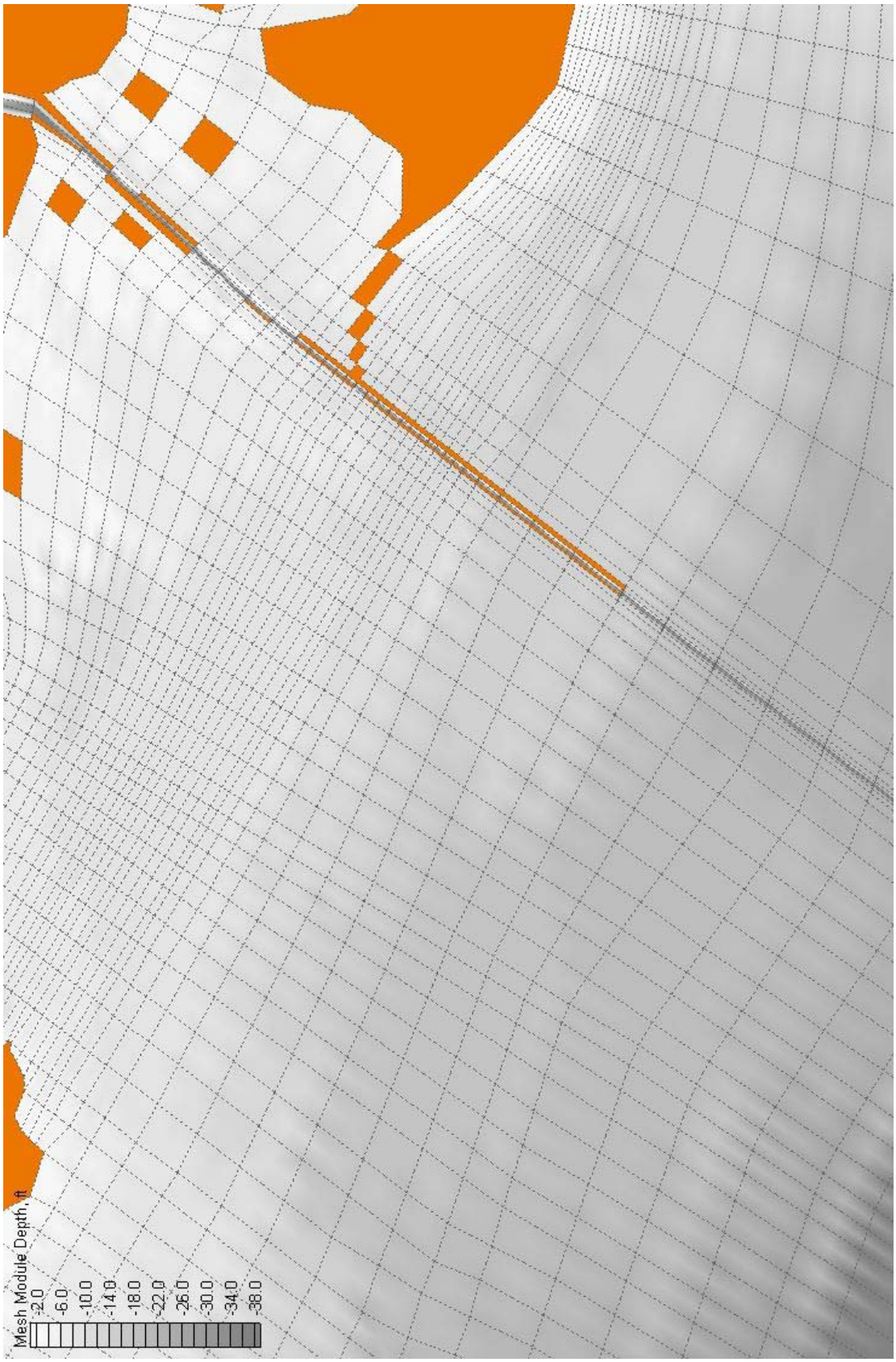

Figure 96. *RJ6* plan configuration

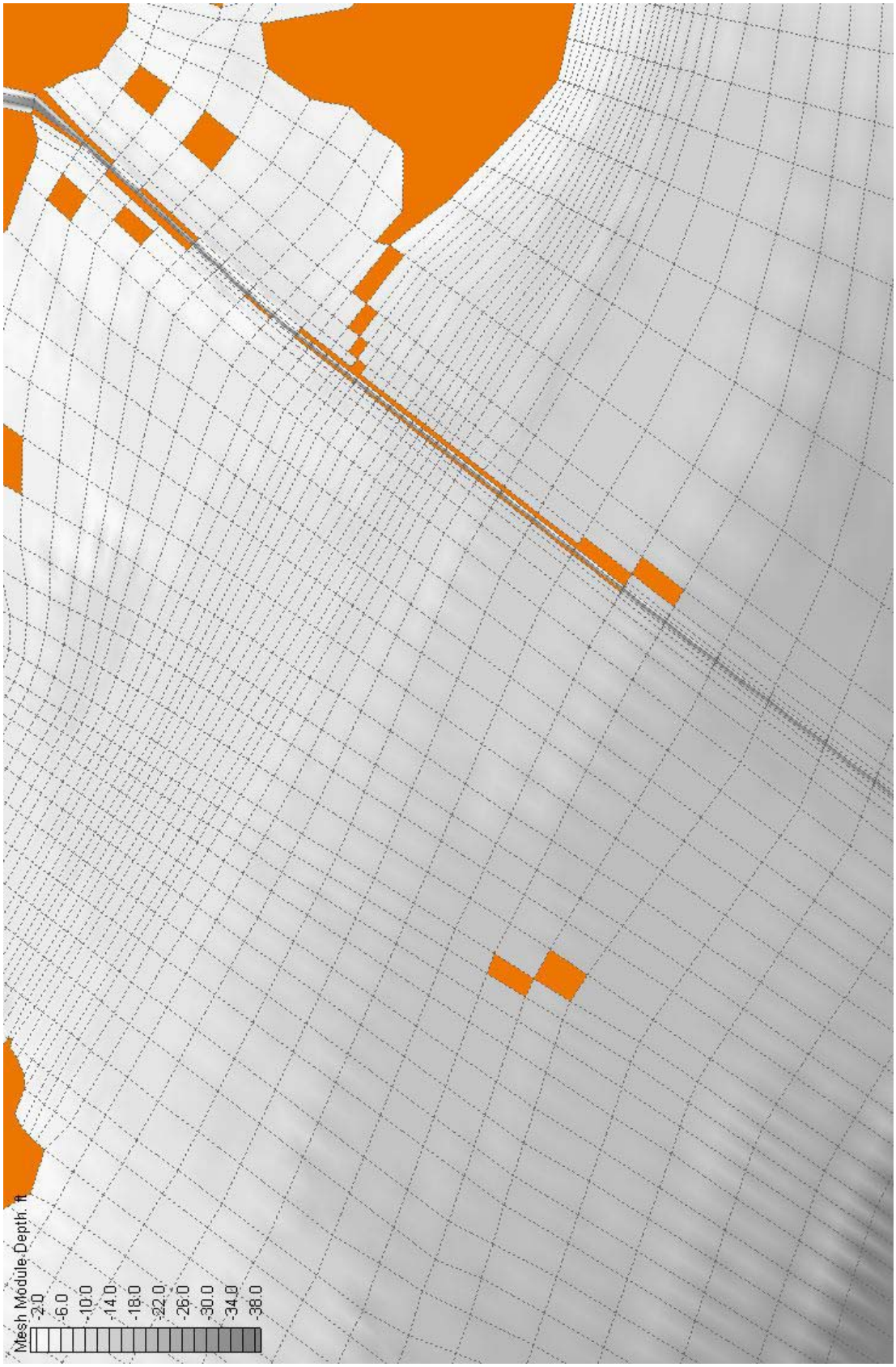

Figure 97. *RJ7* plan configuration

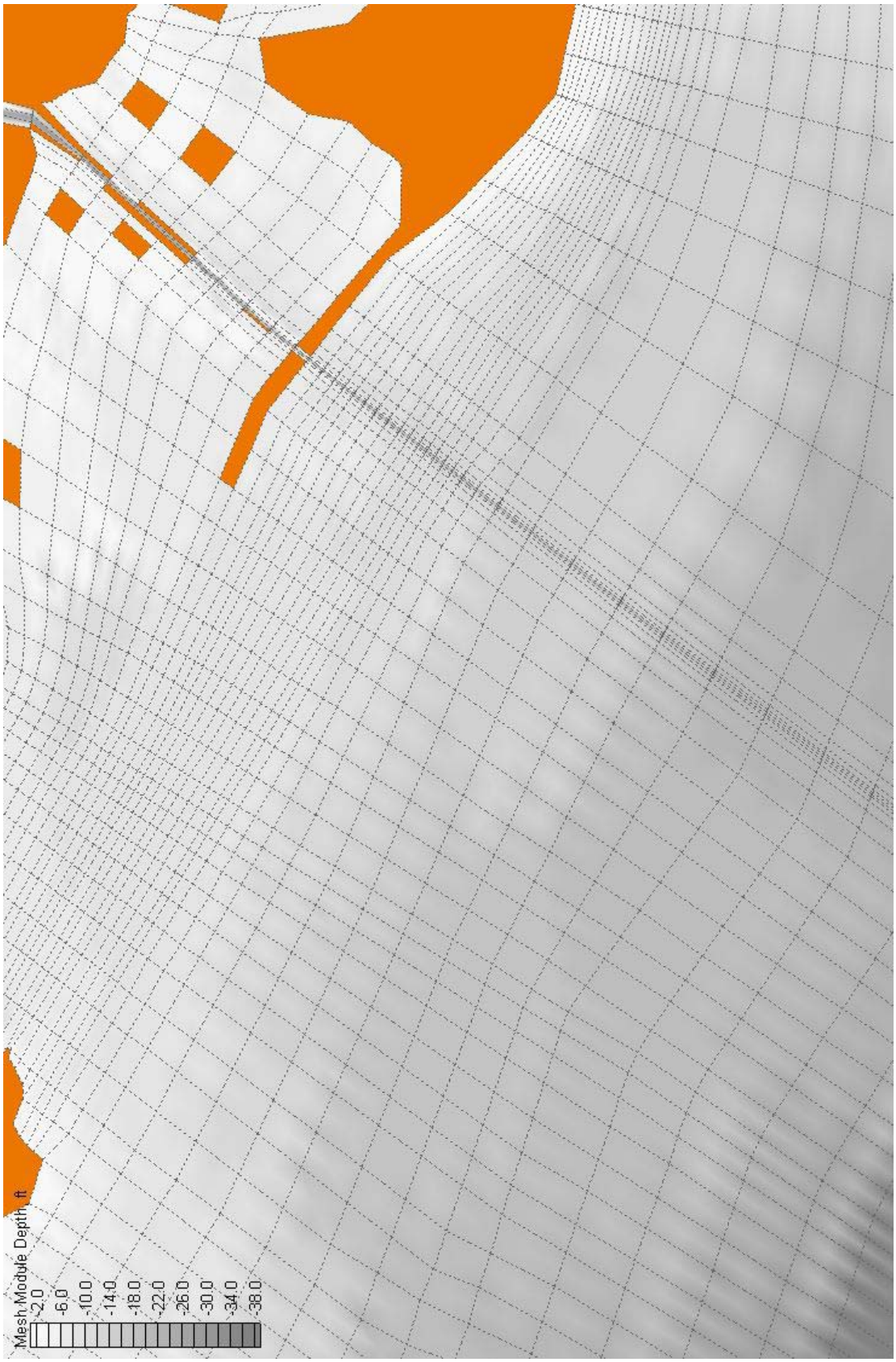

Figure 98. *Reef2* plan configuration

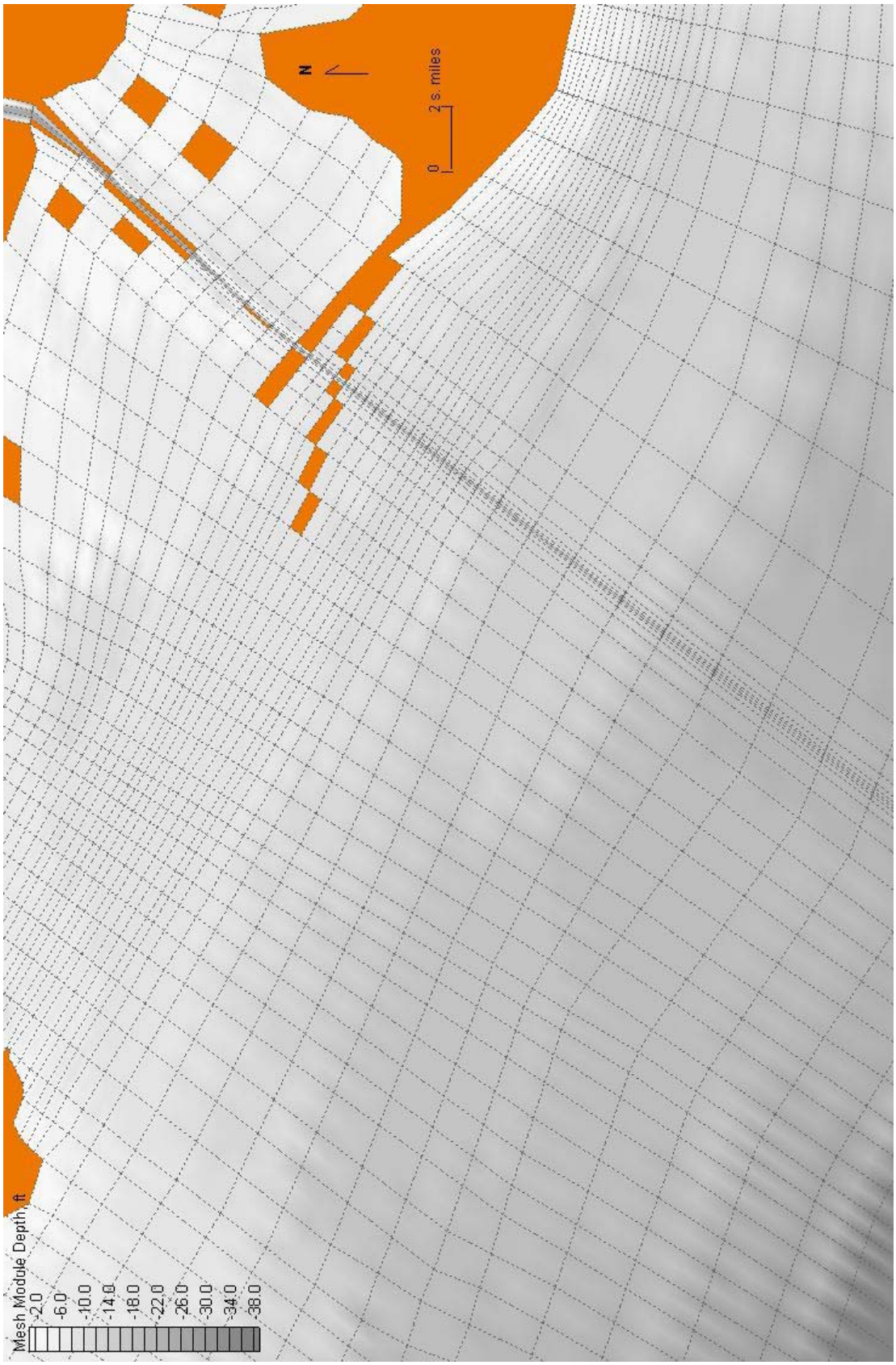

Figure 99. *Reef3* plan configuration

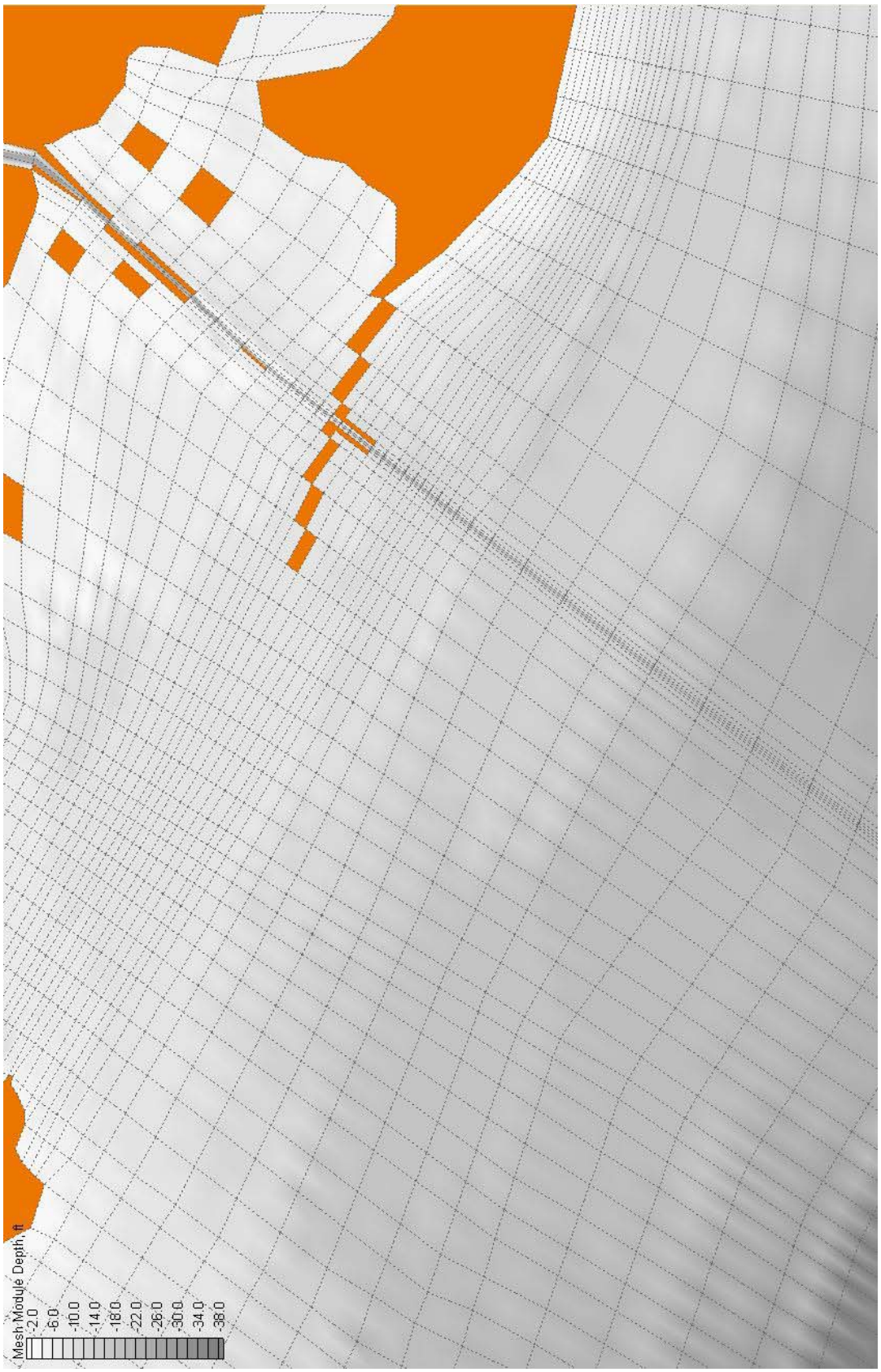

Figure 100. *RJ4* plan configuration

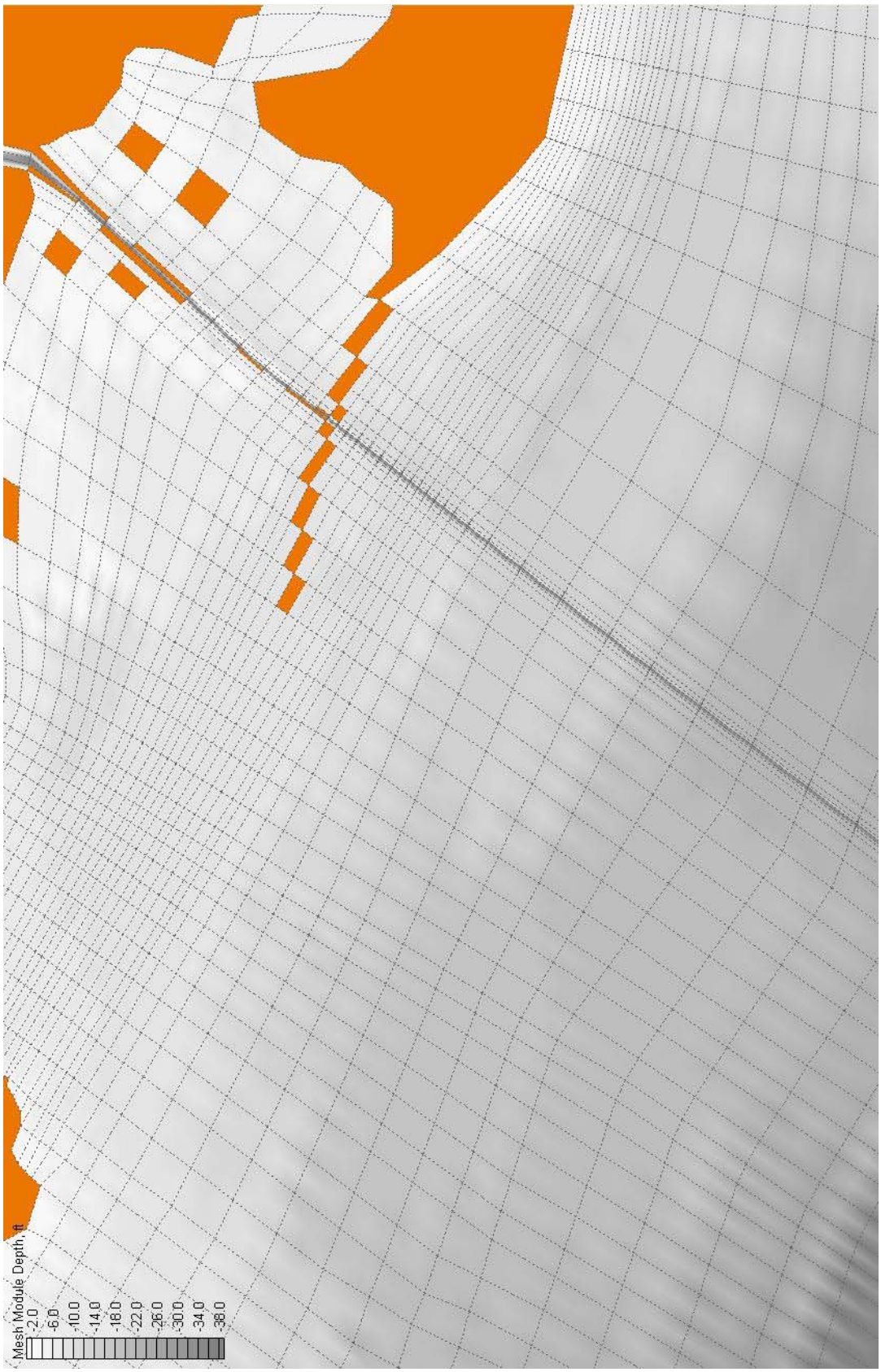

Figure 101. *Reef4* plan configuration

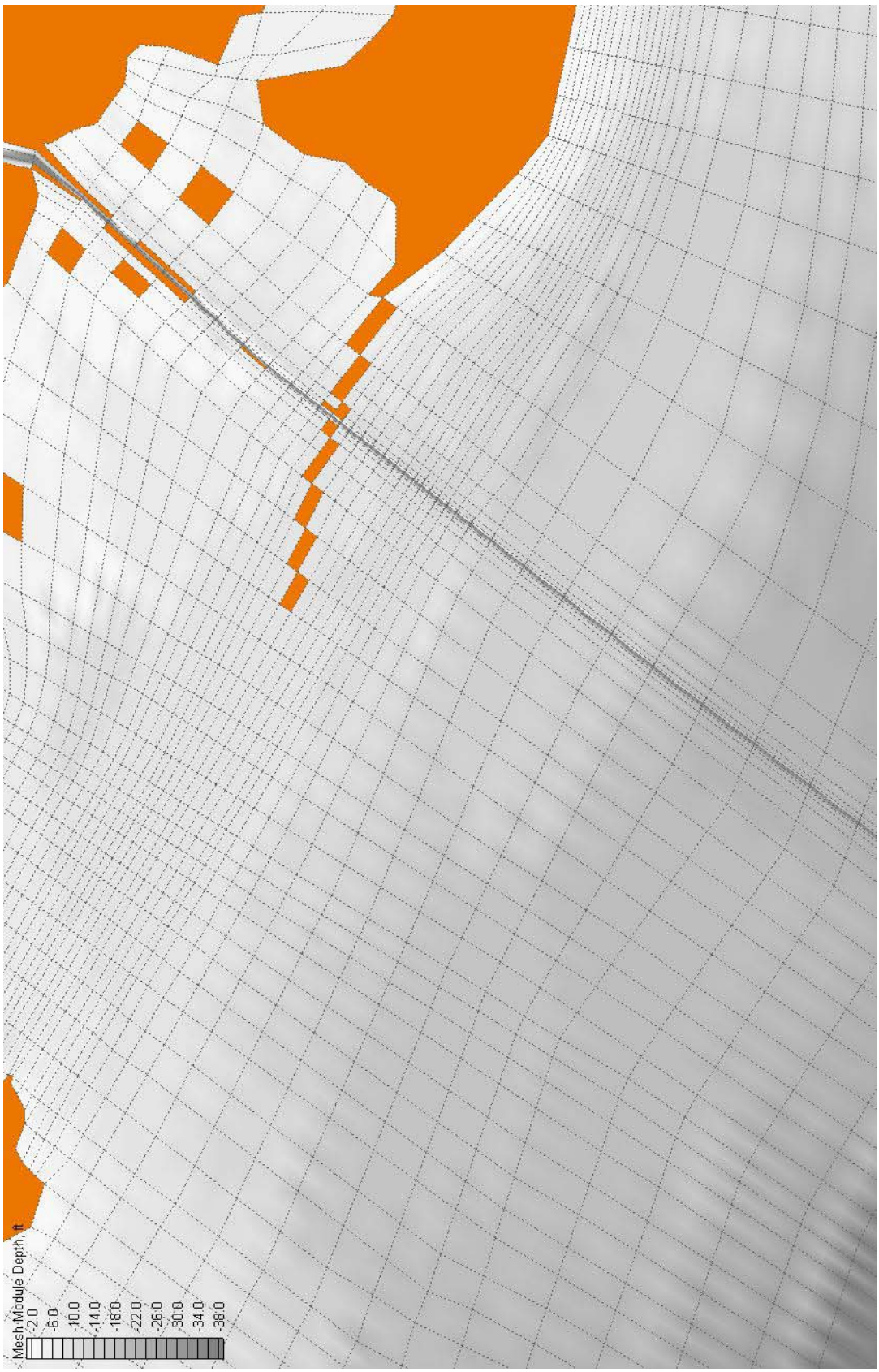

Figure 102. *Reef5* plan configuration

Figure 103. *RJ8* plan configuration

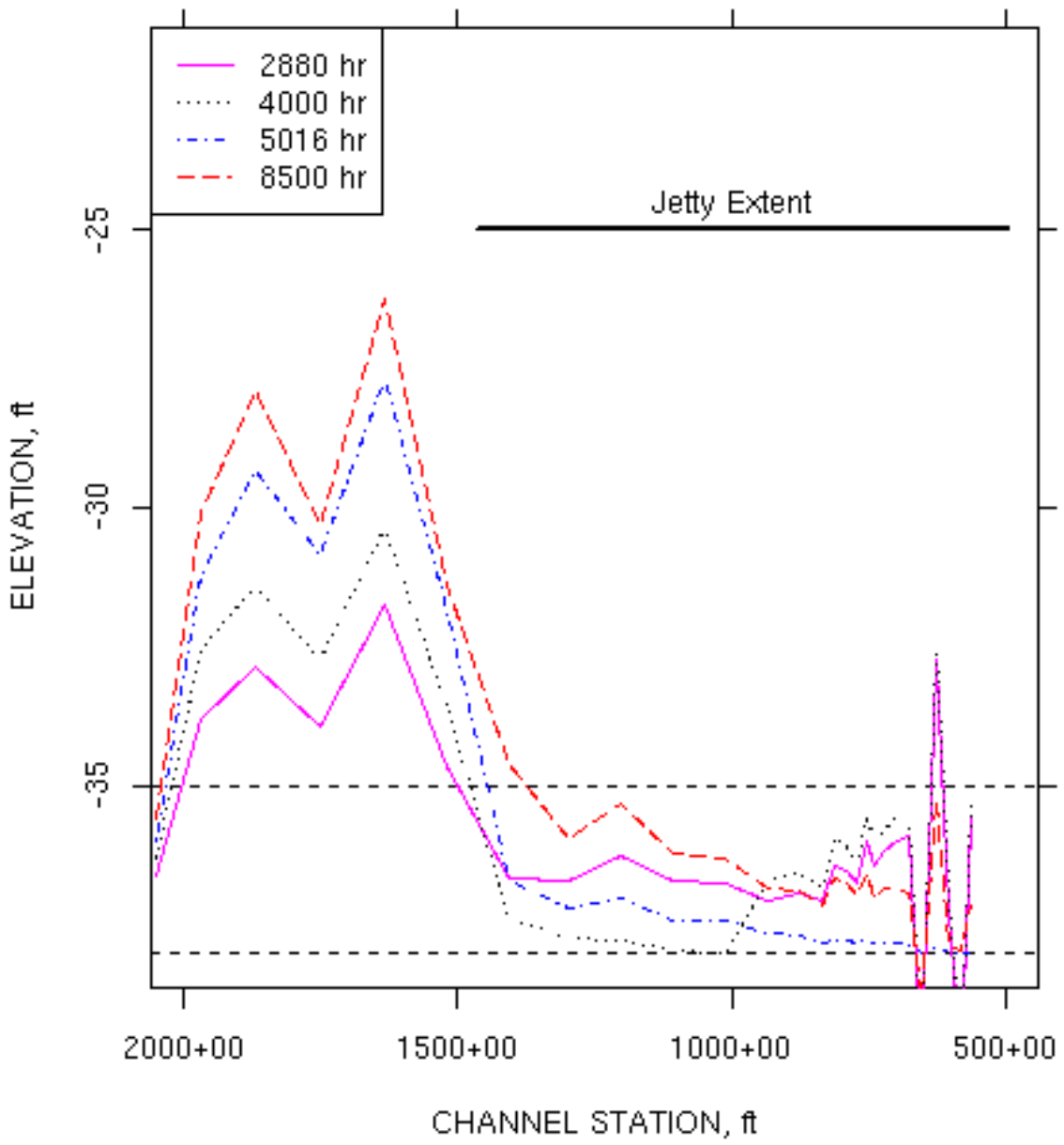

Figure 104. Shoal profiles at select times for *Jetty1* plan

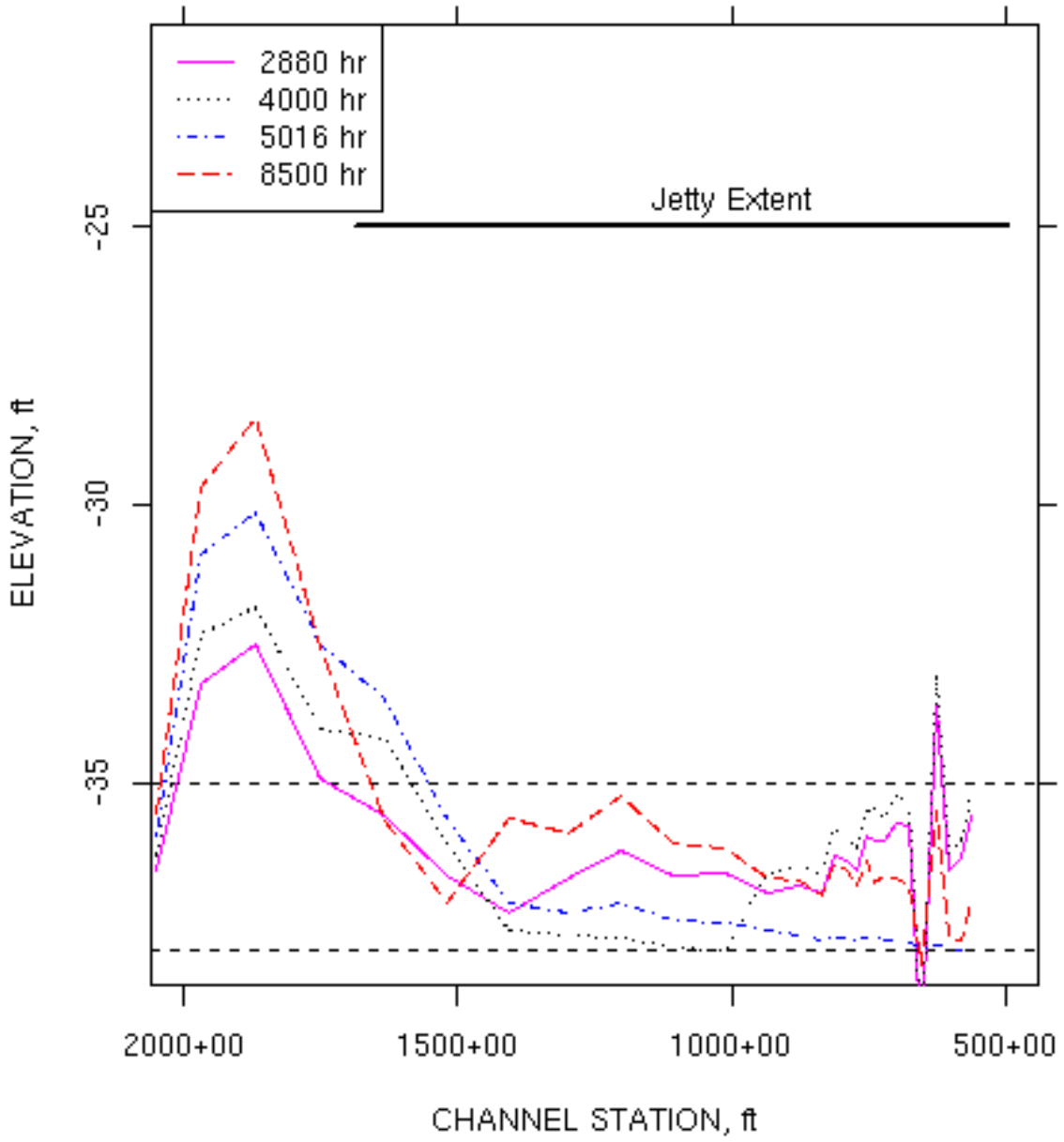

Figure 105. Shoal profiles at select times for *Jetty2* plan

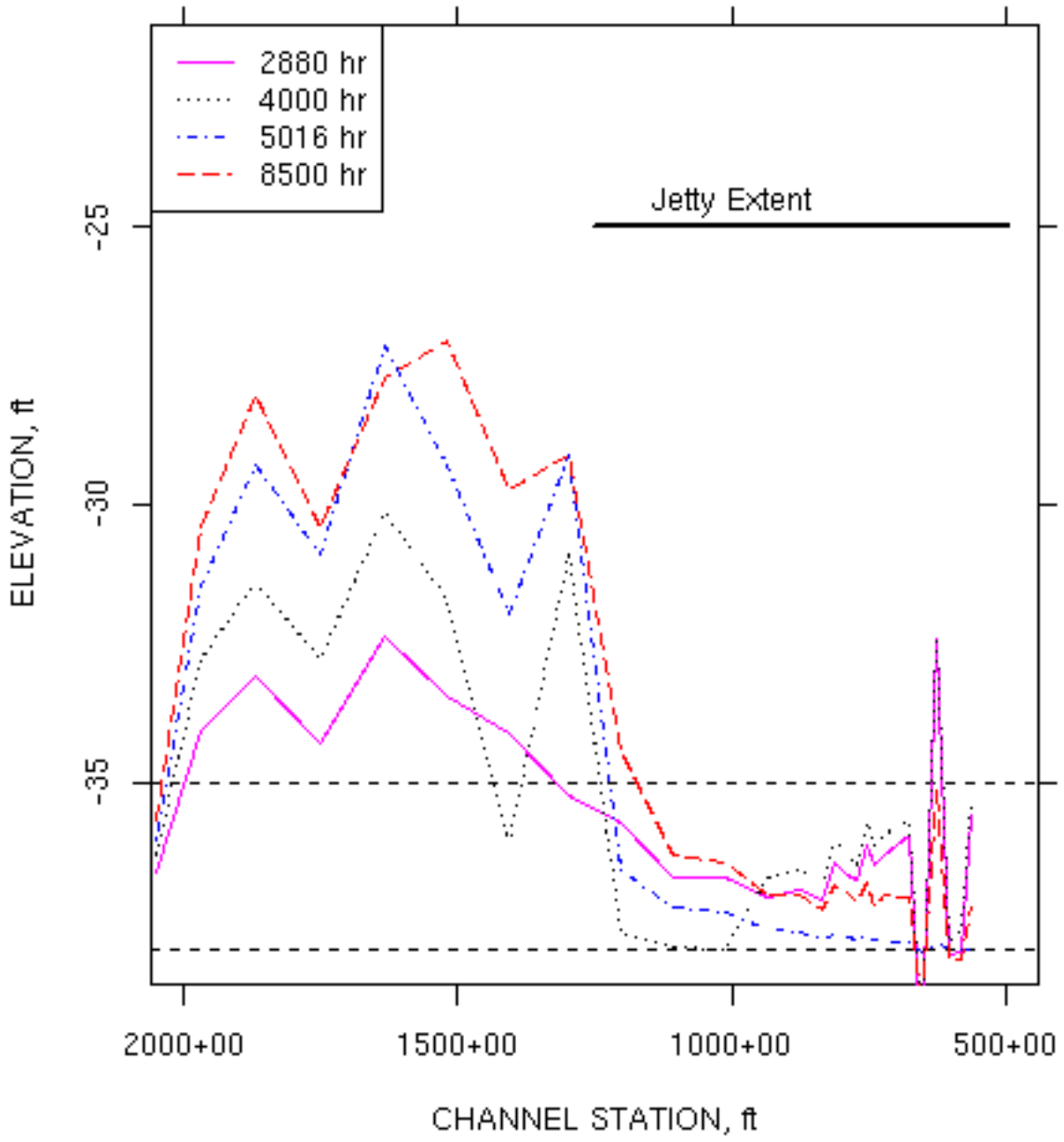

Figure 106. Shoal profiles at select times for *Jetty3* plan

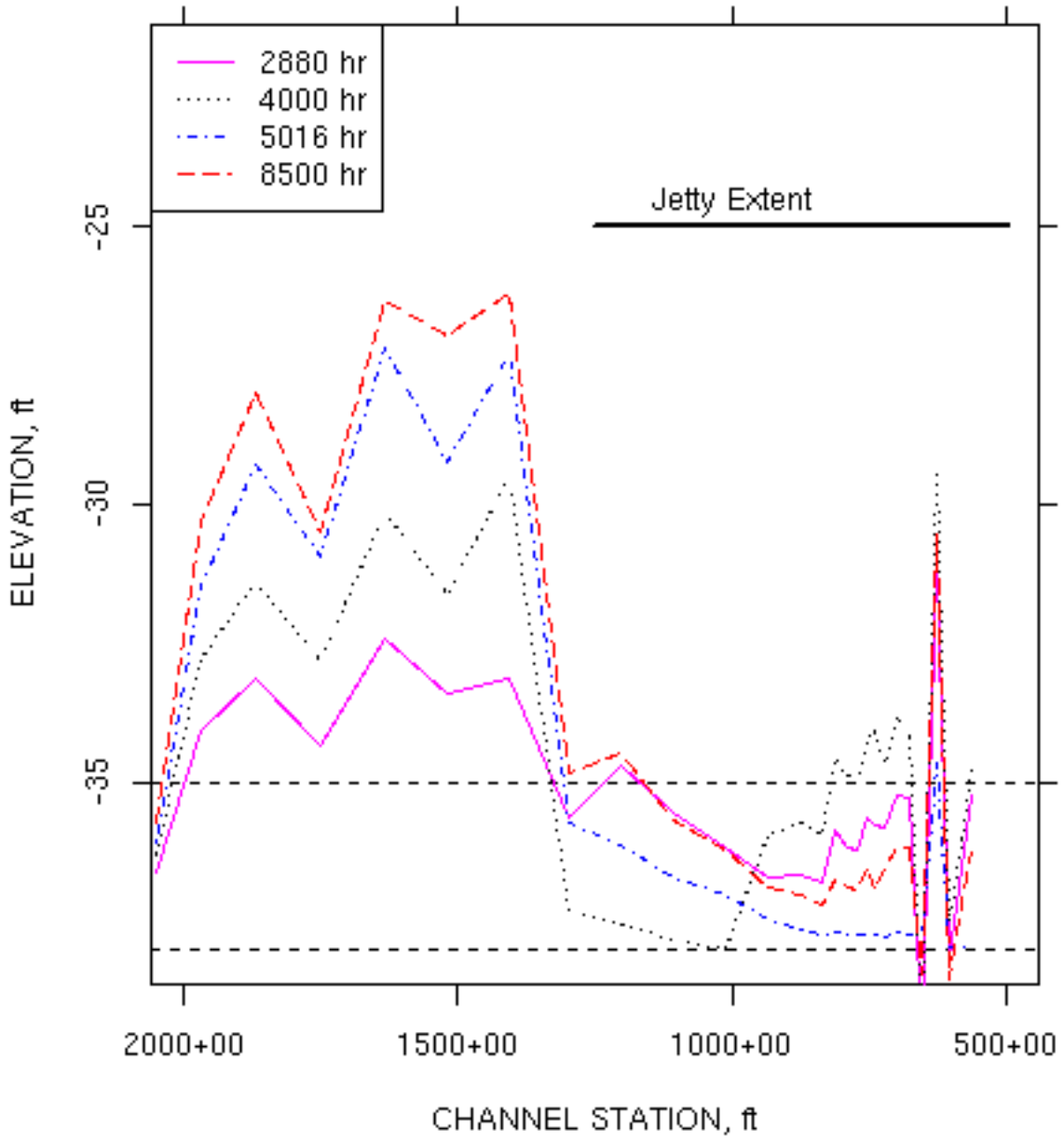

Figure 107. Shoal profiles at select times for *Jetty4* plan

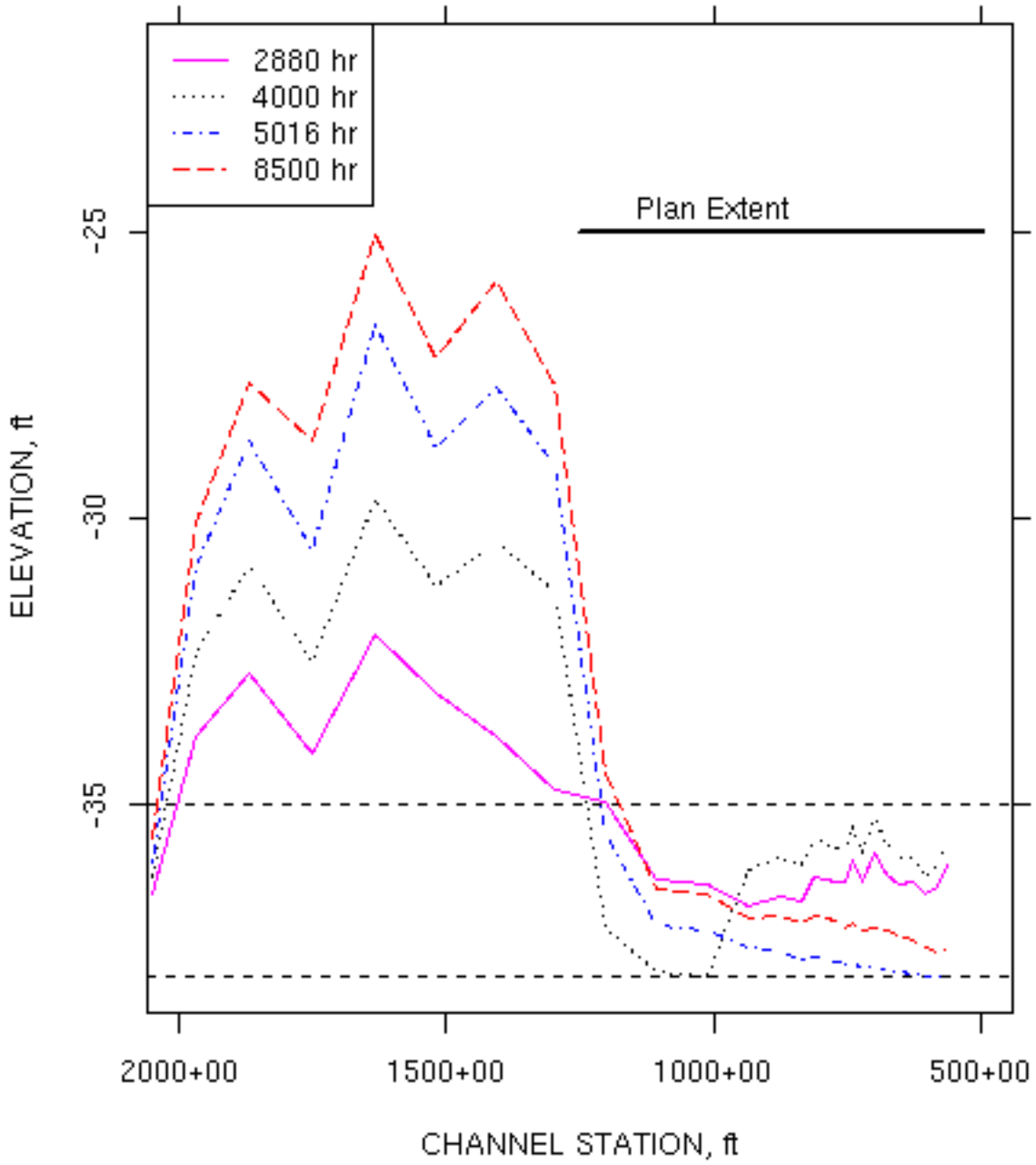

Figure 108. Shoal profiles at select times for *RJ5* plan

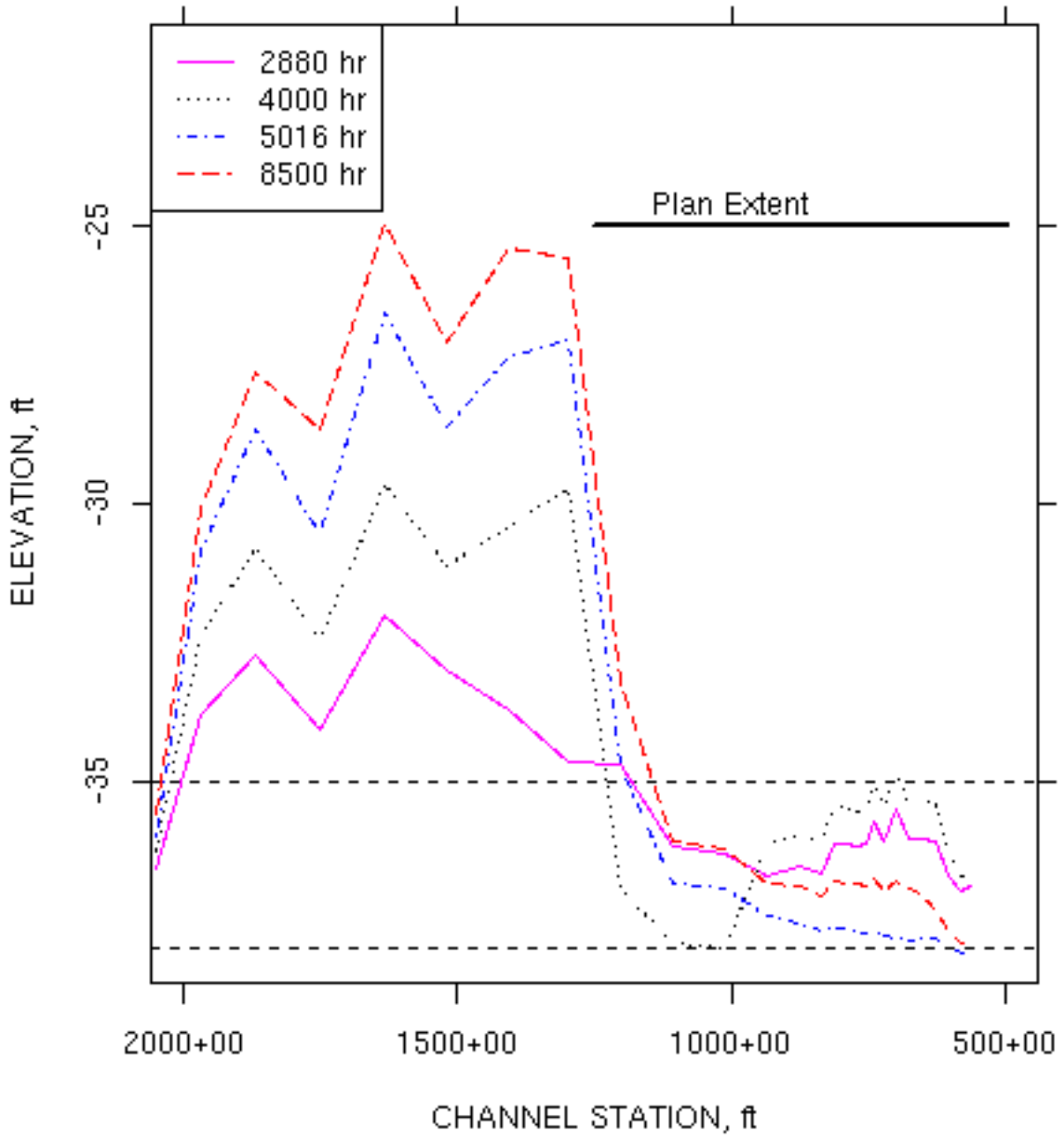

Figure 109. Shoal profiles at select times for *RJ6* plan

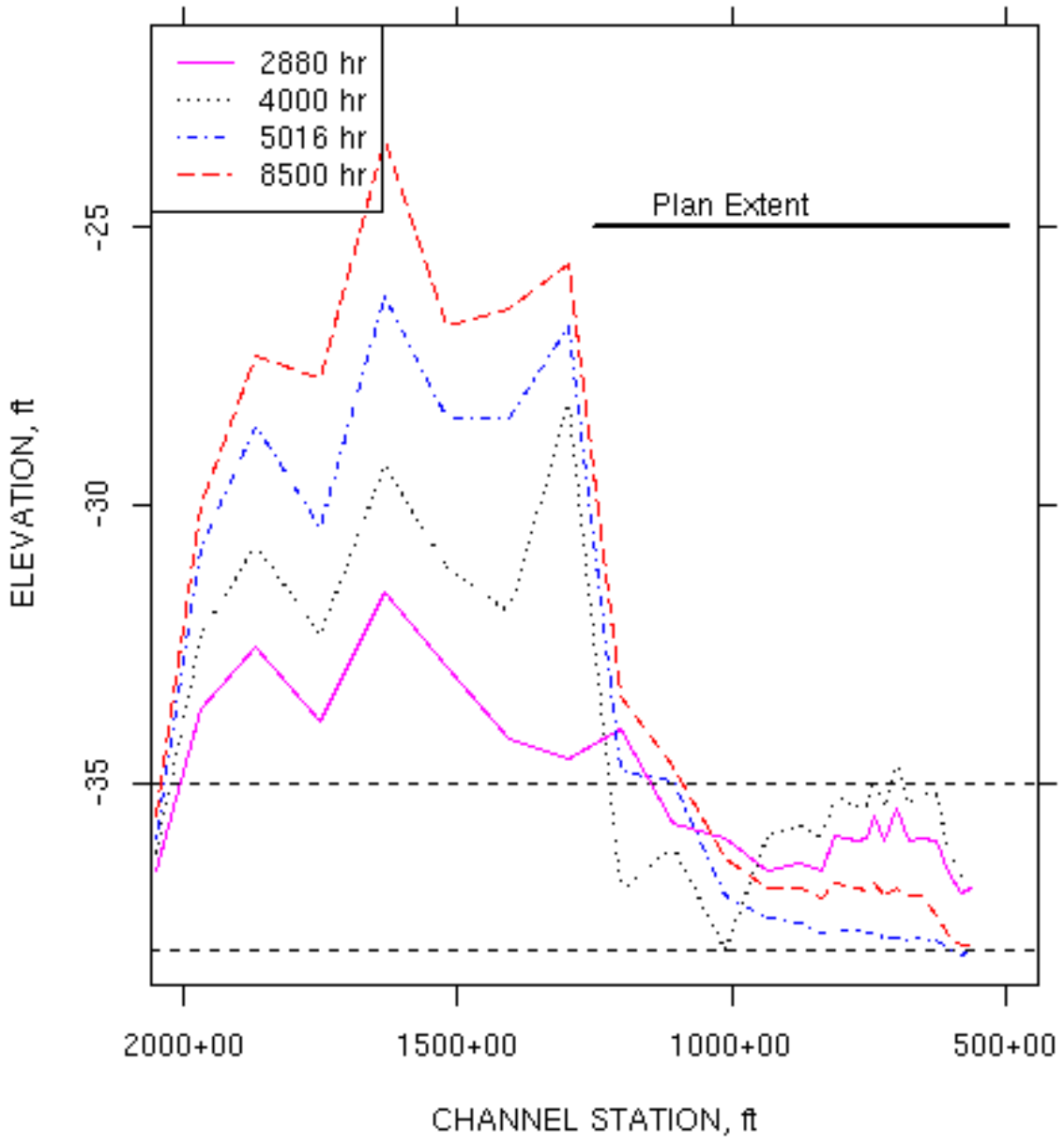

Figure 110. Shoal profiles at select times for *RJ7* plan

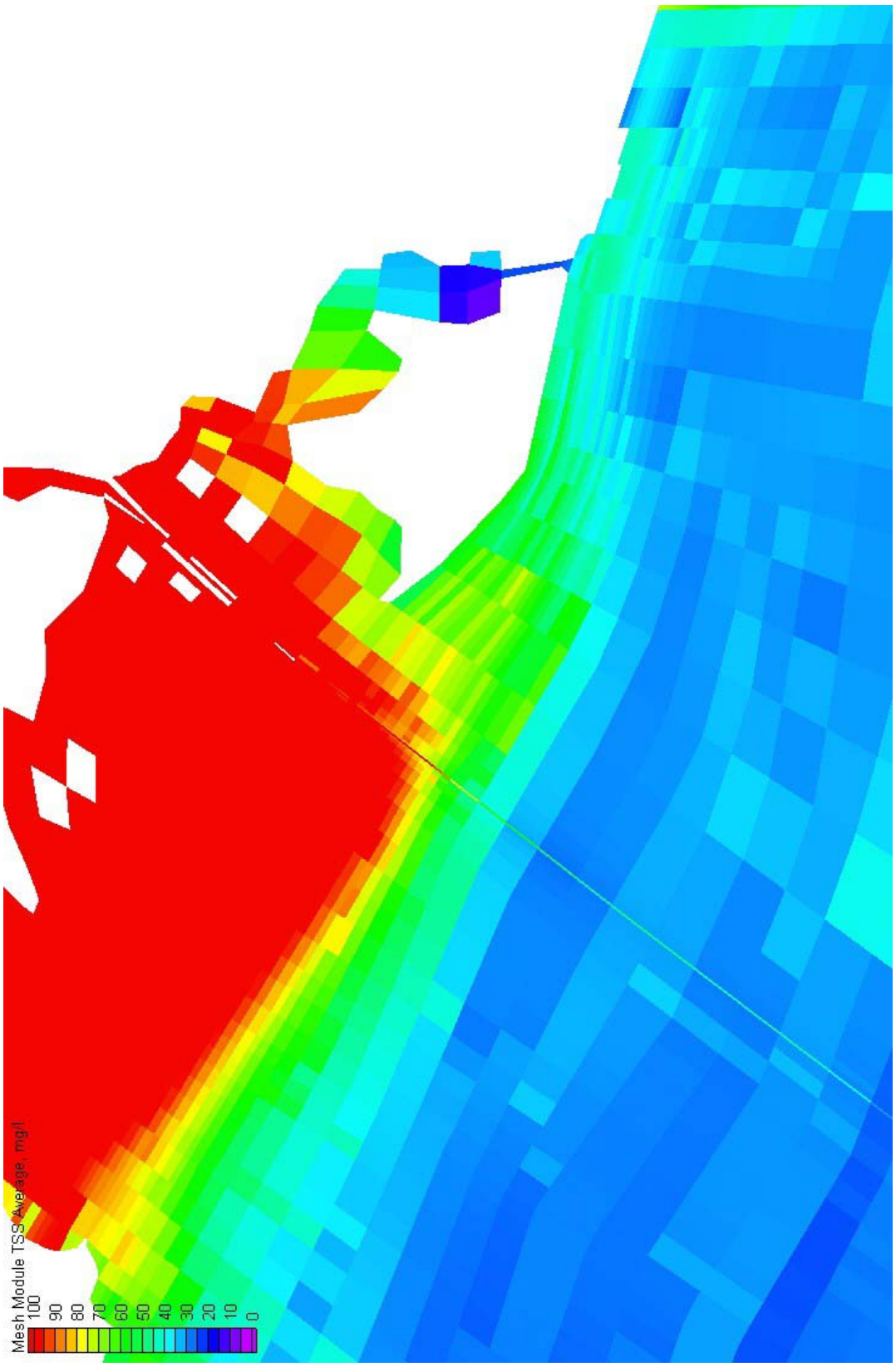

Figure 111. Time and depth averaged TSM for 38-ft channel and existing conditions

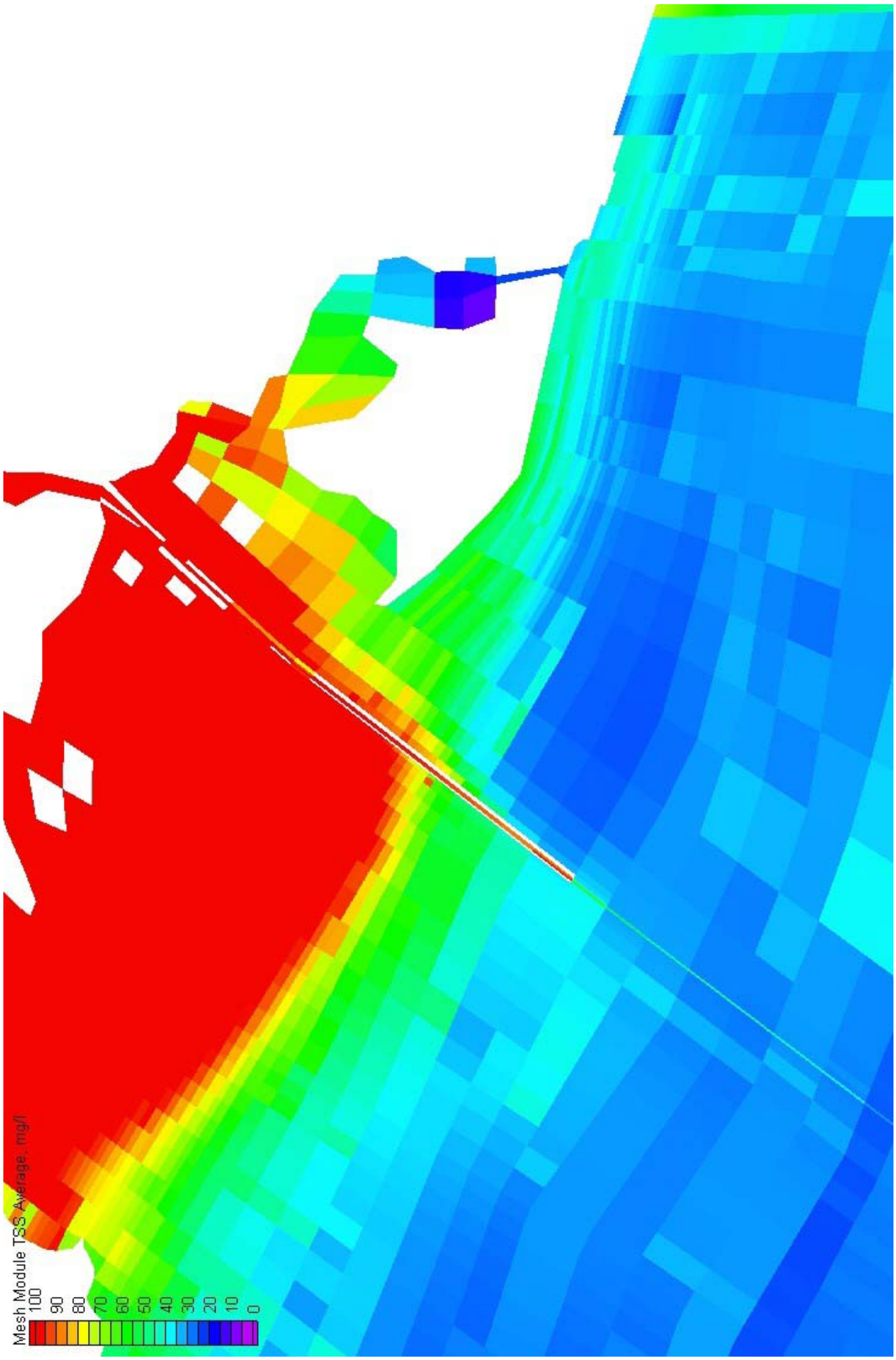

Figure 112. Time and depth averaged TSM for 38-ft channel with *Jetty3* plan

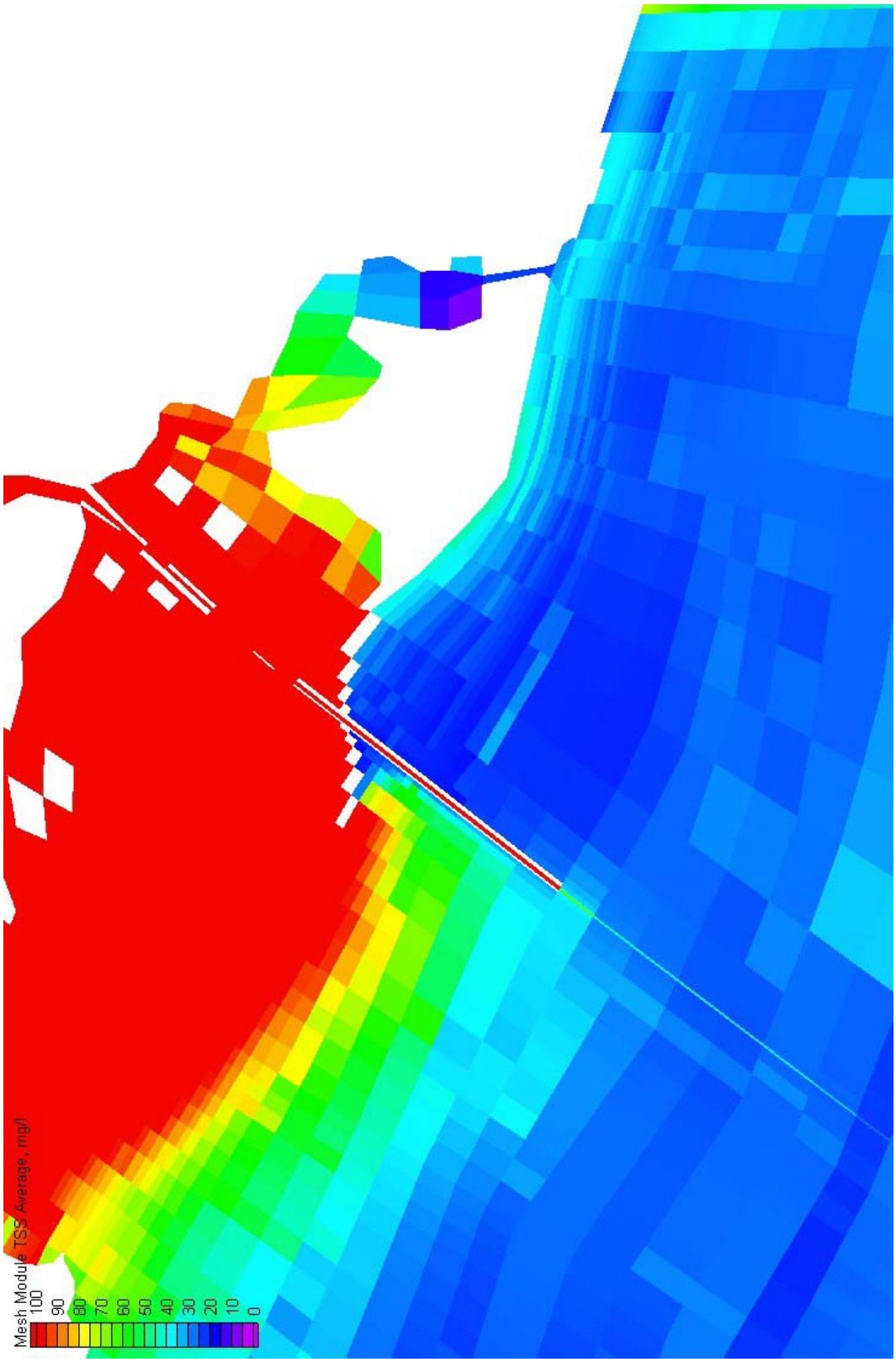

Figure 113. Time and depth averaged TSM for 38-ft channel with *RJ5* plan

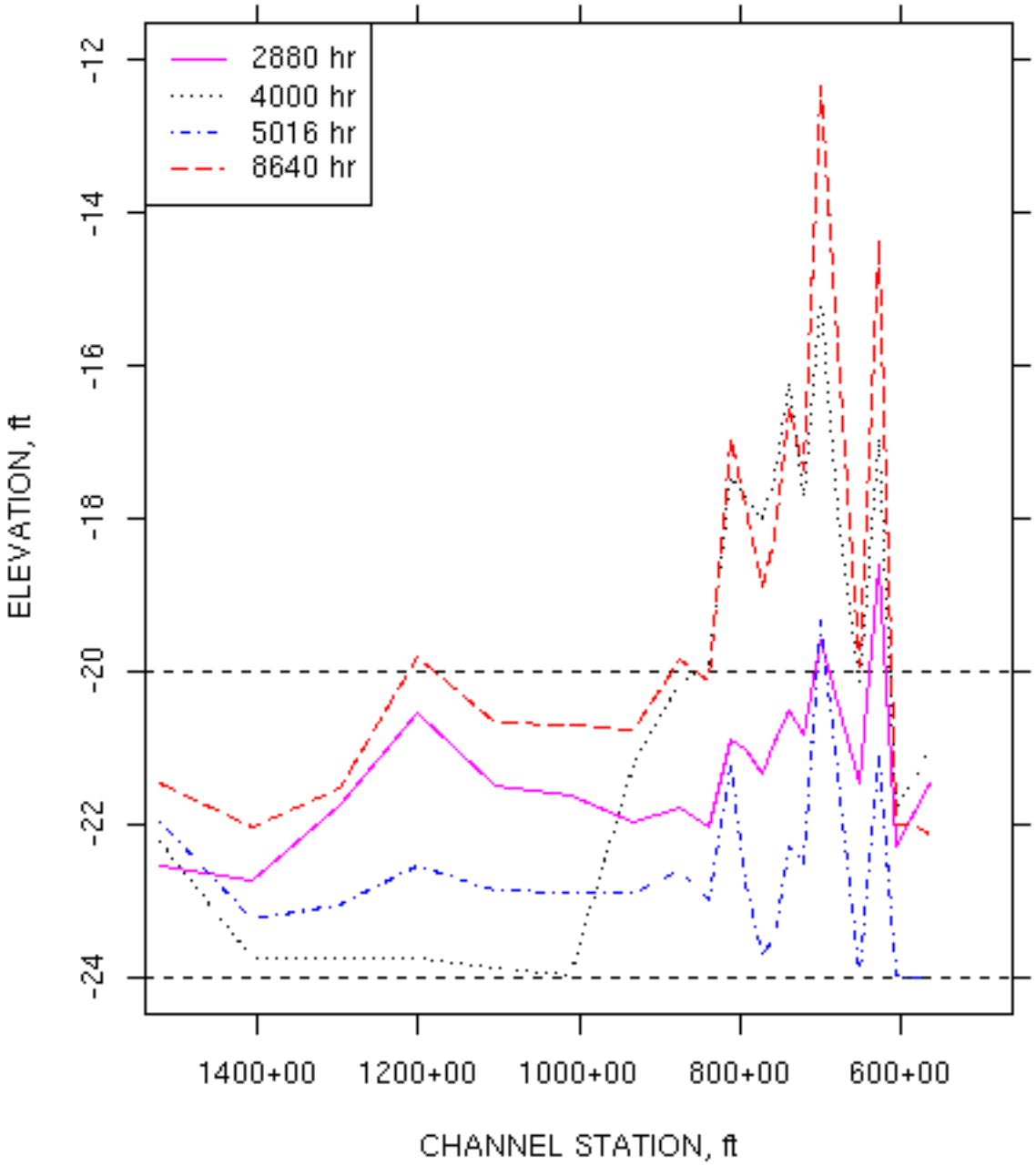

Figure 114. Shoal profiles at select times for *Reef2* plan

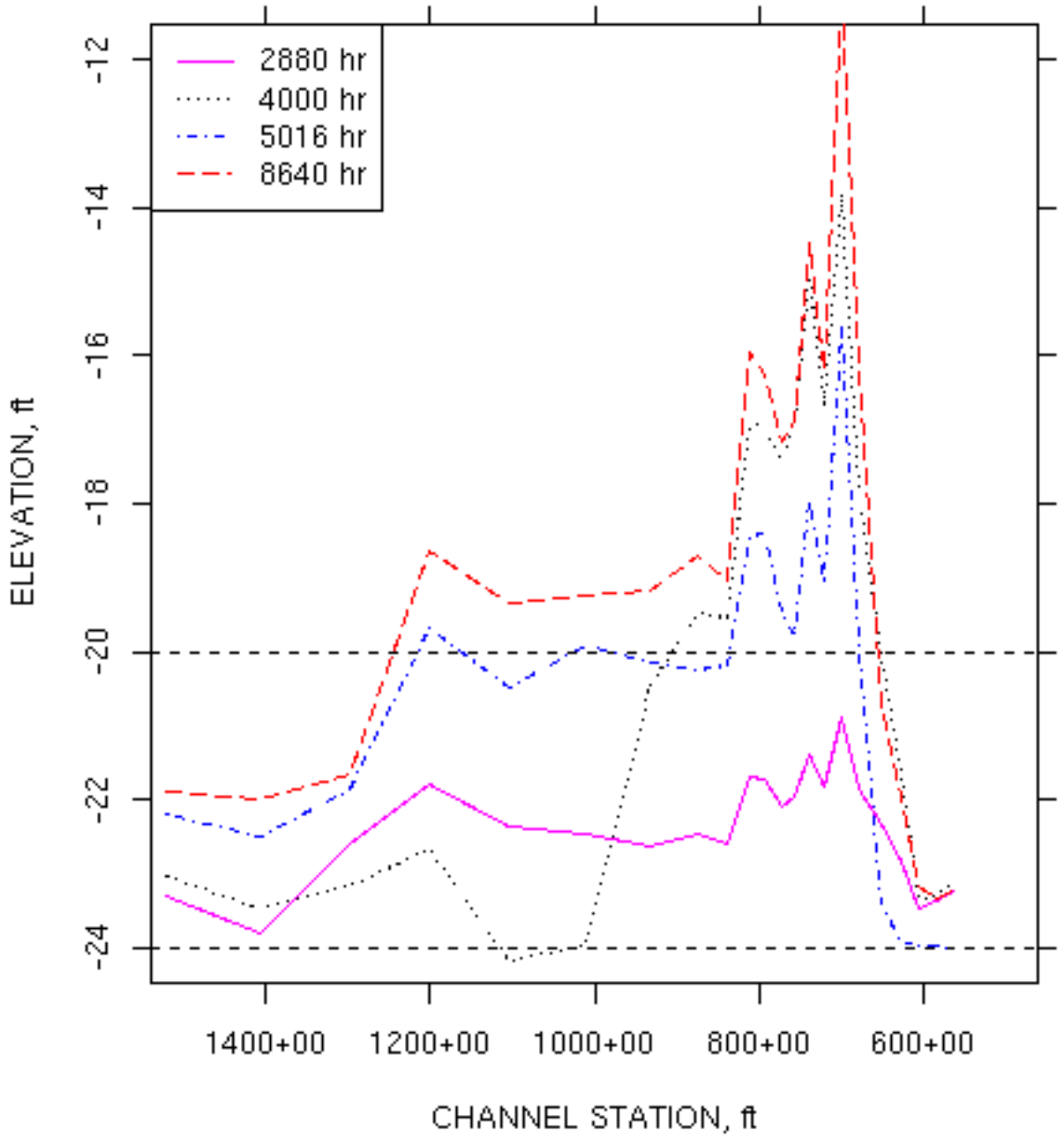

Figure 115. Shoal profiles at select times for *Reef3* plan

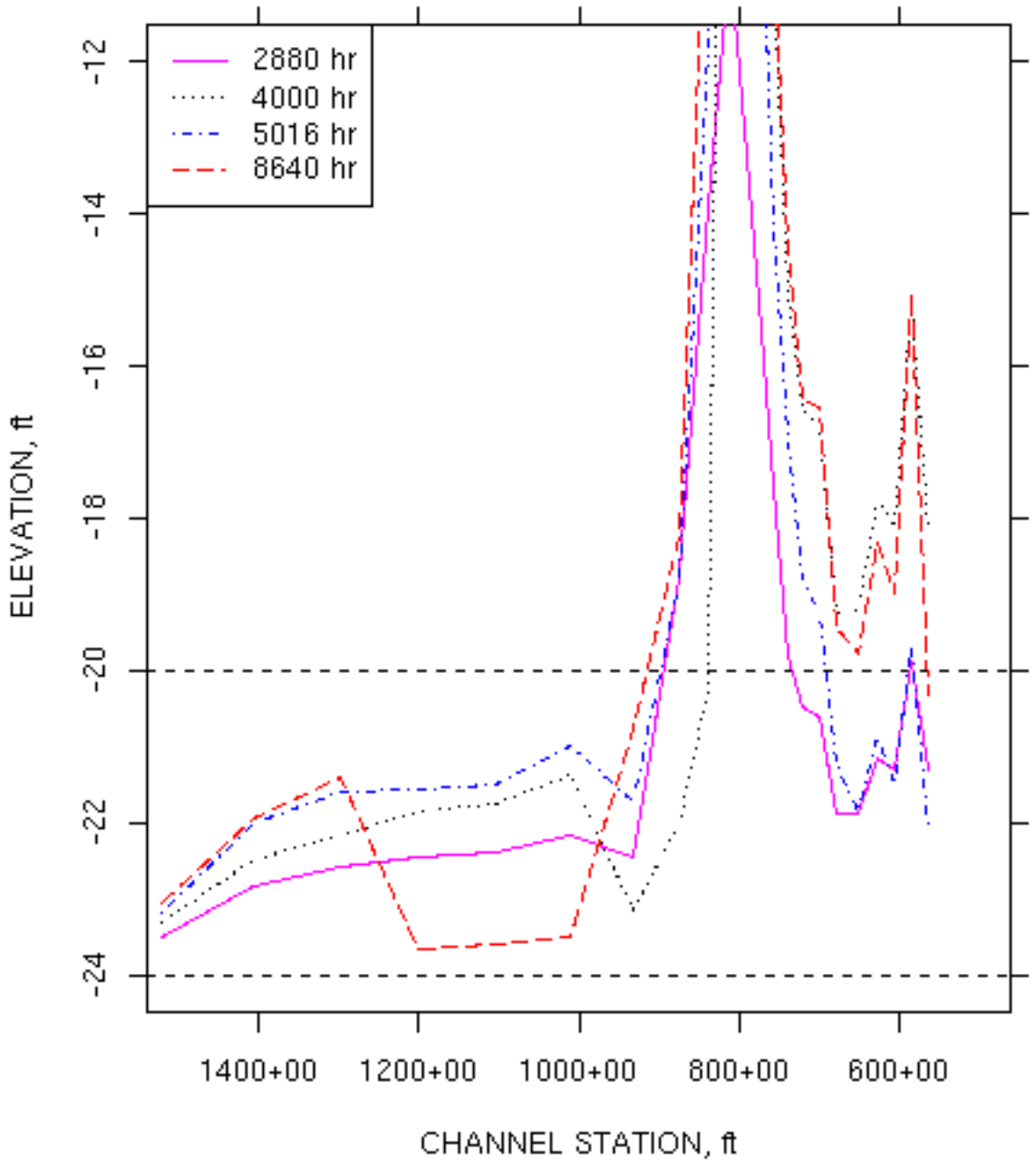

Figure116. Shoal profiles at select times for *RJ4* plan

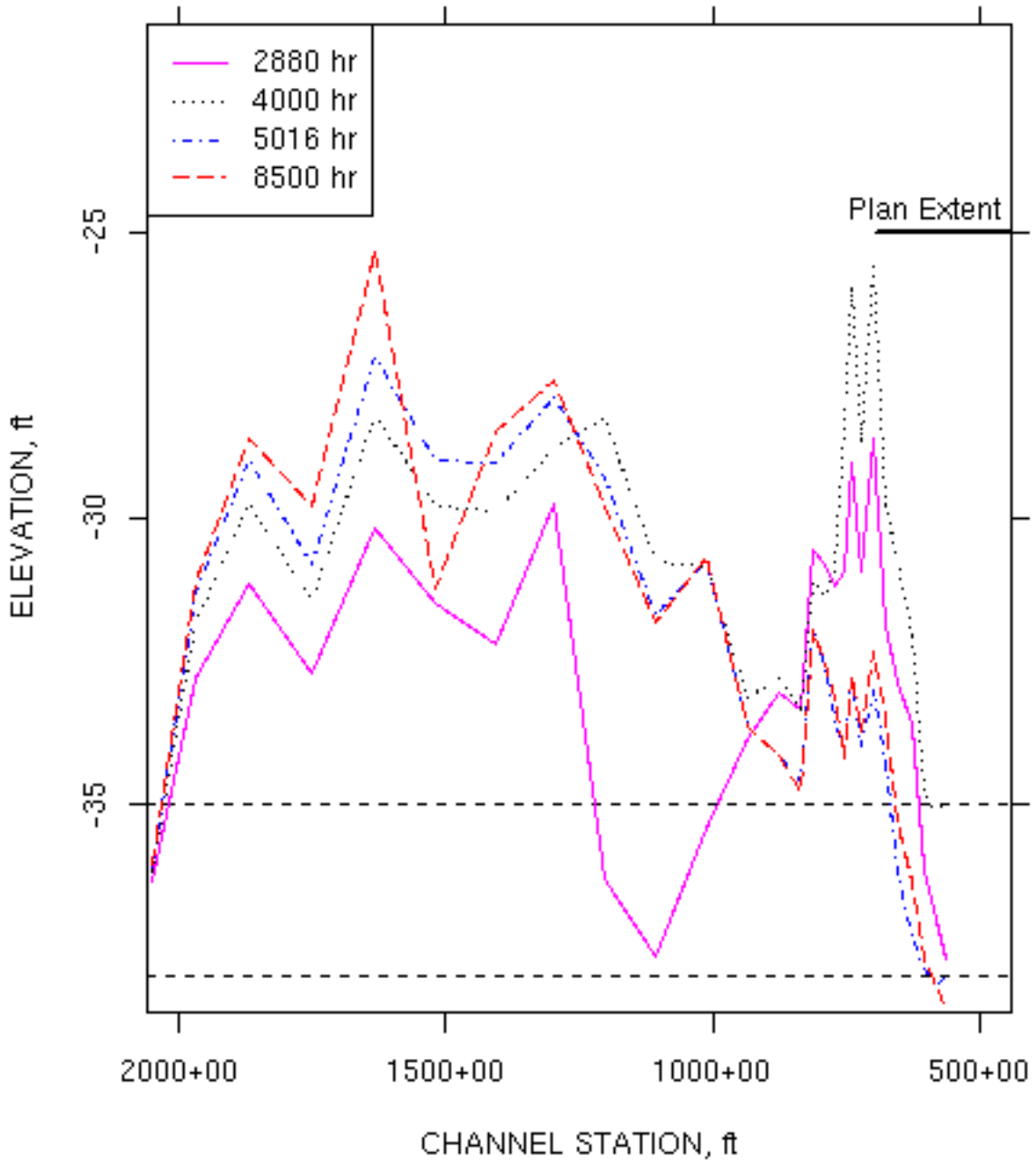

Figure 117. Shoal profiles at select times for *Reef4* plan

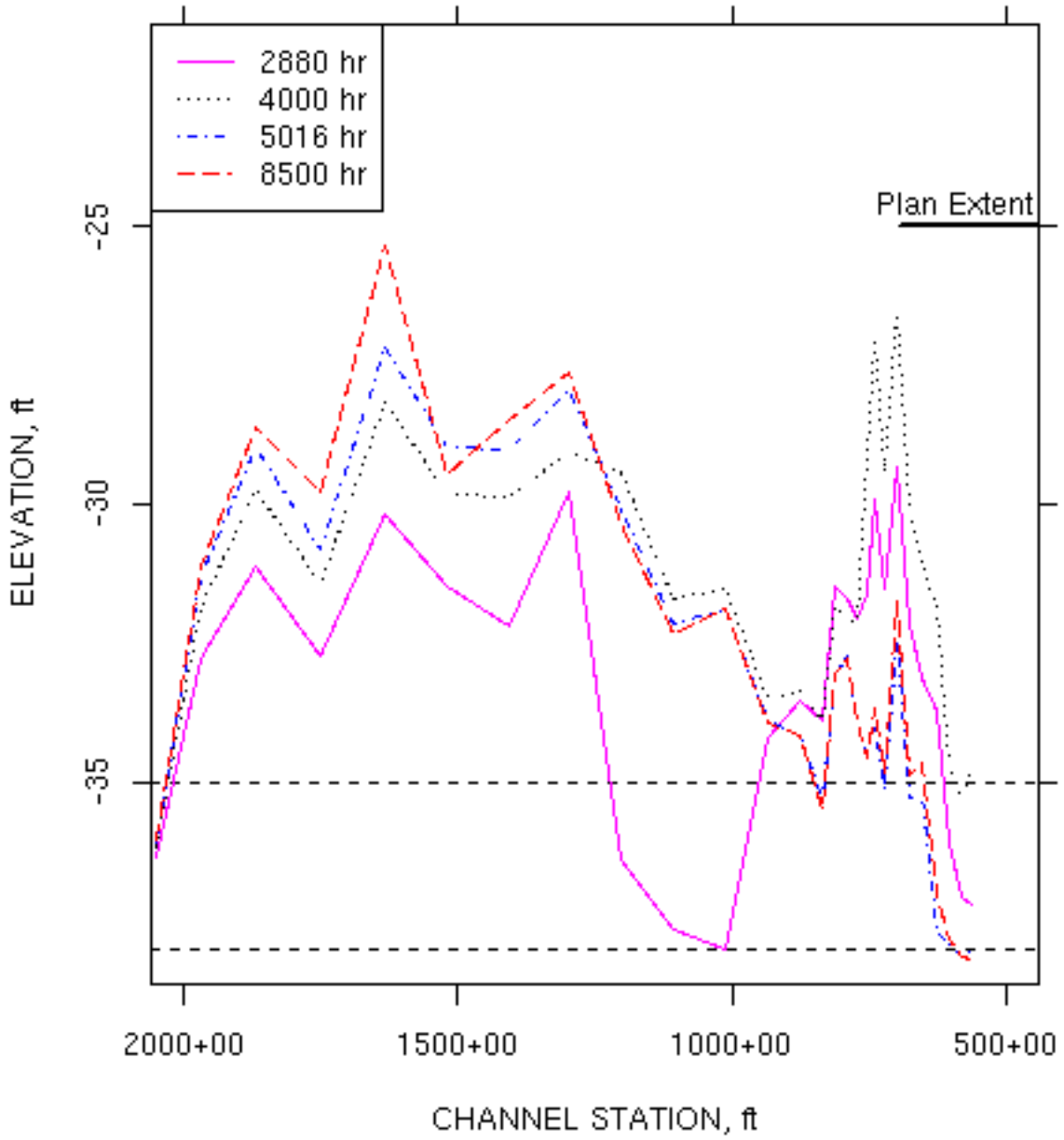

Figure 118. Shoal profiles at select times for *Reef5* plan

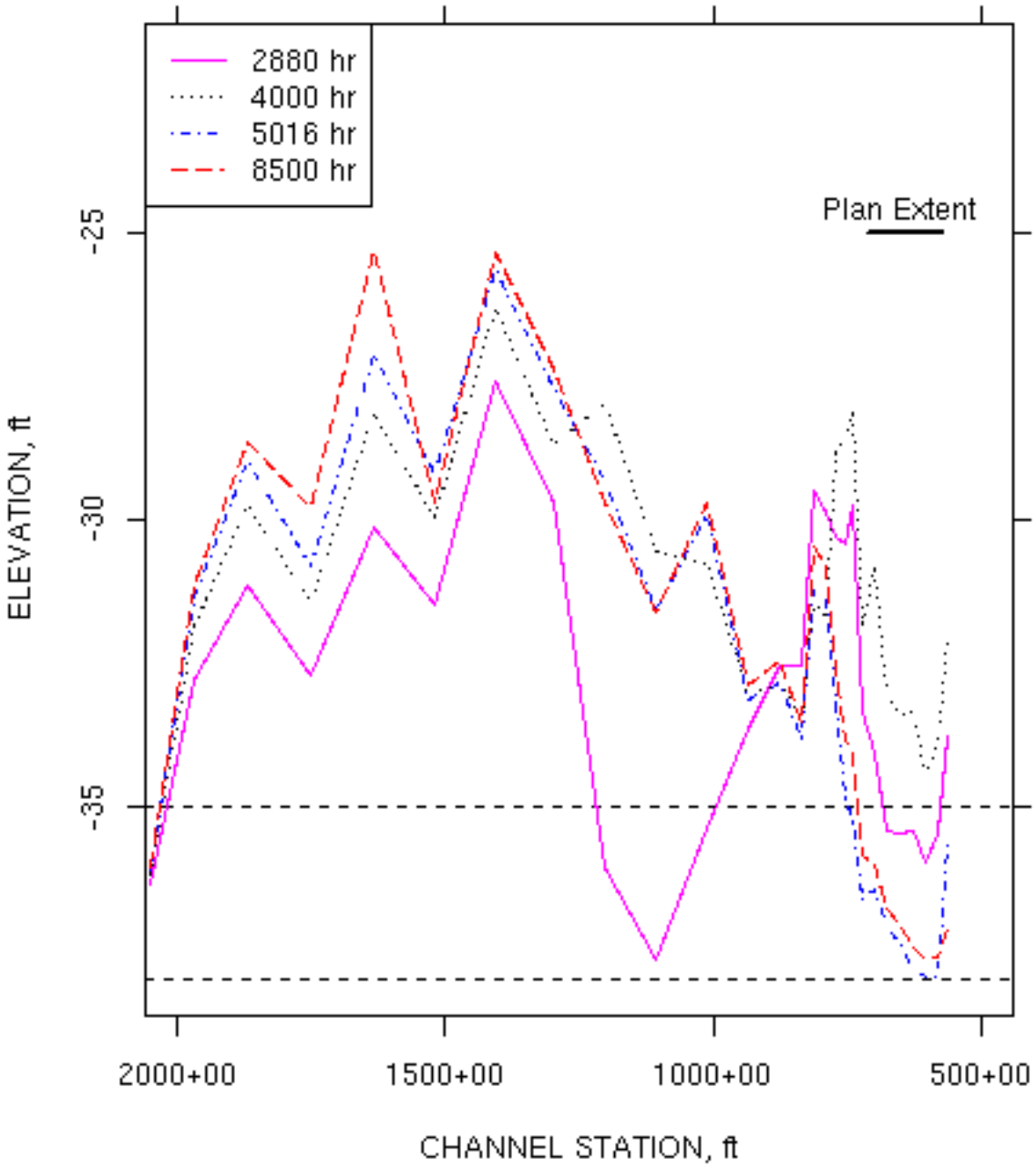

Figure 119. Shoal profiles at select times for *RJ8* plan

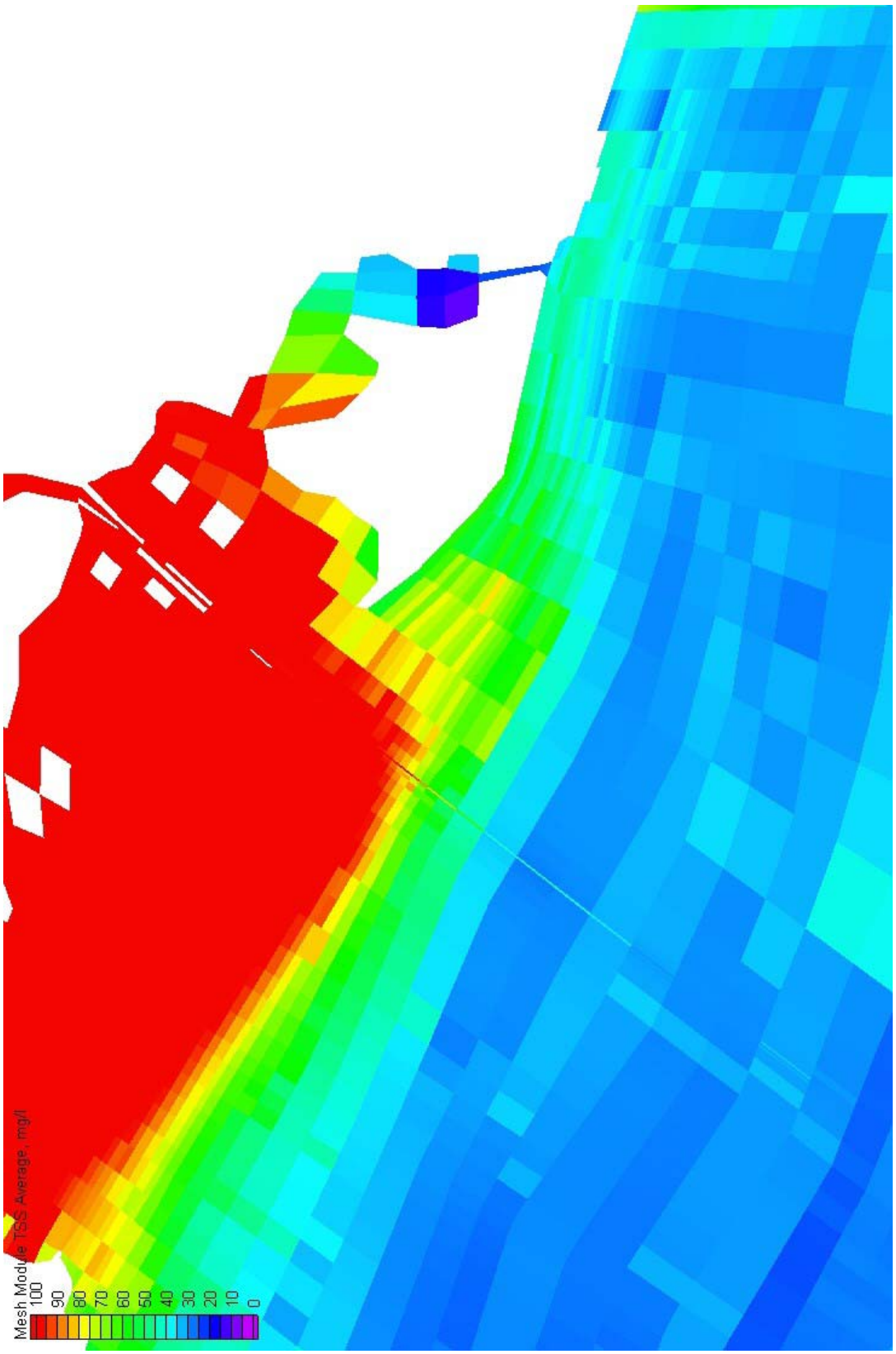

Figure 120. Time and depth averaged TSM for 24-ft channel and existing conditions

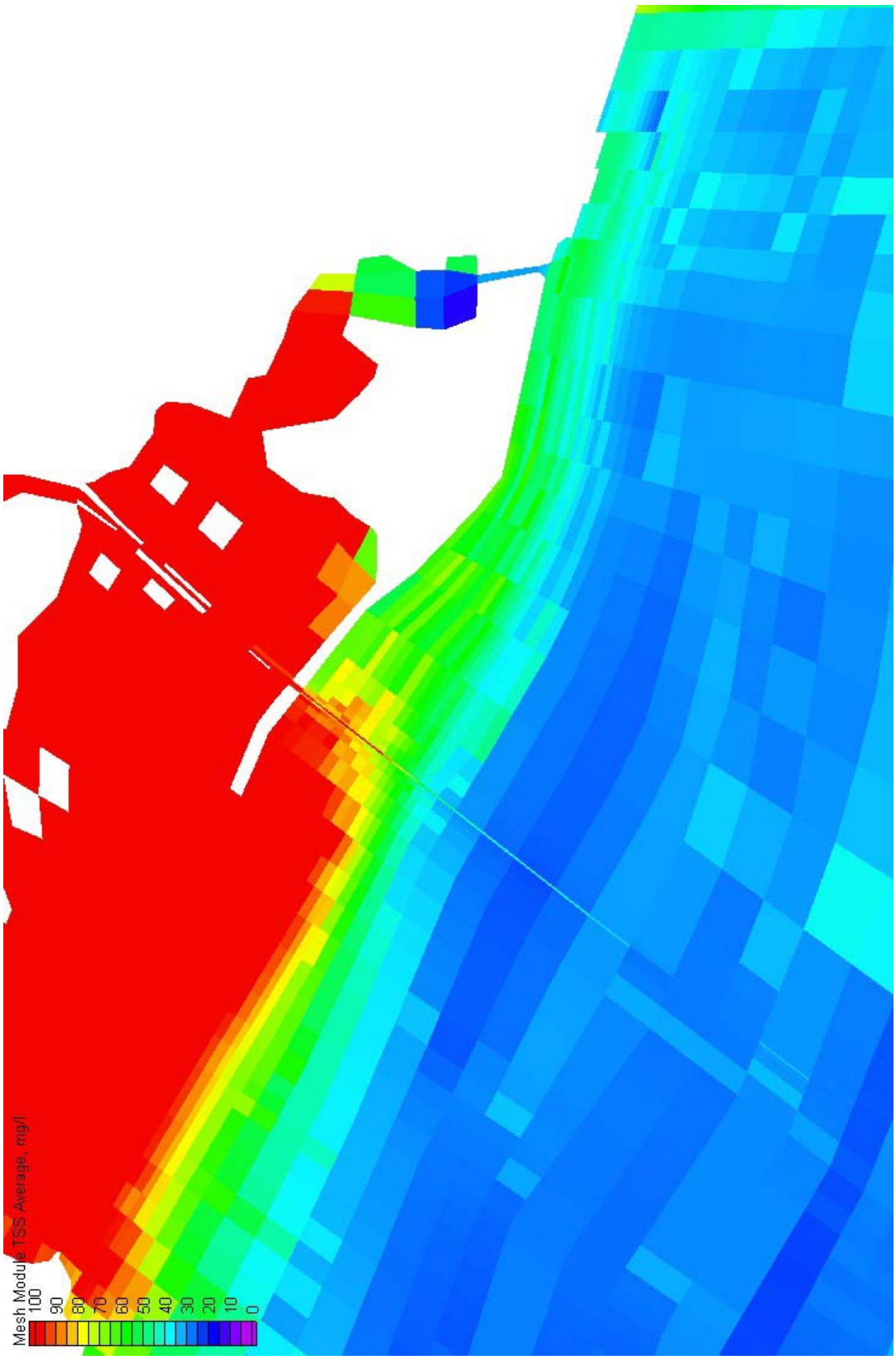

Figure 121. Time and depth averaged TSM for 24-ft channel with *Reef2* plan

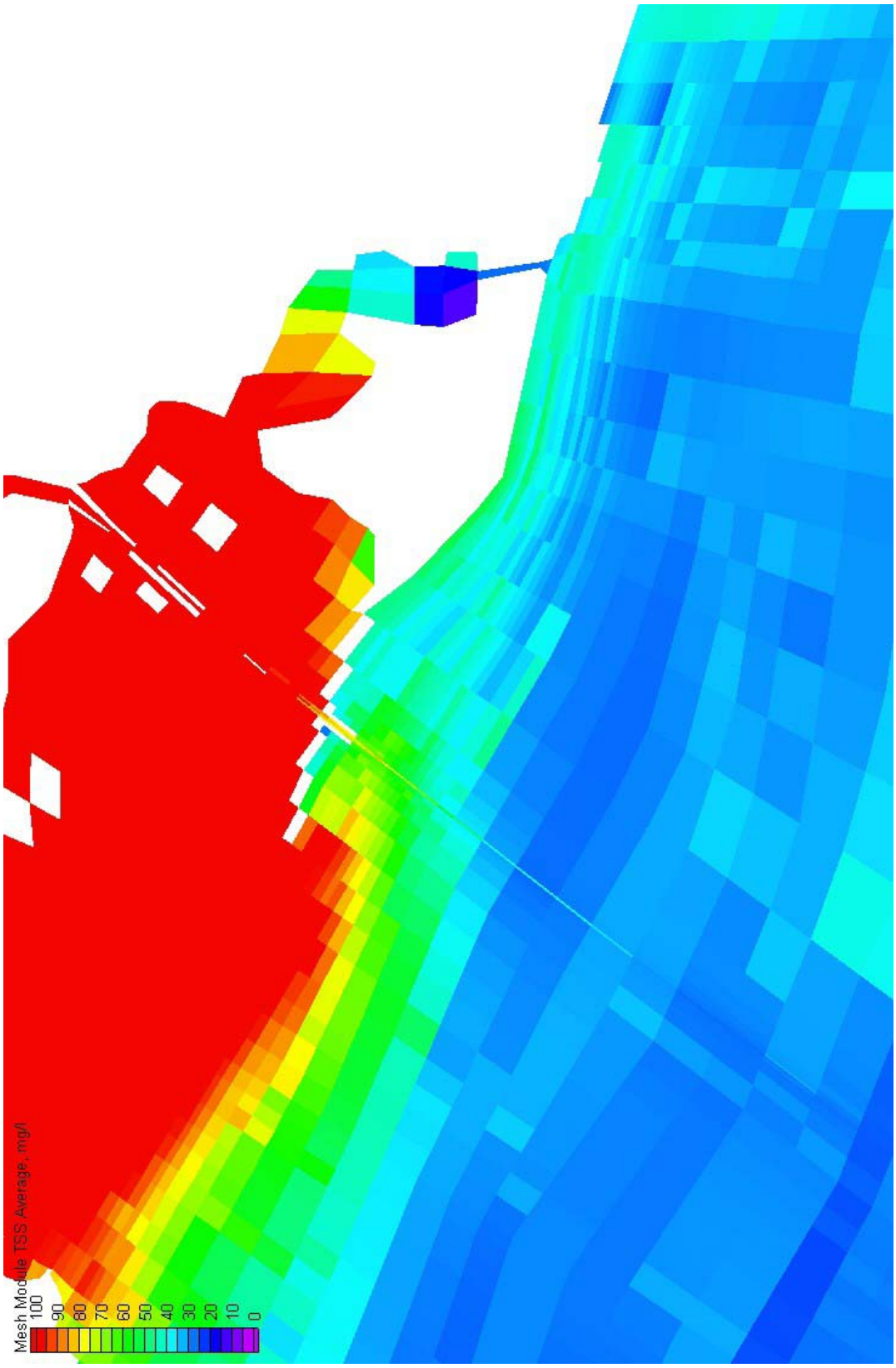

Figure 122. Time and depth averaged TSM for 24-ft channel with *RJ4* plan

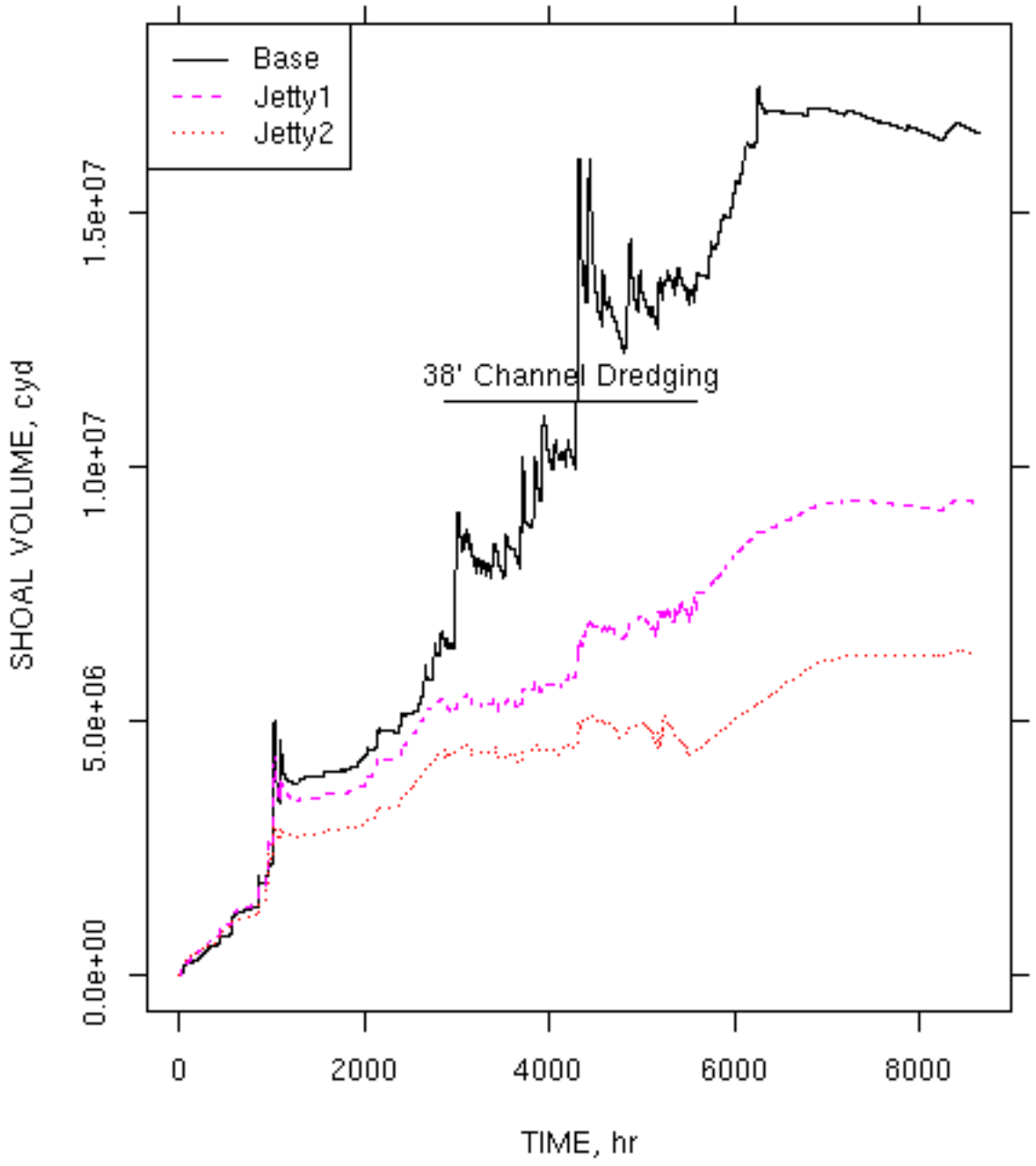

Figure 123. Shoal volume time history for *Jetty1* and *Jetty2* plans

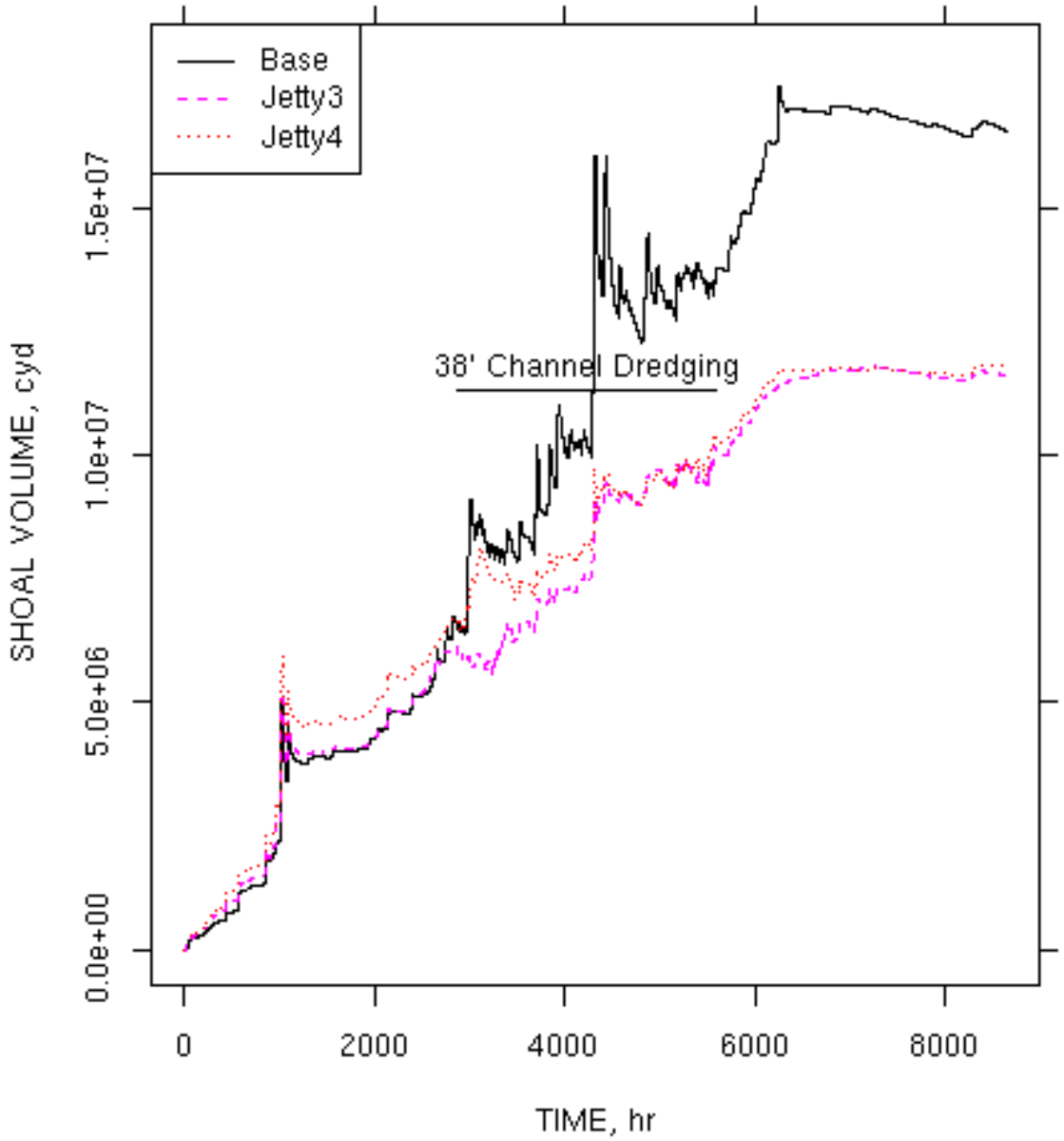

Figure 124. Shoal volume time history for *Jetty3* and *Jetty4* plans

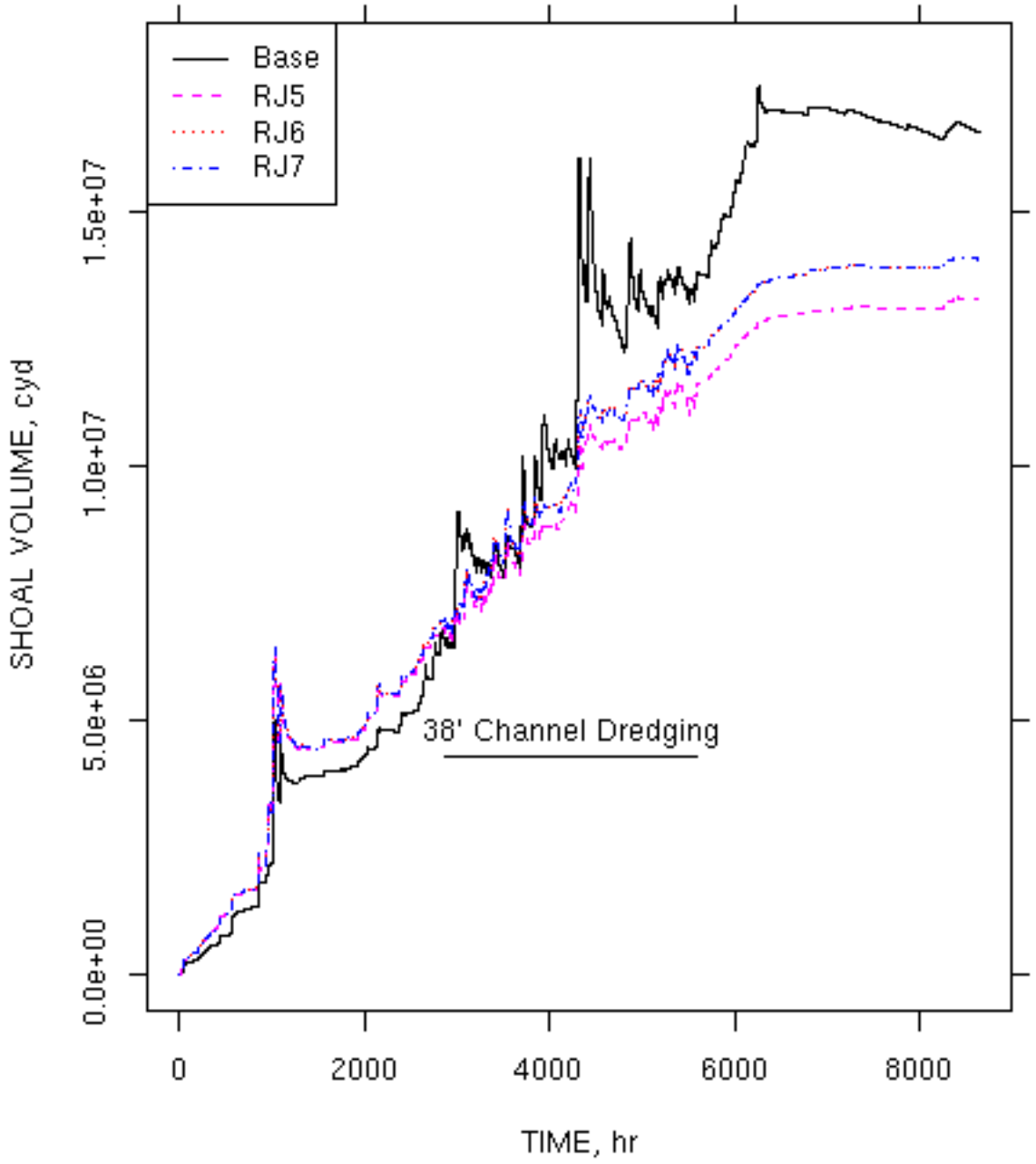

Figure 125. Shoal volume time history for *RJ5, RJ6,* and *RJ7* plans

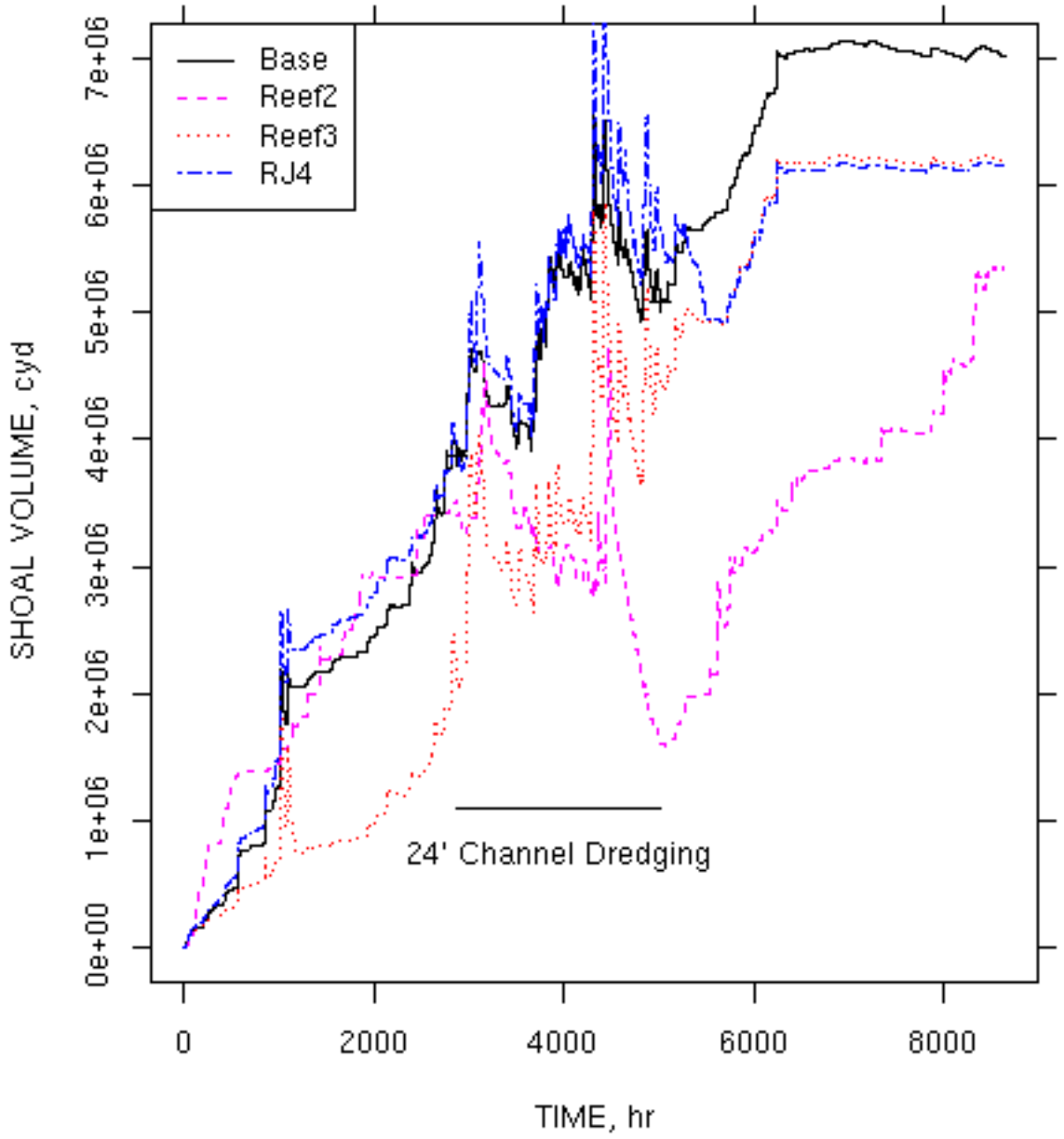

Figure 126. Shoal volume time history for *Reef2, Reef3,* and *RJ4* plans

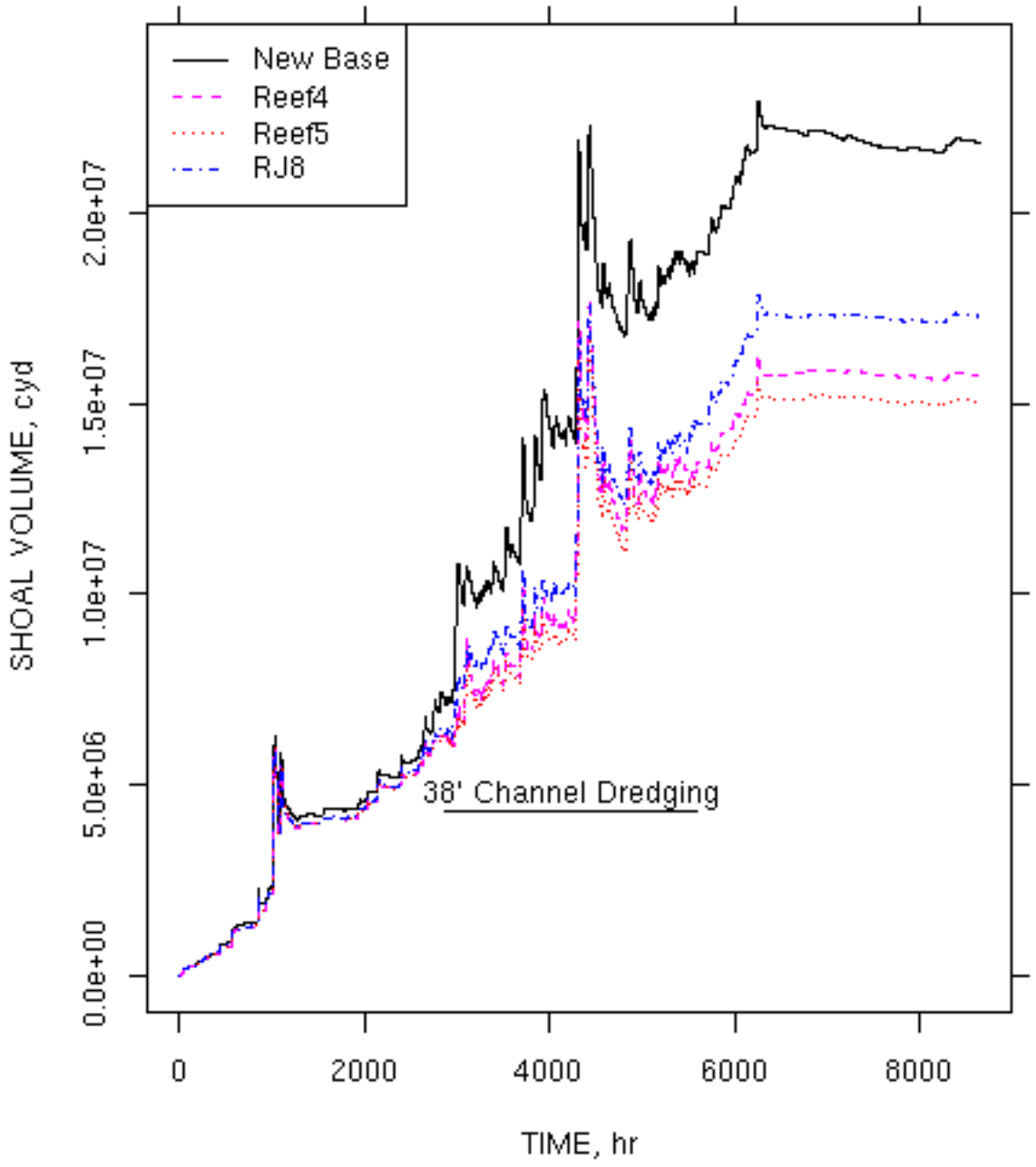

Figure 127. Shoal volume time history for *Reef4, Reef5,* and *RJ8* plans

APPENDIX A: CH3DZ Theory

CH3D-Z is a general-purpose 3D hydrodynamic model for simulating flows in rivers, lakes, and coastal areas. The numerical grid is boundary-fitted in the horizontal with the vertical dimension being either Cartesian (Z-plane) or sigma-stretched. The Z-plane version has been selected for Lake Washington to better model stratification of the water column due to temperature effects.

The basic sigma stretched model CH3D-σ was originally developed by Sheng (1986- the references for this appendix are given in the reference part of the main text) for the US Army Engineer Waterways Experiment Station (WES), but was extensively modified by WES personnel. Those modifications consisted of different basic formulations as well as substantial recoding for more efficient computing. The Cartesian or Z-plane version was developed by Johnson, et al. (1991). As its name implies, CH3D-Z makes hydrodynamic computations on a curvilinear or boundary-fitted planform grid. Processes impacting bay-wide circulation and vertical mixing that are modeled include tides, wind, density effects (salinity and temperature), freshwater inflows, turbulence, and the effect of the earth's rotation.

Adequately representing the vertical turbulence is crucial to a successful simulation of stratification/destratification. What is referred to as a k-$\in$ turbulence model is employed. The boundary-fitted coordinates feature of the model provides enhancement to fit the irregular shoreline configuration of Lake Washington and permits adoption of an accurate and economical grid schematization. The solution algorithm employs an external mode consisting of vertically averaged equations to provide the solution for the free surface to the internal mode consisting of the full 3-D equations. Model details are discussed below.

Basic Equations

The basic equations for an incompressible fluid in a right-handed Cartesian coordinate system (x, y, z) are:

$$\frac{\partial u}{\partial x}+\frac{\partial v}{\partial y}+\frac{\partial w}{\partial z}=0 \tag{A1}$$

$$\frac{\partial u}{\partial t}+\frac{\partial u^2}{\partial x}+\frac{\partial uv}{\partial y}+\frac{\partial uw}{\partial z}=fv-\frac{1}{\rho}\frac{\partial p}{\partial x}+\frac{\partial}{\partial x}\left(A_H\frac{\partial v}{\partial x}\right)$$
$$+\frac{\partial}{\partial y}\left(A_H\frac{\partial u}{\partial y}\right)+\frac{\partial}{\partial z}\left(A_v\frac{\partial u}{\partial z}\right) \tag{A2}$$

$$\frac{\partial v}{\partial t}+\frac{\partial uv}{\partial x}+\frac{\partial v^2}{\partial y}+\frac{\partial vw}{\partial z}=-fu-\frac{1}{\rho}\frac{\partial p}{\partial y}+\frac{\partial}{\partial x}\left(A_H\frac{\partial v}{\partial x}\right)$$
$$+\frac{\partial}{\partial y}\left(A_H\frac{\partial v}{\partial y}\right)+\frac{\partial}{\partial z}\left(A_v\frac{\partial v}{\partial z}\right) \quad \text{(A3)}$$

$$\frac{\partial p}{\partial z}=-\rho g \quad \text{(A4)}$$

$$\frac{\partial T}{\partial t}+\frac{\partial uT}{\partial x}+\frac{\partial vT}{\partial y}+\frac{\partial wT}{\partial z}$$
$$=\frac{\partial}{\partial x}\left(K_H\frac{\partial T}{\partial x}\right)+\frac{\partial}{\partial y}\left(K_H\frac{\partial T}{\partial y}\right)+\frac{\partial}{\partial z}\left(K_v\frac{\partial T}{\partial z}\right) \quad \text{(A5)}$$

$$\frac{\partial S}{\partial t}+\frac{\partial uS}{\partial x}+\frac{\partial vS}{\partial y}+\frac{\partial wS}{\partial z}$$
$$=\frac{\partial}{\partial x}\left(K_H\frac{\partial S}{\partial x}\right)+\frac{\partial}{\partial y}\left(K_H\frac{\partial S}{\partial y}\right)+\frac{\partial}{\partial z}\left(K_v\frac{\partial S}{\partial z}\right) \quad \text{(A6)}$$

$$\rho=\rho(T,S) \quad \text{(A7)}$$

where

(u,v,w) = velocities in x-, y-, z-directions

t = time

f = Coriolis parameter defined as $2\Omega\sin\phi$ where Ω is the rotational speed of the earth and ϕ = latitude

ρ = density

p = pressure

A_H,K_H = horizontal turbulent eddy coefficients

A_v,K_v = vertical turbulent eddy coefficients

g = gravitational acceleration

T = temperature

S = salinity

Equation A4 implies that vertical accelerations are negligible. Thus, the pressure is hydrostatic.

Various forms of the equation of state can be used for Equation A7. In the present model, Equation A8 is used:

$$\rho = P/(\alpha + 0.698P) \tag{A8}$$

where

$$P = 5890 + 38T - 0.375T^2 + 3S \tag{A9}$$

$$\alpha = 1779.5 + 11.25T - 0.0745T^2 \tag{A10}$$

and T is in degrees Celsius (^{o}C), S is in parts per thousand (ppt), and ρ is in g/cm^3.

Working with the dimensionless form of the governing equations makes it easier to compare the relative magnitude of various terms in the equations. Therefore, the following dimensionless variables are used:

$$(u^*, v^*, w^*) = (u, v, wX_r / Z_r)/U_r \tag{A11}$$

$$(x^*, y^*, z^*) = (x, y, zX_r / Z_r)/X_r \tag{A12}$$

$$(\tau_x^*, \tau_y^*) = (\tau_x^w, \tau_y^w)/\rho_0 f Z_r U_r \tag{A13}$$

$$t^* = tf \tag{A14}$$

$$\zeta^* = g\zeta / fU_r X_r = \zeta / S_r \tag{A15}$$

$$\rho^* = (\rho - \rho_o)/(\rho_r - \rho_o) \tag{A16}$$

$$T^* = (T - T_0)/(T_r - T_0) \tag{A17}$$

$$A_H^* = A_H / A_{Hr} \tag{A18}$$

$$A_v^* = A_v / A_{vr} \tag{A19}$$

$$K_H^* = K_H / K_{Hr} \tag{A20}$$

$$K_v^* = K_v / K_{vr} \tag{A21}$$

where

$\left(\tau_x^w, \tau_y^w\right)$ = wind stress in x-, y-directions

ζ = water-surface elevation

ρ_0, T_0 = typical values for the water density and temperature

and S_r, T_r, U_r, ρ_r, X_r, Z_r, A_{Hr}, A_{vr}, K_{Hr}, and K_{vr} are arbitrary reference values of the salinity, temperature, velocity, density, horizontal dimension, vertical dimension, horizontal viscosity, vertical viscosity, horizontal diffusion, and vertical diffusion, respectively. This then yields the following dimensionless parameters in the governing equations:

a. Vertical Ekman number:
$$E_v = A_{vr} / fZ_r^2 \tag{A22}$$

b. Lateral Ekman number:
$$E_H = A_{Hr} / fX_r^2 \tag{A23}$$

c. Vertical Prandtl (Schmidt) number:
$$\mathrm{Pr}_v = A_{vr} / K_{vr} \tag{A24}$$

d. Lateral Prandtl (Schmidt) number:
$$\mathrm{Pr}_H = A_{Hr} / K_{Hr} \tag{A25}$$

e. Froude number:
$$F_r = U_r / \left(gZ_r\right)^{1/2} \tag{A26}$$

f. Rossby number:
$$R_0 = U_r / fX_r \tag{A27}$$

g. Densimetric Froude number:
$$F\mathrm{r}_D = F_r / \sqrt{\epsilon} \tag{A28}$$

where

$$\epsilon = \left(\rho_r - \rho_0\right) / \rho_0 \tag{A29}$$

External-Internal Modes

The basic equations (Equations A1 through A8) can be integrated over the depth to yield a set of vertically integrated equations for the water surface, ζ, and unit flow rates U and V in the x-direction and y-directions. Using the dimensionless variables (asterisks have been dropped) and the parameters previously defined, the vertically integrated equations constituting the external mode are:

$$\frac{\partial \zeta}{\partial t} + \beta\left(\frac{\partial U}{\partial x} + \frac{\partial V}{\partial y}\right) = 0 \tag{A30}$$

$$\begin{aligned}\frac{\partial U}{\partial t} &= -H\frac{\partial \zeta}{\partial x} + \tau_{sx} - \tau_{bx} + V \\ &- R_0\left[\frac{\partial}{\partial x}\left(\frac{UU}{H}\right) + \frac{\partial}{\partial y}\left(\frac{UV}{H}\right)\right] \\ &+ E_H\left[\frac{\partial}{\partial x}\left(A_H\frac{\partial U}{\partial x}\right) + \frac{\partial}{\partial y}\left(A_H\frac{\partial U}{\partial y}\right)\right] \\ &- \frac{R_0}{Fr_D^2}\frac{H^2}{2}\frac{\partial \rho}{\partial x}\end{aligned} \tag{A31}$$

$$\begin{aligned}\frac{\partial V}{\partial t} &= -H\frac{\partial \zeta}{\partial y} + \tau_{sy} - \tau_{by} - U \\ &- R_0\left[\frac{\partial}{\partial x}\left(\frac{UV}{H}\right) + \frac{\partial}{\partial y}\left(\frac{VV}{H}\right)\right] \\ &+ E_H\left[\frac{\partial}{\partial x}\left(A_H\frac{\partial V}{\partial x}\right) + \frac{\partial}{\partial y}\left(A_H\frac{\partial V}{\partial y}\right)\right] \\ &- \frac{R_0}{Fr_D^2}\frac{H^2}{2}\frac{\partial \rho}{\partial y}\end{aligned} \tag{A32}$$

where

$$\beta = gZ_r / f^2 X_r^2 = \left(R_0 / F_r\right)^2 \tag{A33}$$

H = total depth

τ_s, τ_b = surface and bottom shear stresses

As will be discussed later, the major purpose of the external mode is to provide the updated water-surface field.

The dimensionless form of the internal mode equations from which the 3-D velocity, salinity, and temperature fields are computed are:

$$\frac{\partial hu}{\partial t} = -h\frac{\partial \zeta}{\partial x} + E_v \frac{\partial}{\partial z}\left(A_v \frac{\partial hu}{\partial z}\right) + hv$$
$$-R_0\left(\frac{\partial huu}{\partial x} + \frac{\partial huv}{\partial y} + \frac{\partial huw}{\partial z}\right)$$
$$+E_H\left[\frac{\partial}{\partial x}\left(A_H \frac{\partial hu}{\partial x}\right) + \frac{\partial}{\partial y}\left(A_H \frac{\partial hu}{\partial y}\right)\right]$$
$$-\frac{R_0}{Fr_D^2}\left(\int_z^\zeta \frac{\partial \rho}{\partial x} dz\right) \qquad \text{(A34)}$$

$$\frac{\partial hv}{\partial t} = -h\frac{\partial \zeta}{\partial y} + E_v \frac{\partial}{\partial z}\left(A_v \frac{\partial hv}{\partial z}\right) - hu$$
$$-R_0\left(\frac{\partial hvu}{\partial x} + \frac{\partial hvv}{\partial y} + \frac{\partial hvw}{\partial z}\right)$$
$$+E_H\left[\frac{\partial}{\partial x}\left(A_H \frac{\partial hv}{\partial x}\right) + \frac{\partial}{\partial y}\left(A_H \frac{\partial hv}{\partial y}\right)\right]$$
$$-\frac{R_0}{Fr_D^2}\left(\int_z^\zeta \frac{\partial \rho}{\partial y} dz\right) \qquad \text{(A35)}$$

$$w_{k+½} = w_{k-½} - \left(\frac{\partial uh}{\partial x} + \frac{\partial vh}{\partial y}\right) \qquad \text{(A36)}$$

$$\frac{\partial hT}{\partial t} = \frac{E_v}{\mathrm{Pr}_v}\frac{\partial}{\partial z}\left(K_v \frac{\partial T}{\partial z}\right) - R_0\left(\frac{\partial huT}{\partial x} + \frac{\partial hvT}{\partial y} + \frac{\partial hwT}{\partial z}\right)$$
$$+\frac{E_H}{\mathrm{Pr}_H}\left[\frac{\partial}{\partial x}\left(K_H \frac{\partial hT}{\partial x}\right) + \frac{\partial}{\partial y}\left(K_H \frac{\partial hT}{\partial y}\right)\right] \qquad \text{(A37)}$$

$$\frac{\partial hS}{\partial t} = \frac{E_v}{\mathrm{Pr}_v}\frac{\partial}{\partial z}\left(K_v \frac{\partial S}{\partial z}\right) - R_0\left(\frac{\partial huS}{\partial x} + \frac{\partial hvS}{\partial y} + \frac{\partial hwS}{\partial z}\right)$$
$$+\frac{E_H}{\mathrm{Pr}_H}\left[\frac{\partial}{\partial x}\left(K_H \frac{\partial hS}{\partial x}\right) + \frac{\partial}{\partial y}\left(K_H \frac{\partial hS}{\partial y}\right)\right] \qquad \text{(A38)}$$

In these equations h is the thickness of an internal layer, w is the vertical component of the velocity, and k+1/2 and k-1/2 represent the top and bottom, respectively, of the k^{th} vertical layer.

Boundary-Fitted Equations

To better resolve complex geometries in the horizontal directions, CH3D-Z makes computations on the boundary-fitted or generalized curvilinear planform grid shown in Figure 6 of the main text. This necessitates the transformation of the governing equations into boundary-fitted coordinates (ξ,η). If only the x- and y-coordinates are transformed, a system of equations similar to those solved by Johnson (1980) for vertically averaged flow fields is obtained. However, in CH3D-Z not only are the x- and y-coordinates transformed into the (ξ,η) curvilinear system, but also the velocity is transformed such that its components are perpendicular to the (ξ,η) coordinate lines: i.e., contravariant components of the velocity are computed. This is accomplished by employing the following definitions for the components of the Cartesian velocity (u, v) in terms of contravariant components $\bar{u}$ and $\bar{v}$

$$u = x_\xi \bar{u} + x_\eta \bar{v} \tag{A39}$$

$$v = y_\xi \bar{u} + y_\eta \bar{v} \tag{A40}$$

along with the following expressions for replacing Cartesian derivatives

$$f_x = \frac{1}{J}\left[\left(fy_\eta\right)_\xi - \left(fy_\xi\right)_\eta\right] \tag{A41}$$

$$f_y = \frac{1}{J}\left[-\left(fx_\eta\right)_\xi + \left(fx_\xi\right)_\eta\right] \tag{A42}$$

where J is the Jacobian of the transformation defined as

$$J = y_\eta y_\eta - x_\eta y_\xi \tag{A43}$$

With the governing equations written in terms of the contravariant components of the velocity, boundary conditions can be prescribed on a boundary-fitted grid in the same manner as on a Cartesian grid since $\bar{u}$ and $\bar{v}$ are perpendicular to the curvilinear cell faces (e.g., at a land boundary, either $\bar{u}$ or $\bar{v}$ is set to zero).

As noted, the vertical dimension in CH3D-σ is handled through the use of what is commonly called a sigma-stretched grid. However, with a sigma-stretched grid, the bottom layer in one column communicates with the bottom layer in an adjacent column even though they are at different depths. Thus, if depth changes are rather coarsely resolved, channel stratification cannot be maintained. As a result, the governing equations, Equations A44 – A48, presented for solution on the Cartesian or z-plane in the vertical direction are the ones constituting the internal mode.

With the Cartesian coordinates and the Cartesian velocity transformed, the following boundary-fitted equations for $\bar{u}$, $\bar{v}$, w, S, and T to be solved in each vertical layer are obtained.

$$\frac{\partial h\bar{u}}{\partial t} = -h\left(\frac{G_{22}}{J^2}\frac{\partial \zeta}{\partial \xi} - \frac{G_{12}}{J^2}\frac{\partial \zeta}{\partial \eta}\right) + \frac{h}{J}\left(G_{12}\bar{u} + G_{22}\bar{v}\right) + \frac{R_o x_\eta}{J^2}$$
$$\left[\frac{\partial}{\partial \xi}\left(Jy_\xi h\overline{uu} + Jy_\eta h\overline{uv}\right) + \frac{\partial}{\partial \eta}\left(Jy_\xi h\overline{uv} + Jy_\eta h\overline{vv}\right)\right] - \frac{R_o y_\eta}{J^2}$$
$$\left[\frac{\partial}{\partial \xi}\left(Jx_\xi h\overline{uu} + Jx_\eta h\overline{uv}\right) + \frac{\partial}{\partial \eta}\left(Jx_\xi h\overline{uv} + Jx_\eta h\overline{vv}\right)\right] - R_0$$
$$\left[\left(w\bar{u}\right)_{top} - \left(w\bar{u}\right)_{bot}\right] + E_v\left[\left(A_v\frac{\partial \bar{u}}{\partial z}\right)_{top} - \left(A_v\frac{\partial \bar{u}}{\partial z}\right)_{bot}\right]$$
$$-\frac{R_0 h}{Fr_D^2}\left[\int_z^\zeta\left(\frac{G_{22}}{J^2}\frac{\partial \rho}{\partial \xi} - \frac{G_{12}}{J^2}\frac{\partial \rho}{\partial \eta}\right)dz\right] + \textit{Horizontal Diffusion} \qquad \text{(A44)}$$

$$\frac{\partial h\bar{v}}{\partial t} = -h\left(-\frac{G_{21}}{J^2}\frac{\partial \zeta}{\partial \xi} + \frac{G_{11}}{J^2}\frac{\partial \zeta}{\partial \eta}\right) - \frac{h}{J}\left(G_{11}\bar{u} + G_{21}\bar{v}\right) - \frac{R_o x_\xi}{J^2}$$
$$\left[\frac{\partial}{\partial \xi}\left(Jy_\xi h\overline{uu} + Jy_\eta h\overline{uv}\right) + \frac{\partial}{\partial \eta}\left(Jy_\xi h\overline{uv} + Jy_\eta h\overline{vv}\right)\right] + \frac{R_o y_\xi}{J^2}$$
$$\left[\frac{\partial}{\partial \xi}\left(Jx_\xi h\overline{uu} + Jx_\eta h\overline{uv}\right) + \frac{\partial}{\partial \eta}\left(Jx_\xi h\overline{uv} + Jx_\eta h\overline{vv}\right)\right] - R_0$$
$$\left[\left(w\bar{v}\right)_{top} - \left(w\bar{v}\right)_{bot}\right] + E_v\left[\left(A_v\frac{\partial \bar{v}}{\partial z}\right)_{top} - \left(A_v\frac{\partial \bar{v}}{\partial z}\right)_{bot}\right]$$
$$-\frac{R_0 h}{Fr_D^2}\left[\int_z^\zeta\left(-\frac{G_{21}}{J^2}\frac{\partial \rho}{\partial \xi} + \frac{G_{11}}{J^2}\frac{\partial \rho}{\partial \eta}\right)dz\right] + \textit{Horizontal Diffusion} \qquad \text{(A45)}$$

$$w_{top} = w_{bot} - \frac{1}{J}\left(\frac{\partial J\bar{u}h}{\partial \xi} + \frac{\partial J\bar{v}h}{\partial \eta}\right) \qquad \text{(A46)}$$

$$\frac{\partial hS}{\partial t} = \frac{E_v}{\mathrm{Pr}_v}\left[\left(K_v\frac{\partial S}{\partial z}\right)_{top} - \left(K_v\frac{\partial S}{\partial z}\right)_{bot}\right] - \frac{R_o}{J}\left(\frac{\partial hJ\bar{u}S}{\partial \xi} + \frac{\partial hJ\bar{v}S}{\partial \eta}\right) \qquad \text{(A47)}$$
$$-R_0\left[\left(wS\right)_{top} - \left(wS\right)_{bot}\right] + \textit{Horizontal Diffusion}$$

$$\frac{\partial hT}{\partial t} = \frac{E_v}{\mathrm{Pr}_v}\left[\left(K_v \frac{\partial T}{\partial z}\right)_{top} - \left(K_v \frac{\partial T}{\partial z}\right)_{bot}\right] - \frac{R_o}{J}\left(\frac{\partial hJ\overline{u}T}{\partial \xi} + \frac{\partial hJ\overline{v}T}{\partial \eta}\right)$$
$$-R_0\left[\left(wT\right)_{top} - \left(wT\right)_{bot}\right] + \textit{Horizontal Diffusion} \tag{A48}$$

where

$$G_{11} = x_\xi^2 + y_\xi^2 \tag{A49}$$

$$G_{22} = x_\eta^2 + y_\eta^2 \tag{A50}$$

$$G_{12} = G_{21} = x_\xi x_\eta + y_\xi y_\eta \tag{A51}$$

Similarly, the transformed external mode equations become:

$$\frac{\partial \zeta}{\partial t} + \beta\left(\frac{\partial \overline{U}}{\partial \xi} + \frac{\partial \overline{V}}{\partial \eta}\right) = 0 \tag{A52}$$

$$\frac{\partial \overline{U}}{\partial t} = -\frac{H}{J^2}\left(G_{22}\frac{\partial \zeta}{\partial \xi} - G_{12}\frac{\partial \zeta}{\partial \eta}\right)$$
$$+\frac{1}{J}\left(G_{12}\overline{U} + G_{22}\overline{V}\right) + \frac{R_0 x_n}{J^2 H}\left[\frac{\partial}{\partial \xi}\left(Jy_\xi \overline{U}\overline{U} + Jy_\eta \overline{U}\overline{V}\right) + \frac{\partial}{\partial \eta}\left(Jy_\xi \overline{U}\overline{V} + Jy_\eta \overline{V}\overline{V}\right)\right]$$
$$-\frac{R_0 y_\eta}{J^2}\left[\frac{\partial}{\partial \xi}\left(Jx_\xi \overline{U}\overline{U} + Jx_\eta \overline{U}\overline{V}\right) + \frac{\partial}{\partial \eta}\left(Jx_\xi \overline{U}\overline{V} + Jx_\eta \overline{V}\overline{V}\right)\right]$$

$$+\tau_{s\xi} - \tau_{b\xi} - \frac{R_0}{Fr_D^2}\frac{H^2}{2}\left(G_{22}\frac{\partial \rho}{\partial \xi} - G_{12}\frac{\partial \rho}{\partial \eta}\right) + \textit{Horizontal Diffusion} \tag{A53}$$

$$\frac{\partial \overline{V}}{\partial t} = -\frac{H}{J^2}\left(-G_{21}\frac{\partial \zeta}{\partial \xi} + G_{11}\frac{\partial \zeta}{\partial \eta}\right)$$
$$-\frac{1}{J}\left(G_{11}\overline{U} + G_{21}\overline{V}\right) - \frac{R_0 x_\xi}{J^2 H}\left[\frac{\partial}{\partial \xi}\left(Jy_\xi \overline{U}\overline{U} + Jy_\eta \overline{U}\overline{V}\right) + \frac{\partial}{\partial \eta}\left(Jy_\xi \overline{U}\overline{V} + Jy_\eta \overline{V}\overline{V}\right)\right]$$
$$+\frac{R_0 y_\xi}{J^2 H}\left[\frac{\partial}{\partial \xi}\left(Jx_\xi \overline{U}\overline{U} + Jx_\eta \overline{U}\overline{V}\right) + \frac{\partial}{\partial \eta}\left(Jx_\xi \overline{U}\overline{V} + Jx_\eta \overline{V}\overline{V}\right)\right]$$

$$+\tau_{s\eta} - \tau_{b\eta} - \frac{R_0}{Fr_D^2}\frac{H^2}{2}\left(-G_{21}\frac{\partial \rho}{\partial \xi} + G_{11}\frac{\partial \rho}{\partial \eta}\right) + \textit{Horizontal Diffusion} \tag{A54}$$

where $\overline{U}$ and $\overline{V}$ are contravariant components of the vertically averaged velocity.

Equations A52 - A54 are solved first to yield the water-surface elevations, which are then used to evaluate the water-surface slope terms in the internal mode equations. The horizontal diffusion terms are presented in the last section of this appendix.

Numerical Solution Algorithm

Finite differences are used to replace derivatives in the governing equations, resulting in a system of linear algebraic equations to be solved in both the external and internal modes. A staggered grid is used in both the horizontal and vertical directions of the computational domain. In the horizontal directions, a unit cell consists of a ζ-point in the center ($\zeta_{i,j}$), a U-point on its left face ($U_{i,j}$), and a V-point on its bottom face ($V_{i,j}$). In the vertical direction, the vertical velocities are computed at the "full" grid points. Horizontal velocities, temperature, salinity, and density are computed at the "half" grid points (half grid spacing below the full points).

The external mode solution consists of the surface displacement and vertically integrated contrvariant unit flows $\overline{U}$ and $\overline{V}$. All of the terms in the transformed vertically averaged continuity equation are treated implicitly, whereas, only the water surface slope terms in the transformed vertically averaged momentum equations are treated implicitly. If the external mode is used purely as a vertically averaged model, the bottom friction is also treated implicitly. Those terms treated implicitly are weighted between the new and old time-steps. The resulting finite difference equations are then factored such that a ξ-sweep followed by an η-sweep of the horizontal grid yields the solution at the new time-step.

Writing Equations A30 - A32 as

$$\frac{\partial \zeta}{\partial t} + \beta\left(\frac{\partial \overline{U}}{\partial \xi} + \frac{\partial \overline{V}}{\partial \eta}\right) = 0 \tag{A55}$$

$$\frac{\partial \overline{U}}{\partial t} + \frac{H}{J^2} G_{22} \frac{\partial \zeta}{\partial \eta} = M \tag{A56}$$

$$\frac{\partial \overline{V}}{\partial t} + \frac{H}{J^2} G_{11} \frac{\partial \zeta}{\partial \eta} = N \tag{A57}$$

where M and N are the remaining terms in Equations A31 and A32, the ξ-sweep is

$$\xi - sweep \rightarrow \zeta_{ij}^{*} + \frac{\beta\theta\Delta t}{\Delta\xi}\left(\overline{U}_{i+1,j}^{*} - \overline{U}_{ij}^{*}\right)$$
$$= \zeta_{ij}^{n}(1-\theta)\frac{\Delta t}{\Delta\xi}\left(\overline{U}_{i+1,j}^{n} - \overline{U}_{ij}^{n}\right)\frac{\Delta t}{\Delta\eta}\left(\overline{V}_{i,j+1}^{n} - \overline{V}_{ij}^{n}\right) \quad \text{(A58)}$$

where θ is a parameter determining the degree of implicitness and

$$\overline{U}_{ij}^{n+1} + \frac{\theta\Delta t HG_{22}}{\Delta\xi J^{2}}\left(\zeta_{ij}^{*} - \zeta_{i-1,j}^{*}\right)$$
$$= \overline{U}_{ij}^{n} - (1-\theta)\frac{\Delta t HG_{22}}{\Delta\xi J^{2}}\left(\zeta_{ij}^{n} - \zeta_{i-1,j}^{n}\right) + \Delta t M^{n} \quad \text{(A59)}$$

The η-sweep then provides the updated ζ and $\overline{V}$ at the n+1 time level.

$$\eta - sweep \rightarrow \zeta_{ij}^{n+1} + \frac{\beta\theta\Delta t}{\Delta\eta}\left(\overline{V}_{i,j+1}^{n+1} - \overline{V}_{ij}^{n+1}\right)$$
$$= \zeta_{i,j}^{*} - (1-\theta)\frac{\Delta t}{\Delta\eta}\left(\overline{V}_{i,j+1}^{n} - \overline{V}_{i,j}^{n}\right) + \frac{\Delta t}{\Delta\eta}\left(\overline{V}_{i,j+1}^{n} - \overline{V}_{i,j}^{n}\right) \quad \text{(A60)}$$

and

$$\overline{V}_{i,j}^{n+1} + \frac{\theta\Delta t HG_{11}}{\Delta\eta J^{2}}\left(\zeta_{i,j+1}^{n+1} - \zeta_{i,j}^{n+1}\right)$$
$$= \overline{V}_{i,j}^{n} - (1-\theta)\frac{\Delta t HG_{11}}{\Delta\eta J^{2}}\left(\zeta_{i,j+1}^{n} - \zeta_{i,j}^{n}\right) + \Delta t N^{n} \quad \text{(A61)}$$

A typical value of θ of 0.55 yields stable and accurate solutions.

The internal mode consists of computations from Equations A44 - A48 for the three velocity components $\overline{u}$, $\overline{v}$, and w; salinity; and temperature. The same time-step size is used for both internal and external modes. The only terms treated implicitly are the vertical diffusion terms in all equations and the bottom friction and surface slope terms in the momentum equations. Values of the water-surface elevations from the external mode are used to evaluate the surface slope terms in Equations A44 and A45. As a result, the extremely restrictive speed of a free-surface gravity wave is removed form the stability criteria. Roache's second upwind differencing is used to represent the convective terms in the momentum equations, whereas, a spatially third-order scheme developed by Leonard (1979) called QUICKEST is used to represent the advective terms in Equations A47 and A48 for salinity and temperature, respectively. For example, if the velocity on the right face of a computational cell is positive, then with QUICKEST the value of the salinity used to compute the flux through the face is

$$S_R = \frac{1}{2}\left(S_{i,j,k} + S_{i+1,j,k}\right) - \frac{1}{6}\left[1 - \left(\frac{\overline{U}_{i+1,j,k}\Delta t}{\Delta \xi}\right)^2\right]\left(S_{i+1,j,k} - 2S_{i,j,k} + S_{i-1,j,k}\right) - \frac{1}{2}\left(\frac{\overline{U}_{i+1,j,k}\Delta t}{\Delta \xi}\right)\left(S_{i+1,j,k} - S_{i,j,k}\right) \quad \text{(A62)}$$

Turbulence Parameterization

The effect of vertical turbulence is modeled using the concept of eddy viscosity and diffusivity to parameterized the velocity and density correlation terms that arise from a time averaging of the governing equations. The eddy coefficients are computed through the implementation of what is referred to as a k-$\in$ turbulence model. This model is a two-equation model for the computation of the kinetic energy of the turbulence (k) and the dissipation of turbulence ($\in$). Both time evolution and vertical diffusion are retained, and the effects of surface wind shear, bottom shear, velocity gradient turbulence production, dissipation, and stratification are included. The basic idea behind the k-$\in$ turbulence model (Rodi 1980) is that the vertical eddy viscosity coefficient can be related to the turbulent kinetic energy per unit mass, k, and its rate of dissipation, $\in$, and an empirical coefficient ($c_v = 0.09$) by:

$$A_z = c_v \frac{k^2}{\in} \quad \text{(A63)}$$

The transport equations for the turbulence quantities are:

$$\frac{\partial(k)}{\partial t} - \frac{\partial}{\partial z}\left(A_z \frac{\partial k}{\partial z}\right) = \left(P_z - \in + G\right) \quad \text{(A64)}$$

$$\frac{\partial(\in)}{\partial t} - \frac{\partial}{\partial z}\left(\frac{A_z}{\sigma_\in}\frac{\partial \in}{\partial z}\right) = \left(c_1 \frac{\in}{k} P_z - c_2 \frac{\in^2}{k}\right) \quad \text{(A65)}$$

in which $\sigma_\in = 1.3$, $c_1 = 1.44$, and $c_2 = 1.92$ (Rodi 1980). The source and sink terms on the right-hand side of Equations A64 and A65 represent mechanical production of turbulence due to velocity gradients (P_z) and buoyancy production or destruction (G) due to water column stratification. Surface (s) and bottom (b) boundary conditions for the turbulence quantities are specified as:

$$k_{s,b} = \frac{U_*^2}{\sqrt{c_v}} \quad \text{(A66)}$$

$$\in_{s,b} = \frac{U_*^3}{\mathrm{K}\dfrac{\Delta z}{2}} \tag{A67}$$

where κ is the von Karman constant (= 0.4). The friction velocity, U_*, used for the surface boundary condition is defined as the square root of the resultant wind shear stress divided by the water density. The bottom friction velocity is computed in an identical way with the wind shear stress being replaced by the bottom shear stress. The suppression of the vertical diffusivity by stratification is given by:

$$\mathrm{K}_z = A_v \left(1 + 3R_i\right)^{-2} \tag{A68}$$

where R_i is the Richardson Number (Bloss et at. 1988).

Boundary Conditions

The boundary conditions at the free surface are

$$A_v \left(\frac{\partial \bar{u}}{\partial z}, \frac{\partial \bar{v}}{\partial z} \right) = \left(\tau_{s\xi}, \tau_{s\eta} \right) / \rho = \left(CW_\xi^2, CW_\eta^2 \right) \tag{A69}$$

$$\frac{\partial T}{\partial z} = \frac{\mathrm{Pr}}{E_v} \mathrm{K} \left(T - T_e \right) \tag{A70}$$

$$\frac{\partial S}{\partial z} = 0 \tag{A71}$$

whereas the boundary conditions at the bottom are

$$A_v \left(\frac{\partial \bar{u}}{\partial z}, \frac{\partial \bar{v}}{\partial z} \right) = \left(\tau_{b\xi}, \tau_{b\eta} \right) / \rho = \frac{U_r}{A_{vr}} Z_r C_d \left(\bar{u}_1^2 + \bar{v}_1^2 \right)^{1/2} \left(\bar{u}_1, \bar{v}_1 \right) \tag{A72}$$

$$\frac{\partial T}{\partial z} = 0 \tag{A73}$$

$$\frac{\partial S}{\partial z} = 0 \tag{A74}$$

where

C = surface drag coefficient

W = wind speed

K = surface heat exchange coefficient

T_e = equilibrium temperature

C_d = bottom friction coefficient

$\bar{u}_1$, $\bar{v}_1$ = values of the horizontal velocity components next to the bottom

With z_1 equal to one-half the bottom layer thickness, C_d is given by

$$C_d = k^2 \left[1n\left(z_{1/} z_0 \right) \right]^{-2} \tag{A75}$$

where

k = von Karman constant

z_0 = bottom roughness height

Manning's formulation is employed for the bottom friction in the external mode equations if the model is used purely to compute vertically averaged flow fields.

As can be seen from Equation A69, the surface shear stress is computed from wind data. As presented by Garratt (1977), the surface drag coefficient is computed from

$$C = \left(0.75 + 0.067W \right) \times 10^{-3} \tag{A76}$$

with the maximum allowable value being 0.003.

As discussed by Edinger, Brady, and Geyer (1974), the surface heat exchange coefficient, K, and the equilibrium temperature, T_e, are computed from meteorological data (wind speed, cloud cover, dry bulb air temperatures, and either wet bulb air temperature or relative humidity).

At river boundaries, the freshwater inflow and its temperature are prescribed and the salinity is assumed to be zero. At tidal boundaries, the water-surface elevation is prescribed along with time-varying vertical distributions of salinity and temperature. In the next chapter, it will be seen that this type of boundary condition was selected at the dam in the Ship Canal.

Initial Conditions

At the start of model run, the values of ζ, $\bar{u}$, $\bar{v}$, w, $\overline{U}$, and $\overline{V}$ are all set to zero. Values of the salinity and temperature are read from input files. These initial fields are generated

from known data at a limited number of locations. Once the values in individual cells are determined by interpolating from the field data, the resulting 3-D field is smoothed several times.

Horizontal Diffusion Terms

The X and Y horizontal diffusion terms used in the boundary-fitted contravariant velocity component Equations A44, A45, A53, and A54 for both internal and external modes, and in the salinity and temperature transport Equations A47 and A48 are presented below.

X – Horizontal Diffusion

$$
\begin{aligned}
&= \frac{Y_\eta}{J^2}\left[\frac{A_h G_{22}}{J}\left[\left(X_\xi H\bar{u}\right)_\xi + \left(X_\eta H\bar{v}\right)_\xi\right]\right]_\xi \\
&+ \frac{Y_\eta}{J^2}\left[\frac{A_h G_{11}}{J}\left[\left(X_\xi H\bar{u}\right)_\eta + \left(X_\eta H\bar{v}\right)_\eta\right]\right]_\eta \\
&- \frac{X_\eta}{J^2}\left[\frac{A_h G_{11}}{J}\left[\left(Y_\xi H\bar{u}\right)_\eta + \left(Y_\eta H\bar{v}\right)_\eta\right]\right]_\eta \\
&- \frac{Y_\eta}{J^2}\left[\frac{A_h G_{12}}{J}\left[\left(X_\xi H\bar{u}\right)_\eta + \left(X_\eta H\bar{v}\right)_\eta\right]\right]_\xi \\
&- \frac{Y_\eta}{J^2}\left[\frac{A_h G_{12}}{J}\left[\left(X_\xi H\bar{u}\right)_\xi + \left(X_\eta H\bar{v}\right)_\xi\right]\right]_\eta \\
&+ \frac{X_\eta}{J^2}\left[\frac{A_h G_{12}}{J}\left[\left(Y_\xi H\bar{u}\right)_\eta + \left(Y_\eta H\bar{v}\right)_\eta\right]\right]_\xi \\
&+ \frac{X_\eta}{J^2}\left[\frac{A_h G_{12}}{J}\left[\left(Y_\xi H\bar{u}\right)_\xi + \left(Y_\eta H\bar{v}\right)_\xi\right]\right]_\eta
\end{aligned}
\qquad \text{(A77)}
$$

Y – Horizontal Diffusion

$$
\begin{aligned}
&= \frac{X_\xi}{J^2}\left[\frac{A_h G_{11}}{J}\left[\left(Y_\eta H\overline{v}\right)_\eta + \left(Y_\xi H\overline{u}\right)_\eta\right]\right]_\eta \\
&- \frac{Y_\xi}{J^2}\left[\frac{A_h G_{11}}{J}\left[\left(X_\eta H\overline{v}\right)_\eta + \left(X_\xi H\overline{u}\right)_\eta\right]\right]_\eta \\
&+ \frac{X_\xi}{J^2}\left[\frac{A_h G_{22}}{J}\left[\left(Y_\eta H\overline{v}\right)_\xi + \left(Y_\xi H\overline{u}\right)_\xi\right]\right]_\xi \\
&- \frac{Y_\xi}{J^2}\left[\frac{A_h G_{22}}{J}\left[\left(X_\eta H\overline{v}\right)_\xi + \left(X_\xi H\overline{u}\right)_\xi\right]\right]_\xi \\
&- \frac{X_\xi}{J^2}\left[\frac{A_h G_{12}}{J}\left[\left(Y_\eta H\overline{v}\right)_\eta + \left(Y_\xi H\overline{u}\right)_\eta\right]\right]_\xi \\
&- \frac{X_\xi}{J^2}\left[\frac{A_h G_{12}}{J}\left[\left(Y_\eta H\overline{v}\right)_\xi + \left(Y_\xi H\overline{u}\right)_\xi\right]\right]_\eta \\
&+ \frac{Y_\xi}{J^2}\left[\frac{A_h G_{12}}{J}\left[\left(X_\eta H\overline{v}\right)_\eta + \left(X_\xi H\overline{u}\right)_\eta\right]\right]_\xi \\
&+ \frac{Y_\xi}{J^2}\left[\frac{A_h G_{12}}{J}\left[\left(X_\eta H\overline{v}\right)_\xi + \left(X_\xi H\overline{u}\right)_\xi\right]\right]_\eta
\end{aligned}
\qquad \text{(A78)}
$$

APPENDIX B: Sediment Transport Model Description for CH3DZ-FM

This appendix describes the cohesive sediment transport formulation added to CH3DZ. The three-dimensional, curvilinear, hydrostatic hydrodynamics model CH3DZ was modified to include single-grain, cohesive sediment suspended transport and bed transport of fluid mud on a slope. CH3DZ is a z-plane finite difference model that has fixed layer thickness (except for the top layer) and is described in Appendix A.

Important differences between coarse- and fine-grained sediment transport characteristics can be attributed to cohesive effects. Cohesive forces act at very small distances and are affected by clay mineralogy, ion content and composition, pH, and temperature. Cohesive bonding under field conditions also includes organic coatings and steric bonds of organic origin. Cohesion acts to form several structural levels of progressively weaker aggregation for clay minerals. Three general differences between cohesive and coarse-grained (greater than 62 μm) sediment transport under moderate shear stresses included in the sediment model include:

1. Cohesive sediments are only transported in suspended state, whereas coarse-grained sediments are also transported in quasi-contact with the bed as bed load.
2. Cohesive sediments are not transported as dispersed, individual particles. Flocculation increases settling velocities by many orders of magnitude and is responsible for deposition.
3. Cohesive sediment beds undergo appreciable volume and erodibility changes with time.

When rapid deposition occurs, deposits are low-density and have little hydraulic shear strength. Cohesive beds can be uniform but more often are vertically stratified by density and hydraulic shear strength.

Both settled mud and fluid mud processes are included in the model and are applied in the model depending on the local surface concentration or density. A layered bed structure simulates the formation of a surface layer through hindered-settling consolidation of newly-deposited material and tracks the descent of an

erosive surface into the bed, if necessary. Depending on the sediment surface density, cohesive sediment transport is treated either as settled mud (particle erosion and floc deposition) or as fluid mud (fluid entrainment and settling). Wind wave resuspension is an important process to suspended sediment, and winds are used by both hydrodynamic and sediment transport sub-models. A model module computes down slope gravity forces and density-dependent yield stresses through the fluid mud layer and moves material accordingly.

Coupling to Hydrodynamics

The sediment transport model is directly coupled to the hydrodynamic model. For three dimensions, the advection-diffusion equation for sediment transport is

$$\frac{DC}{Dt} - \frac{\partial}{\partial x}\left(D_x \frac{\partial C}{\partial x}\right) - \frac{\partial}{\partial y}\left(D_y \frac{\partial C}{\partial y}\right) - \frac{\partial}{\partial z}\left(D_z \frac{\partial C}{\partial z}\right) = 0 \qquad \text{(B1)}$$

where C is the concentration of suspended material, DC/Dt is the total derivative that includes advection, and D_x , D_y , $D_z = x, y, z$ eddy diffusivity components for sediment mass. Diffusivities generally include the effects of small-scale motions such as Langmuir circulations, as well as turbulence. The effective vertical velocity w_e is substituted for w in the total derivative DC/Dt where $w_e = w - Ws$, and Ws is the settling velocity. The surface boundary is given a no-flux condition and the bottom boundary condition is

$$\frac{\partial}{\partial z}\left(w_e C - D_z \frac{\partial C}{\partial z}\right) = E - D \qquad \text{(B2)}$$

where E is the vertical erosional flux and D is the vertical depositional flux. Dimensions of the erosion and deposition fluxes are mass per unit area per unit time. The sediment model formulations described later in this appendix specify expressions for E and D and conditions over which they operate. With these exceptions, the numerical scheme used for suspended sediment transport is the same as used for salinity transport as described in Appendix A.

Suspended sediment affects fluid density and is included in the hydrodynamic equation of state. The density of the water depends on salinity S and temperature T, and the equation of state is

$$\rho = \rho(S,T) + \Delta\rho \,, \quad \Delta\rho = C\,(\rho_s - \rho(S,T))\,/\,\rho_s \qquad \text{(B3)}$$

where $\rho(S,T)$ is the CH3DZ salinity- and temperature-dependent fluid density described in Appendix A, and ρ_s is the sediment particle density. Through density,

hydrodynamic vertical diffusivities and circulation are coupled to the concentration effect of suspended sediments.

Another way the sediment model is coupled to CH3DZ is through the effect of salinity on settling velocity *Ws*. Most of this effect is manifest at low salinity values *S*, and the description used for this is

$$Ws(S,C) = Ws(C)\,(S + c1) / (S + c2) \tag{B4}$$

where $Ws(C)$ is the fully-flocculated, concentration-dependent settling velocity described below, and *c1* and *c2* are constants. Thus, *Ws* reaches one-half its maximum value when $S = c2 - 2c1$.

The hydrodynamic and sediment models are also coupled through sedimentation effects on the bed elevation. During model execution, CH3DZ-FM checks changes in bed thickness resulting from deposition, erosion, or bed consolidation, and if that change exceeds the thickness of a computational cell, a cell is added or dropped from the computational mesh.

Cohesive Sediment Processes

Concentration effects on settling velocity.

Floc settling velocity is defined as the sinking rate in quiescent fluid. It affects vertical transport and distribution in the water column and maximum rate of deposition. Settling velocity of cohesive sediments varies with concentration and with fluid shear rate (Camp 1946, Krone 1962, Van Leussen 1989, Kranck and Milligan 1992, Malcherek and Zielke 1996, Teeter 2001). Suspension concentration affects cohesive sediment aggregate collision frequency, floc size, and settling rate. Enhanced settling occurs over a concentration range from a lower concentration limit C_{ll} to an upper concentration limit C_{ul}. Below C_{ll}, particle collisions are too infrequent to promote aggregation. C_{ll} is typically 50 to 300 mg/l depending on sediment characteristics. At C_{ul}, collisions are so numerous that particles interact completely, causing all floc settling rates to converge to one value. At concentrations greater than C_{ul}, particle interactions begin to hinder settling, and dense suspensions settle as masses. Camp (1946) found the onset of concentration-hindered settling to be 1 to 5 kg/m^3 for turbid river water. The C_{ul} has been found to be 1 to 10 kg/m^3 for estuarine sediments (Krone 1962, Teeter and Pankow 1989a, Teeter 1993, Teeter 2002, Teeter, et al. 2002).

A general form for velocity *Ws* is used in the model

$$Ws = a_1\left(\frac{C}{C_{ul}}\right)^n, \quad C_{ll} \le C \le C_{ul} \tag{B5}$$

where *a1* is a maximum floc settling velocity, *n* is an exponent, and C_{ll} and C_{ul} are lower and upper reference concentrations, respectively, over which concentration-enhanced settling occurs. The exponent *n* has been determined to range below a value of about 1.33 as estimated with this method. Teeter and Pankow (1989a) found that *n*'s for the 50 and 75 percentile values were progressively less than for the 25 percent slowest settling fraction.

At concentrations below C_{ll}, *Ws* has a constant value. At concentrations above C_{ul}, hindered settling begins and

$$Ws = a1\left(1 - b1\,C\right)^{b2}, \quad C > C_{ul} \tag{B6}$$

where *b1* and *b2* are constants.

Deposition rate.

Deposition removes sediment from the water column at a rate equal to the product of effective settling and concentration. To deposit, sediment must transit the zone just above the bed, which can have very high shear rates. Previous laboratory experiments (Krone 1962, Teeter and Pankow 1989b) have observed that effective *Ws* based on deposition are lower than those measured in the water column. The calculation procedures presented in this section first assess the deposition process for individual grain classes, then couple grain-size classes such that the final result depends on deposition of the coarsest active class and the grain-size spectra.

Potential deposition of each grain-size class is first assessed. Deposition is assessed differently for the cohesive fraction than for silts. The cohesive fraction is taken to follow Krone's deposition law (Krone 1962), which uses the concept of a critical shear stress for deposition and the depositional probability. The effective settling velocity is the settling velocity times the depositional probability *P* defined by Krone (1962) and for the finest cohesive fraction is

$$P = \left(1 - \frac{\tau}{\tau_{cd}}\right), \quad \tau < \tau_{cd} \tag{B7}$$

where τ is the bed shear stress and τ_{cd} is the critical threshold shear stress for deposition. According to Equation B7, all sediment eventually deposits at shear stresses less than the critical value. Threshold shear-stresses for mutually exclusive

erosion and deposition are used in the model formulation to be consistent with previous laboratory investigations.

However, wind-wave resuspension seems to not always follow mutually exclusive erosion and deposition (Aalderink et al 1985, Luettich et al. 1990, Sanford and Halka 1993). While a well-sorted cohesive suspension will steadily deposit in a flow below a critical shear stress (Krone 1962), a suspension of silts and clays will partially deposit to a steady state, constant-suspension concentration level (Partheniades et al. 1968). A similar paradox is that clay minerals segregate during transport in a manner that is similar to their settling rates based on dispersed particle size (Gibbs 1977). Thus, even though grain classes are coupled by cohesion, dispersed particle size affects transport properties, and size-distribution imprints form clearly detectable patterns in estuarine and lake sediments.

Mehta and Partheniades (1975) performed annular-flume deposition experiments, starting with high shear stresses. Initially-suspended fine-grained cohesive sediments deposited when shear stresses were reduced, and formed constant, steady-state concentrations that depended on the initial suspension concentrations and the bed shear-stresses. Each experiment had 1 g/l initial concentration of kaolinite. The kaolinite sediment material contained about 35 percent sediment coarser than 2 μm and a maximum particle size of about 45 μm. Similar results were obtained for coarser, fine-grained sediments from San Francisco Bay and Maracaibo Bay, Venezuela. The degree of deposition ($1 - C_f / C_o$) was found not to depend on initial concentration. This result, plus other experiments on kaolinite suspensions by Partheniades et al. (1968) and Lau and Krishnappan (1994), confirms that these steady-state concentrations were not caused by a balance between erosion and deposition.

The cohesive clay-silt deposition results follow Krone's deposition law for bed shear-stresses less than 0.16 Pa, when all sediment eventually deposited. At higher bed shear stresses, however, they do not follow Krone's deposition law, as only a certain fraction of material, depending on shear-stress, deposited. Material either deposited or remained in suspension, with the transition time consistent with typical settling velocities.

To account for high shear-stress steady state suspensions, an alternate expression for depositional probability is substituted when τ becomes greater than τ_{cd}. An expression was developed specifically for single-grain modeling of wind-wave resuspension of silty clay and clayey silt fine-grained sediments (Teeter and Best, 2003):

$$P = e1 \exp(-e2\, \tau_{cd} / (\tau - \tau_{cd})) \quad , \quad \tau > \tau_{cd} \tag{B8}$$

where *e1* and *e2* are constants. The depositional flux D is

$$D = P\,Ws\,C \tag{B9}$$

where C here is the concentration just above the bed. At high shear stresses, the P according to Equation B8 approaches 1.0 and steady-state concentrations are formed approximately as

$$C(steady-state) \cong C_{ul}^{\frac{n}{n+1}} \left(\frac{M}{a1}\right)^{\frac{1}{n+1}} \left(\frac{\tau_{ce}}{\tau} - 1\right)^{\frac{m1}{n+1}}, \quad \tau >> \tau_{ce}$$

where the new terms will be defined in the following subsection. Though this equation is not directly used in the model, it illustrates how Equations B2, B5, B8, B9, and B10 (presented below) act together in the model to effectively form steady-state suspensions.

Erosion rate.

The single grain-class erosion flux depends first on the erosion threshold of the cohesive fraction and then on the erosion thresholds for silt fractions. The form of the cohesive erosion model depends on excess bed shear stress τ similarly to the erosion equation of Alishahi and Krone (1964), and is

$$E = M\left[\frac{\tau}{\tau_{ce}} - 1\right]^{m1}, \qquad \tau > \tau_{ce} \tag{B10}$$

where M is an erosion rate parameter and τ_{ce} is the erosion threshold, both evaluated at the sediment bed surface. With the exponent $m1 = 1$, Equation B10 is similar to the erosion equations of Kandia (1974) and Ariathurai et al. (1977). If $\tau < \tau_{ce}$, no cohesive sediments are eroded even if the bed shear-stress exceeds the critical threshold for some silts. The critical shear stress for erosion of the cohesive fraction is estimated by a power law depending on the concentration of the cohesive fraction in the bed layer exposed to the flow (Thorn and Parsons 1980, Teeter 1987) and generally increases vertically downward in the bed. The erosion rate parameter M is functionally related to the τ_{ce} value according to the expression of Lee and Mehta (1994).

$$\tau_{ce} = d1\,Cs_i^{d2} \tag{B11}$$

$$M = 200\,\tau_{ce}\exp\left(-s1\;\tau_{ce}^{s2}\right) \tag{B12}$$

where *d1*, *d2*, *s1* and *s2* are constants and Cs_i is the solids content at the bed surface.

Bed-layer model.

Cohesive sediment erodibility depends on surface density and is also linked to the structure of the bed (Dixit 1982), so sediment models often use a layered bed structure (Ariathurai et al. 1977, Teisson 1991, Hamm et al. 1997). A layered-bed algorithm was developed with variable concentrations by layers, depending on initial conditions, and on local erosion and deposition history. The bed layer module is similar to that used in TABS-MDS for Laguna Madre (Teeter, et al. 2002) except that in this case the density varies more smoothly in the vertical. For the fully settled condition, and in the absence of any erosional contacts between layers, the density/concentration profile of the bed is continuous. This eliminates artificial discontinuities in density structure that can occur in some bed layer formulations. Each layer is initially assigned a solids concentration *Cs* (mass per unit volume) at its bottom and top surfaces and a thickness *Hs*. The concentration at the bottom of a layer is forced to match the concentration of the top of the layer immediately below it, etc. Ths is accomplished by specifying the layer top solids content *Cs*(*bl*). Then at the bottom of the layer *Cs* = *Cs*(*bl* + 1). If the bed layer thickness is equal to the fully-settled condition *Hso*, then the solids content at the top of the layer $Cs_i = Cs(bl)$. If the layer thickness is less than *Hso*, then

$$Cs_i(bl) = Cso(bl+1) - (Cso(bl+1) - Cso(bl))\, Hs(bl)/Hso(bl) \tag{B13}$$

If the layer thickness is greater than *Hso*(*bl*), $Cs_i(bl)$ remains equal to *Cso*(*bl*).

A fully-settled, near-surface concentration distribution is assumed. After deposition occurs, hindered-settling rate is calculated by bed layer, and material is transported vertically downward in the bed until the specified density distribution is achieved. The conservation equation for sediment mass *S* for bed layer consolidation is

$$\frac{dS(bl)}{dt} = -\frac{W_h(bl)S(bl)}{H_s(bl)} + \frac{W_h(bl-1)S(bl-1)}{H_s(bl-1)}, \quad H_s(bl) > H_{so}(bl) \tag{B14}$$

where $H_s(bl)$ is the bed layer thickness, $H_{so}(bl)$ is the specified fully-settled thickness, and the bed-layer hindered-settling rate is

$$W_h(bl) = W_{ho}\left[1 - b_1\frac{S(bl)}{H_s(bl)}\right]^{b_2}, \qquad \frac{S(bl)}{H_s(bl)} < \frac{1}{b_1} \tag{B15}$$

where W_{ho} is a reference settling rate, and b_1 and b_2 are coefficients. Hindered settling is inhibited by deposition or erosion greater than 0.01 g/m^2/sec. In the bed, volumes of grain-size classes are taken into account during the conversion between mass and concentration. The sediment mixture is composed of sediment and water. Specifically, it is assumed that

$$H_s(bl) = \frac{S(bl)}{\rho_s} + \frac{O_c S(bl)}{\rho_l} \tag{B16}$$

where O_c is the ratio of cohesive silt and clay mass to water masses, and ρ_s and ρ_l are the particle and fluid densities. While mass is transported vertically downward as a result of consolidation, the layer concentration of the cohesive fraction is maintained constant over time. Bed layer sediment concentration (mass per unit volume) *Cs* is $S(bl)/H_s(bl)$.

To reproduce observed hindered settling interface descent curves, some restrictions must be applied due to the discrete nature of the model. The step changes in layer concentration must be such that $(Cs(bl) - Cs(bl-1))/Cs(bl)$ is about constant over depth, and a factor based on this ratio must be applied to W_{ho} .

The bed-layer model formulation is based on the kinematic sedimentation theory and is a simplification of a number of complex processes. It is intended to be used for calculating the settling and consolidation of thin layers of newly-deposited sediment over time scales of days to a small number of weeks. For thicker deposits especially, permeability becomes important as the upward velocity of water must equal downward sedimentation (Tan et al. 1990, Pane and Schiffman 1997). At longer times and greater deposit thicknesses, inter-particle stresses develop, and self-weight consolidation occurs. Over an important range of times and concentrations, both sedimentation and self-weight consolidation probably occur (Toorman and Berlamont 1991).

Bed layers are numbered vertically downward starting with *bl* equal zero. If a layer is withered away by erosion, it disappears, at least temporarily. The erosion surface thus descends through the bed as the surface layer thins, then step-wise through progressively deeper layers. The effect of erosion on bed mass are evaluated as

$$\left.\frac{dS(bl=a)}{dt}\right|_e = -E \tag{B17}$$

where a is the exposed bed layer index. On the other hand, deposition, always occurs into the first layer ($bl = 1$), and the effect of deposition on bed mass is evaluated as

$$\left.\frac{dS(bl=1)}{dt}\right|_d = F \tag{B18}$$

In this way, the bed structure is formed by consolidation from the top layer down. After appreciable deposition has occurred, the bed (in the absence of erosion or further deposition) will eventually return to the specified fully-settled structure.

Fluid Mud Processes

Entrainment and settling.

When cohesive sediment bed density is very low, τ_{ce} approaches zero and the material is referred to as fluid mud. Fluid mud can form in areas of high sediment availability and where hydrodynamic energy is great enough and consistent enough to prevent settling and consolidation. The behavior of fluid mud is more like that of a fluid than a settled mud. The fluid mud entrainment process is identical to other two-fluid system with density variations.

Entrainment depends on the local momentum balance, turbulence at the fluid mud interface, and the magnitude of density differences. At high interfacial Richardson numbers (Ri_*), dimensionless entrainment (Em) is the result of perturbations in the interface between the turbulent water column and the underlying fluid mud. (Also assuming that the molecular Peclet number = $u_1 l_1 / \nu$ is greater than 200 where u_1 and l_1 are the turbulent velocity and length scales, and ν is molecular diffusivity.) Under conditions of turbulence without mean-flow, the laboratory experiments of Long (1975) and E and Hopfinger (1986) confirmed the -3/2 power law described by Linden (1973), i.e.,

$$Em = \frac{u_e}{u_*} = K Ri_*^{-3/2} \tag{B19}$$

where u_e is the entrainment velocity or the downward velocity of the interface, K is a constant, and the interfacial Richardson number is defined slightly differently from Ri as

$$Ri_* = \frac{g\Delta\bar{\rho}h}{\bar{\rho}u_*^2} \tag{B20}$$

where the density step across the interface $\Delta\bar{\rho} = \rho - \bar{\rho}$, $\bar{\rho}$ is the average density of the layers, and h is the depth of the water column above the underlying fluid mud. The scales for $\Delta\bar{\rho}$ and length can be chosen differently in different entrainment systems. Although the underlying fluid mud is stratified, the mechanism here causing that stratification involves settling and not diffusion across an interface. Thicknesses of density interfaces are typically about 6 percent of the depth of mixed layers, much thinner than the stratified underlying fluid mud layers observed here. Values of Ri_* are large, and interfacial perturbations are probably intermittent, consisting of vortex rebounding. Thus, $\Delta\bar{\rho}$ and h were scaled by the overall density step and the depth of the water column.

Entrainment and deposition to the underlying fluid mud by settling are assumed to be simultaneous processes in this case. Teeter (1994) reviewed laboratory entrainment experiments involving suspensions and found them to be consistent with an assumption of simultaneous entrainment and settling. Thus at a point over an underlying fluid mud

$$E - D = Em u_* Cs_i - Ws C \qquad \text{(B21)}$$

are the combined entrainment and settling flux rates at the interface.

Estimates for K were made based on field observations near a hydraulic dredge pipeline discharge (Teeter, et al. 2002). The median K value was 2.8 in fair agreement with the laboratory result of 3.8 reported by E and Hopfinger (1986).

Fluid mud flow on a slope.

Despite fluid-like character, fluid mud has psuedo-plastic and visco-elastic properties. If left undisturbed, fluid mud often gels and develops elasticity. The visco-plastic flow equation is

$$\tau - \alpha\tau_y = \eta_e G \qquad \text{(B22)}$$

where τ s the shear stress within the cohesive body, τ_y is the yield or initial shear stress, η_e is the effective viscosity, α is a numerical coefficient allowing for the effect of τ_y on the resistance to movement, and G is the shear or deformation rate. If τ_y exceeds τ, then no movement occurs (and $\alpha = 1$). If τ_y just exceeds τ, then movement is initiated and cohesion is partly disrupted with small particle movements. In this case, $0 < \alpha < 1$. At still higher τ, such as on a steep incline, disruption of the cohesive structure is complete and $\alpha = 0$. In the case of submarine mud slides on low slopes, the initiation of movement as the result of

its own weight occurs without much disruption of the cohesive body. This results in movement as a solid block (Pykhov 1973).

Once sheared or disrupted, the undisturbed static yield strength in the fracture zone is largely lost (thixotropy). The existence of a static yield stress may lead to an unsheared plug flow zone (Coussot 1994) if the underlying fluid mud is on a slope. The flow regime of the underflow is described by Richardson and Reynolds numbers. The bulk Richardson number for the flow is

$$Ri = \frac{g\,\Delta\rho\, hf \cos\theta}{\rho f\, Uf^2} \tag{B23}$$

where g is the acceleration of gravity, $\Delta\rho$ is the density difference between the underflow and the water column, hf is the underflow thickness, θ is the bed slope, ρf is the underflow density, and Uf is the underflow velocity. The head of a fluid mud underflow has Ri values of about 1.5 which is in sub-critical flow regime. The Reynolds number depends on viscous and yield properties of the fluid mud. These properties are very different from water and strongly dependent on both sediment concentration and clay content. The Reynolds number determines the transition from laminar to turbulent and hence is important to entrainment, frictional characteristics, and deposition.

For flow to initiate, the gravity stress τ_g developed by the fluid mud layer must exceed the yield stress for the material τ_y where

$$\tau_g = G1\, g\, \Delta\rho\, h_f \sin\theta \tag{B24}$$

$G1$ is a constant assumed to be 1.0, g is the acceleration of gravity, hf is the fluid mud layer thickness, and θ is the slope of the fluid mud interface. The yield stress can be empirically expressed as

$$\tau_y = TUY1 \left(\frac{Cs}{\rho_s} \right)^{TUY2} \tag{B25}$$

where TUY1 and TUY2 are constants. Rheological data on muds are relatively scarce.

To determine if fluid mud flow is initiated, the cell-centered slope is calculated from the corresponding CH3DZ cell-center distance ΔX, bottom elevation Z, and sediment layer thickness change db at each time step. The slope of the energy grade line is

$$Se = \frac{Z_1 - Z_2}{\Delta X} + \frac{db_1 - db_2}{\Delta X} + \frac{Uf_1^2 - Uf_2^2}{2g\Delta X} \quad \text{(B26)}$$

where *Uf* is the layer-average flow speed of the fluid mud layer and subscript indices refer to adjoining cells.

While analytical solutions for Equations B24 and B25 are possible when fluid mud density is uniform and constant, this is generally not the case. A numerical procedure is used that makes no assumption about the density structure of the material. Starting at the fluid mud surface and stepping downward in steps of about 2 mm, the local gravity stress is compared to the yield stress. There are three possible outcomes: (a) if the gravity stress is always less than the yield stress, no flow occurs; (b) if the gravity stress reaches the value of the yield stress at one point, flow occurs as a plug above this level; and (c) the gravity stress exceeds the yield stress over a finite layer thickness, flow occurs as a shear flow below a plug flow.

If fluid flow occurs, the layer average flow speed *Uf* is taken as equivalent to $Ri = 2$. Therefore *Uf* is

$$Uf = \left(\frac{1}{2} g\, hf \frac{\Delta\rho}{\rho} \cos\theta \right)^{1/2} \quad \text{(B27)}$$

and the plug flow speed *Up* is

$$Up = \frac{2\, hf\, Uf}{hf + hp} \quad \text{(B28)}$$

where *hp* is the plug flow thickness and *hf* is the total plug and shear flow thickness. A linear vertical profile is assumed below the plug layer and the flow speed goes to zero where $\tau_y(z)$ again is greater than $\tau(z)$.

The thicknesses and flow speeds from the fluid mud flow module are mapped onto the bed layer system described earlier. Fluxes are determined at upstream and downstream cell faces and used to update the layer mass structure of the cell layer-by-layer.

Example fluid-mud flow model results for two test cases are presented in Figure B1. In both cases, top layers were composed of a 0.5-m-thick layer of

51 kg/m^3 material over a 0.1-m-thick layer of 75 kg/m^3 material over a 0.19-m-thick layer of 109 kg/m^3 material. Yield parameters *TUY1* and *TUY2* were set at 16,320 Pa and 3.3. The first case was an overly-steep peak, and the second case was a trench with overly-steep sides. Computations were done over a short, seven-node channel with 1,000 m node spacing. No-flux conditions were imposed at the channel ends. In both cases, mass was conserved during simulations.

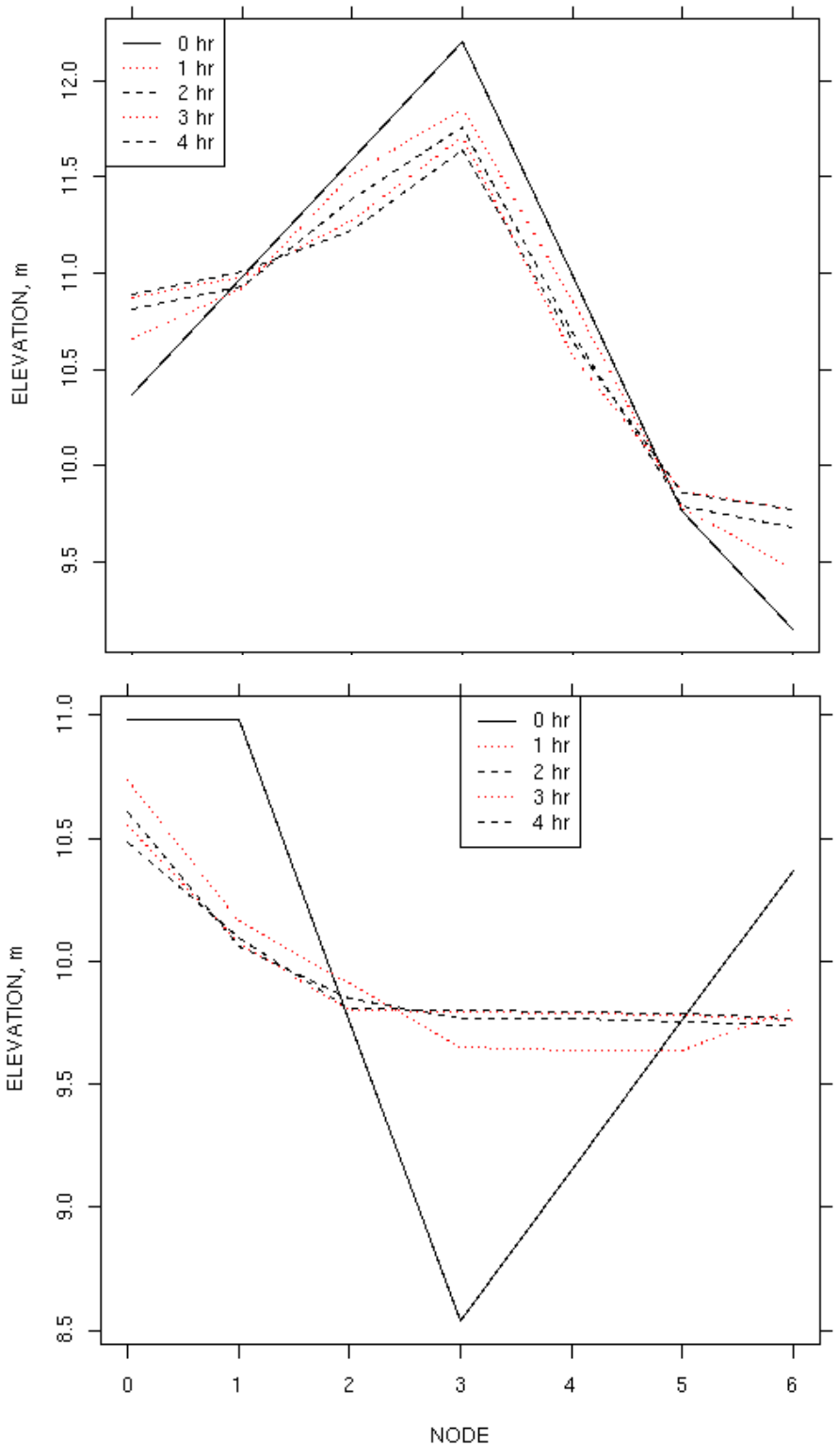

Figure B1. Fluid-mud flow test cases for peak (top) and trench (bottom)

Wind-Wave Shear Stress

The CH3DZ-FM model uses an atmospheric shear stress accounting to apply wind-wave shear stress to the sediment bed. This subsection first presents background information on other modeling approaches, atmospheric shear stress, depth-limited waves, and then presents the shear-stress budget approach used in the model.

Wind-generated waves produce shear stresses important to resuspension in shallow water areas, and are often included in sediment transport modeling. However, some resuspension models have successfully used wind alone without calculation of wave characteristics directly. Aalderink et al. (1985) compared four models, two using maximum near-bed wave orbital velocity and two using wind speed. Suspended sediment (TSM) data for a 1 m deep lake, collected hourly for two weeks were used in the model evaluation. The two models using wind alone (with and without wind thresholds) better matched the observed TSM than did the two resuspension models using wave-induced flows. All models compared used simultaneous erosion and deposition and a background concentration that was not subject to deposition.

Pejrup (1986) points out that, where wave heights and depths change appreciably, wind speed (being relatively constant over an area) may correlate better to TSM concentrations than wave height measured at a point. Analysis of time-series TSM from a micro-tidal estuary indicated that wind alone, regardless of direction, had the best correlation to TSM levels (Pejrup, 1986). Arfi et al. (1993) tested an expression relating wind speed and water column buoyancy to calculate thresholds for resuspension and obtained results that were similar in magnitude to wave-based threshold estimators. Although wave characteristics are critical, wave shear stress and the overall balance of momentum input from the atmosphere are critical to resuspension in large shallow lagoons and estuaries. These shallow water bodies respond to winds at small spatial scales (for example, depth-limited wind-generated waves, Langmuir circulation cells and buoyant eddy overturning).

Resuspension model studies of shallow systems have used wave measurements or results from wave models driven by winds to provide wave parameters for bottom shear stress calculations, and have been reasonably successful simulating TSM levels (Luettich et al. 1990, Hawley and Lesht 1992, Sheng et al. 1992, Lick et al. 1994). Near-bed wave orbital velocity depends on wave height and wave period and is the critical parameter for resuspension of bed sediments. Short-period oscillatory currents forced by wind-generated waves are more effective at developing bed shear stress than the same current magnitudes forced by tides due to

boundary layer effects (Luettich et al. 1990). In shallow water areas, waves "feel' the bottom when wave length exceeds twice the depth, and the resulting bottom stress can resuspend sediments and dissipate the waves. Moreover, wave growth in very shallow areas appears to be limited by depth, bottom friction, and fetch.

Whatever wave modeling approach is employed, a model requirement for an enclosed shallow water system should be that the total bed shear-stress over the model domain be less than the total atmospheric shear-stress. This cannot be assured unless atmospheric shear stress is calculated and compared to that from waves. Some amount of wave shear-stress is normally expended where waves break at the shoreline The interest here, however, is the wave shear-stress over the greater area of the sediment bed, and therefore shoreline processes will not be considered.

The most popular wave models for shallow water are the analytical methods presented in the Shore Protection Manual (CERC 1984). Relationships for wave energy loss due to bed friction and percolation were first developed by Bretschneider and Reed (1953). These have been used in successive approximations of shallow-water waves where wind stress was balanced by bed friction (CERC, 1984). Luettich and Harleman (1990) compared two analytical methods for estimating wave characteristics, including CERC (1984), for a large, shallow lake with a mean depth of 3.2 m. Wave measurements were collected at sites 2.0- and 2.2-m deep. Wind velocity was collected at 2-m height above the water surface. Wave hindcasts were found to give good wave height estimates but wave periods estimates were about 20 percent lower than the observations.

Atmospheric shear stress.

Atmospheric shear stress (τ_a , Pa) was calculated on the basis of wind speed U_a , in meters per second, at 10-m height:

$$\tau_a = \rho_a C_d U_a^2 \tag{B29}$$

where ρ_a is the air density (about 1.225 kg/m^3), and C_d is the atmospheric friction factor appropriate for wind referenced to 10-m height (CERC 1984). An important component of atmospheric shear stress comes from wave roughness at various scales, and C_d generally increases with increased wind speed, at least up to some high wind speed. The main transfer of momentum from the atmosphere to waves occurs at relatively short wave lengths of about 0.3-m (range 0.06 to 1 m) wavelength (Gemmrich et al. 1994), but transfer to slightly longer wavelengths is also appreciable (Donelan 1990, Lionello et al. 1998). Short waves are advected by the long-wave orbitals, reducing wind speed relative to short waves at long-wave crests and diminishing the

importance of short-wave roughness to atmospheric drag. The wind field is modified by dominant wavelengths (Lionello et al. 1998). Significant wave height H_s is the most often used, physically important, length scale used to estimate C_d. However, when waves are fetch- and/or duration-limited, the stage of wave development affects C_d. For a constant wind speed, C_d decreases as waves become higher, longer, and less steep.

With an assumed logarithmic velocity profile and neutral atmospheric stability, the atmospheric friction factor is dependent on surface roughness

$$C_d = \left(\frac{\kappa}{\ln (10/z_o)} \right)^2 \tag{B30}$$

where κ is the von Karman constant (0.4), and z_o is the surface roughness coefficient in meters. The latter is much smaller than H_s. At wind speeds greater than about 2.5 m/sec (those important in this study) air flow becomes aerodynamically rough and z_o is approximately a quadratic function of wind speed (Donelan 1990). For the turbulent-rough regime, Hsu (1974) related z_o to both wave steepness (significant wave height H_w over wave length L_w) and wave age (wave celerity C_w over atmospheric friction velocity U_{*a}) starting with

$$z_o = \frac{H_w}{g L_w} U_{*a}^2 \tag{B31}$$

and then substituting a deep-water relationship for L_w to obtain

$$z_o = \frac{H_w}{2 \pi C_w^2} U_{*a}^2 \tag{B32}$$

Hsu originally compared this latter formulation to a number of data sets, and recent comparisons have also found it to be reliable (Donelan 1990).

Various expressions have been developed for C_d. For fully-developed oceanic wave conditions, Hsu (1988) developed the following expression for C_d from Equation B30 by setting the ratio of C_w to U_{*a} equal to 29 and substituting an analytical expression for H_w into Equation B32:

$$C_d = \left(\frac{0.4}{14.56 - 2 \ln U_a} \right)^2 \tag{B33}$$

Various linear expressions have been proposed that relate C_d to U_a. For example, for oceanic conditions and neutral atmospheric stability, Garratt (1977) proposed $C_d = (7.5 + 0.67 U_a) x 10^{-4}$, Wu (1980) proposed $C_d = (8.0 + 0.65 U_a) x 10^{-4}$, while Atakturk and Katsaros (1999) found $C_d = (8.7 + 0.78 U_a) x 10^{-4}$ for Lake Washington, Washington.

The roughness height has also been related to Charnock's parameter α_c to include the effect of wave development

$$z_o = \alpha_c U_{*a}^2 / g \tag{B34}$$

Reported field values for α_c generally range from 0.012 to 0.035 for "old" and "young" waves respectively (Wu 1980, Hsu 1988, and Lionello et al. 1998). During the initial stage of wave development, roughness heights are much greater. Wu recommended using $\alpha_c = 0.0185$ in Equation B34 and proposed an additional term based on dimensional arguments

$$z_o = \frac{\alpha_c U_{*a}^2}{g}\left(\frac{\mu U_{*a}}{\gamma}\right)^{\beta-2} \tag{B35}$$

where μ is the dynamic viscosity of water, and γ is the surface tension. Wu suggests that the value of the exponent $2 < \beta < 2.5$ correctly defines the dependence of z_o on U_{*a}.

Janssen (1989) developed the following relationship for wave roughness:

$$z_o = \frac{\alpha_{cr} U_{*a}^2}{g(1 - \tau_{aw}/\tau_a)^{1/2}} \tag{B36}$$

where τ_{aw} is the atmospheric shear-stress going into the waves, and α_{cr} is a reference or reduced Charnock's parameter ($\equiv 0.01$). Lionello et al. (1998) used Equation B36 to test two-way coupling for atmospheric and ocean-wave models.

Reported values for the fraction of momentum transferred from the atmosphere to waves vary widely. Lionello et al. (1998) indicate that $\tau_a > \tau_{aw} > 0.15\tau_a$. As with surface roughness, the stage of wave development affects the fraction of momentum transferred from the atmosphere to waves. "Young," steep waves absorb a greater fraction of atmospheric shear stress as waves develop. Equations B34 and B36 suggest that

$$\frac{\tau_{aw}}{\tau_a} = 1 - (\alpha_{cr}/\alpha_c)^2 \tag{B37}$$

which implies that the shear-stress fraction transferred to waves is related to wave age, with about 95 percent of τ_a transferred to τ_{aw} during initial wave development and about 40 percent for old waves. Apparently, wave dissipation mechanisms more effectively shunt momentum into currents for old waves.

In a fully-developed wave field, when temporal and spatial variations of wave spectra are minimal, shear-stress input from the atmosphere is about equal to wave dissipation. Wave dissipation comes from various losses: friction, wave-wave interactions, white capping, and wave breaking. Wave breaking occurs in deep water when the wave steepness reaches or exceeds 0.14, and in shoaling water when the wave height exceeds about 80 percent of the depth (CERC 1984). White-capping occurs when wind separates at and de-stabilizes wave crests and especially when $C_w/U_{*a} < 1$ (Wu 1980). The resulting loss of wave energy is converted into mean-flow momentum and to turbulent mixing. Wave dissipation is not well understood in general, but it is recognized as important to momentum transfer from the atmosphere to the water column (Lionello et al. 1998). No consensus exists among researchers about the relative magnitudes of dissipation mechanisms, and more research is probably needed before a consensus can be reached.

For open-ocean, deep-water conditions, most of the atmospheric input eventually goes to the upper part of the water column (Richman and Garrett 1977). However, in shallow-water wave shear-stresses transmitted to the bed can be of the same order as the atmospheric shear stresses. For example, Sanford (1994) measured wave conditions during a January-1990 wind-wave resuspension event at a 3.4-m deep tripod station near Pooles Island in Upper Chesapeake Bay and estimated the wave shear stress to be 0.6 Pa at the bed. Winds were offshore at 11 m/sec and τ_a was apparently about 0.25 Pa. If in fact wave shear stress is of the same order as τ_a , less of the total τ_a input is transferred to currents in shallow water than in deeper water.

Depth-limited waves.

Analytical models for waves in shallow water are based on dimensionless parameters used to collapse data to power-law relations. For depth-limited waves, but otherwise fully-developed, models are of the form

$$E* = a_1 h*^{a_2} \tag{B38}$$

$$f* = a_3 h*^{a_4} \tag{B39}$$

where $E* = g^2 E_w/U_a^4$ is dimensionless wave energy, $h* = gh/U_a^2$ is dimensionless depth, $f* = U_a/gT_p$ is dimensionless wave frequency, $E_w = \sigma^2$ is the variance of the wave height field, and $E_w = H_w^2/16$, U_a is the wind speed adjusted to 10 m height in meters per second, and T_p is the spectral-peak wave period in seconds. CERC (1984) found the coefficients to be $a_1 = 1.4 \times 10^{-3}$, $a_2 = 1.5$, $a_3 = 0.16$, and $a_4 = -0.375$. Young and Verhagen (1996) found coefficients for Equations B38 and B39 to be $a_1 = 1.06 \times 10^{-3}$, $a_2 = 1.3$, $a_3 = 0.20$, and $a_4 = -0.375$.

Formulations that include the effects of fetch length are slightly more complicated. The depth-limited and deep-water cases form asymptotic limits which include the dimensionless fetch length $X^* = gx/U_a^2$ where x is the fetch length. For example, Young and Verhagen (1996) found

$$E^* = 3.64 \times 10^{-3} \left(\tanh A_1 \tanh \left[\frac{B_1}{\tanh A_1} \right] \right)^{1.74} \tag{B40}$$

where

$$A_1 = 0.493 h^{*0.75}, \qquad B_1 = 3.13 \times 10^{-3} X^{*0.57} \tag{B41}$$

Teeter, et al. (2002) used an alternate scaling for dimensionless wave energy and wave frequency in ultra-shallow water where the atmospheric friction velocity, $U_{*a} = C_d^{0.5} U_a$, was used in place of U_a. The wave-model expressions corresponding to Equations B38 and B39 are

$$E` = a_5 h^{*a_6} \tag{B42}$$

$$f` = a_7 h^{*a_8} \tag{B43}$$

where the new dimensionless parameters $E`$ and $f`$ equal $g^2 E_w/(C_d^2 U_a^4)$ and $C_d^{1/2} U_a/(g\, T_p)$, respectively. With these scalings, data were brought closer into line when plotted against h^*. Regressions were performed between $E`$ and h^* with data subsets for uniform wind, winds greater than 3 m/sec, and H_w values greater than the 25th percentile conditions. Results yielded exponents a_6 for h^* of between 1.73 and 2.11. The assumption of an exponent of 2.0 implies that $H_w \propto C_d h$, and regression with this form yielded the following empirical expression:

$$H_w = 84.6 h C_d - 0.056 \tag{B44}$$

where the intercept is apparently caused by the range of C_d which does not converge to zero at zero wind speed.

Regressions performed between $f`$ and h^* indicated an exponent a_8 of -0.5, thus $T_p \propto (h\, C_d/g)^{1/2}$ and further analysis indicated that

$$T_p = 126.5 (h C_d/g)^{0.5} \tag{B45}$$

approximates the peak wave period.

Shear stress budget.

Charnock's parameter decreases with wind speed, so that according to Equation B37, almost all shear stress is transferred to waves at low wind speeds, and greater portions of τ_a are dissipated by white-capping and/or water-column mixing, and less of the total input is dissipated by wave friction at higher wind speeds. Wave dissipation as a result of mixing or by excess steepness or relative depth was not considered.

For fully-developed waves (constant wave spectra), wave dissipation through total friction and white capping is assumed to be equal to the atmospheric shear stress at the water surface. Even when only a few percent of τ_a goes directly into currents as τ_{ac} , some part of τ_{aw} is subsequently transferred to τ_{ac} by white-capping, thus, τ_a is assumed to be partitioned between shear stress imparted to waves (τ_{aw}) and to currents (τ_{ac}):

$$\tau_a = \tau_{aw} + \tau_{ac} \tag{B46}$$

Ratios of τ_{aw}/τ_a were estimated by Teeter, et al. (2002). Regressing this ratio against wind speed gives an indication of the amount of atmospheric shear stress going into wave shear stress. By assuming that almost all atmospheric shear stress goes into waves at wind speeds 3 to 5 m/sec where a peak in the ratio occurred (assumed to be 0.97), results indicated that the amount decreases at higher wind speeds as

$$\frac{\tau_{aw}}{\tau_a} = 2.169\, U_a^{-0.5}, \qquad U_a > 5 \text{ m/sec} \tag{B47}$$

The peak wave shear stress is then 2.38 times the average shear stress.

A correction is applied so that if local wave conditions are deep-water, wave shear stress does not reach the bed. The correction is

$$\frac{\tau'_{aw}}{\tau_{aw}} = \exp(-l1\, h / Ua^2) \tag{B48}$$

where *l1* is a constant. There is an additional correction for the case when waves pass from shallow water over a channel. From linear wave theory

$$\frac{\tau''_{aw}}{\tau'_{aw}} = \frac{A''^2}{A'^2} = \frac{\sinh(2\pi d/Lw)^2}{\sinh(2\pi (d + \Delta H)/Lw)^2} \tag{B49}$$

where double primes denote values in the channel, A is the wave displacement at the bottom, d is the off-channel water depth, and ΔH is the depth difference between the channel and the surrounding area. For the model, an equivalent simpler expression was used

$$\frac{\tau''_{aw}}{\tau'_{aw}} = -0.16 - 0.33 \log\left(\frac{\Delta H}{d}\right) \tag{B50}$$

The wave shear stresses are added to current shear stresses vectorially using the wind direction as the direction of the waves.

References

Aalderink, R.H., Lijklema, L., Breukelman, J., van Raaphost, W., and Brinkman, A.G. (1985). "Quantification of wind induced resuspension in a shallow lake," *Wat. Sci. Tech*. 17: 903-914.

Ariathurai, R., MacArthur, R.C., and Krone, R.B. (1977). "Mathematical model of estuarine sediment transport," Tech. Rep. D-77-12, U.S. Army Engineer Waterways Experiment Station, Vicksburg, MS, 158 pp.

Alishahi, M.R., and Krone, R.B. (1964). "Suspension of cohesive sediments by wind-generated waves," Tech. Rep. HEL-2-9, Hydraulic Engrg. Lab., Univ. of California, Berkeley, 24 pp.

Arfi, R., Guiral, D., and Bouvy, M. (1993). "Wind induced resuspension in a shallow tropical lagoon," *Estua., Coastal Shelf Sci.* 36, 587-604.

Atakturk, S.S., and Katsaros, K.B. (1999). "Wind stress and surface waves observed on Lake Washington," *J. Phys. Oceanogr*. 29: 633-650.

Bretschneider, C.L., and Reid, R.O. (1953). "Change in wave height due to bottom friction, percolation and refraction," 34th Annual Meeting, American Geophys. Union, Washington, DC.

Camp, T.R. (1946). "Sedimentation and the design of settling tanks," American Society of Civil Engineers *Transactions* 111, 895-958.

CERC. (1984). Shore protection manual, volume 1. U.S. Army Engineer Waterways Experiment Station, Vicksburg, MS, 502 pp.

Dixit, J.G. (1982). "Resuspension potential of deposited kaolinite beds," M.S. Thesis, Univ. of Florida, Gainesville, FL, 168 pp.

Donelan, M. (1990). “Air-sea interactions,” In: B. LeMehaute and D. Hanes (eds.), *The Sea: Ocean Engineering Science, Volume 9A*, John Wiley & Sons, New York, NY.

E, X., and Hopfinger, E.J. (1986). "On mixing across an interface in stably stratified fluid," *J. Fluid Mech.* 166, 227-244.

Garratt, J. R. (1977). “Review of Drag coefficients over Oceans and Continents,” *Monthly Weather Review* 105, 915-29.

Gemmrich, J.R., Mudge, T.D., and Polonichko, V.D. (1994). "On the energy input from wind to surface waves," *J. Phys. Oceanogr.* 24, 2,413-2,417.

Gibbs, R.J. (1977). “Clay mineral segregation in the marine environment,” *J. Sedim. Petrol*. 47, 237-243.

Hamm, L., Chester, T., Fettweis, M., Pathirana, K.P.P. and Peltier, E. (1997). “An intercomparison exercise of cohesive transport models,” In: N. Burt, R.Parker, and J. Watts (eds), *Cohesive Sediments*. John Wiley and Sons, New York, NY, 449-458.

Hawley, N., and Lesht, B.M. (1992). “Sediment resuspension in Lake St. Clair,” *Limnol. Oceanogr*. 37, 1720-1737.

Hsu, S.A. (1974). “A dynamic roughness equation and its application to wind stress determination at the air-sea interface,” *J. Phys. Oceanogr*. 4, 16-20.

Hsu, S.A. (1988). Coastal meteorology. Academic Press, Inc., New York, NY, 260 pp.

Janssen, P.A.E.M. (1989). “Wave induced stress and the drag of the air over sea waves,” *J. Phys. Oceanogr*. 19, 745-754.

Kandiah, A. (1974). “Fundamental aspects of surface erosion of cohesive soils,” PhD. Thesis, Univ. Of California, Davis.

Kranck, K., and Milligan, T.G. (1992). “Characteristics of suspended particles at an 11-hour anchor station in San Francisco Bay, California,” *J. Geophys. Res*. 98(C6), 10279-10288.

Krone, R.B. (1962). “Flume studies of the transport of sediment in estuarial shoaling processes,” Hydraul. Engnr. Lab. and Sanit. Engnr. Res. Lab.,Univ. of California, Berkeley, CA, 109 pp.

Lau, Y.L. and Krishnappan, B.G. (1994). “Does reentrainment occur duringcohesive sediment settling?,” *J. Hydraul. Eng*. 120, 236-244.

Lee, S.-C., and Mehta, A.J. (1994). “Cohesive sediment erosion,” Contract Rep. DRP-94-6, U.S. Army Engineers Waterways Experiment Station, Vicksburg, MS, 83 pp.

Linden, P.F. (1973). “The interaction of a vortex ring with a sharp density interface: a model for turbulent entrainment,” *J. Fluid Mech*. 60, 467-480.

Lionello, P., Malguzzi, P., and Buzzi, A. (1998). “Coupling between the atmospheric circulation and the ocean wave field: An idealized case,” *J. Phys. Oceanogr*. 28, 161-177.

Long, R.F. (1975). “The influence of shear on mixing across density interfaces,” *J. Fluid Mech*. 70(20), 305-320.

Luettich, R.A., Harleman, D.R.F., and Somlyody, L. (1990). “Dynamic behavior of suspended sediment concentrations in a shallow lake perturbed by episodic wind events,” *Limnol. Oceanogr*. 35, 1050-1067.

Malcherek, A., and Zielke, W. (1996). “The role of macroflocs in estuarine sediment dynamics and its numerical modeling,” Proceedings American Society of Civil Engineers Estuarine and Coastal Modeling Conference, San Diego, CA.

Mehta, A.J., and Partheniades, E. (1975). “An investigation of the depositional properties of flocculated fine sediments,” *J. Hydraul. Res*. 13, 1037-1057.

Pane, V., and Schiffman, R.L. (1997). “The permeability of clay suspensions,” *Geotechnique* 47(2), 273-288.

Pejrup, M. (1986). "Parameters affecting fine-grained suspended sediment concentrations in a shallow micro-tidal estuary, Ho Burt, Denmark," *Estu., Coast., Shelf Sci.* 22, 241-254.

Partheniades, E., Cross, R.H., and Ayora, A. (1968). “Further results on the deposition of cohesive sediments,” Proc. 11th Conference on Coast. Engnr., London, England, 2, 723-742.

Pykhov, N.V.(1973). “The movement of sediments over an inclined seafloor after disturbance of their stability,” *Oceanology* 13, 893-896.

Richman, J. and Garrett, C. (1977). “The transfer of energy and momentum by the wind to the surface mixed layer,” *J. Phys. Oceanogr*. 7, 876-881.

Sanford, L.P. (1994). “Wave forced resuspension of upper Chesapeake Bay muds,” *Estuaries* 17(1B), 148-165.

Sanford, L.P., and Halka, J.P. (1993). “Assessing the paradigm of mutually exclusive erosion and deposition of mud, with examples from Upper Chesapeake Bay,” *Mar. Geol*. 114, 37-57.

Tan, T.S., Yong, K.Y., Leong, E.C., and Lee, S.L. (1990). “Sedimentation of clayey slurry,” *J. Geotechn. Engrg*. 116(6), 885-898.

Teeter, A.M. (1987). “Alcatraz disposal site investigation; Report 3: San Francisco Bay-Alcatraz disposal site erodibility,” Miscell. Paper HL-86-1,U.S. Army Engineer Waterways Experiment Station, Vicksburg, MS, 120 pp.

Teeter, A.M. (1993). “Suspended transport and sediment-size transport effects in a well-mixed, meso-tidal estuary,” In: A.J Mehta (ed.), *Nearshore and Estuarine Cohesive Sediment Transport*, American Geophysical Union, Washington, DC, 411-429.

Teeter, A.M. (1994). “Erosion by entrainment of fluidized cohesive sediments," Technical Note DRP-1-15, U.S. Army Engineer Waterways Experiment Station, Vicksburg, MS.

Teeter, A.M. (2001). “Clay-silt sediment modeling using multiple grain classes. Part I: Settling and deposition,” In: W.H. McAnally and A.J. Mehta (eds.), *Coastal and estuarine fine sediment processes*. 157-171.

Teeter, A.M. (2002). “Sediment dispersion near a dredge pipeline discharge in Laguna Madre, Texas,” ERDC TN-DOER-N17, U.S. Army Engineer Research and Development Center, Vicksburg, MS.

Teeter, A.M., and Pankow, W. (1989a). "The Atchafalaya River Delta; Report 2, field data; settling characteristics of bay sediments," Technical Rep. HL-82-15. U.S. Army Engineer Waterways Experiment Station, Vicksburg, MS.

Teeter, A.M., and Pankow, W. (1989b). "Deposition and erosion testing on the composite dredged material sediment sample from New Bedford Harbor, Massachusetts," Technical Rep. HL-89-11, U.S. Army Engineer Waterways Experiment Station, Vicksburg, MS, 61 pp.

Teeter, A.M., Brown, G.L., Alexander, M.P., Callegan, C.J., Saruff, M..S., and McVan, D.C. (2002). "Wind-wave resuspension and circulation of sediment and dredged material in Laguna Madre, Texas," Final Draft Report. U.S. Army Engineering Research and Development Center, Vicksburg, MS.

Teeter, A.M., and Best, E.P. (2003). "Modeling wind-wave resuspension in a shallow reservoir: Peoria Lake, IL," In: K.J. Bathe (ed), *Computational Fluid and Solid Mechanics 2003*, Elsevier Science, Ltd., Oxford, England.

Teisson, C. (1991). "Cohesive suspended sediment transport: Feasibility and limitations of numerical modeling," *J. Hydraul. Res*. 29, 755-769.

Thorn, M.F.C., and Parsons J.G. (1980). "Erosion of cohesive sediments in estuaries: an engineering guide," Proc. Third Interna. Sympos. on Dredging Technol; paper F1, Bordeaux, France.

Toorman, E.A., and Berlamont, J.E. (1991). "A hindered settling model for the prediction of settling and consolidation of cohesive sediment," *Geo-Marine Letters* 11, 179-183.

Van Leussen, W. (1989). "Aggregation of particles, settling velocity of mud flocs - a review. In: J. Dronkers and W. van Leussen (ed.), *Physical processes in estuaries*, Springer-Verlag, N.Y.

Young, I.R., and Verhagen, L.A. (1996). "The growth of fetch limited waves in water of finite depth. Part 1: Total energy and peak frequency," *Coast. Engnr*. 29, 47-78.

Wu, J. (1980). "Wind-stress coefficients over seas surface near neutral conditions - a revisit," *J. Phys. Oceanogr*. 10, 727-739.

APPENDIX C: Value Engineering Plan Tests

As an add-on to the original scope of work, three additional plans were tested in the model. These plans came from a November-2003 Value Engineering (VE) workshop conducted by U.S. Army Engineer District, New Orleans (MVN), to identify possible solutions to the LAR Bar Channel maintenance problems[1]. These model tests were not part of the feasibility study. Three of the VE plans were selected by MVN for the model testing as described herein.

The VE test procedure was to modify the numerical mesh to incorporate all necessary features in the horizontal plane. To install plan features, cell depths of this common base mesh were modified accordingly. A 24-ft-deep channel (project depth plus over-depth and advance maintenance allowances) was used as the main channel depth for all tests. Since MVN had collected additional shoal density information and since one of the plans involves density-dependent bed movement, the model bed structure was adjusted. This required a re-validation of the model since important sediment processes are related to bed density structure. Model tests used the same test period of 1 September 2001 to 31 August 2002 and the same boundary condition specification as described in the main report. Since only minor modifications to mesh resolution were made, it was not necessary to re-validate the hydrodynamic model.

The three VE plans tested were: crossing channels, parallel channels, and a sloped channel reach. The rationale for the crossing channels was that east-west coastal currents would flow through the crossing channels and thereby sweep out the channel water column at these locations – destratifying the channel and decreasing sediment trapping. The rationale for the parallel channels was that suspended sediment moving laterally across the channel would deposit in the parallel channel first – reducing sediment supply to the channel. The rationale for the sloped channel and slump was that newly-deposited fluid mud would slide on the slope into the slump before gaining hydraulic shear strength – keeping the channel prism un-obstructed. Each plan was installed into a clean 24-ft-deep channel at the beginning of one-year water level, current, salinity, suspended sediment, and sedimentation simulations. Dredging was simulated only in the case of the sloped channel reach plan.

Description of Test Plans

The 24-ft-channel base mesh was modified from the original planform numerical mesh by creating two new columns and six new rows. The higher-resolution channel area for the new base mesh is shown in Figure C1.

The crosscut or crossing-channel plan consisted of six channel sections perpendicular to and crossing the existing project channel, each about 400-ft-wide by 24-

[1] GVI. (2003). "Value engineering report: Atchafalaya Bar Channel fluff and fluid mud study, Morgan City, Louisiana," CEMVN-04-01, GeoVal, Inc., San Diego, CA.

ft-deep by 1,200-ft-long with channel ends sloped 1:6 to ambient depths. The crosscuts were spaced fairly uniformly along the heaviest shoaling reach of the channel. The crosscut mesh bathymetry is shown in Figure C2.

The parallel channels plan consisted of two 70,000-ft-long by 300-ft-wide by 30-ft-deep channels parallel to and with centerlines offset 1,270 ft on each side from the project channel centerline. Two gaps were left at ambient depth in each parallel channel to allow for pipeline crossings. The parallel-channel mesh bathymetry is shown in Figure C3.

The sloped channel consisted of a channel reach 16,000-ft-long sloped from -24 ft at the downstream end to -36 ft at the upstream end. A 4,000-ft-long by 1,290-ft-wide by 44-ft-deep sump was located at the upstream end of the sloped channel reach. The volume of the sump was 1.53 Mcyd between –36 and –44 ft. The sloped channel reach was located on the upstream portion of the project channel shoal area (about channel stations 650+00 to 800+00 ft). The sloped-channel and sump mesh bathymetry is shown in Figure C4.

Re-validation of the Sediment Model

The MVN survey branch began collecting shoal density measurements in 2004 using a DensiTune® drop probe. Eight profiles were collected along the channel on 9 March 2004. This was the first information available on density from relatively deep within the shoal. A plot of those data indicated that the bed structure described in the main report had surface fluid mud layers too thin and deeper layers too thick. Field data, previous bed structure, and adjusted bed layer thickness are shown in Figure C5.

As mentioned earlier, adjusting bed structure required re-validation of the model. Erosion is particularly sensitive to bed density structure, and a new bed initialization was found by trial and error. Erosion parameters were not adjusted. Settling parameter *a1* was increased slightly to 0.9 mm/sec and C_{wl} decreased to 45 mg/l. The hindered settling reference Wh_o was reduced to 0.01 mm/sec. The fluid mud yield stress parameter *TUY1* was reduced to 10,000 Pa (from 16,320 Pa) based on the sensitivity tests described in the main report. All other sediment parameters were set as described in the main report.

The model was compared to ERDC suspended sediment data and to shoal information as in the previous validation. Model suspended sediment TSM and salinity data are compared to field data in Table C1. The entire ERDC data set was compared to the entire hourly model results in a statistical manner. The suspended sediment validation was slightly better than the original study. The root-mean-square difference between the 16^{th}, 50^{th}, and 84^{th} percentile values (n = 18) was 92 mg/l, slightly better than the original 99 mg/l.

The final shoal volume for the one-year simulation was 9.39 Mcyd, closer to the field range of 8.2 to 9.2 Mcyd than the original 7.02 Mcyd. The model shoal profile is presented in Figure C6 along with some field profiles. The shoal distribution is more like

the field distributions with respect to the peak location and smoothness than the original validation.

Additional bed-profile comparisons were made after simulating a seven-day, 30,000 cyd per day dredging event at one cell in the model. The dredging event started on day 170 after the shoal had grown to 6.5 Mcyd. Dredging in the model occurs instantaneously each day at midnight. Shoal profiles pre-dredging (-1 days), 1, 3, 5, and 6 days after the start of dredging are shown in Figure C7. Note that since the profiles were taken immediately after dredging, the day 1 profile was taken after the first two instantaneous dredgings of 30,000 cyd each. Immediately before any dredging occurred in the model, the volume in the cell dredged was 41,480 cyd. Immediately after dredging in the model, the cell volume dropped to 11,480. Within one hour, about 22,000 cyd of material slumped into the cell, mostly from adjacent cells. With time, most bed slopes decreased, especially during the first few days, as seen in Figure C7. The slopes immediately upstream and downstream of the cell appear to remain steep but this is an artifact related to the instantaneous dredging. Profiles immediately and one-hour after the last two dredgings are shown in Figure C8. Profiles one hour after dredging are more representative of most conditions and indicate fairly constant bed slopes. Slopes were about 0.0012 downstream and 0.0014 upstream of the hole created by the dredging. Immediately after dredging, slopes were much steeper, roughly 0.005.

Field surveys made along the channel centerline during dredging were compared to model results. The Dredge *Missouri H* moved downstream at roughly 600 ft per day in early 2002. Channel centerline profiles are shown in Figures C9 to C11. Dredging rates were 42,800, 71,800, and 76,100 cyd per day, respectively. The steeper slopes in the direction of dredge advance were about 0.003, 0.0048, and 0.0046, respectively. These slopes resemble the steep initial slopes of 0.005 in the model test. The trailing slopes from the field surveys were about 0.0017, 0.0020, and 0.0016, respectively. These resemble the final slopes in the model test.

Overall, the VE model re-validation was very good and slightly better than the original validation.

Test Procedures

As mentioned earlier, model tests of the three plans used the same initial and boundary conditions used in the previous model tests described in the main text. The simulation period was 1 September 2001 to 31 August 2002. Channel depths were initialized at 24 ft except for the sloped channel reach that had greater depths as part of the plan. No dredging was specified except for the case of the sloped channel where dredging of 80,000 cyd per day was specified over the sump to keep it clear and effective.

VE Test Results

Sediment and shoaling results for the VE base and plan runs are summarized in Table C2. ERDC- (A to F) and channel-station (CS, 480+00 to 1400+00) locations are shown in

Figure 2 of the main report. The ERDC data were collected 3 ft up from the bottom. The CS station data are also for 3 ft up from the channel bottom. Other terms are defined in the main report. Shoal volumes at 2,880, 5,016, and 8,500 hours were tabulated to allow comparisons to results presented in the main report. For the parallel channel case, the total shoal volume for all three channels is reported ("Project Shoal End"). Dredging was performed only in the sloped channel case and, in that case, only in the sump. The assumption was that the sump would be periodically dredged to keep the sloped channel effective. The amount actually dredged is limited to that material above –44 ft and was most often less than the prescribed volume. The total volume dredged is reported in Table C2 and averaged 20,100 cyd per day. However, during episodes of high shoaling, dredging did not always keep up with shoaling and some temporary shoal accumulation occurred. The final shoal volume above the sloped channel reach is also reported in Table C2 ("Project Shoal End").

Depth-averaged TSM model fields were averaged over the simulation period (n = 2880) and presented for the vicinity of the channel in Figures C12 to C15 for the VE base, crosscut, parallel and sloped channels, respectively. These plot indicate that the VE plans had only minor effects on TSM fields as compared to the structural alternative tests presented in the main report.

Salinity and channel stratification results are important indicators of channel conditions and trapping efficiency and are presented in Table C3. The crosscut channel plan had generally reduced channel salinities and stratification while the opposite was true for the parallel and sloped channel plans.

Channel shoal profiles at select times are presented in Figures C16 to C18. Profiles for the sloped and sump channel reach are shown in Figure C19. Note that some material accumulated at the downstream end of the slope hour 5016 but then eventually moved into the sump. At the end of simulation, the bed surface slope over the reach was about 0.0012 or 1:850. Shoal volume time histories for the VE base and plans are shown in Figure C20.

The crossing channel plan did reduce density (salinity) stratification in the channel (see Table C3), which was the main rationale for the plan. It's possible that the crosscuts allowed delivery of sediments more directly to the channel bottom (than in the base condition) offsetting the decreased stratification. Some reduced shoal heights can be seen at the crosscuts in Figure C17. The plan reduced the shoal volume by only 8.4 percent at the end of the simulation year (a shoal volume of 8.60 Mcyd compared to 9.39 Mcyds for the base condition). The average shoaling rate was 0.92 times the base-condition shoaling rate.

The parallel channel plan was most effective early in the simulation year when the trap channels were empty of sediment (see Figure C20). By the end of the year, the parallel channels had shoaled almost as much as the project channel so that the total shoal volume for all three channels was 22.8 Mcyd. The average shoaling rate in the project channel was 0.90 times that of the base condition. The parallel channel plan did reduce

suspended sediment concentrations in the area surrounding the project channel, which was the main rationale for the plan. The parallel channel plan reduced shoal volume by only 8.0 percent (or from 9.39 Mcyd base to 8.67 Mcyd) at the end of the simulation year. As described in the main report, the channel only traps roughly 3 of the 45 million dry-tons of sediment leaving the Atchafalaya Bay annually. Trapping substantial amounts of sediment before it can enter the channel is therefore a monumental task here.

For the sloped channel reach, dredging was simulated to keep the sump almost empty during the one-year period. Shoal height over all 20,000 ft of project channel length was affected by the plan. Shoal elevation for 15,000-ft of channel length remained below the -20 ft project prism throughout the simulation year. Over an additional 5,000 ft of channel, shoal height was reduced compared to the base condition. At the end of the simulation year, the total shoal volume above project channel and plan channel profile was 7.38 Mcyd or 21.4 percent less than the base condition. The 1.5-Mcyd sump was dredged a total of 6.93 Mcyd during the model simulation year. It appears the sump would require dredging about every three months on average but as frequently as every six weeks during periods of intense sedimentation (winter/spring). Density (salinity) stratification and salinity intrusion increased appreciably in the deeper portion of this plan. The average shoaling rate over the entire project channel was 1.72 times the base condition. The reason for the shoaling rate increase was that dredging was included in the calculation of the average shoaling rate in this case.

TABLE C1.
VE Re-validation to ERDC Data for All Model Hourly Values (n=8610)

		TSM, mg/l		Salinity, ppt	
Station (Field n)	Percentile	Field	Model	Field	Model
A (n=219)	16	27	25	8.05	17.29
	50	74	82	18.5	32.54
	84	256	280	26.7	34.46
	95	845	611	28.0	34.63
B (n=116)	16	25	24	13.7	17.47
	50	81	81	21.1	32.73
	84	199	271	27.7	34.45
	95	513	593	28.7	34.62
C (n=98)	16	35	22	15.5	7.35
	50	97	65	21.7	27.70
	84	310	207	26.9	33.81
	95	427	449	28.5	34.24
D (n=96)	16	35	24	10.2	8.65
	50	80	72	19.6	28.83
	84	187	239	26.8	33.84
	95	292	545	27.8	34.24
E (n=164)	16	39	44	1.41	0.31
	50	93	118	10.0	13.78
	84	212	386	22.5	30.73
	95	400	1146	26.2	32.79
F (n=158)	16	49	33	3.78	0.48
	50	133	85	12.5	14.34
	84	602	286	23.4	30.69
	95	1074	785	26.6	32.64

TABLE C2.
Sediment and Shoaling Results for VE Plans

Condition, Existing/Test		Base	Cross-Cut	Parallel	Sloped
TSM Stations, mg/l (std)	A	82 (3.1)	81 (3.1)	75 (3.0)	82 (3.1)
	B	81 (3.1)	78 (3.1)	75 (3.0)	80 (3.1)
	C	65 (2.9)	60 (2.9)	62 (2.8)	64 (2.9)
	D	72 (3.0)	69 (3.0)	68 (2.9)	71 (3.0)
	E	118 (2.9)	105 (3.1)	101 (3.1)	111 (3.0)
	F	85 (3.0)	84 (2.9)	81 (2.9)	84 (2.9)
CS TSM, mg/l (std)	480	252 (1.5)	263 (1.5)	254 (1.4)	320 (1.5)
	630	142 (2.4)	133 (2.7)	139 (2.4)	132 (2.2)
	762	128 (3.0)	110 (3.2)	113 (3.1)	111 (3.0)
	884	116 (3.4)	85 (3.4)	102 (3.3)	113 (3.3)
	1004	92 (3.4)	89 (3.4)	82 (3.5)	91 (3.4)
	1200	70 (3.6)	69 (3.6)	67 (3.4)	70 (3.6)
	1400	66 (3.6)	66 (3.7)	67 (3.6)	67 (3.7)
CS $\prod TSM / \overline{TSM}$ (std)	480	0.31 (1.7)	0.32 (1.6)	0.29 (1.7)	-0.79 (2.8)
	630	0.69 (0.9)	0.60 (0.8)	0.68 (0.9)	0.58 (1.2)
	762	1.17 (0.6)	0.99 (0.7)	1.11 (0.6)	0.99 (0.6)
	884	1.90 (0.7)	1.38 (0.8)	1.73 (0.7)	1.82 (0.7)
	1004	1.91 (0.4)	1.89 (0.5)	1.81 (0.5)	1.92 (0.4)
	1200	2.05 (0.4)	2.04 (0.4)	1.95 (0.4)	2.05 (0.4)
	1400	2.24 (0.7)	2.23 (0.8)	2.28 (0.5)	2.25 (0.7)
Total Dredging, Mcyd		0	0	0	6.93
Shoal Hr 2880, Mcyd		4.48	4.12	4.03	3.56
Shoal Hr 5016, Mcyd		8.56	7.91	7.82	7.22
Chnl. Shoal End Yr, Mcyd		9.39	8.60	8.67	7.38
Project Shoal End, Mcyd				22.81	1.15 (vs 1.81)

TABLE C3.
Salinity Results for VE Plans

Condition Existing/Plan		Base	Cross-Cut	Parallel	Sloped
Salinity Sta., ppt (std)	A	32.54 (0.5)	32.64 (0.5)	32.52 (0.5)	32.51 (0.5)
	B	32.73 (0.5)	32.92 (0.5)	32.74 (0.5)	32.68 (0.5)
	C	27.70 (1.0)	27.23 (1.0)	27.99 (0.9)	27.67 (0.9)
	D	28.83 (0.9)	28.60 (0.9)	28.86 (0.9)	28.68 (0.9)
	E	13.78 (2.2)	12.87 (2.3)	14.51 (2.1)	13.77 (2.2)
	F	14.34 (2.1)	13.90 (2.2)	14.28 (2.1)	13.58 (2.2)
CS Salinity, ppt (std)	480	0.17 (142.2)	0.14 (157.7)	0.17 (155.6)	0.00 (*)
	630	5.14 (5.9)	3.95 (6.7)	6.46 (4.8)	16.67 (1.8)
	762	17.48 (1.9)	15.05 (2.1)	19.13 (1.7)	21.81 (1.4)
	884	30.03 (0.8)	27.80 (0.9)	30.20 (0.8)	29.79 (0.8)
	1004	32.93 (0.5)	32.88 (0.5)	33.01 (0.4)	32.85 (0.5)
	1200	34.31 (0.3)	34.43 (0.3)	34.33 (0.3)	34.29 (0.3)
	1400	34.72 (0.2)	34.77 (0.1)	34.76 (0.1)	34.72 (0.2)
CS ΔS, ppt (std)	480	0.0 (*)	0.0 (*)	0.0 (*)	0.0 (*)
	630	0.67 (9.8)	0.41 (7.2)	1.14 (7.1)	3.97 (3.6)
	762	1.76 (2.6)	1.18 (2.4)	2.06 (2.9)	3.33 (2.8)
	884	1.52 (1.8)	1.12 (2.7)	1.63 (2.0)	1.43 (2.0)
	1004	1.21 (3.8)	1.06 (4.5)	1.22 (4.3)	1.14 (4.0)
	1200	0.56 (8.7)	0.43 (11.4)	0.56 (9.2)	0.55 (8.8)
	1400	0.23 (19.7)	0.14 (31.4)	0.25 (18.0)	0.23 (19.7)

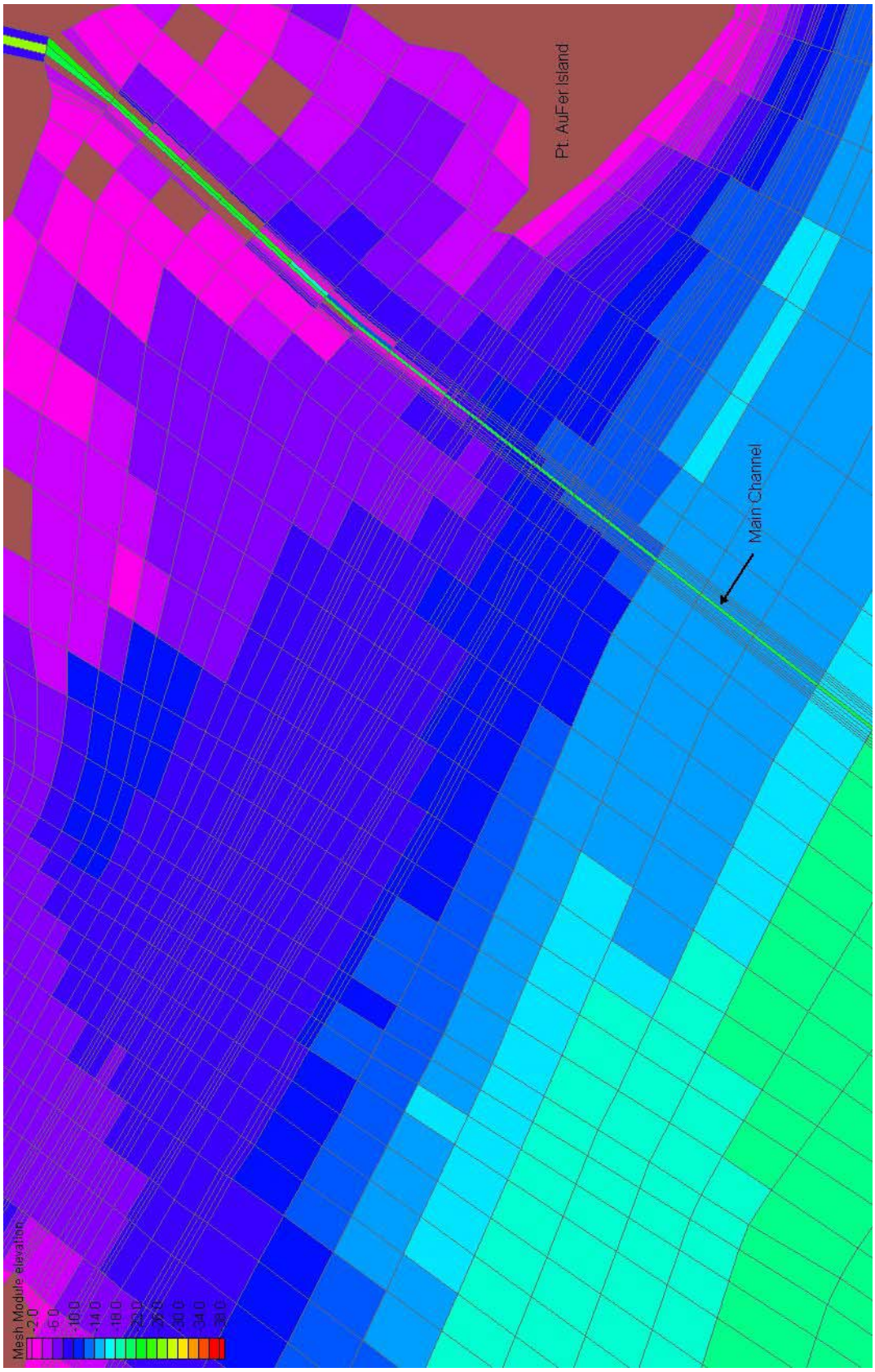

Figure C1. Base VE numerical mesh

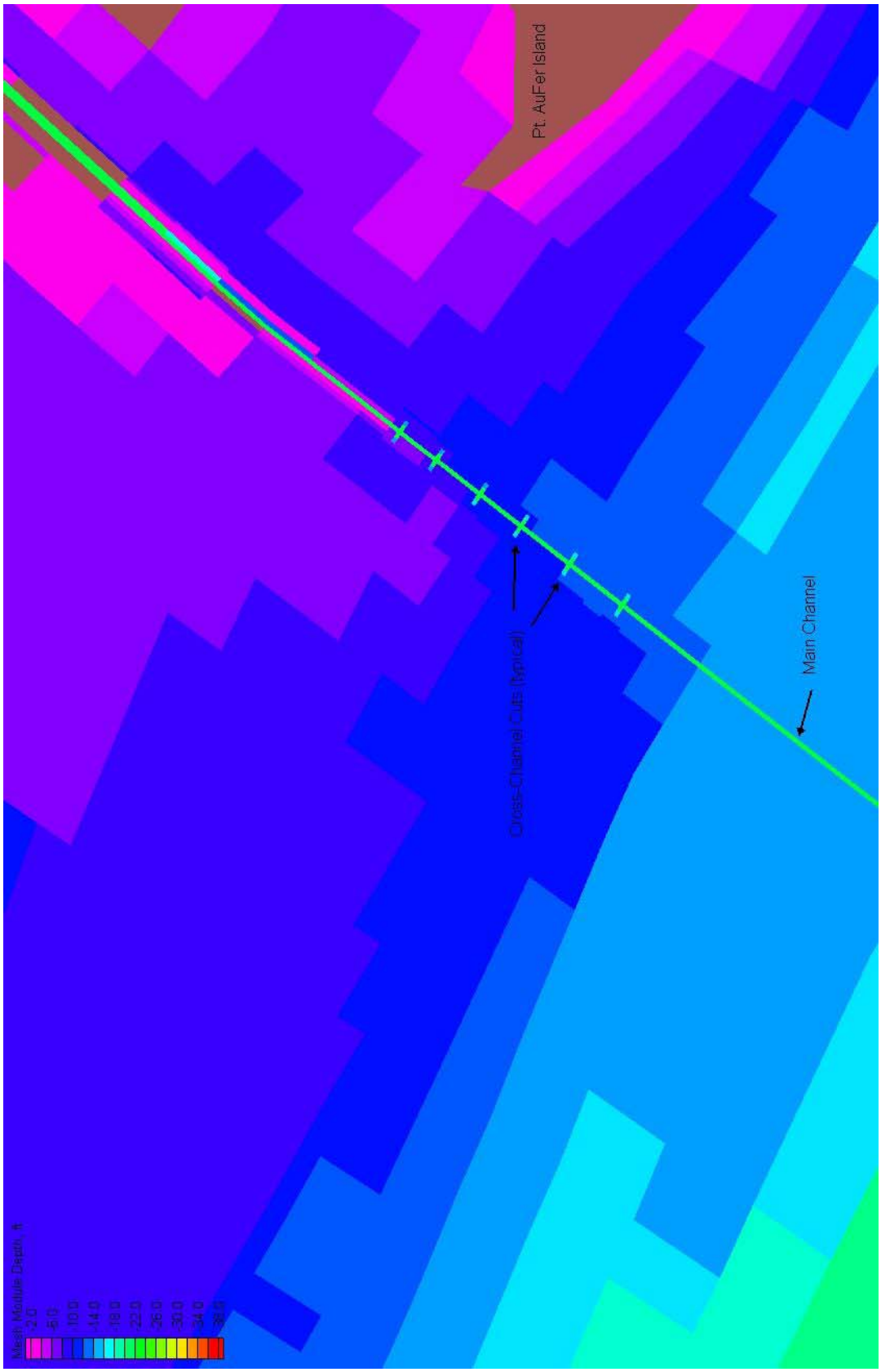

Figure C2. Crosscut channel bathymetry

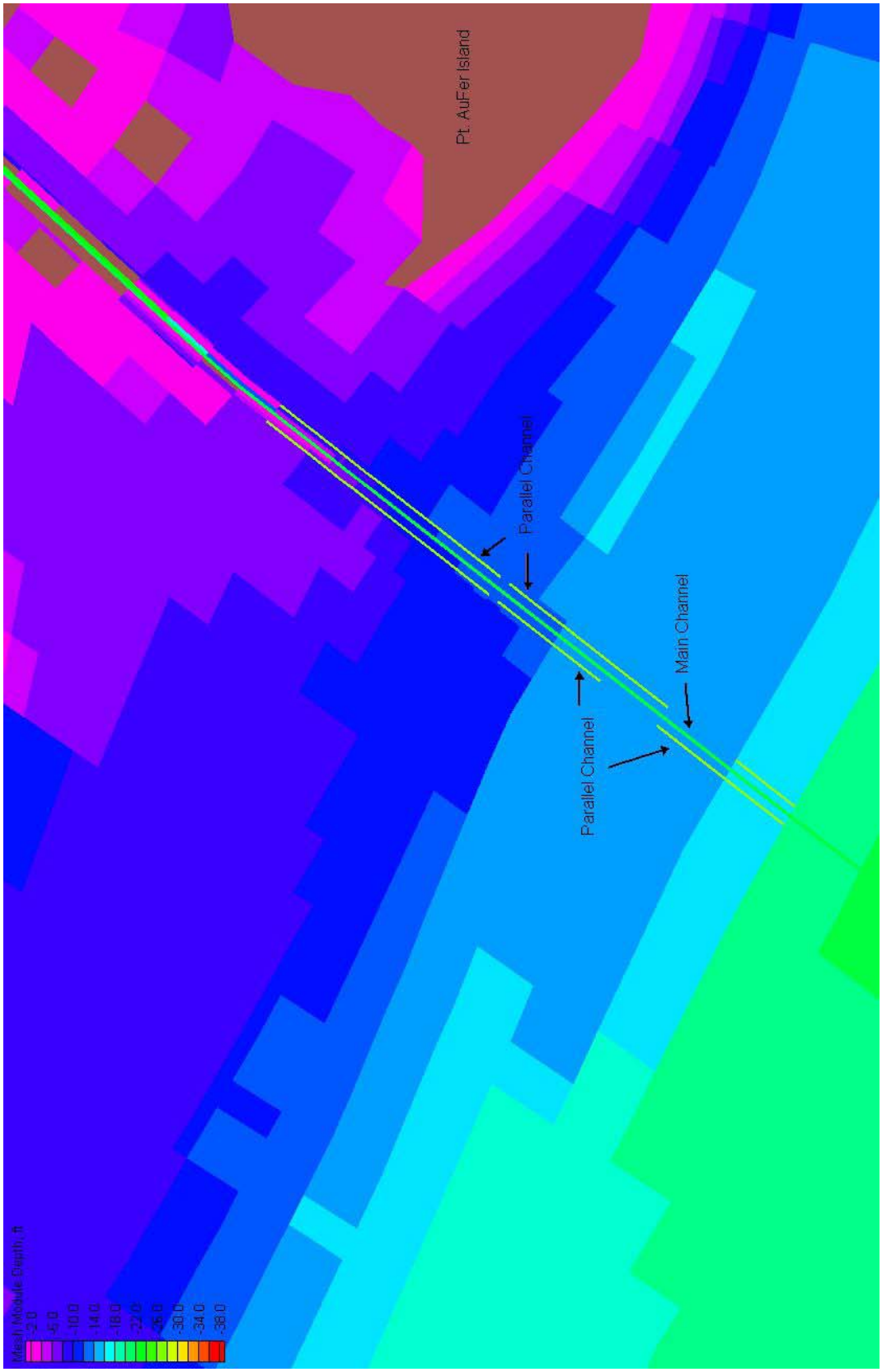

Figure C3. Parallel channel plan bathymetry

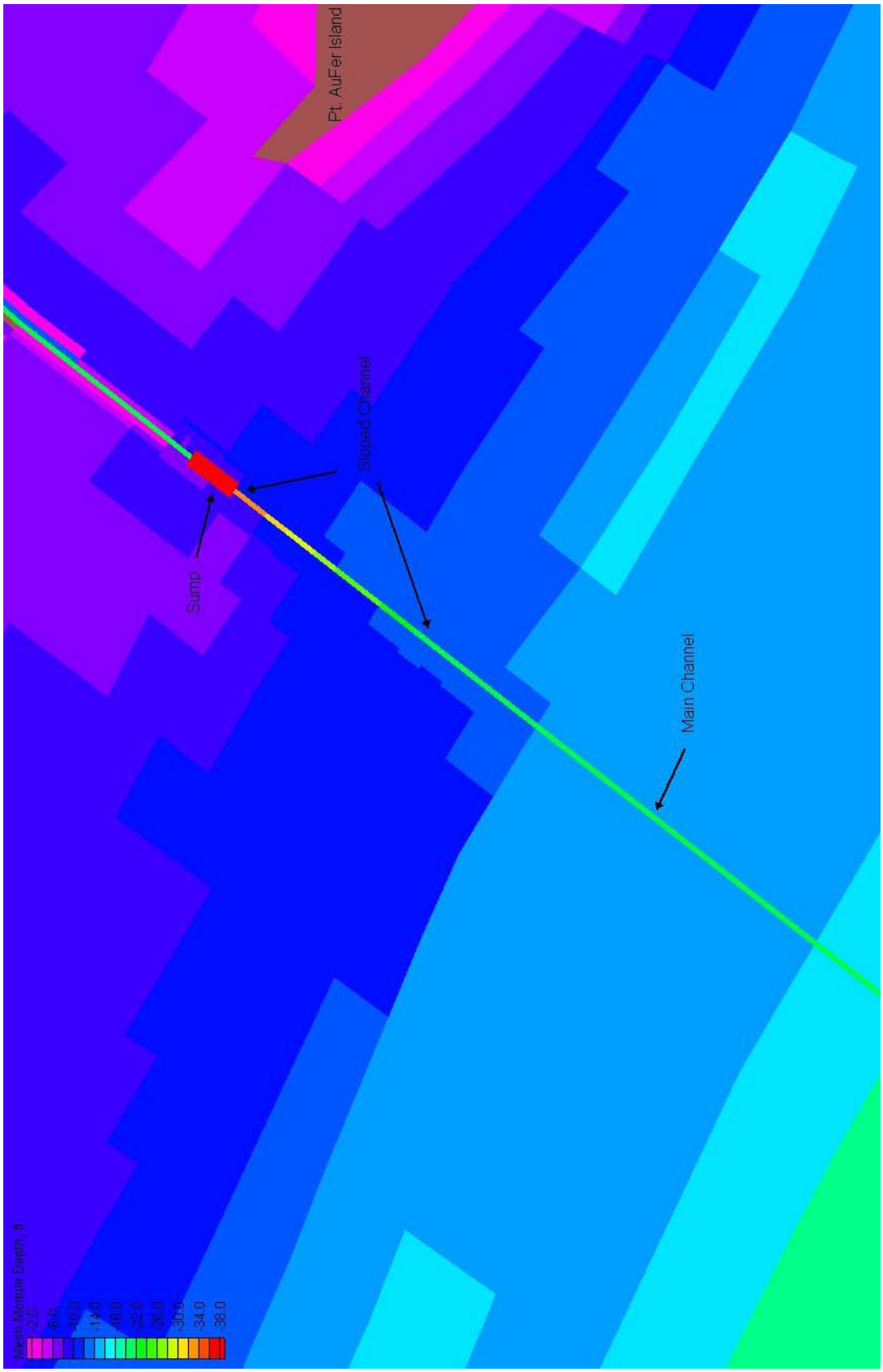

Figure C4. Sloped channel plan bathymetry

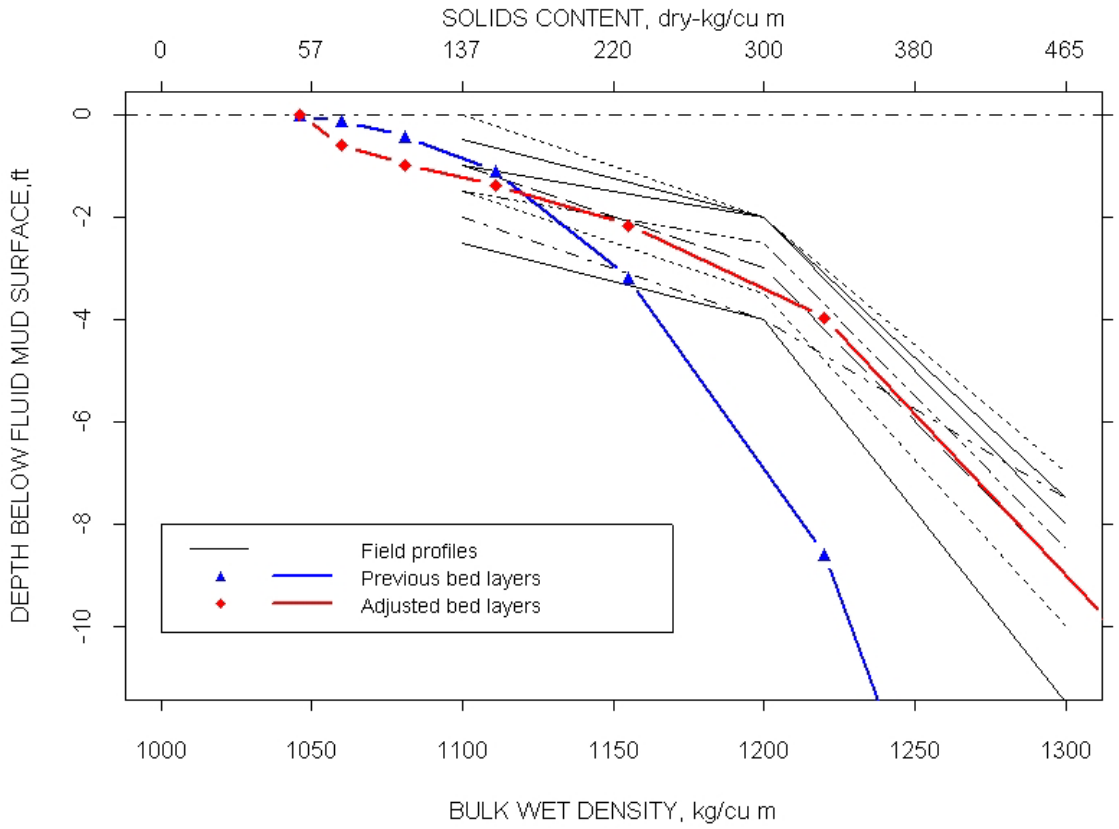

Figure C5. Field and model bed density structure

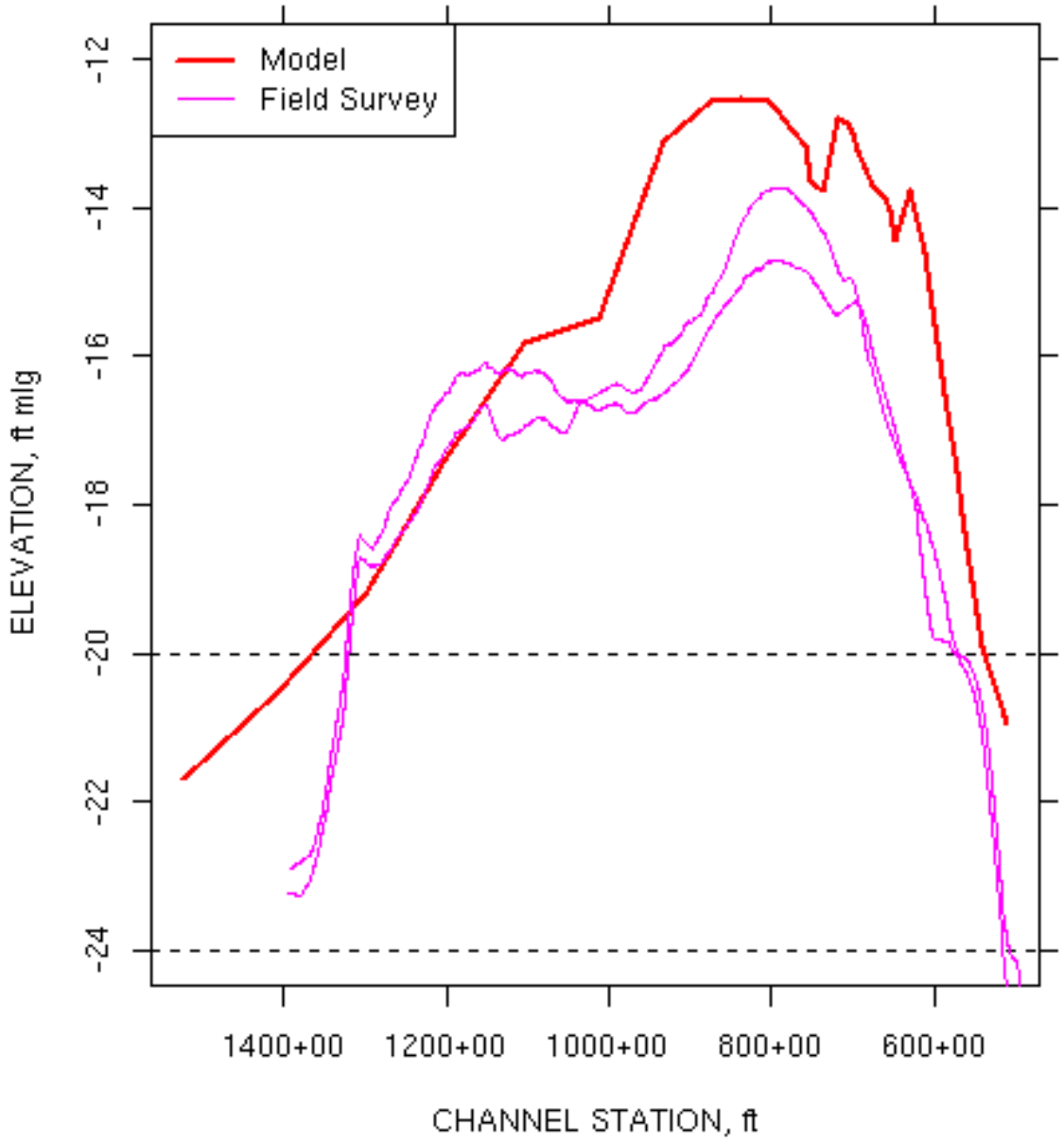

Figure C6. VE model validation shoal profile and field surveys from 05/06/02 and 7/16/02

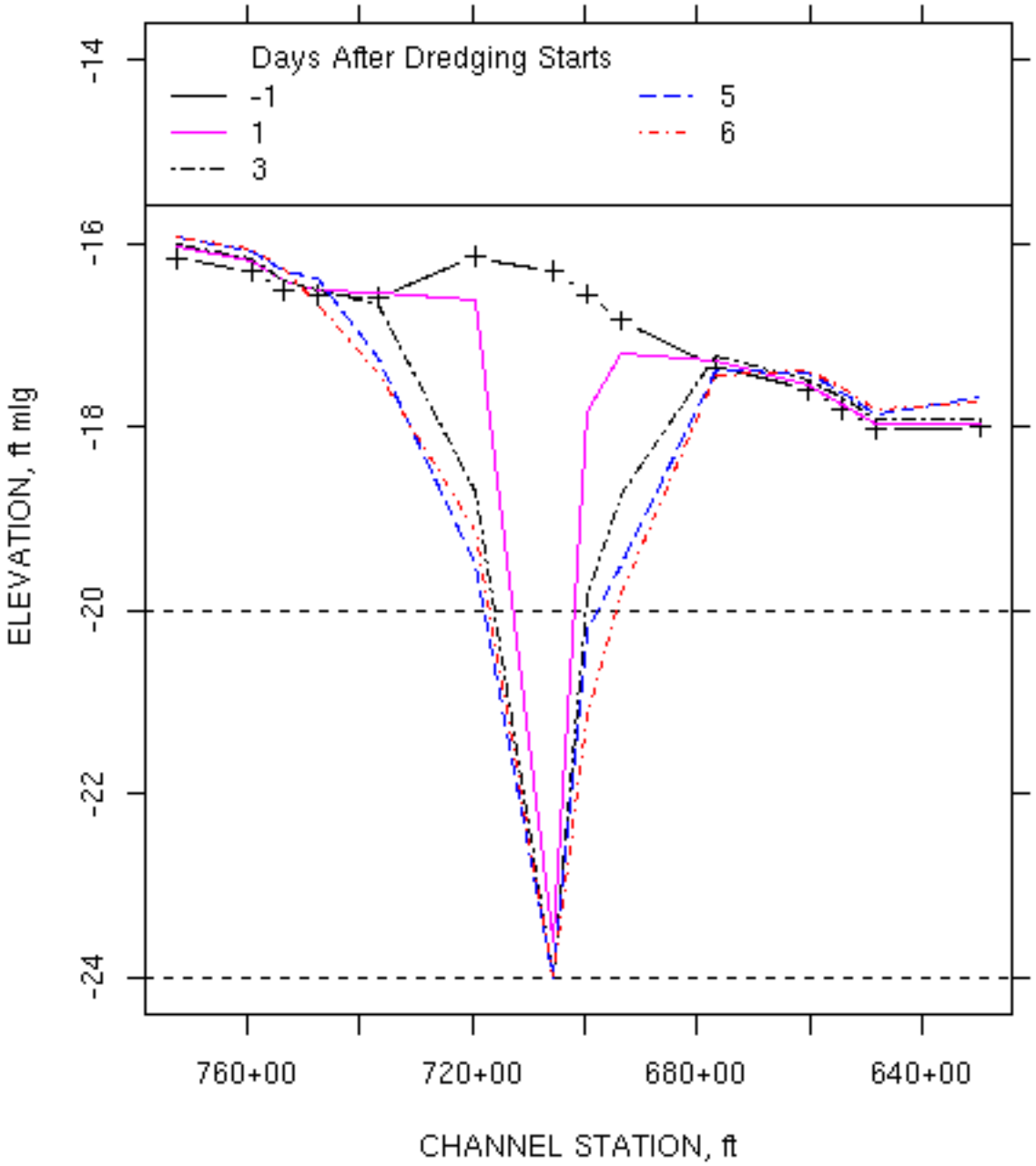

Figure C7. Bed profiles immediately after dredging (crosses on the pre-dredge line are cell centers)

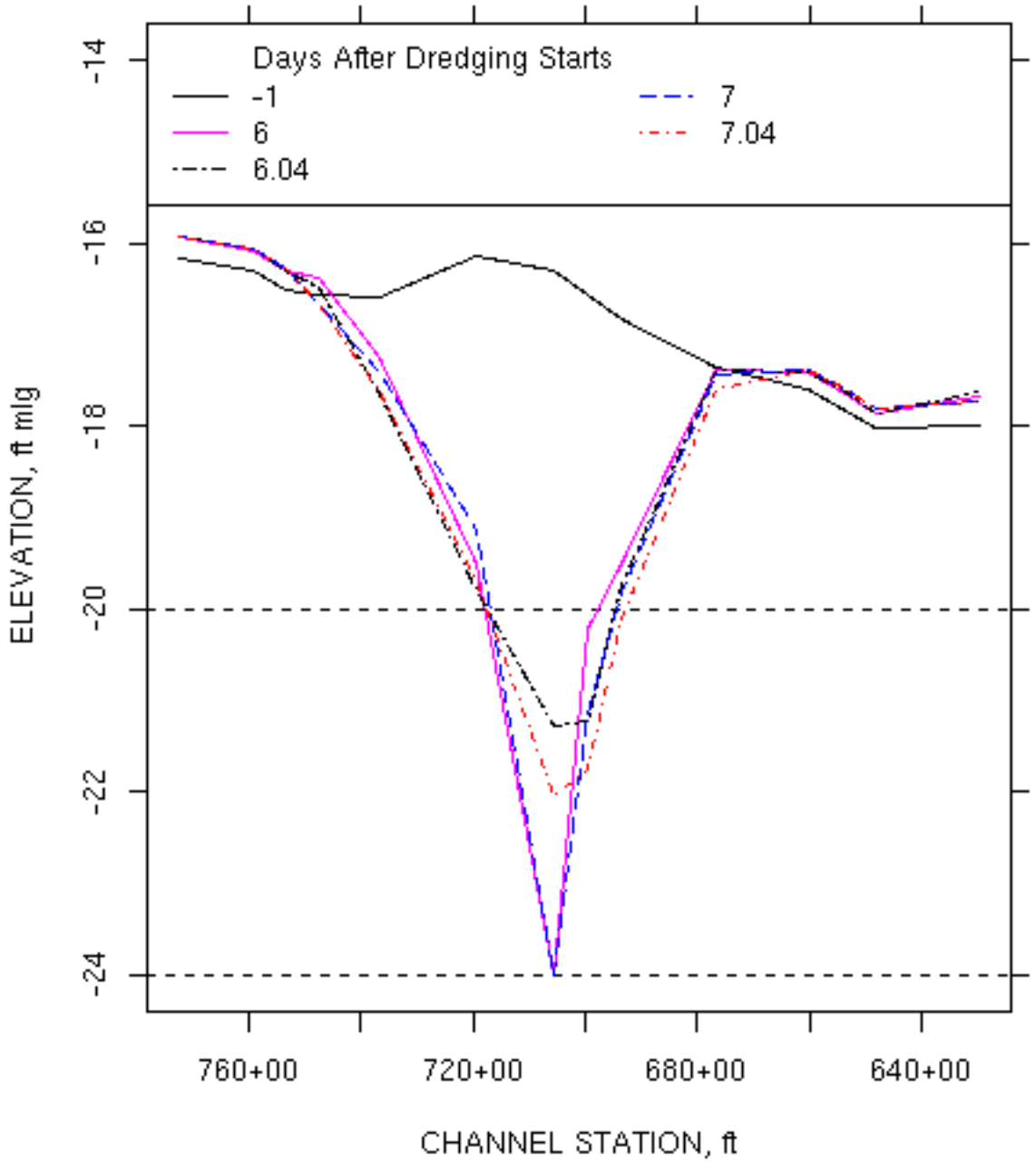

Figure C8. Profiles immediately and one-hour after dredging

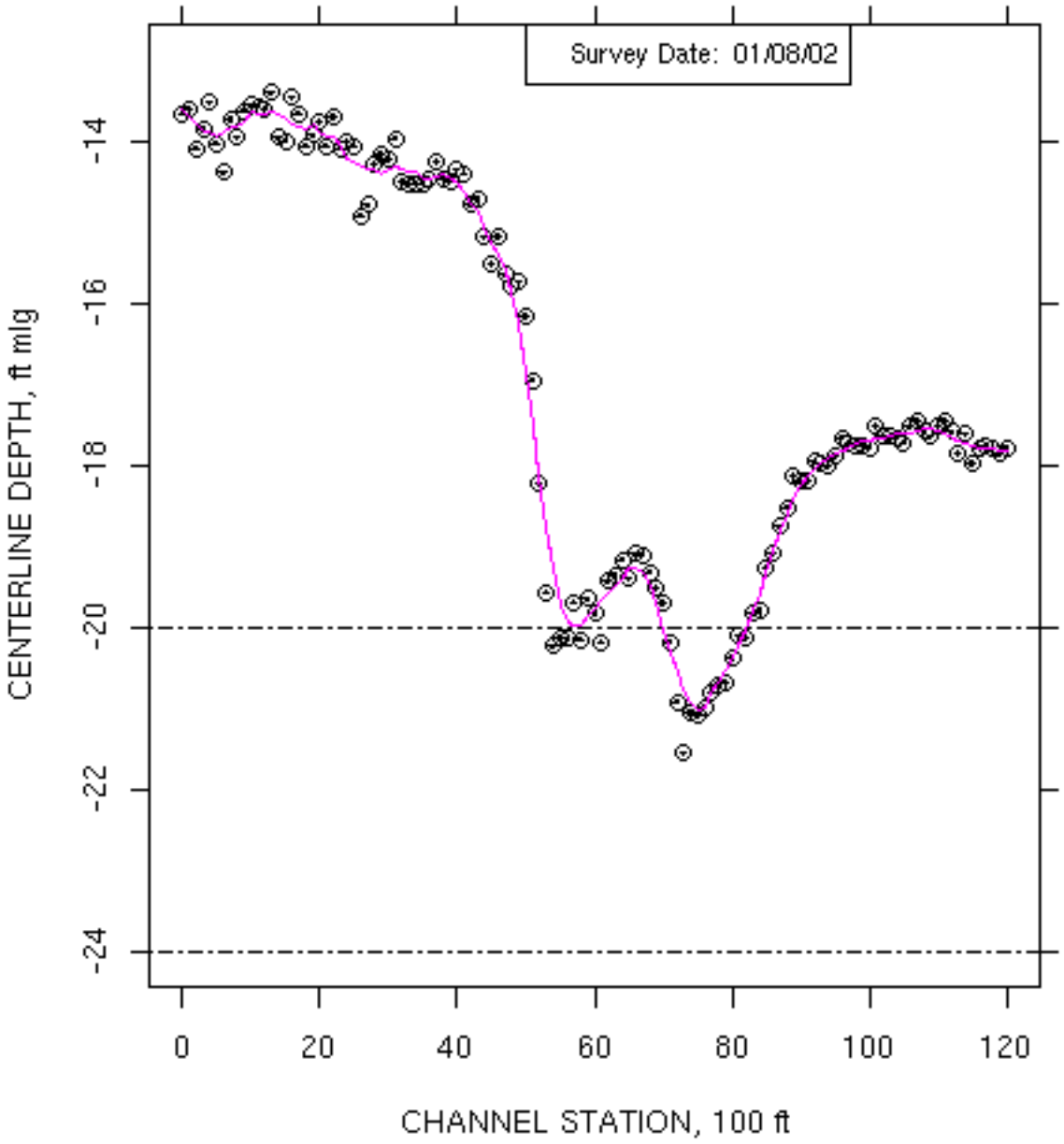

Figure C9. Centerline shoal profile from 01/08/02 near the Dredge *Missouri H*

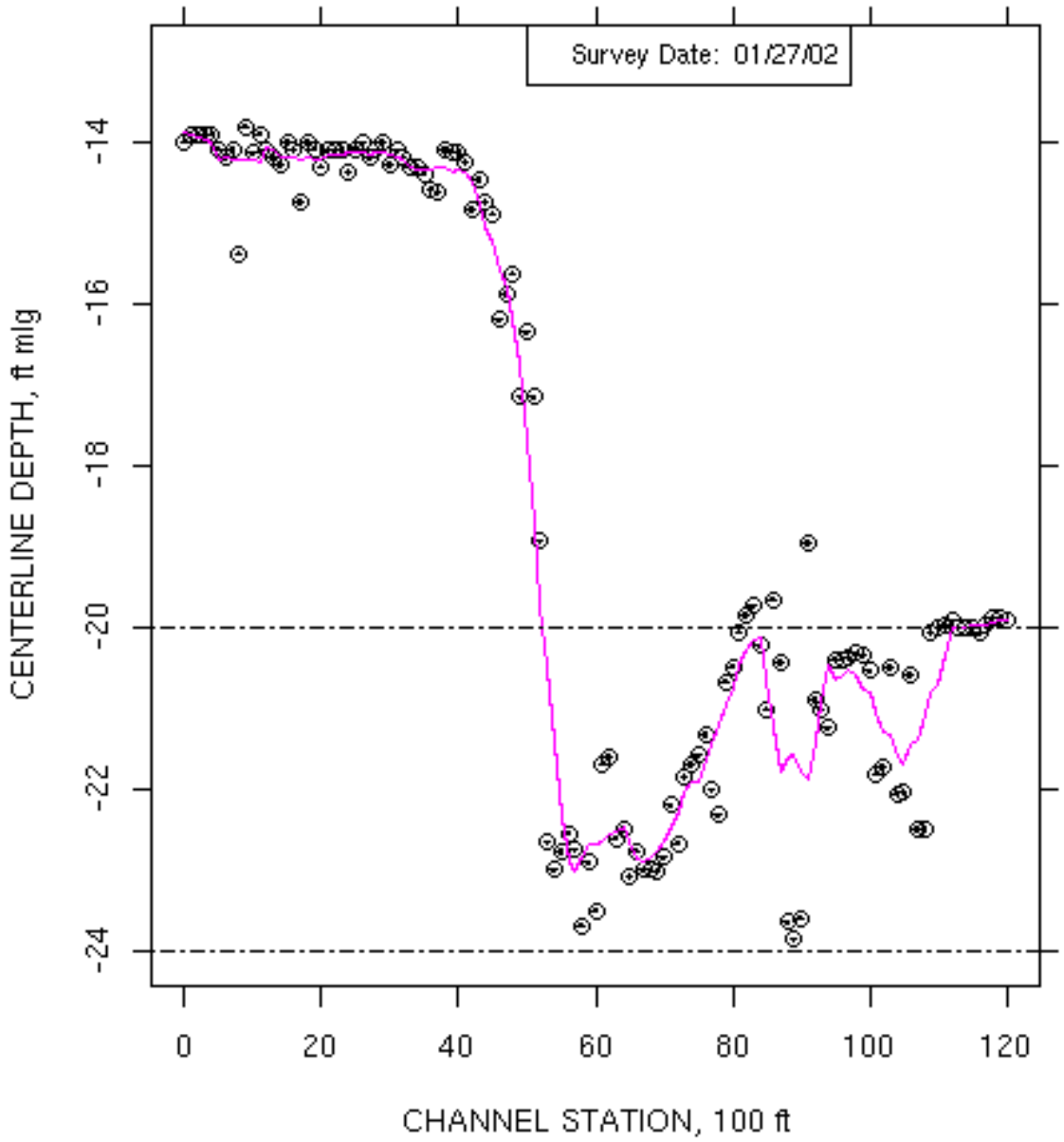

Figure C10. Centerline shoal profile from 01/27/02 near the Dredge *Missouri H*

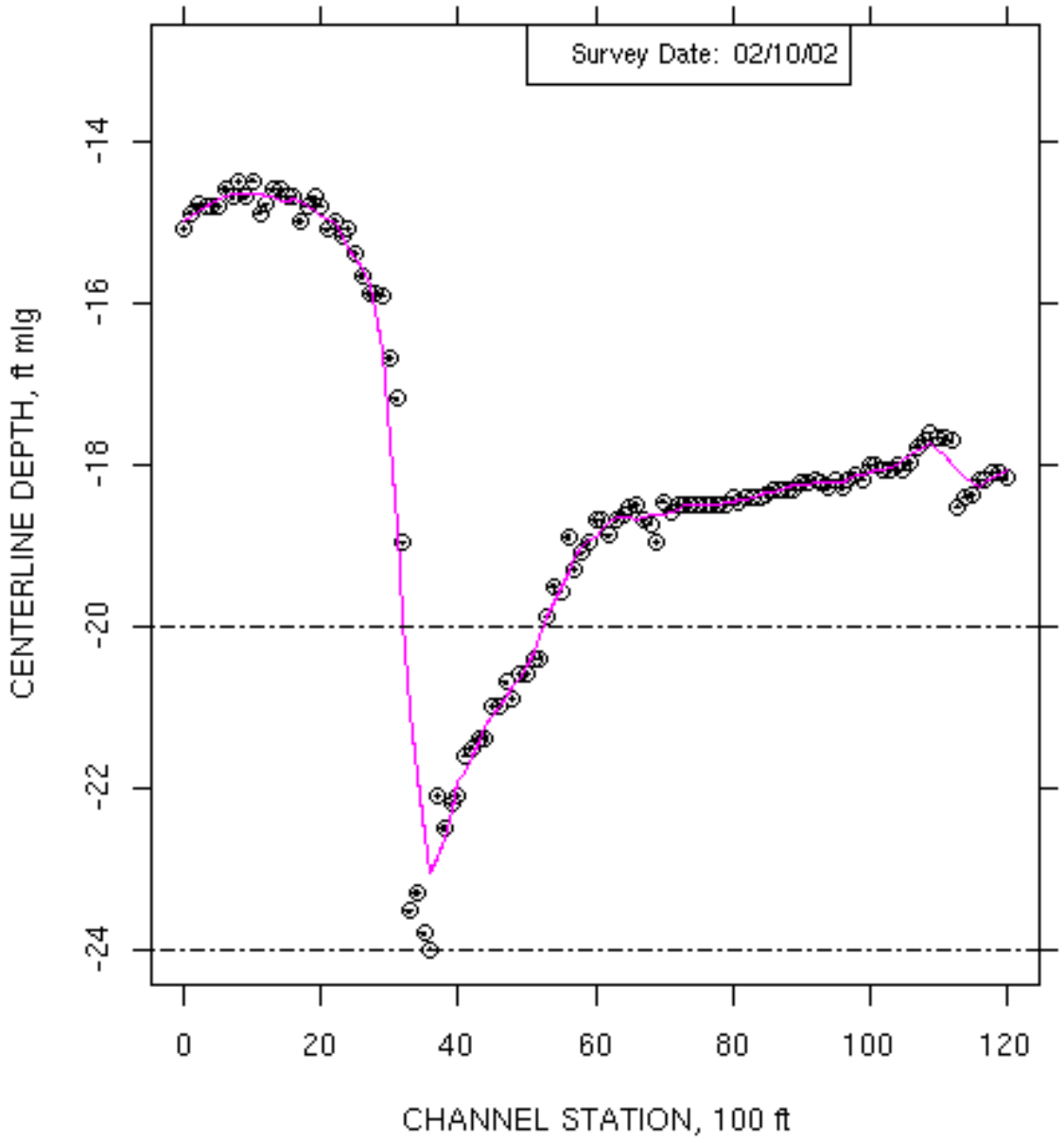

Figure C11. Centerline shoal profile for 02/10/02 near the Dredge *Missouri H*

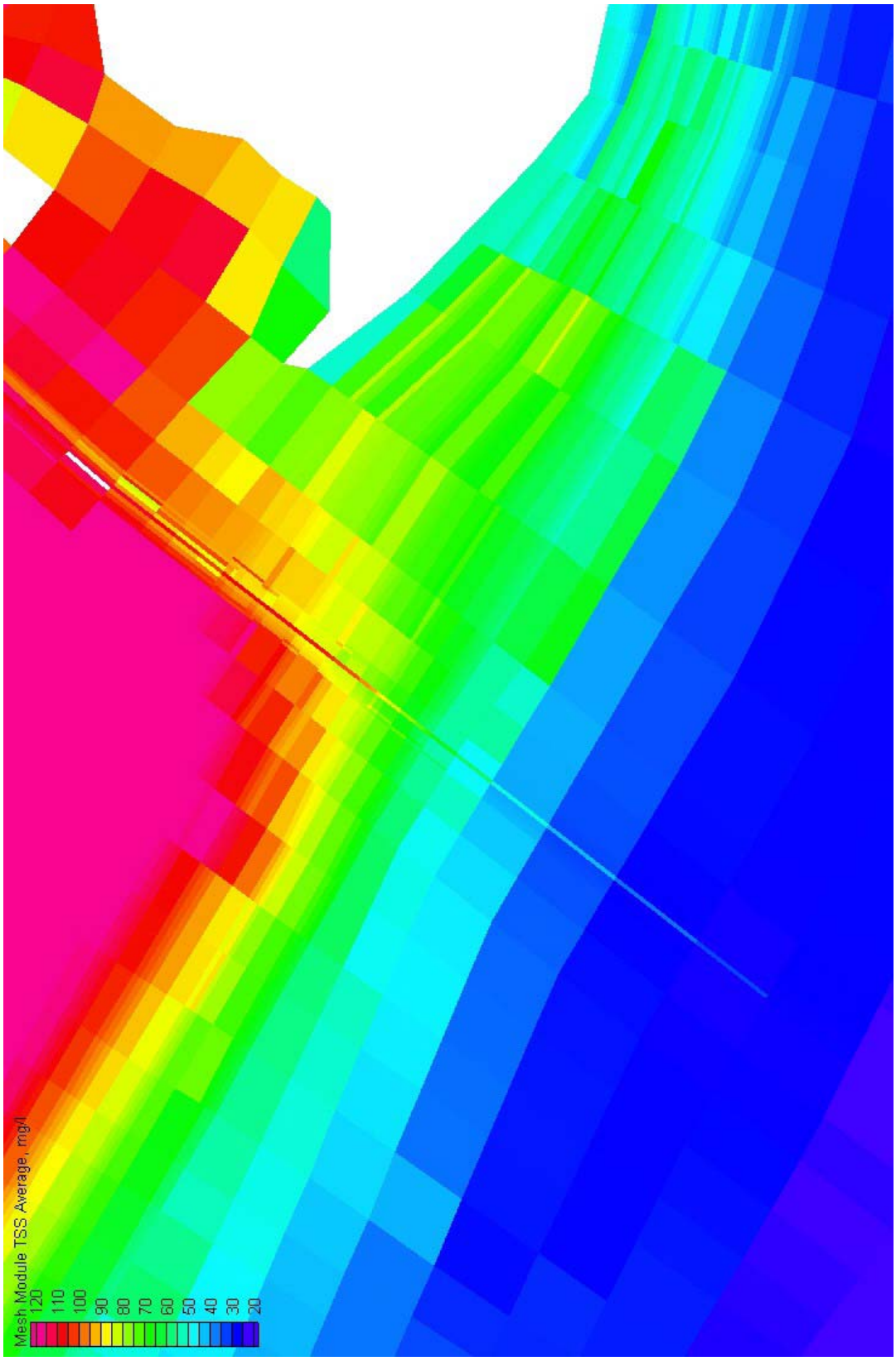

Figure C12. Time and depth average TSM for the VE base condition

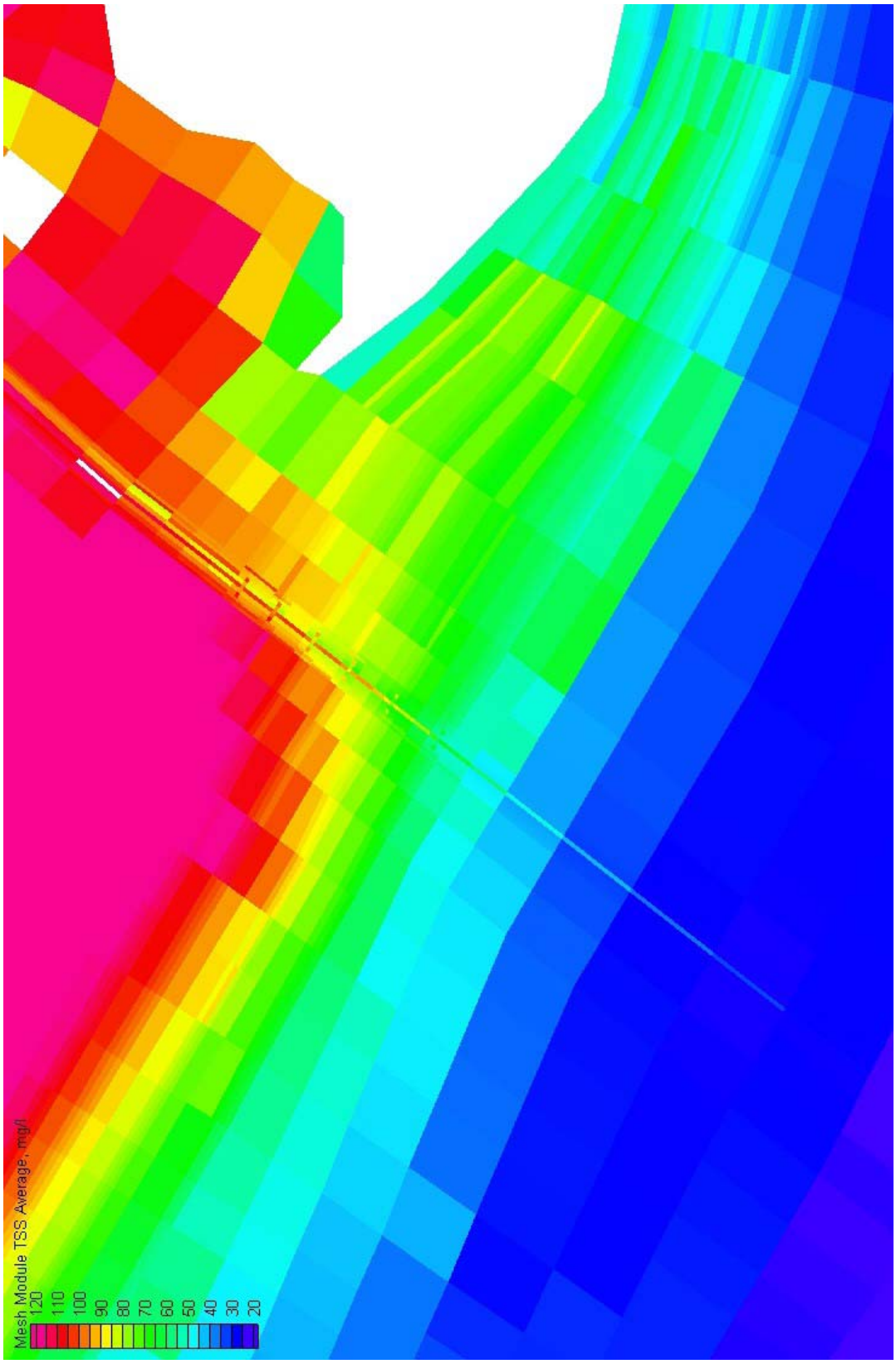

Figure C13. Time and depth averaged TSM for the crosscut VE plan

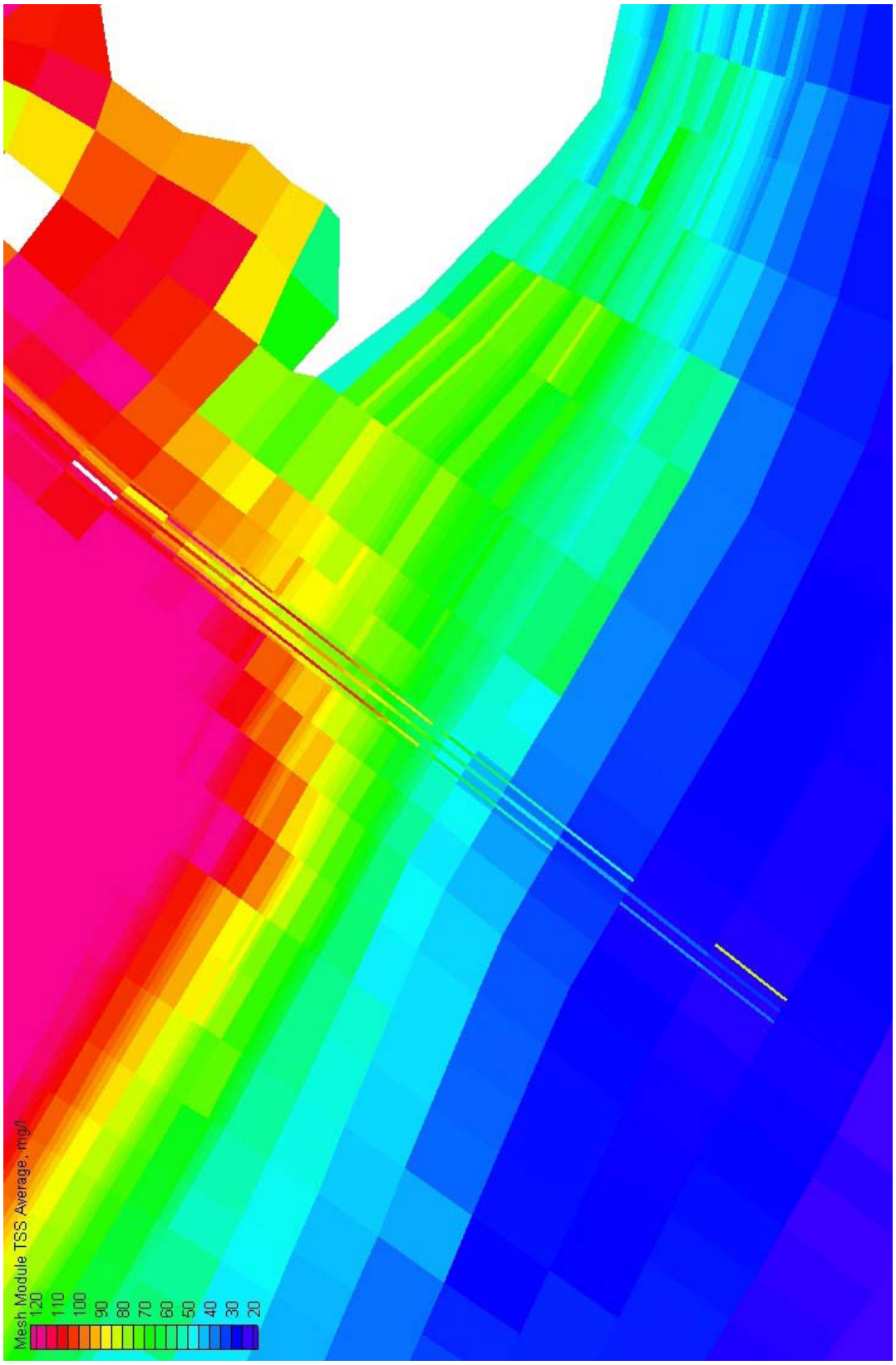

Figure C14. Time and depth averaged TSM for the parallel channel VE plan

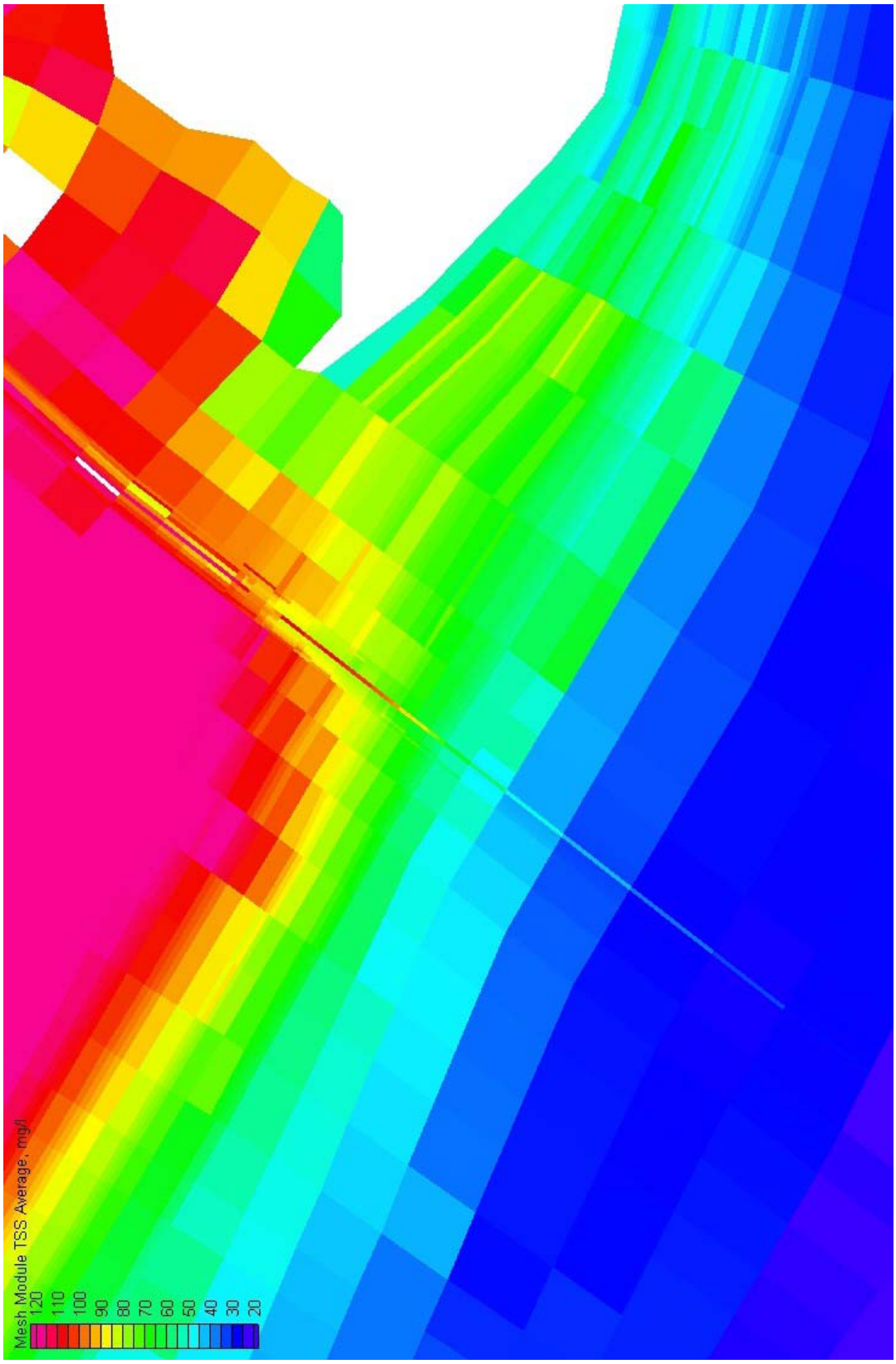

Figure C15. Time and depth averaged TSM for the sloped channel VE plan

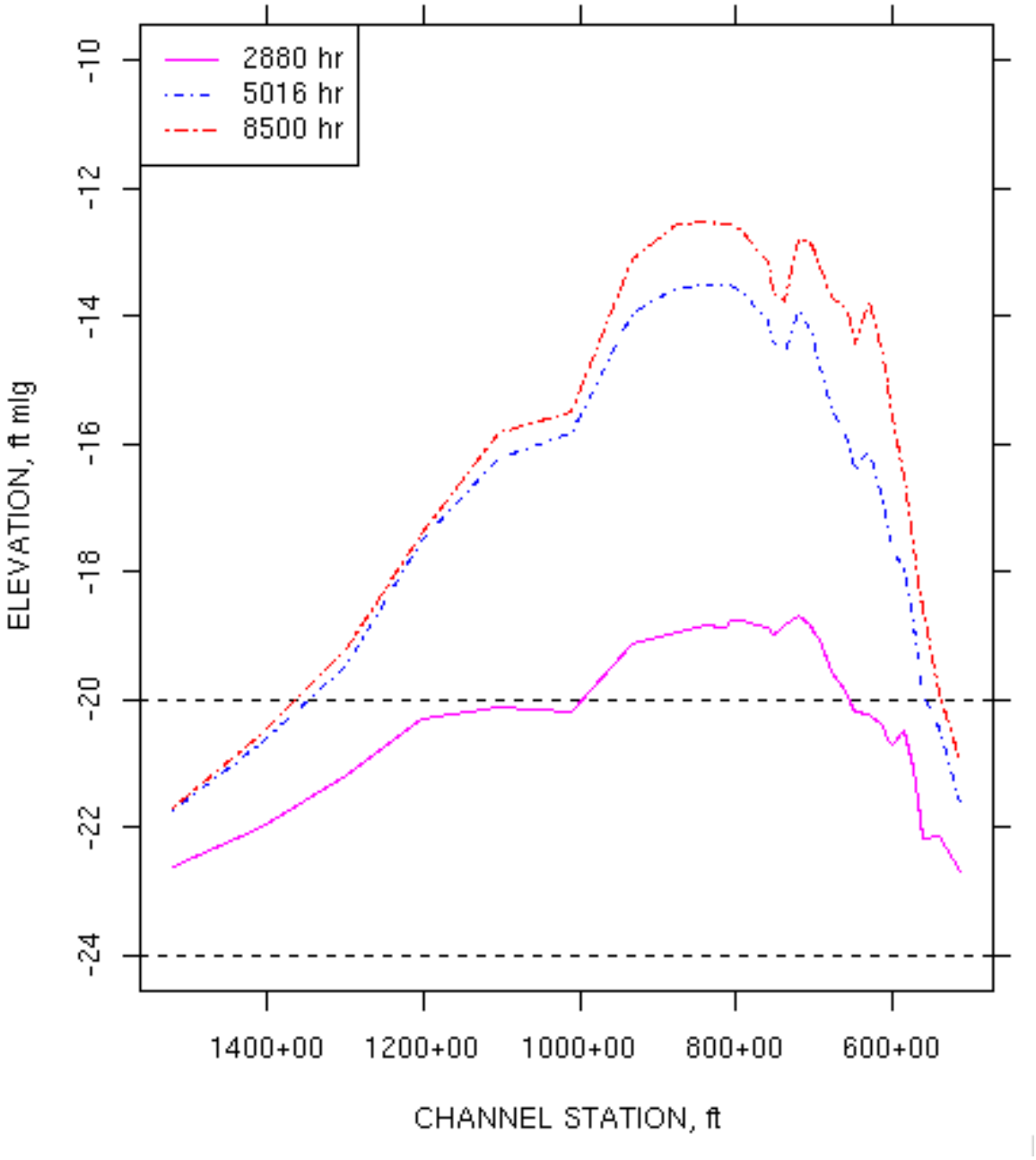

Figure C16. VE base condition shoal profiles at select times

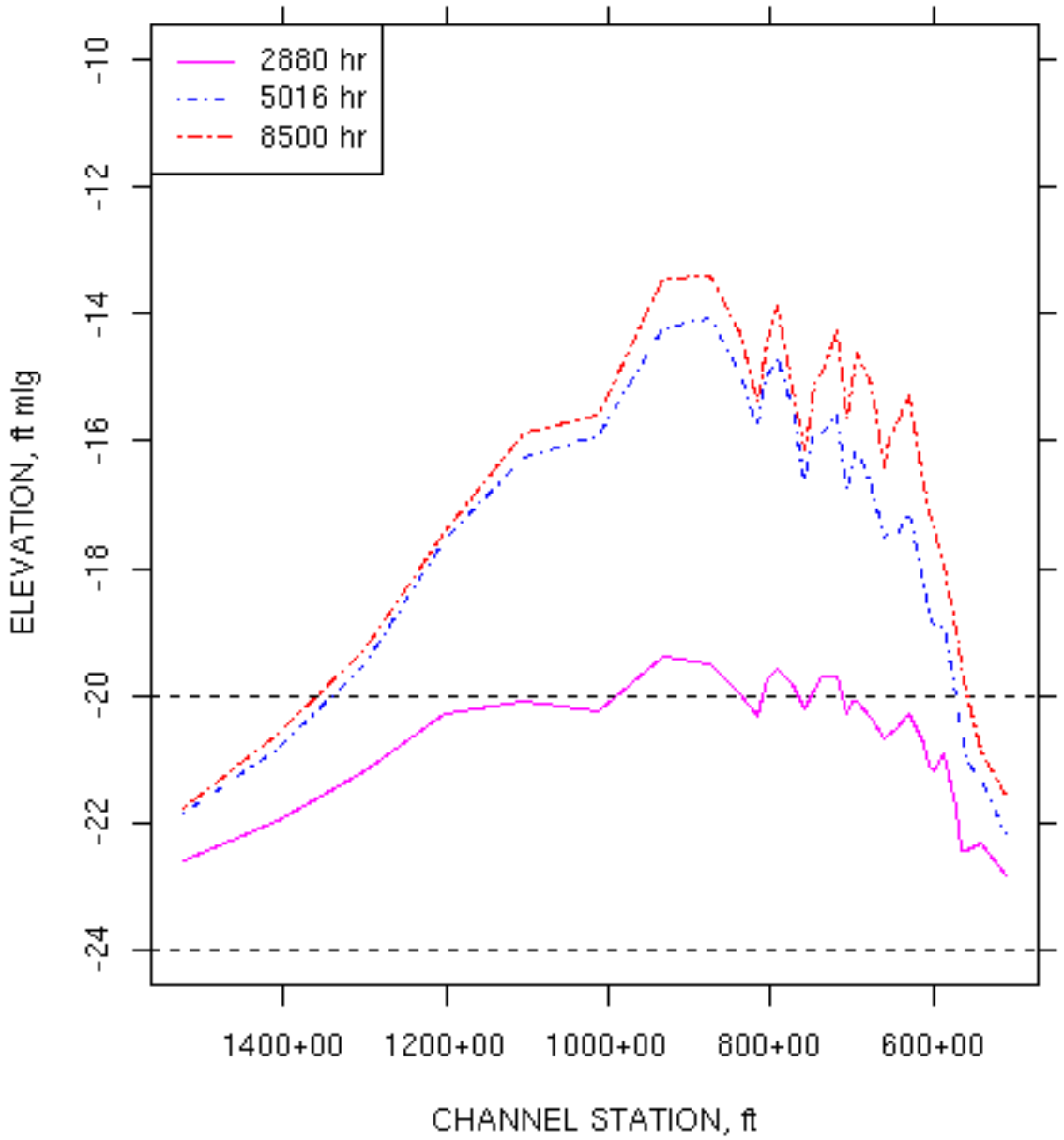

Figure C17. VE crosscut plan shoal profiles at select times

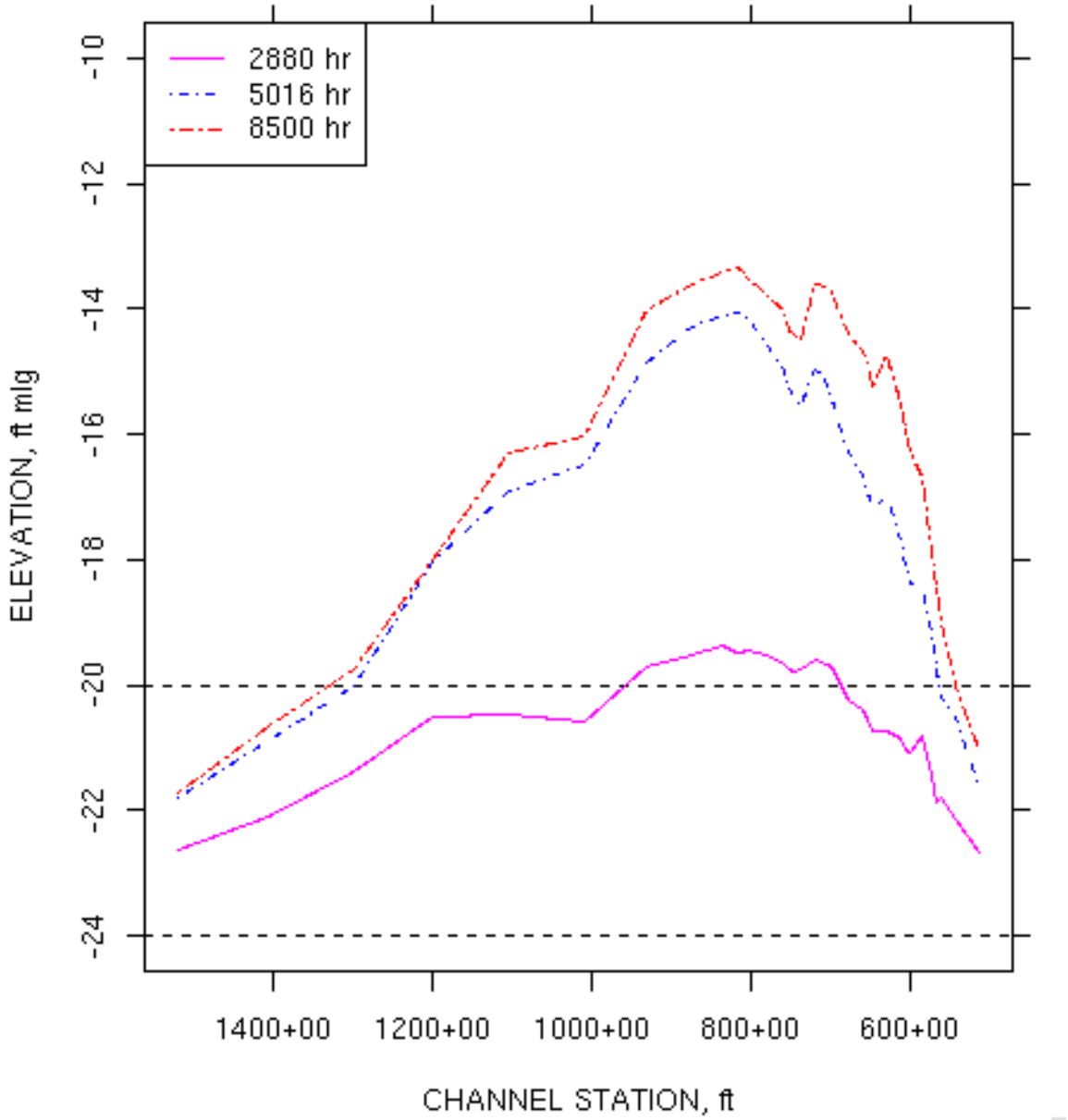

Figure C18. VE parallel channel plan shoal profiles at select times

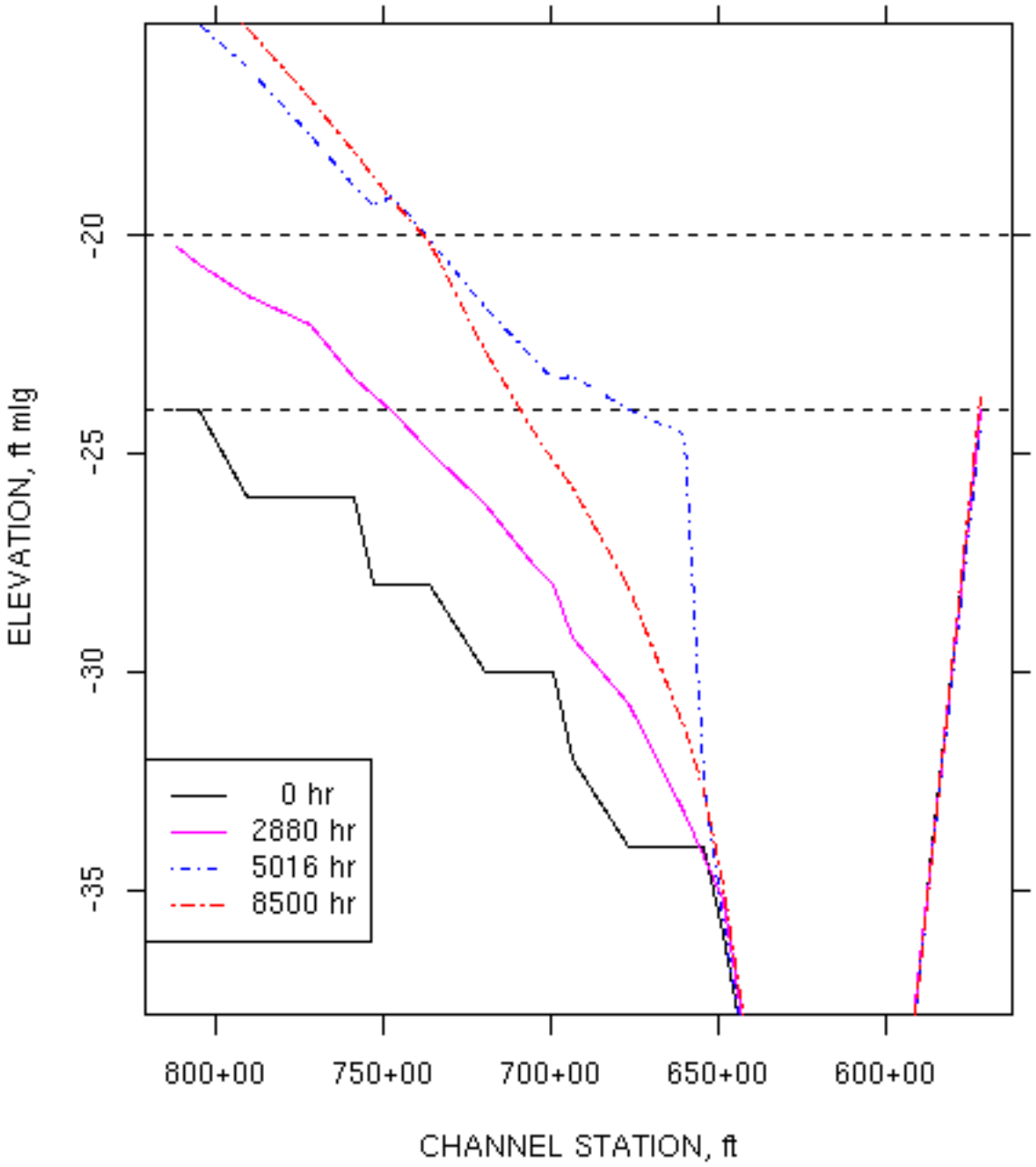

Figure C19. VE sloped channel reach plan bed and shoal profiles at select times

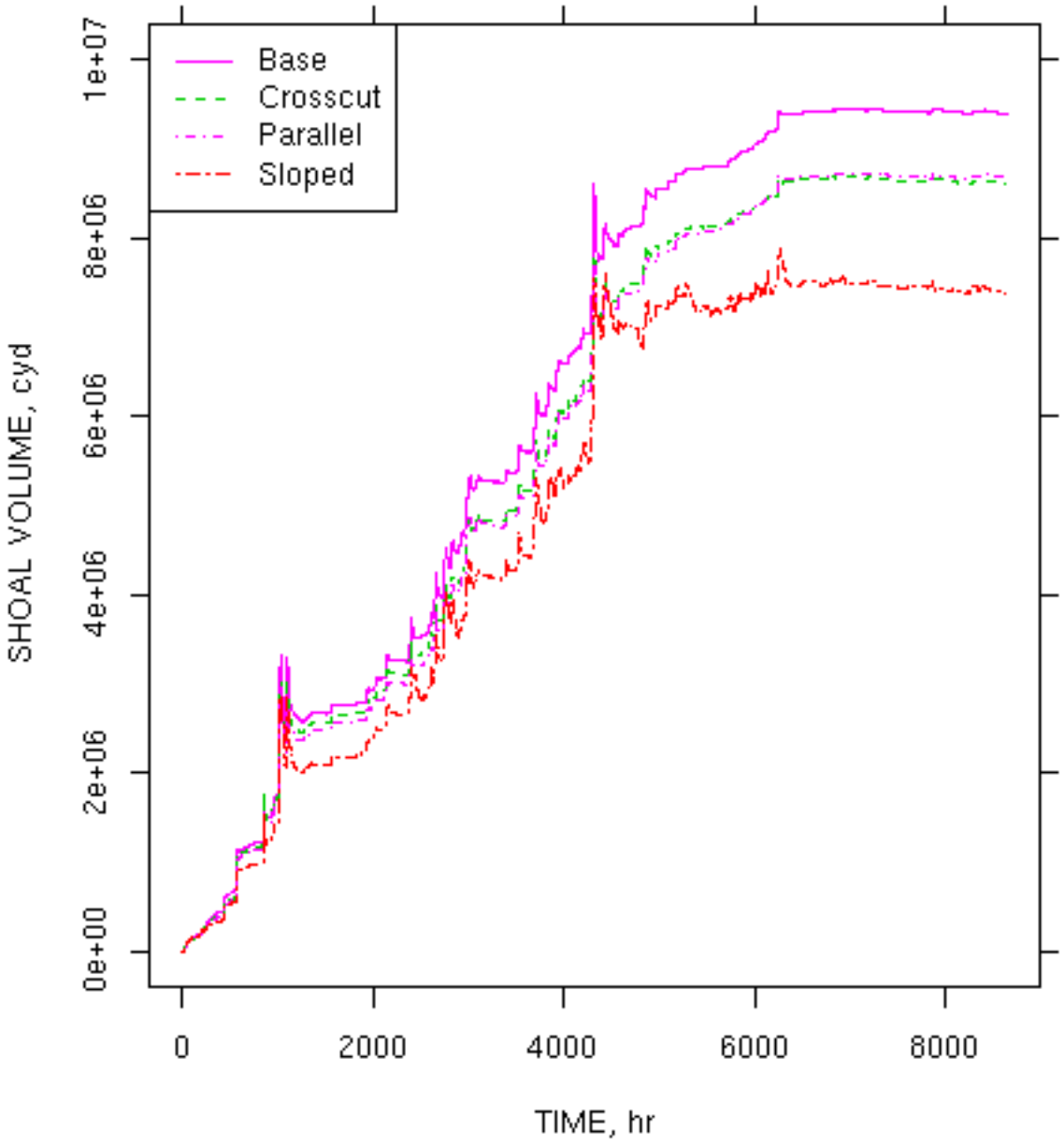

Figure C20. Shoal volume time histories for VE base and plans